

The University of Nottingham

UNITED KINGDOM · CHINA · MALAYSIA

Design of a High Performance Machine with an Innovative Cooling Method to Achieve the FreedomCar 2020 Traction Machine Targets

Adam Walker, MEng (Honours)

Thesis submitted to the University of Nottingham for the degree of Doctor of Philosophy

February 2017

Abstract

The thesis details a successful attempt at meeting the US Department of Energy FreedomCar 2020 targets. These targets include a set of challenging specifications for traction machines for hybrid electric vehicle applications. Previously the main barrier to achieving these targets was designing a machine which could meet the high speed efficiency targets whilst not sacrificing attaining the peak torque. The need for this high performance across a wide speed range is to allow for direct drive electric vehicles.

The thesis covers the design process for a machine to reach these targets from the very beginning, comparing machine topologies and technologies based on qualitative indices to decide which is the most appropriate. Next, interior permanent magnet machines are designed for these targets using the current technology standards and their shortcomings are highlighted. This leads into a permanent magnet assisted synchronous reluctance design, which improved the high speed efficiency but performed worse thermally. A large section of the thesis is dedicated to the innovative thermal management method used to push the boundaries of efficiency in this application. This discussion of the cooling method includes experimental proof of its potential and validated simulations supplementing this into the further machine design. Finally a more in-depth optimisation is performed for the electromagnetic design, with the new less restrictive thermal limits, which produces the ideal design, a permanent magnet assisted synchronous reluctance motor, for reaching the FreedomCar 2020 traction machine targets.

Acknowledgments

I want to thank all those who helped me achieve the challenging targets set for me and completing this difficult journey.

First of all I want to thank my supervisors Prof. Chris Gerada and Dr. Michael Galea for giving me the opportunity to work on this thesis and for supporting and encouraging me throughout the project and beyond.

As well as my internal supervisors, Dr. Salem Mebarki and Dr. David Gerada, from Cummins Generator Technologies through the majority of the project, provided insight and industrial awareness to my work whilst helping to guide the direction of my research.

I would like to show my appreciation to the PEMC research group, both the technical staff for making the experimental work possible and all of my colleagues for making the office and lab an enjoyable place to work.

Finally my friends and family for sustaining me throughout the whole PhD and constantly reminding me that there is more to life than my research.

Table of Contents

Chapter 1. Introduction 1

1.1 Aims and objectives 2
1.1.1 Aims 2
1.1.2 Objectives and anticipated project outcomes 2
1.2 Link to Cummins Generator Technologies 4
1.3 Thesis outline 4
1.3.1 Chapter 1 - Introduction 4
1.3.2 Chapter 2 - Background 4
1.3.3 Chapter 3 - Machine Topologies Study 4
1.3.4 Chapter 4 - Initial Machine Design 5
1.3.5 Chapter 5 - Initial PMa-SynRelM Design 5
1.3.6 Chapter 6 - Implementation of an Improved Thermal Management System 5
1.3.7 Chapter 7 - Final Machine Design 5
1.3.8 Chapter 8 - Conclusion 6
1.3.9 Appendices 6

Chapter 2. Background 7

2.1 Hybrid and fully electric vehicles 7
2.1.1 Background for the technology push 7
2.1.2 Challenges 8
2.1.3 Fully electric vehicles 11
2.1.4 Hybrid electric vehicles 13
2.1.5 Plug-in hybrid electric vehicles (PHEV) and range extender hybrid (REV) 15
2.1.6 Current initiatives related to electrification of cars 15
2.2 FreedomCar 2020 targets 16
2.3 Electrical machines 18
2.3.1 Magnetics 18
2.3.2 Machine classification 20
2.3.3 Materials and limitations 20
2.4 Previous attempts at the FreedomCar targets by others 25
2.4.1 High pole number SMPMSM 25
2.4.2 SMPMSM vs. IPMSM 25
2.4.3 V-shape IPMSM 29
2.4.4 Flux focusing machine 32
2.4.5 Summary of previous attempts 34

Chapter 3. Machine Topologies Study 36

3.1 Conventional motor types 36
3.1.1 Synchronous machine (SM) 36
3.1.2 Brushless direct current machines (BLDCM) 40
3.1.3 Induction machine (IM) 40

3.1.4 Switched reluctance machine (SRM) 41
3.2 Unconventional flux direction machines 43
3.2.1 Axial flux machines 43
3.2.2 Transverse flux machines (TFM) 44
3.3 Unconventional machine topologies 46
3.3.1 Flux switching machine (FSM) 46
3.3.2 Synchronous reluctance machine (SynRelM) 48
3.3.3 Synchronous–induction hybrid machine (SIM) 50
3.3.4 Flux memory motor (FMM) 51
3.3.5 Multi air gap machines 52
3.3.6 Synchronous homopolar motors 54
3.4 Comparison of machines technologies 56
3.5 Optimal machine topology for DoE FreedomCar 2020 targets 60
3.5.1 IPMSM rotor configurations 61

Chapter 4. Initial Machine Design 63

4.1 Introduction 63
4.2 Design considerations 63
4.2.1 Slot pole combination 63
4.2.2 Concentrated vs. distributed wound 64
4.2.3 Torque production 65
4.2.4 Phasor diagram 67
4.2.5 Torque ripple 69
4.3 Design process 70
4.3.1 Methodology 70
4.3.2 Initial designs 70
4.4 Concentrated wound designs 71
4.4.1 Initial range 72
4.4.2 Comparisons 74
4.4.3 Final concentrated slot pole combination 80
4.4.4 Finite element analysis 81
4.4.5 Selection of final concentrated wound slot pole combination 86
4.4.6 Final concentrated wound designs 87
4.4.7 Concentrated wound IPMSM summary 94
4.5 Distributed wound designs 94
4.5.1 Initial range 94
4.5.2 Comparisons of distributed wound IPMSMs 95
4.5.3 Slot pole combination comparison 100
4.5.4 Final distributed wound IPMSM design 101
4.5.5 Distributed wound IPMSM summary 102
4.6 Concentrated vs. distributed IPMSM comparison 103
4.6.1 Torque, voltage and current 104
4.6.2 Efficiency 104
4.6.3 Breakdown of Losses 105
4.6.4 Temperature 107
4.6.5 IPMSM comparison summary 107

4.7 Conclusions 108
4.7.1 Comparison to the FreedomCar 2020 targets 108
4.7.2 Summary of key findings and contributions 110
4.7.3 Next Steps 110

Chapter 5. Initial PMa-SynRelM Design 111
5.1 Introduction 111
5.2 Design process 111
5.3 Comparison to IPMSM 112
5.3.1 Current and advance angle 113
5.3.2 Efficiency 114
5.3.3 Loss break down 115
5.3.4 Thermal 117
5.4 Conclusion 117

Chapter 6. Implementation of an Improved Thermal Management System 119
6.1 Introduction 119
6.2 Concepts for improved thermal management 120
6.2.1 Pipe cooling 121
6.2.2 Potting compound 123
6.2.3 Altering the pipe position 124
6.2.4 Using multiple pipes 125
6.2.5 Redesigned end windings 125
6.2.6 Qualitative comparison to existing solutions 126
6.3 Initial thermal simulations 127
6.3.1 Thermal theory 128
6.3.2 Lumped parameter thermal network 131
6.3.3 Results 135
6.3.4 Uncertainties 136
6.4 Experimental validation 137
6.4.1 Tests 137
6.4.2 Experimental results 139
6.4.3 Comparisons 147
6.5 Calibration of thermal networks 148
6.5.1 Dummy stator thermal model 149
6.5.2 Optimisation 149
6.6 Application to a full machine 150
6.6.1 Silicone pipe on the end winding surface 150
6.6.2 Copper pipe in potting compound 152
6.6.3 Silicone pipe with modified end windings 153
6.6.4 Comparison 154
6.7 Conclusion 154

Chapter 7. Final Machine Design 157
7.1 Introduction 157

7.2 Optimisation of PMa-SynRelM design 157
7.2.1 Maximising reluctance torque 157
7.2.2 Minimising magnet mass 159
7.2.3 Minimising losses 161
7.3 Final design geometry 166
7.3.1 Rotor geometry 169
7.3.2 Stator geometry 172
7.4 Finite element results 174
7.4.1 3D Finite Element Results 181
7.5 Comparison to previous designs 183
7.6 Comparison to attempts by others 186
7.7 Construction 188
7.8 Conclusion 188

Chapter 8. Conclusion 191

8.1 Project summary 191
8.2 Key findings and contributions 192
8.2.1 Performance enhancement methodology 193
8.2.2 FreedomCar 2020 targets 193
8.2.3 Thermal management method 195
8.2.4 Literature review 196
8.2.5 Publication of work 197
8.3 Future work 198

Appendix A. Technical Skills 200

A.1 Software 200
A.1.1 MATLAB [118] 200
A.1.2 Infolytica MagNet [100] 200
A.1.3 MotorCAD [99] 200
A.1.4 SPEED [98] 201
A.1.5 Simulink 201
A.2 Experimental 201
A.2.1 Electrical machine testing 201
A.2.2 Thermal experiments 201

Appendix B. Design Equations and Procedure 202

B.1 Design equations 202
B.1.1 Machine size 202
B.1.2 Torque estimation 202
B.1.3 Electrical loading 202
B.1.4 Magnetic loading 203
B.1.5 Stator dimensions 204
B.1.6 Winding layout 205
B.2 Simulation process 206
B.2.1 Determine the required current 206
B.2.2 Determination of the appropriate number of turns 207

B.2.3 Achieve a reasonable slot fill factor 207
B.2.4 Determine the optimum tooth width 208
B.2.5 Producing the torque-speed characteristic 210

Appendix C. Thermal Networks 211

C.1 Thermal resistance parameters 211
C.2 Thermal network models 214

Appendix D. Thermal experimental setup 224

D.1 Materials 226

Appendix E. Thermal Model Calibration 227

E.1 No cooling applied 227
E.2 Water jacket cooling 228
E.3 With silicone pipe on the end winding surface 229
E.4 Commercial potting compound 230
E.5 High performance potting compound 232
E.6 Silicone pipe with modified end winding 233

Appendix F. Machine engineering drawings 236

Bibliography…… 241

List of Acronyms

AC	Alternating current
AlNiCo	Aluminium nickel cobalt
APC	Advanced Propulsion Centre
BLDCM	Brushless direct current machine
CGT	Cummins Generator Technologies
CIC	Cummins Innovation Centre
DoE	Department of Energy
DC	Direct current
DR	Double rotor
DS	Double stator
DSSRM	Double stator switched reluctance machine
Dy	Dysprosium
EV	Electric vehicle
EMF	Electromotive force
EU	European Union
FE	Finite element
FEA	Finite element analysis
FMM	Flux memory motor
FSM	Flux switching machine
FSCW	Fractional slot concentrated winding
GCD	Greatest common divider
HEV	Hybrid electric vehicle
IM	Induction machine
ISDW	Integral slot distributed winding
IPMSM	Interior permanent magnet synchronous machine
ICE	Internal combustion engine
LCM	Least common multiple
MTPA	Maximum torque per amp
NdFeB	Neodymium iron boron
NP	No paste
PM	Permanent magnet
PMa-SynRelM	Permanent magnet assisted synchronous reluctance machine
PMFSM	Permanent magnet flux switching machine
PHEV	Plug-in hybrid electric vehicle
QI	Quality index
REV	Range extender hybrid electric vehicle
SmCo	Samarium cobalt

SPP	Slot per pole per phase
SMPMSM	Surface mount permanent magnet synchronous machine
SRM	Switched reluctance machine
SM	Synchronous machine
SynRelM	Synchronous reluctance machine
SIM	Synchronous–induction hybrid machine
TFM	Transverse flux machine
UK	United Kingdom
US	United States
VA	Voltage ampere
WJ	Water Jacket
WP	With paste
WFFSM	Wound field flux switching machine

List of Symbols

A	Area (m^2)
A_{load}	Current loading (A/m)
B	Flux density (T)
B_{core}	Yoke flux density (T)
B_g	Air gap flux density (T)
bN	Thickness of rotor barrier N (m)
B_r	PM remnant flux density (T)
B_t	Tooth flux density (T)
C	Capacitance (F)
c_p	Specific heat capacity (J/K)
C_{th}	Heat capacity (J/K)
d_{pipe}	Pipe outer diameter (m)
D_r	Rotor diameter (m)
D_s	Stator outer diameter (m)
D_{sinner}	Inner diameter of the stator (m)
d_{wire}	Wire diameter (m)
E	Electromotive force (V)
e	emissivity
F	Force (N)
f	Frequency (Hz)
f_e	Electrical frequency (Hz)
F_r	Ratio of AC to DC resistance
h_{air}	Convection coefficient of air to housing (W/m^2K)
h_c	Heat transfer coefficient (W/m^2K)
H_c	PM coercive force (A/m)
h_{pipe}	Convection coefficient of water flow in pipe (W/m2K)
h_{WJ}	Convection coefficient of water flow in water jacket (W/m2K)
I	Current (A)
I_a	Total armature current (A)
I_d	D-axis current (A)
I_q	Q-axis current (A)
I_{rms}	RMS current (A)
j	Imaginary number, $\sqrt{-1}$
k_{al}	Aluminium thermal resistivity (mK/W)
k_B	Interface material thermal resistivity (mK/W)
$k_{contact}$	Thermal resistivity of contact between two materials (mK/W)
k_{copper}	Copper thermal resistivity (W/mK)
K_e	Eddy current loss constant

k_{eq_EW}	End winding equivalent thermal resistivity (mK/W)
k_{eq_S}	Slot equivalent thermal resistivity (mK/W)
K_h	Hysteresis loss constant
k_{junct}	Junction thermal resistivity (mK/W)
k_{Liner}	Slot liner thermal resistivity (mK/W)
k_{pipe}	Pipe thermal resistivity (mK/W)
k_{sc}	Stefan's constant ($Wm^{-2}K^{-4}$)
k_{Steel}	Stator Steel thermal resistivity (mK/W)
k_t	Torque constant
k_{Temp}	Temperature coefficient of resistance
L	Length (m)
L_{bridge}	Magnet bridge thickness (m)
$L_{Contact_Cu_Barrier}$	Contact thickness between the end winding and interface material (m)
$L_{Contact_Pipe_Barrier}$	Contact thickness between the pipe and interface material (m)
L_{EW_H}	Horizontal (axial) length of end winding bundle (m)
L_{EW_V}	Vertical (Radial) length of end winding bundle (m)
L_g	Air gap length
L_{House}	Housing radial thickness (m)
L_{junct}	Length of gap between top and bottom end winding bundles (m)
L_{Liner}	Slot Liner Thickness (m)
L_m	Magnet thickness
L_{pipe}	Pipe wall thickness (m)
$L_{Stator_WJ_Junct}$	Junction thickness between stator and water jacket (m)
L_{stk}	Stack/active machine length (m)
L_{WJ}	Water jacket radial thickness (m)
$L_{WJ_Housing_Junct}$	Junction thickness between water jacket and housing (m)
m	Number of phases
$M_{percent}$	Percent of the pole pitch occupied by PM mass (%)
N_c	Number of parallel conductors per turn
N_s	Number of slots
N_t	Number of turns per phase
$N_{Total\ turns}$	Total number of turns in the whole machine
$N_{turns\ per\ slot}$	Number of turns per slot
p	Number of pole pairs
P_{cu}	Copper losses (W)
P_{fe}	Iron Losses (W)

P_{in}	Input power (W)
P_{mag}	Magnetic losses (W)
PM_{ang}	Ratio of magnet span to pole pitch in radians
P_{mech}	Mechanical losses (W)
P_{out}	Output power (W)
q	Charge (C)
R	Electrical resistance (Ω)
R_0	Resistance at reference temperature (Ω)
RPM	Rotational speed (rpm)
r_R	Rotor radius (m)
r_{split}	Split ratio
R_{th}	Thermal resistance (K/W)
s	Stacking factor of laminations
SD	Slot Depth (m)
SO_r	Slot opening ratio
SO_w	Slot opening width (m)
SW	Slot Width (m)
T	Torque (Nm)
$Temp$	Temperature (°C)
$Temp_0$	Reference temperature (°C)
T_{mag}	Magnet alignment torque (Nm)
T_{rel}	Reluctance torque (Nm)
T_{tot}	Total torque (Nm)
U	Magnet segmentation loss reduction factor
v	Velocity (ms^{-1})
V	Voltage (V)
V_d	D-axis voltage (V)
Vol_R	Volume of the rotor (m^3)
V_q	Q-axis voltage (V)
WEW	Width (circumferential length) of one slot pitch of the end winding bundle (m)
W_m	Magnet width (m)
W_t	Tooth width (m)
W_y	Thickness of stator yoke (m)
X_d	D-axis reluctance (H^{-1})
X_q	Q-axis reluctance (H^{-1})
α	Hysteresis loss frequency constant
αN	Angle to tip of rotor barrier N (°)
β	Hysteresis loss flux density constant
γ	Phase angle (°)

δ	Skin depth (m)
λ_p	Pole pitch (m)
λ_s	Slot pitch (m)
$\mu 0$	Permeability of free space (Hm^{-1})
μ_m	PM relative permeability
σ	Electrical conductivity (S)
σ_{therm}	Thermal conductivity (W/mK)
Φ	Flux linkage (Wb t)
φ	Magnetic flux (Wb)
Φ_{th}	Heat flow rate (W)
ω_e	Electrical rotational speed ($rads^{-1}$)
ω_s	Mechanical synchronous speed ($rads^{-1}$)

List of Figures

Figure 2.1 – UK fuel prices [1] 8
Figure 2.2 - UK fuel prices in the past 10 years [2] 8
Figure 2.3 - Neodymium price over last decade [18] 10
Figure 2.4- Dysprosium over last decade [18] 10
Figure 2.5 - Comparison of general torque speed characteristics 12
Figure 2.6 - Parallel-series hybrid layout [28]. 13
Figure 2.7 – FreedomCar 2020 torque speed requirement 18
Figure 2.8- Conventional machine classification [37] 21
Figure 2.9 – Comparison of core losses and yield strength for high performance electrical steels [39] 23
Figure 2.10 – SMPMSM design [42] 27
Figure 2.11 - IPMSM simulated losses [42] 27
Figure 2.12 - Experimental IPMSM characteristics [42] 28
Figure 2.13 - SMPMSM simulated losses [42] 29
Figure 2.14 - Double layer FSCW IPMSM 'Design A' [43] 30
Figure 2.15 - Double layer ISDW IPMSM 'Design C' [43] 31
Figure 2.16 - Losses vs. speed for the four designs [43] 33
Figure 2.17 - Efficiency vs. speed for the four designs [43] 33
Figure 2.18 - Flux Focusing Machine [44] 34
Figure 3.1 - Wound field synchronous machine 37
Figure 3.2 - SMPMSM 38
Figure 3.3 - IPMSM 39
Figure 3.4 - IM 41
Figure 3.5 - SRM 42
Figure 3.6 - Double rotor axial IPMSM [62] 44
Figure 3.7 - Cross section of a transverse flux machine [63] 45
Figure 3.8 - Two phase outer rotor transverse flux machine [64] 45
Figure 3.9 - Outer rotor WFFSM [67] 47
Figure 3.10 - Synchronous reluctance machine 48
Figure 3.11 - PMa-SynRelM with ferrite magnets [74] 49

Figure 3.12 – Synchronous-induction hybrid machine [75] 50
Figure 3.13 - Flux memory motor, partially demagnetised [40] 51
Figure 3.14 - Double rotor SMPMSM [80] 53
Figure 3.15 - Double stator switched reluctance machine [82] 54
Figure 3.16 - Synchronous homopolar machine 55
Figure 3.17 - Weighted QI values 58
Figure 3.18 – Optimum operating aspects for the range of machine topologies 59
Figure 3.19 – Different IPMSM topologies 61
Figure 4.1 - Maximum torque per amp [37] 67
Figure 4.2- Phasor diagram of an IPMSM during normal operation [37] 68
Figure 4.3- Phasor diagram of an IPMSM at maximum speed 69
Figure 4.4 – High level design methodology 71
Figure 4.5 – Comparison of the current across the speed range for the analytical concentrated wound designs 75
Figure 4.6 – Comparison of the voltage across the speed range for the analytical concentrated wound designs 77
Figure 4.7 - Comparison of the input power across the speed range for the analytical concentrated wound designs 78
Figure 4.8 - Comparison of the efficiency across the speed range for the analytical concentrated wound designs 79
Figure 4.9 - Comparison of the temperature across the speed range for the analytical concentrated wound designs 80
Figure 4.10- a) SPEED design b) Wider tooth design 88
Figure 4.11 - Torque, current and voltage comparison for both concentrated wound IPMSM FEA designs 90
Figure 4.12- Power in and out across the speed range for both concentrated wound IPMSM FEA designs 91
Figure 4.13- Power in and out across the speed range for both concentrated wound IPMSM FEA designs 92

Figure 4.14 – Breakdown of losses across the speed range for both concentrated wound IPMSM FEA designs. a) Stator iron losses, b) rotor iron losses, c) copper losses, d) magnet losses.....92
Figure 4.15 - Comparison of the current across the speed range for the analytical distributed wound designs.....96
Figure 4.16 - Comparison of the input power across the speed range for the analytical distributed wound designs 98
Figure 4.17 - Comparison of the efficiency across the speed range for the analytical distributed wound designs 99
Figure 4.18 - Comparison of the temperature across the speed range for the analytical distributed wound designs 100
Figure 4.19 – Comparison of current requirement of concentrated and distributed wound IPMSMs.....104
Figure 4.20 - Comparison of efficiency of concentrated and distributed wound IPMSMs 105
Figure 4.21 - Comparison of loss components of concentrated and distributed wound IPMSMs 106
Figure 5.1 - Initial PMa-SynRelM design.....112
Figure 5.2 - Peak phase current comparison between the IPMSM and initial PMa-SynRelM.....114
Figure 5.3 - Advance angle comparison between IPMSM and initial PMa-SynRelM 115
Figure 5.4 - Efficiency comparison between the IPMSM and initial PMa-SynRelM design 115
Figure 5.5 - Loss component comparison between IPMSM and initial PMa-SynRelM 116
Figure 6.1 - Motor-CAD Thermal simulation 120
Figure 6.2 - Plastic and copper pipes attached to the end windings 121
Figure 6.3 - Comparison of properties of various rubbers [41] 123
Figure 6.4 - Copper pipe and end windings in a potting compound.....124
Figure 6.5- a) Pipe over end wind side view. b) Front view 125

Figure 6.6 - Plastic pipe in end winding gap 126
Figure 6.7 - Methods of thermal transfer [122] 128
Figure 6.8 – Conduction through block [119] 130
Figure 6.9 - Location of cooling source 132
Figure 6.10 - Comparison of contact area with different goodness factors 133
Figure 6.11 - Slot diagram 133
Figure 6.12 - Slot thermal network diagram 134
Figure 6.13 - End winding cooling thermal network 135
Figure 6.14 - Photo of dummy stator without additional cooling methods 138
Figure 6.14 - Photo of dummy stator with copper pipe cooling end windings 142
Figure 6.15 - Photo of dummy stator with potting compound 144
Figure 6.16 - Pipe expanding within the modified end windings 146
Figure 6.17 - Temperature reduction, cost and relative complexity of the cooling methods 147
Figure 7.1 – PMa-SynRelM rotor geometry parameters 158
Figure 7.2 - Reluctance torque based on total barrier angle and cumulative barrier thickness 159
Figure 7.3 – Reluctance torque based on the distribution of total barrier thickness between the three barriers. 160
Figure 7.4 – Rotor geometry with added PM 160
Figure 7.5 – Current and winding temperature for the feasible range of magnet spans 161
Figure 7.6 – Stator geometry parameters 162
Figure 7.7 - Variation in copper losses due to slot depth and tooth width at rated speed 163
Figure 7.8 - Variation in iron losses due to slot depth and tooth width at rated speed 164
Figure 7.9 - Variation in total losses due to slot depth and tooth width at rated speed 165

Figure 7.10 - Variation in copper losses due to slot depth and tooth width at maximum speed....166
Figure 7.11 - Variation in iron losses due to slot depth and tooth width at maximum speed....167
Figure 7.12 - Variation in total losses due to slot depth and tooth width at maximum speed....168
Figure 7.13 – Final machine geometry....169
Figure 7.14 – Final machine rotor skew....170
Figure 7.15 – Final machine winding pattern....173
Figure 7.16 – Section of final machine winding pattern....174
Figure 7.17 - Torque, current and voltage vs speed for the final machine....175
Figure 7.18 - Instantaneous skewed torque at peak torque, rated speed....176
Figure 7.19 - Instantaneous skewed torque at rated torque, rated speed....177
Figure 7.20 - Instantaneous skewed torque at rated torque, max speed....178
Figure 7.21 – Final machine efficiency vs speed....179
Figure 7.22 - Final machine thermal response with only water jacket cooling....180
Figure 7.23 - Final machine thermal response with potting compound cooling....181
Figure 7.24 – 3D FEA Model....182
Figure 7.25 – 3D FEA Torque results for rated torque rated speed....182
Figure 7.26 – Comparison of current requirement of the final machine vs earlier designs....184
Figure 7.27 – Comparison of advance angle of the final machine vs earlier designs, needed to maintain the voltage limit....184
Figure 7.28 - Comparison of the four major loss contributors of the final machine vs earlier designs....186
Figure 7.29- Comparison of efficiency of the final machine vs earlier designs....186
Figure B.1 - Star of slots for 4 pole 9 slot machine....205
Figure C.1 - Full slot thermal network....215

Figure C.2 - Detailed slot thermal network 216
Figure C.3 - Full end winding thermal network 217
Figure C.4 - Detailed end winding thermal network 218
Figure C.5 - Connection between thermal network sections 219
Figure C.6 - Dummy stator full slot model 220
Figure C.7 – Dummy stator detailed slot model 221
Figure C.8 - Dummy stator full end winding model with potting compound 222
Figure C.9 - Dummy stator detailed end winding model with potting compound 223
Figure D.1 - Dummy stator design model 224
Figure D.2 - Water jacket model 225
Figure D.3 - Complete dummy stator model 225
Figure E.1- Comparison of practical and simulation of double silicone pipe with paste cooling test 230
Figure E.2- Comparison of practical and simulation of commercial potting compound 231
Figure E.3- Comparison of practical and simulation of high performance potting compound 233
Figure E.4- Comparison of practical and simulation of the silicone pipe with modified end windings 234
Figure F.1 - View of the full housed machine 236
Figure F.2 - Coloured axial cross section of the final machine 237
Figure F.3 - Radial cross sections of the final machine 237
Figure F.4- Labelled axial cross section of the final machine 238
Figure F.5 - Labelled outer housing of the final machine 238

List of Tables

Table 2.1- Levels of hybridisation [29] 14
Table 2.2- FreedomCar 2020 targets [14] 17
Table 2.3 - PM materials 24
Table 2.4 - SMPMSM vs IPMSM design parameters [42] 26
Table 2.5 - Constant design parameters [43] 31
Table 2.6 - Variable design parameters [43] 31
Table 3.1- Topology QI scores 57
Table 3.2 - Performance comparison of machine topologies 59
Table 4.1 – Concentrated design initial parameters for analytical design 71
Table 4.2 - Concentrated wound slot pole combinations 73
Table 4.3 – Concentrated designs analytical results summary 76
Table 4.4 - Comparison of final analytical concentrated design combinations 81
Table 4.5 – Concentrated Machine Design Parameters 88
Table 4.6 – Operating table - SPEED concentrated FEA Design 89
Table 4.7 – Operating table – wider tooth concentrated FEA Design 89
Table 4.8 – Temperature comparison of the FEA concentrated wound machines 93
Table 4.9 - Distributed wound slot pole combinations 95
Table 4.10 - Concentrated designs analytical results summar 97
Table 4.11 - Comparison of final analytical distributed wound design combinations 101
Table 4.12 - Distributed IPMSM design parameters 102
Table 4.13 - Operating table - distributed FEA Design 103
Table 4.14 - Distributed wound temperatures from FEA losses 103
Table 4.15 - Temperature comparison between concentrated and distributed 107
Table 4.16 – Comparison of IPMSM designs to FreedomCar 2020 targets 109
Table 5.1 – Initial PMa-SynRelM design parameters 113
Table 5.2 - Operating table – Initial PMa-SynRelM FEA Design 113

Table 5.3 - Thermal comparison between the IPMSM and Initial PMa-SynRelM 117
Table 6.1 – Thermal parameters and their electrical equivalent [123] 129
Table 6.2 - Initial thermal simulation results 136
Table 6.3 - Silicone pipe dummy stator results 139
Table 6.4 – Silicone pipe difference in end winding temperature reduction 141
Table 6.5 - Copper pipe dummy stator results 142
Table 6.6 - Commercial potting compound dummy stator results 144
Table 6.7 - High performance potting compound dummy stator results 145
Table 6.8 - Modified end windings dummy stator results 146
Table 6.9 – Comparison of experimentally achieved goodness factors 151
Table 6.10 - Validated Plastic Pipe Simulation Results 152
Table 6.11 - Validated potting compound simulation results 153
Table 6.12 - Validated silicone pipe with modified end windings results 154
Table 6.13 - Potential increase in current density and torque with the new thermal limits 155
Table 7.1- Final machine general parameters 169
Table 7.2 – Final machine rotor parameters 171
Table 7.3 – Final machine stator parameters 173
Table 7.4 – Final machine Winding Parameters 173
Table 7.5 – Operating table for final machine 174
Table 7.6 - Peak torque values 176
Table 7.7 - Rated torque values 177
Table 7.8 – Max speed torque values 178
Table 7.9 – Peak temperature based on machine location, with only water jacket cooling 180
Table 7.10 – Peak temperature based on machine location, with only water jacket cooling 181
Table 7.11 – Mean and ripple torque comparison of 2D and 3D FEA 183
Table 7.12 – Loss comparison of 2D and 3D FEA 183

Table 7.13 – Comparison of against previous attempts at the FreedomCar 2020 targets 187
Table 7.14 - Final machine comparison to FreedomCar 2020 targets 189
Table 8.1 – Comparison of four designs to the FreedomCar 2020 targets 194
Table 8.2 – Summary of thermal management methods 196
Table B.1 – Star of slot group limits 206
Table C.1 - Slot thermal network resistances 211
Table C.2 - Parameters for slot thermal network 212
Table C.3 - End winding thermal network resistances 213
Table C.4 - Parameters for the end winding thermal network 214
Table E.1 - No cooling validation parameters 227
Table E.2 - Comparison of results - no cooling 228
Table E.3 – Water jacket validation parameters 228
Table E.4 - Comparison of results water jacket 229
Table E.5 – Double silicone pipe with paste validation parameters 229
Table E.6– Comparison of Results Double Pipe with Paste 230
Table E.7 –Commercial potting compound validation parameters 231
Table E.8– Comparison of results for commercial potting compound 232
Table E.9 – High performance potting compound validation parameters 232
Table E.10– Comparison of results for high performance potting compound 233
Table E.11 – Silicone pipe with modified end windings validation parameters 234
Table E.12– Comparison of results for silicone pipe with modified end windings 234
Table F.1 – Final machine component names 239

Chapter 1. Introduction

This thesis is concerned with the use and implementation of electrical machines in hybrid electric vehicle (HEV) traction applications. The focus is upon meeting the FreedomCar 2020 targets, a range of goals set by the US Department of Energy (DoE) for plug-in hybrid electric vehicle (PHEV) applications. The aim of these targets was to produce a traction machine which enhances the state of the art in terms of machine mass, efficiency, kVA requirements, thermal management and performance, with special care for economic aspects (e.g. permanent magnet (PM) mass).

This thesis details the work done towards the achievement of these targets, starting in October 2012. First, the aims and objectives of the project will be explained. A comprehensive literature review will be presented, containing a study of electric vehicles (EV), machine topologies and previous attempts at the FreedomCar 2020 targets.

An analytic trade-off study was then performed on the most promising machine topologies, focusing on the top level machine geometry; slot pole combination, winding configuration, split ratio, outer diameter and stack length, narrowing down to a select few designs. These favourable designs were then modelled using finite element (FE) software, to investigate in more detail which was the most fitting for the targets. A brief optimisation was performed which quickly highlighted that the difficulty of the targets was balancing the high speed efficiency with peak torque thermal requirements and that this combination could not be achieved with state of the art technology. The method the project chose to accomplish this was to design a machine that could meet the high speed efficiency but if traditional cooling methods were used, would run the risk of overheating at the at peak torque conditions.

To overcome the damaging temperatures at high torque values an innovative thermal management system was proposed, prototyped and implemented.

This allowed the machine to remain within the winding thermal limits across the whole operating range without sacrificing high speed efficiency.

After the efficiency at maximum speed had been achieved, a more detailed optimisation process was completed. The target of which was minimising the permanent magnet (PM) mass, to reduce cost, and improving the efficiency of the other operating points, aided by the consideration of a less common machine family. The final machine design met all of the performance specifications of the FreedomCar 2020 targets.

1.1 Aims and objectives

1.1.1 Aims

The overall aim of this project was to design an electrical machine for use in a PHEV for traction. The goal was to meet the FreedomCar 2020 targets. The ideal was for the motor to use less Neodymium Iron Boron (NdFeB) PMs than current machines designed for this application, whilst retaining a high torque density and efficiency over the wide speed range.

The secondary goal was the development of a novel cooling method, that allows a significant increase in the current density of the machine (without an impact on the operating temperatures) in order to achieve the required power density.

1.1.2 Objectives and anticipated project outcomes

- The first objective was to perform a literature review, split into 4 sections namely electric traction in general, machine topologies and previous attempts, the FreedomCar targets and advanced cooling methods of electrical machines.
    - The electric traction study covered the various applications, layouts and systems of electric vehicles as a whole.
    - The review of machines highlighted those currently being used in hybrid and fully electric vehicles and also less traditional

topologies. The machine technologies were compared based on several qualitative indices (QIs).

  - The published FreedomCar endeavours were be used as a starting point to build upon and as benchmarks to compare future designs back to.
  - The review of current cooling methods will be presented in Section 6.2.6. This covered previously suggested advance cooling methods and why they would not be appropriate for this application. Also shown is that the method presented has not been considered before.

- An innovative, machine performance enhancement methodology was implemented that combines analytical and finite element electromagnetic simulations with thermal analysis. This algorithm allowed for rapid simulation of a very wide range of designs whilst ensuring accuracy of the results.
- An initial machine was designed to achieve as many as possible of the FreedomCar targets with current technology and materials. This highlighted which targets need more effort to be met and what potential solutions can be implemented.
- An innovative cooling system was proposed and prototyped. In addition to being implemented in this project, the potential for the method to be applied in other applications was also considered.
- A final machine will be optimised including advanced ideas for the rotor design and the improved thermal management system. This will achieve all of the performance requirements of the FreedomCar 2020 targets.
- An objective not directly linked to the progression of the project is the reporting of work in high profile publications.

1.2 Link to Cummins Generator Technologies

This project was part of the Cummins Innovation Centre (CIC), a strategic alliance between Cummins Generator Technologies (CGT) and The University of Nottingham's PEMC group. This means that CGT has had an influence on the project from the start, suggesting routes to look into and providing their current hybrid machine to be used for training purposes. CGT has also monitored and supported the progress of the project with regular meetings and reviews to ensure that the research done here is applicable to their industrial requirements.

A perceived outcome of this work was that the proposed and developed machine would have the potential to be used in their hybrid vehicle applications, with a reduced cost in comparison to their current machine. Other significant outcomes of this project, such as the improved thermal management system will also inform CGT and be exploited for their development requirements.

1.3 Thesis outline

1.3.1 Chapter 1 - Introduction

The main focus of the introduction was to explain the project as a whole detail the aims and objectives of the thesis.

1.3.2 Background

The intelligence found during the literature review of hybrid electric and full electric vehicles has also been written up into a full literature review, in Chapter 2 of this thesis. This also includes the US DoE FreedomCar 2020 targets, and previous attempts at them. Achieving these targets was the goal of this thesis.

1.3.3 Chapter 3 - Machine Topologies Study

The first stage in attempting to meet the FreedomCar targets was determining which machine technology is optimal for this application. In Chapter 3 another section of the literature review is presented, discussing different machine topologies and their inherent advantages and drawbacks. Following this is a qualitative comparison to establish the topology to be used.

1.3.4 Chapter 4 - Initial Machine Design

Chapter 4 looks into the initial designs, focusing on interior permanent magnet synchronous machines (IPMSM). As well as the design process and equations, it shows the wide range of slot pole combinations considered and the comparison between distributed and concentrated wound designs.

1.3.5 Chapter 5 - Initial PMa-SynRelM Design

The previous chapter highlights some of the shortcomings of IPMSM, in reaching the high speed efficiency target. Here a permanent magnet synchronous reluctance machine (PMa-SynRelM) is proposed. This new machine vastly improves on the high speed efficiency but struggles with the thermal limitations, which leads to the next chapter.

1.3.6 Implementation of an Improved Thermal Management System

One of the significant outcomes of this work has been the innovative thermal management system proposed in Chapter 6. This involved applying water cooling pipes to the end windings. The chapter details the benefits of this method and includes simulation and experimental results.

1.3.7 Chapter 7 - Final Machine Design

After the thermal management system had been implemented, it allowed more freedom to optimise the design before the winding temperature limits were met. Chapter 7 looks at the optimisation of a PMa-SynRelM and details the final design.

1.3.8 Chapter 8 - Conclusion

Finally the thesis is concluded, summarising the work and highlighting the key findings and outcomes.

1.3.9 Appendices

Included in the appendices are the technical skills used and learnt during the project, the equations and simulation procedures, the thermal networks, the experimental set up, the thermal model calibration and the engineering drawings of the final machine.

Chapter 2. Background

This chapter introduces the current state of the art relative to hybrid and fully electric vehicles, as well as introducing the FreedomCar targets which are the main goal of the project.

2.1 Hybrid and fully electric vehicles

The popularity of hybrid and fully electric vehicles is increasing rapidly; this is because they offer a solution to the reducing supply and increasing costs of fossil fuels used in conventional combustion engines, as well as reducing emissions.

2.1.1 Background for the technology push

The push for more electric vehicles is based on two main reasons.

Over the past few decades, the cost of both petrol and diesel has been steadily increasing, as seen in Figure 2.1 [1]. As can be observed in Figure 2.2 fuel prices have stabilised in the past decade and actually dropped in the last year. However, it is predicted that prices will increase again when the natural resources diminish or availability changes due to world politics or conflict [2].

Hybrid vehicles attain a greater number of miles per gallon than conventional internal combustion engine (ICE) vehicles because a portion of the traction comes from the electrical machine [3, 4]. Also fully electric vehicles require no petrol or diesel and so are barely affected by the instability in the price of oil.

Another issue is legislations being introduced, both by the EU and UK government, that increase taxes on vehicles which have higher emissions. These legislations are increasing to the point at which all new cars in the EU must be below 95 g/km of CO_2 by 2020 [5]. Relative legislation is also being imposed worldwide. Therefore to increase the performance of the vehicle beyond these limits, electrical traction must be implemented. Hybrid and fully

electric vehicles will also reduce the greenhouse gases produced, as the overall 'sun to mile' efficiency is increased.

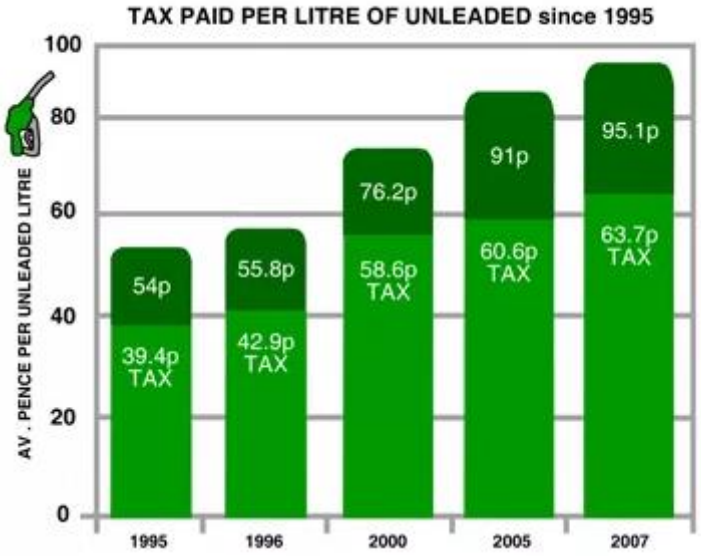


Figure 2.1 – UK fuel prices [1]

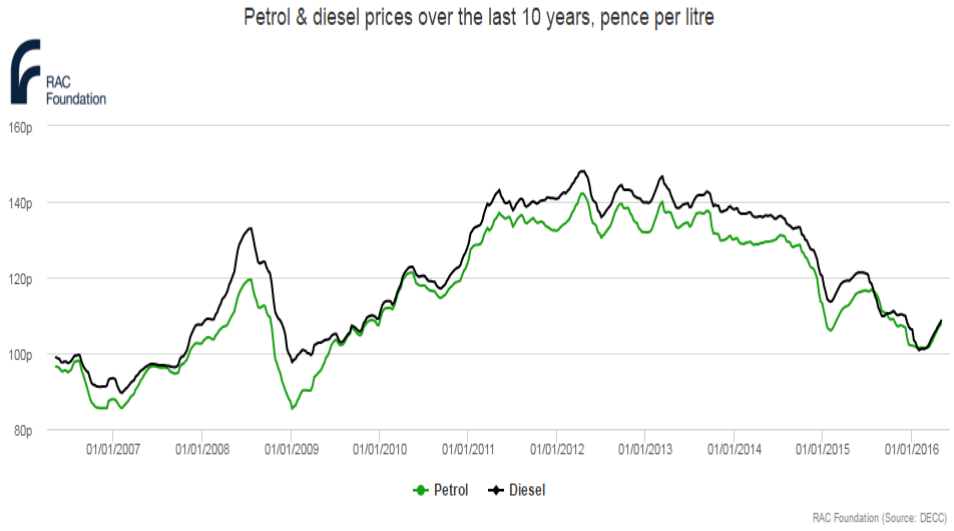


Figure 2.2 - UK fuel prices in the past 10 years [2]

2.1.2 Challenges

While both HEVs and EVs are attractive technologies, there are still significant drawbacks and challenges that need to be addressed.

The main obvious challenge is that related to energy storage capabilities, i.e. current battery technology. The limits are the maximum charge value, the discharge and recharge rates and the cost [6-9]. The maximum charge value along with the relatively fast discharge value constrains the range a vehicle can travel on pure electric energy. The power density performances achieved by today's battery and charging technologies restrict how quickly the vehicle can get on the road again. Two types of energy storage technology are prominent in this application, lithium ion batteries with higher energy densities (in the order of 100 Wh/kg [10, 11]) but low power density (150-500 W/kg [10]) and super capacitors with a higher power density (10 kW/kg [12, 13]) but lower energy density (lower than 5Wh/kg [12, 13]). The energy storage challenges and potential solutions will be further discussed when the drawbacks of fully electric vehicles are detailed in section 2.1.3.2.

Linked to the limited battery charging capabilities is the efficiency of the overall drivetrain. Reducing the wasted power from the drivetrain is very important as this has a significant effect on the operating costs of the vehicles. Gearboxes are known to be inefficient and not robust. Because of this, wide speed range traction machines for gearless operation are of interest [14]. However traditionally, it is very challenging to achieve wide speed range machines with appropriate efficiency values over the whole speed range [15-17].

The majority of currently available HEV and EVs use electrical machines with PMs as these produce the largest torque density. Higher torque density gives greater acceleration which is often used to assess the performance of vehicles. Today PMs that are recognised for their maximum energy densities are NdFeB and samarium cobalt (SmCo) because of their high remnant flux and high coercive force. The drawback is that these magnets have been rising in cost over the past few decades and while this has stabilised in the past years the price per kg is still high [18]. The price of neodymium is shown in Figure 2.3. As well as the named metals of NdFeB other expensive components are required, such as

dysprosium (price shown in Figure 2.4), to allow the PMs to withstand higher temperatures.

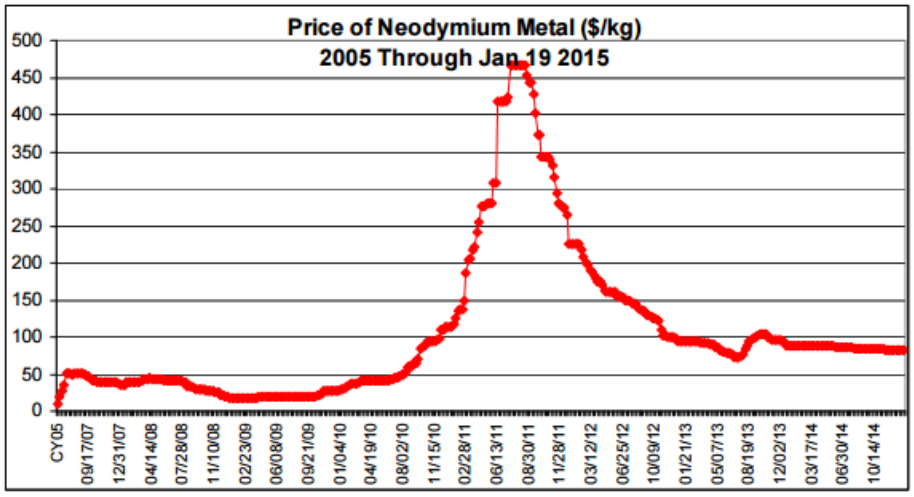


Figure 2.3 - Neodymium price over last decade [18]

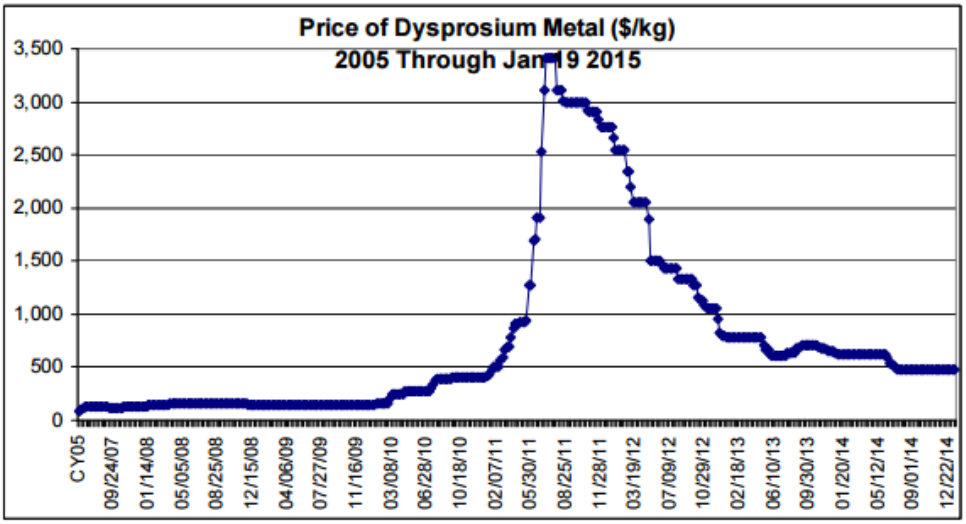


Figure 2.4- Dysprosium over last decade [18]

Along with the price of rare earth materials the further hurdle is that a single country, China, has a monopoly on the market, producing 90% of the world total [19]. A monopoly not only allows for the control of the cost of the materials, but also their availability. Currently China are restricting the export of certain rare earth materials, such as dysprosium, and stockpiling them for their own uses [20, 21].

Other, cheaper, PM materials exist but they either have much lower remnant flux or are easy to demagnetise and thus unlikely to be suitable for this application.

2.1.3 Fully electric vehicles

Fully electric vehicles are typically completely powered by one, or multiple, electrical machines fed from a battery supply.

2.1.3.1 Benefits

There are many advantages of EVs over conventional combustion vehicles, the most obvious being that they do not directly burn fossil fuels.

Another benefit is that electric motors produce less acoustic noise than ICEs, which will result in lower overall vehicle noise.

The high torque at low speed available from electric motors, as shown in Figure 2.5, gives faster acceleration than a similarly powered ICE from a standstill.

2.1.3.2 Perceived drawbacks

The main drawback of the pure EV is the restricted range due to the limited energy density of the storage systems. As previously mentioned lithium-ion batteries have high energy density. This typical relates to ranges lower than 100 miles excluding very high-end models [22, 23]. While this range is normally sufficient for commuter vehicles, it would be an issue for long distance journeys, which leads onto the next issue. EVs need to be plugged in to charge, and this takes time, a normal full replenishment of stored energy in lithium-ion batteries takes around 8 hours, due to their relatively low power density [10]. This does not give them same convenience as refuelling an ICE vehicle. Fast charging, taking 30 minutes, and battery swapping services exist but they are still not ideal solutions. Super-capacitors have a high power density although lower energy density, example values provided previously in section 2.1.2. This allows for much faster re-charging but shorter ranges. The current solution to

this is a hybrid system which includes both lithium-ion batteries, for the high energy density, and supercapacitors for the high power density [12, 13].

A disadvantage linked to the torque speed performance is that the top speed is usually lower in an EV than ICE vehicle, as the torque is inversely proportional to the speed (Figure 2.5), so at high speeds acceleration becomes weaker.

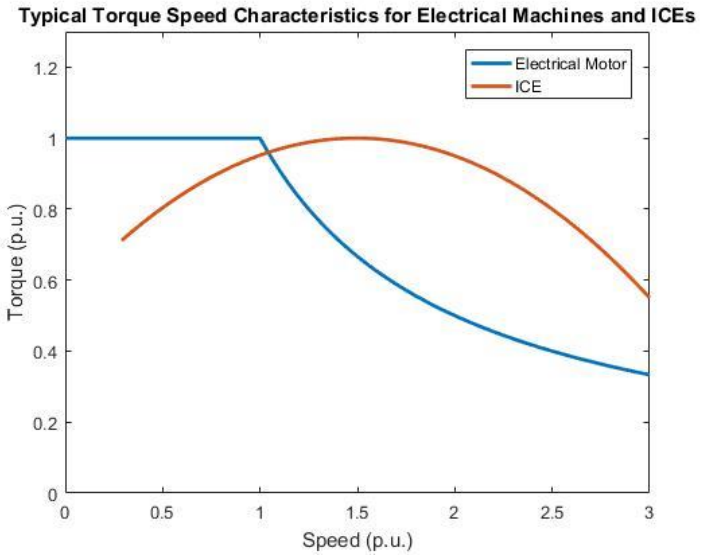


Figure 2.5 - Comparison of general torque speed characteristics

2.1.3.3 Dependency of fossil fuels

Although EVs do not depend on burning of fossil fuels during their operation, the underlying resources required to permit EV operation still depend on fossil fuel burning. This of course includes the regular charging of batteries (during the car's lifetime), typically done via the electrical grid (fed from a power station).

However, it is important to note that when comparing fossil fuels burnt for charging of EVs against fuel burnt from ICE cars, a much higher effective miles per gallon is achieved in EVs. In 2016 the average for ICE vehicles was 30 mpg [24] whilst the mpg equivalent of some key fully electric vehicles has been shown to be much higher; Chevrolet Spark (119 mpg-e [25]), BMW i3 (118 mpg-e [26]), and Nissan Leaf (114 mpg-e [27]).

A perceived improvement to this situation is the ever-increasing production of energy from renewable sources, which could in the future be developed to a point where relatively speaking, EV operation would be independent of fossil fuels.

2.1.3.4 *Summary of fully electric vehicles*

Overall this results in EVs being excellent for short range journeys with a long shut down at either end, such as commuting, but not at long distance trips.

2.1.4 *Hybrid electric vehicles*

HEVs are a combination between conventional vehicles and EVs; they have both an internal combustion engine and an electrical machine, giving some of the benefits of EV without fully relying on battery storage and electrical traction. Most HEVs do not need to be plugged in to recharge, all the recharging of the batteries is done from the internal generator, which is rotated by an ICE as seen in Figure 2.6. HEVs still require a fuel input, although less frequently than a traditional ICE vehicle. Some prevalent models of hybrid vehicles are the Toyota Prius and Honda Insight, although many manufactures offer hybrid versions of their mainstream models, such as Volkswagen Golf and Peugeot 308.

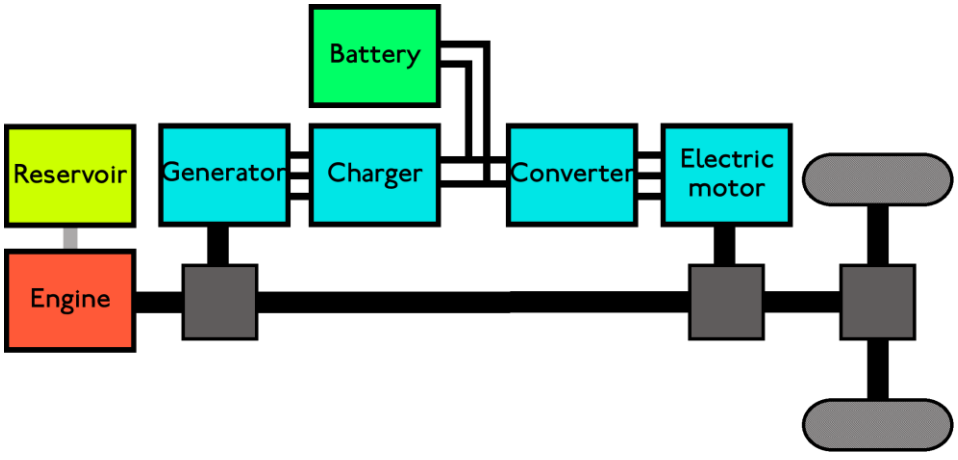


Figure 2.6 - Parallel-series hybrid layout [28].

Hybrid vehicles have two forms of classification, layout and degree of hybridisation. Three layouts are commonly used series, parallel, and parallel-series. In a series hybrid the traction is provided fully by the electric motor, with the ICE only being used to generate power, either for direct use or to be stored in the batteries. A parallel hybrid has both the electric motor and ICE attached to the same shaft (usually with gearing involved) and both provide traction; however both must constantly be rotating at the same relative speed. Series-parallel (also called power split or combined), shown in Figure 2.6 combines these two layouts decoupling the speed of the electric motor and ICE to each provide traction independently or at the same time, depending on the performance requirement and battery state of charge.

The degree of hybridisation is a sliding scale ranging from conventional ICE with a small electric boost (e.g. stop-start) to almost a full EV, as shown in Table 2.1.

Table 2.1- Levels of hybridisation [29]

Hybrid family	Configuration	ZEV range (km)	CO_2 Reduction (%)	
			City	NEDC
Micro & Mild Hybrid	Micro	0	4-7	3-5
	Mild		5-9	4-7
	Mild Plus		7-14	7-12
Full Hybrid	Power Split	~ 2	18-28	15-25
	Parallel		17-27	15-25
	Serial		12-27	10-23
	Combined		12-28	10-25
Plug-In Hybrid	Parallel	20 - 80	17-85	15-80
	Power Split		18-85	15-80
	Serial		12-85	10-80
	Combined		12-85	10-80
Range Extender Hybrid	Range Extender	80 - 120	12-95	10-80

2.1.5 Plug-in hybrid electric vehicles (PHEV) and range extender hybrid (REV)

PHEV and REV are the stages between EV and HEV and are the highest level of hybridisation before pure EV is reached. They rely on an electric motor for traction which gives all the performance benefits of the full EV. A small ICE and generator are included purely to recharge the batteries. This removes the range limitation and partially removes the issue of long charge times from an EV.

The downside is that a PHEV/REV requires the user to both charge their vehicle and refill the fuel tanks. There is also added mass in comparison to an EV which will affect the acceleration and top speeds of the vehicle.

2.1.6 Current initiatives related to electrification of cars

Today there are a lot of initiatives that encourage the uptake of green transport.

In the UK the Department of Transport [30] are producing a high amount of publications and incentives on more electric transport, including automotive, rail, marine and aerospace. A key section of this is the Low Carbon Vehicle Partnership which produced a transport roadmap in 2015 [31] for meeting the Renewable Energy Directive transport targets for 2020 set by the EU [32].

Another UK directive is the Advanced Propulsion Centre (APC) [33] an industry wide collaboration of innovators and producers of low carbon propulsion systems. The aim of the APC is to position the UK as a centre of excellence for low carbon propulsion development and production. This is achieved by funding high technology readiness level projects related to improving all of the electrical systems in vehicles.

Horizon 2020 is the biggest EU research and innovation programme ever [34], part of this is funding research into smart, green and integrated transport. Horizon 2020 Green Vehicles often puts out funding topics with the ultimate goal again being the Renewable Energy Directive transport targets [35].

For applications in the US the dominating proposer of initiatives is the DoE, a cabinet level department of the US government. Though there are other roadmaps and initiatives, such as from Nature Energy [36]. The DoE has set the FreedomCar 2020 targets for the electrical motors used for providing traction in PHEVs, to be achieved by the year 2020 [14].

A significant benefit of the FreedomCar targets for this work is that they give detailed specifications for the electrical traction machines, whilst the other initiatives only provide targets for the overall system of the vehicle.

2.2 FreedomCar 2020 targets

The FreedomCar 2020 specifications were used for this project for two reasons. First of all these targets are what need to be met in this application for PHEVs to stay competitive in cost and performance to ICE vehicles. While the targets are US based, it can be seen from the above that the UK and EU have similar goals. The main difference is that the UK and EU directives are only given for the overall system of the vehicle, while the FreedomCar targets allow the focus to be on the machine itself. The other reason is the link to CGT, detailed in Chapter 1, CGT is very interested in both meeting these targets for their own traction machines and applying any novel technologies developed by this push into their synchronous generators.

While the main purpose of these targets is to provide ideal performance requirements as objectives, also of high interest is how much the boundaries of current technology can be pushed for traction motor drives and electrical machines in general. Part of the targets is also to overcome the need for a standardisation of products, whilst ensuring high performance at a low cost.

The targets are shown in Table 2.2, while Figure 2.7, shows the required rated torque across the speed range, and the peak torque value.

A literature review of previous attempts at these targets will be detailed later in this chapter, showing which are achievable with standard machines and which are more challenging.

Table 2.2 shows all the FreedomCar 2020 targets, of note is the very low unit cost when considering the torque density and efficiency requirement, across the wide speed range, with a narrow temperature band.

Table 2.2- FreedomCar 2020 targets [14]

Rated Power	30kW
Peak Power	55kW for 18sec.
Peak Torque	200Nm for 18sec
Maximum Torque Ripple	5% of peak torque
Rated Speed	2800rpm
Maximum Speed	14000rpm
DC Link Voltage	200-450V (325V rated)
Maximum Back EMF at 100% of maximum speed	600V
Maximum Per Phase Current	400A
Maximum Machine Diameter	250mm
Maximum Machine Length	200mm
Maximum Machine Volume	9.7l
Maximum Machine Mass	35kg
Ambient Temperature	-40/+140C
Cooling System	Liquid
Maximum coolant temperature	>105C
Lifetime Target	>49khrs B10
Minimum Peak Efficiency	>95%
Technology	Preferred non-rare earth IPM or magnetless
Unit cost in quantities of 100,000 ($)	275
Ingress Protection	>=IP56
Insulation class	H
Altitude Range of Operation	5000m

In Figure 2.7, the rated torque speed requirement for the targets can be seen. Also shown is the efficiency requirement and the peak torque location with the time this is required for. This also implies the duty cycle of the requirements, expecting continuous operation anywhere on or below the rated torque speed

characteristic and 18 second capability at the peak torque, including a ramp up and down time.

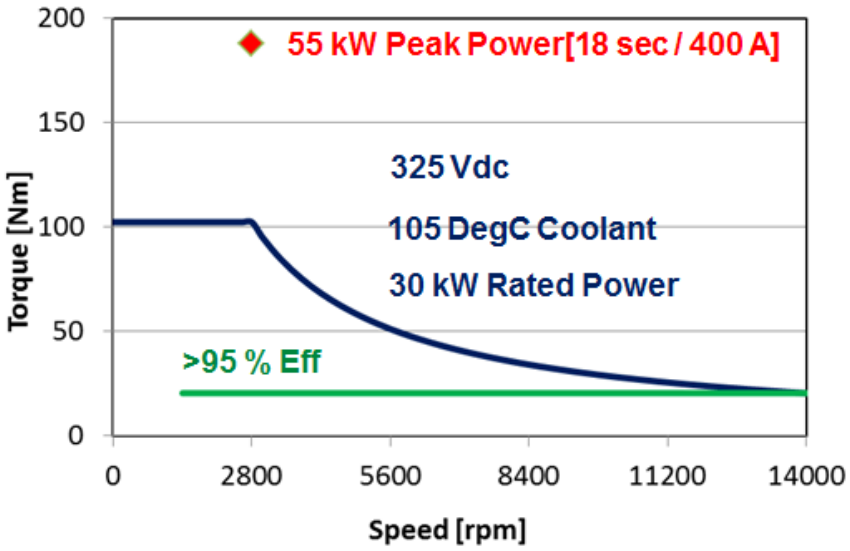


Figure 2.7 – FreedomCar 2020 torque speed requirement

2.3 Electrical machines

To design the optimal electrical machine for the FreedomCar targets the understanding of machine operation must be investigated, presented in this section.

The basic operation of electrical machines is that they either convert electrical energy into mechanical (motor) or mechanical into electrical (generator). Typically machines are made up of a rotating component (rotor) and a fixed component (stator). This section is also doubly important, as it sets the context and atmosphere for the proposed design methodology that will be presented later in Chapter 4.

2.3.1 Magnetics

The rotation of a motor is based on the principle of the Lorentz Force, which states that if a charged particle passes through a magnetic field, there will be a force produced on the particle. The Lorentz Force equation is shown in Eqn. 2.1, where F is the force produced, q is the charge of the particle, v the velocity

and B the magnetic field density. A conductor with current flowing through it can be simplified as a constant stream of electrons moving along it. Therefore if a current carrying conductor is placed in a magnetic field a force will act upon the conductor, the modified equation for this is Eqn. 2.2, where I is the current and L the length of the conductor. If the conductors are placed on a cylindrical rotor, this force can be exploited to create cyclical motion and is the basis of a motor's operation.

$$\vec{F} = q\vec{v} \times \vec{B} \qquad \textbf{Eqn. 2.1}$$

$$\vec{F} = \vec{I}L \times \vec{B} \qquad \textbf{Eqn. 2.2}$$

What can be seen as a complimentary effect to the Lorentz force is the BLV law, which states that a voltage will be induced in a winding moving through a magnetic field. This law is shown in Eqn. 2.3, where E is the electromotive force (EMF) generated. While this is the principle of how a generator operates, the induced voltage is also present in motors and is called back EMF.

$$\vec{E} = \vec{B} \times L\vec{v} \qquad \textbf{Eqn. 2.3}$$

Of key importance in both these phenomena is the magnetic flux density, this is the definition of the strength of a magnetic field, while magnetic flux, φ, is the density multiplied by the area, A, it crosses (Eqn. 2.4). Flux linkage, Φ, is a measure of the interaction between the magnetic field and a coil and relates back to the voltage requirement of a motor or the voltage produced by a generator, V, Eqn. 2.5 and Eqn. 2.6.

$$\varphi = BA \qquad \textbf{Eqn. 2.4}$$

$$\Phi = N\varphi = NBA \qquad \textbf{Eqn. 2.5}$$

$$V = \frac{d\Phi}{dt} \qquad \textbf{Eqn. 2.6}$$

In an electrical machine, there are two interacting magnetic flux fields, the armature flux and the field flux. How the field flux and armature flux are set

up and their variation during operation is the major difference between machine topologies (which will be briefly covered in Section 2.3.2 and discussed further in Chapter 3). However, as a loose rule, the field flux is set up with a DC current in windings or PMs and is generated as a fixed value; the armature flux is generated by multiphase AC or pulsed current in windings. The interaction between these two fields generates the Lorentz force.

2.3.2 Machine classification

As there are multiple different topologies and technologies involved in the design of electrical machines several different classifications and sub-classifications exist. Some examples of these classifications are:

- Supply for the armature:
  - AC, DC or Pulsed
- Field flux production:
  - Windings (either externally supplied or through inductance), PMs or none if pure reluctance
- Stator and Rotor position:
  - Radial inner rotor, Radial outer rotor, axial, transverse, linear or multiple rotors or stators
- Rotation speed:
  - Synchronous or asynchronous with the armature frequency

A chart showing one method of classification of a selection of conventional machines is presented in Figure 2.8.

2.3.3 Materials and limitations

2.3.3.1 Soft magnetic steel components

The stator and rotor of a machine are constructed out of laminations of electrical steel. The important parameters of the steel are the flux density saturation value, the loss coefficients, the mechanical strength and to a lesser extent the mass density.

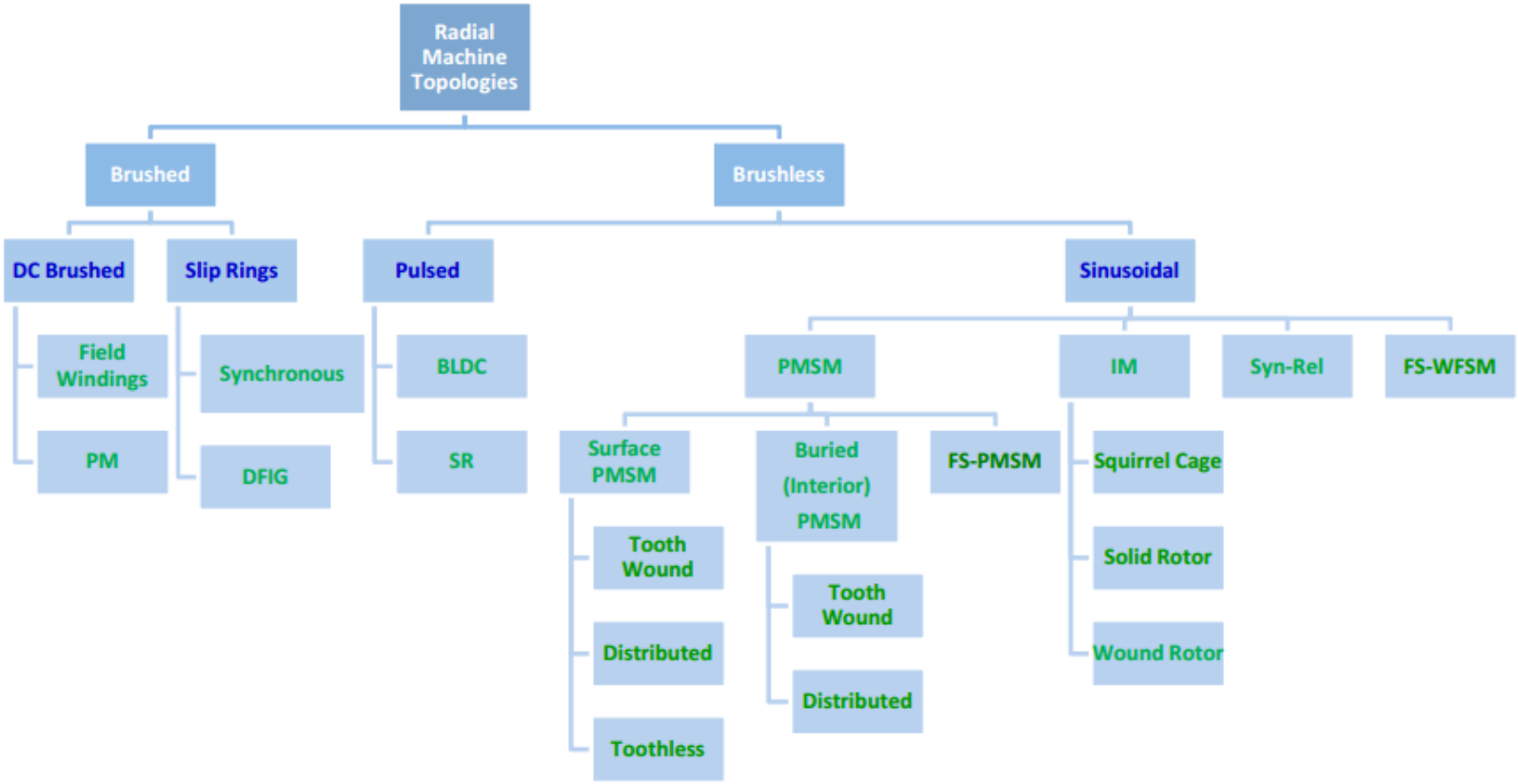


Figure 2.8- Conventional machine classification [37]

Electrical steels have a value at which the flux density no longer increases linearly, called the saturation point. Different materials, such as silicon, can be added to the metal to increase this saturation point. The higher this value is, the higher the flux density can be applied, increasing the torque density of the machine [38, 39].

Each different addition to the steel changes the loss profile which, as well as the material used, is based on the frequency, f, stacking factor of the laminations, s, and flux density. There are several constants based on the material, for the hysteresis losses K_h, α and β and for the eddy current losses K_e. The simplified expression for this is the Steinmetz equation, given in Eqn. 2.7. For a specific material, these losses limit how high of a flux density and frequency can be used whilst maintaining a high efficiency.

$$P_{fe} = K_h f^{\alpha} B^{\beta} + K_e (sfB)^2 \qquad \textbf{Eqn. 2.7}$$

While the saturation point and loss profile are more critical for the stator, where the flux densities are higher, the mechanical strength is important for the rotor. In certain machine topologies, such as when PMs are buried under the surface of the rotor, having the PMs closer to the surface of the rotor improves the machine performance. However the rotor spins at high speeds and will generate centrifugal forces on these PMs, therefore there is a limit to how close to the surface they can be based on rotation speed, PM mass, rotor radius and finally mechanical strength. The stronger the rotor material, the closer these PMs can be to the air gap.

Figure 2.9 shows a range of high performance electrical steel based on the losses and yield strength. The blue marks are silicon iron, while the red are cobalt iron. For the stator material low losses are important so 10JNEX900 and 10JNHF600 are commonly used. For the rotor the three HXT steels and are popular for their high strength without excessive losses.

The mass density of the material will not greatly affect the electromagnetic properties of the machine, but the mass of the rotor will affect its inertia, limiting the acceleration and deceleration rates of the motor. Also, specifications often have a maximum machine mass and if this is a strict limit reducing the mass density can help achieve this.

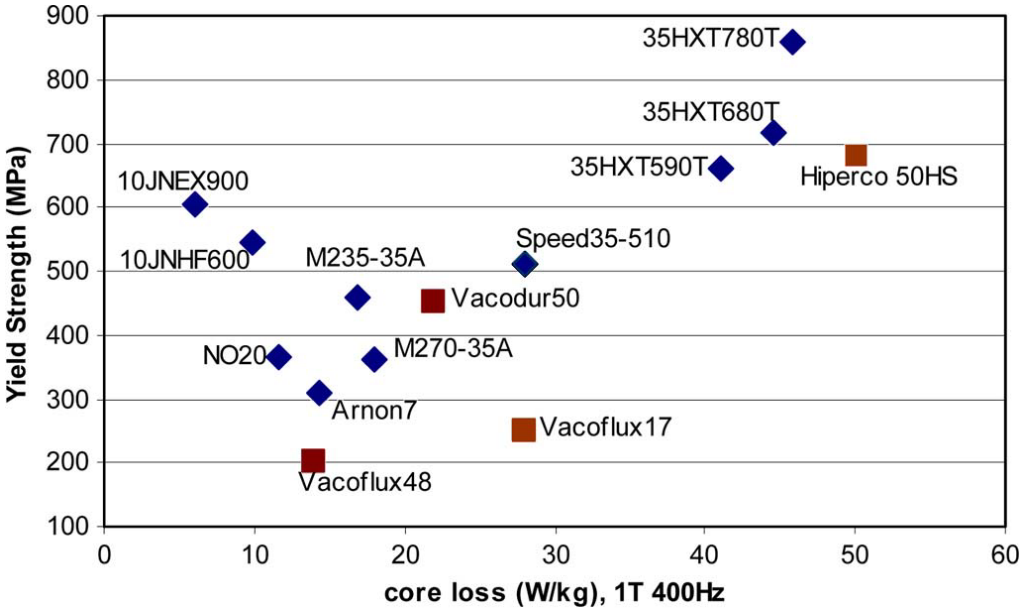


Figure 2.9 – Comparison of core losses and yield strength for high performance electrical steels [39]

2.3.3.2 *Windings*

The majority of the time the conductors are copper wires, however, there are some exceptions to this. Aluminium can be used, although it has a lower conductivity resulting in a higher winding resistance, R, and thus produces higher losses, P_{cu}, for the same current, I, as shown in Eqn. 2.8. The benefits are aluminium is much lighter than copper when mass is critical and more malleable which allows for a higher slot fill factor.

$$P_{Cu} = I^2 R \qquad \textbf{Eqn. 2.8}$$

Another variation is to not use standard round conductors, but instead bars, foil or less conventional methods such as machined or cast windings to specific shapes or hairpin windings. These different conductor shapes allow for higher

fill factors, smaller end windings or easier constructions, but often decrease one of the other two or increase cost.

To protect against turn to turn short circuits the windings are insulated. As well as adding size to the windings, reducing the slot fill factor, this insulation will be rated up to a specific temperature (with higher temperatures being more expensive). The temperature limit of the winding insulation is typically the first thermal limit reached and thus the most critical.

2.3.3.3 PM material

There are a wide range of PM materials but they mainly fall into 4 categories; ferrite, aluminium nickel cobalt (AlNiCo), NdFeB and SmCo. These materials are summarised in Table 2.3.

Table 2.3 - PM materials

Material	Cost	Remnant Flux Density (B_r)	Coercive Force (H_c)	Thermal Limits
Ferrite	Low	Low	Med	High
AlNiCo	Medium	High	Low	Med
NdFeB	High	High	High	Med
SmCo	V. High	High	High	Med

NdFeB is the standard for high torque density applications due to its high B_r and H_c. For low temperatures NdFeB is cheaper than SmCo; however the dysprosium (Dy) needed to be added to NdFeB to increase its thermal limit is very expensive and so SmCo is the better option when the PMs are likely to go above 150˚C.

Ferrites can either be used in low torque density machines or in large quantities to overcome their lower B_r. As a rough guideline ferrites are 10 times cheaper than NdFeB, whilst having 3 times lower energy density, so from a cost standpoint using a higher quantity is beneficial. However with large amounts (of any of the PM materials) comes the issue of space. As stated when discussing the rotor material, the PMs need to be close to the air gap, increasing their thickness has diminishing returns as the additional material must be placed

deeper and deeper. The increased mass will also make the centrifugal forces larger and thus the PMs must be placed even further from the air gap for mechanical strength.

AlNiCo would be a great choice, not too expensive and high B_r if it were not for its low H_c. This means it can be easily demagnetised, and thus the B_r plummets. Some topologies and technologies, such as flux memory machines [40], find ways to overcome or even utilise this, however, they generally involve complex additions to the machine design.

2.4 Previous attempts at the FreedomCar targets by others

The public nature of the targets set by the DoE has made this project very attractive to a number of companies and institutions. Some design attempts come close to meeting the targets, but often by comprising one or more of the most restrictive specifications. In this section, an overview of the more promising design cases is presented.

2.4.1 High pole number SMPMSM

One documented attempt at using high pole numbers for the FreedomCar targets has been found. This uses a 36 slot 30 pole surface mount permanent magnet synchronous machine (SMPMSM). A major drawback with these designs is that the back EMF exceeds the limit due to this high pole number. The designs slightly exceed the stator diameter limit. Also shown is that for the peak torque the current must exceed the target's limit. Not discussed here is the machine efficiency or iron loss values, but the high pole number and referencing the need to reduce the losses lead to the belief that these targets have not been met [41].

2.4.2 SMPMSM vs. IPMSM

In general, SMPMSMs are usually assumed to be the best topology to use for the DoE targets due to the high peak torque density required. In [42] an IPMSM

is compared to an SMPMSM to find which is superior for meeting the targets. This is a quantitative assessment of achievability of the targets and its aim is to highlight trade-offs between IPMSMs and SMPMSMs.

2.4.2.1 Designs

A moderate level of detail has been explained for both machines, while not enough to accurately reproduce the results, it gives a good idea of the scale and design of the machines. The design parameters for each machine, and current and back EMF values, are given in Table 2.4. Both machines meet the power and torque requirements of the targets.

Table 2.4 - SMPMSM vs IPMSM design parameters [42]

Parameter/Dimension	IPMSM	SMPMSM
Poles	10	10
Slots	12	12
Stator outer diameter (mm)	237	247.2
Rotor outer diameter (mm)	150	149.3
Active stack length	85	73.4
Total length (mm)	123	105
Magnet height (mm)	7	11.5
Air gap thickness (mm)	0.73	1
Total mass (kg)	27	27.8
Maximum per phase current (Arms)	400	320
Back EMF at 100% of maximum speed, peak line to line (V)	800	673

Both the designs have the same 12 slot segmented stator with a double layered fractional slot concentrated winding (FSCW) with a 50% slot fill factor and use the same steel, copper and PM materials. Both rotors have 10 poles, the IPMSM has V-shaped PMs, the SMPMSM has a carbon fibre retaining sleeve. Figure 2.10 shows the SMPMSM design.

2.4.2.2 Results

Both simulated and experimental tests were completed on the IPMSM. The SMPMSM was also simulated and practically tested; however the experiment only went up to 5000 rpm.

2.4.2.2.1 IPMSM

The simulated electrical losses of the IPMSM can be seen in Figure 2.11.

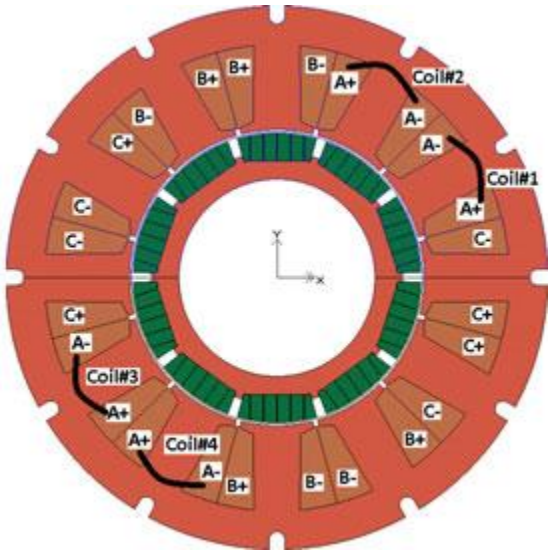


Figure 2.10 – SMPMSM design [42]

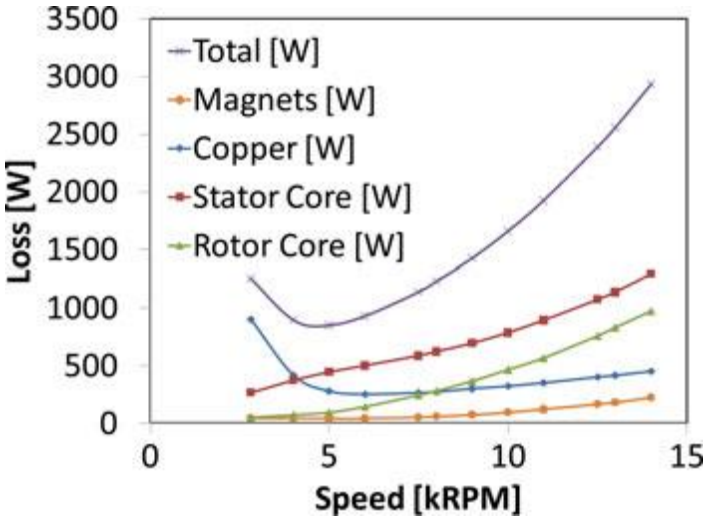


Figure 2.11 - IPMSM simulated losses [42]

It can be seen that the magnets losses are low due the segmentation of the PMs and because they are buried in the rotor. The copper losses are low as this is a benefit of the FSCW. Both stator and rotor iron losses are high, due to high speed and the harmonics from the slot pole combination.

From the simulated results, the efficiency is above the target of 95% between 2800 to 8500 rpm, the torque ripple is slightly above the target amount at 5.5%.

The simulated temperature reaches 185°C in the end windings, here C class insulation has been used, which can withstand up to 220°C, whereas the targets specify H class (limited to 180°C).

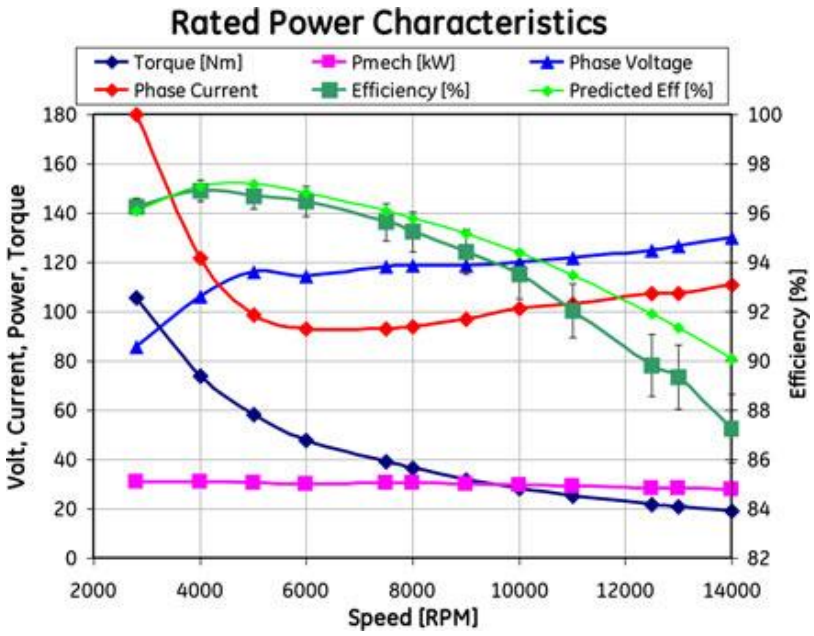


Figure 2.12 - Experimental IPMSM characteristics [42]

Figure 2.12 shows the results of the practical tests after the IPMSM had been constructed. It can be seen that the torque and power requirements are met across the range with the voltage and current within the limits. The real efficiency is less than the predicted efficiency, this is mainly due to the mechanical losses which have been calculated to be 3% at the maximum speed, bringing the minimum down to 87%, dropping below the target 95% at 8000rpm.

2.4.2.2.2 SMPMSM

The simulated results for the SMPMSM are shown in Figure 2.13, as stated earlier experimental tests were done on this design but not up to a high speed.

In contrast to the IPMSM, the rotor iron losses are low, with the copper losses also still being low. The stator iron losses are still high, but the big difference is the magnet loss. The magnets are more exposed to the harmonics and as such have much higher losses. This causes the efficiency to drop to 94% at 4800 rpm,

although the simulations show the SMPMSM will have a slightly higher efficiency at the maximum speed.

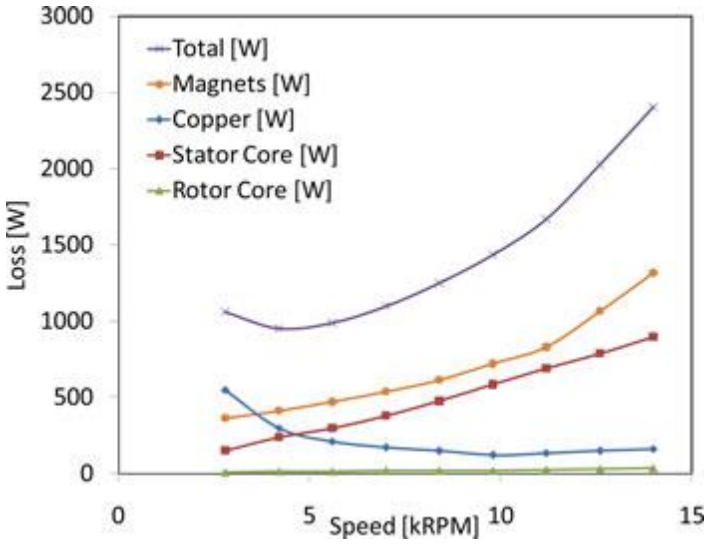


Figure 2.13 - SMPMSM simulated losses [42]

2.4.2.3 Summary of SMPMSM vs. IPMSM previous attempts

The paper shows that the machines have similar torque densities, as both produce the same torque with similar masses. The IPMSM had a lower PM mass due to the existence of the reluctance torque but required higher currents to meet the peak torque. The IPMSM met the efficiency requirement for more of the speed range, but was predicted to be lower at maximum speed.

Comparing the machines to the FreedomCar 2020 targets, neither machine met the efficiency requirements or the cost target, both cost $4/Nm whereas the target equates to $1.4/Nm. The SMPMSM design has a stator outer diameter larger than the limits and the IPMSM has a back EMF that exceeds the target.

2.4.3 V-shape IPMSM

One good example of reaching these targets with a range of machines is given in [43], four designs were suggested, two with FSCW and two with integral slot distributed windings (ISDW). All four had the same rotor designs with the same air gap length and the same current loading, but with different stack

lengths to obtain the output power. The stator was then modified to allow for different designs. [43]

The advantages of FSCW are higher power density, shorter end turns, compatibility with segmented stators and low cogging torque [43]. However they have multiple sources of electromagnetic nonlinearity. ISDW machines offer their own advantages of higher reluctance torque and lower high-speed losses [43]. A main advantage due to the segmented stator of the FSCW designs is that they can typically be implemented with a higher slot fill factor, 0.55, instead of the 0.4 for ISDW [43].

The FSCW designs both have a slot per pole per phase (SPP) of 2/5, and differ as one has a double layer winding (Design A) and the other is single layer (Design B). The ISDW designs are both double layer but one has 1 SPP (Design C) and the other 2 SPP (Design D) [43]. Design A and C are show in Figure 2.14 and Figure 2.15 respectively.

The paper focuses upon achieving the high torque/power density, treating the back EMF target as less critical, and because of this the back EMF exceeds the 600V target at max speed. [43]

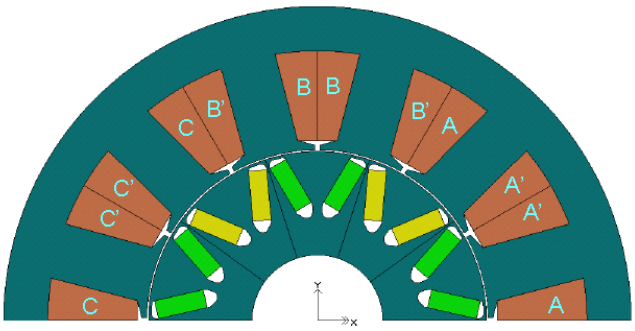


Figure 2.14 - Double layer FSCW IPMSM 'Design A' [43]

2.4.3.1 Design Parameters

Detailed sizing of each machine and electrical parameters were given, so these designs could be reproduced if needed. Table 2.5 gives some of the design

parameters which are the same for all four designs, while Table 2.6 gives the values which differ between the designs.

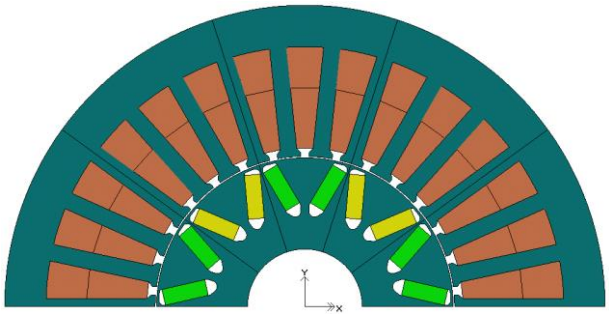


Figure 2.15 - Double layer ISDW IPMSM 'Design C' [43]

Table 2.5 - Constant design parameters [43]

Parameter	Value
Number of Poles	10
Air-gap (mm)	0.73
Rotor Outer Diameter (mm)	147.84
Magnet Height (mm)	8
Magnet Outer Span	0.978

Of note from Table 2.6 is the very high back EMF. Although the current is low and turns per phase are high, so the winding could be redesigned to overcome this.

Table 2.6 - Variable design parameters [43]

Parameter	Design A	Design B	Design C	Design D
SPP	2/5	2/5	1	2
Turns/phase	34	22	34	36
Stack Length [mm]	81.45	107.23	77.01	82.35
Peak l-l Back EMF [V]	910.75	802.58	872.33	910.3
Characteristic Current [A]	95.76	98.63	164.71	175.3
Peak Power [kW]	55	55	55	55
Magnet Mass [kg]	2.22	2.93	2.1	2.25
Total Active Mass [kg]	36.78	36.32	39.36	41.91

2.4.3.2 Results

The torque and output power are the same for all four designs, matching the DoE targets values. Torque is constant at 100Nm until 2800rpm where it decreases at a rate to keep power constant, until 14000rpm. Output power increases linearly to 30kW at 2800rpm and then stays level for the field weakening range.

Figure 2.16 and Figure 2.17 show that at low speed, all the machines have similar losses. However as the speed increases, the higher the SPP the lower the efficiency is. This could be due to the higher input current needed (with constant voltage and output power) and higher iron losses, as the same flux is trying to pass through smaller teeth, giving higher flux densities.

From Figure 2.16 and Figure 2.17 it can be seen that design A is the most efficient across the speed range (dropping below 95% at 10000rpm) making it the optimal choice for this target. However design D has the lowest rotor losses and so would be a lot easier to cool [43].

2.4.3.3 Summary of V-shape IPMSM attempt

This study shows that designs with lower numbers of slots per pole require lower current for a fixed torque target. However the study is limited to the comparison of 2 designs (each with 2 slight variations). The cost target was not considered and the designs exceeded the maximum back EMF, so these designs are still a way off the targets.

2.4.4 Flux focusing machine

The paper, [44], focuses on a segmented stator FSCW IPMSM with a spoke rotor design (also known as a flux focusing machine), with 10 poles and 12 slots and a double layer winding pattern. While this only shows one design, it is one of the best attempts found at reaching the targets. The design is shown in Figure 2.18.

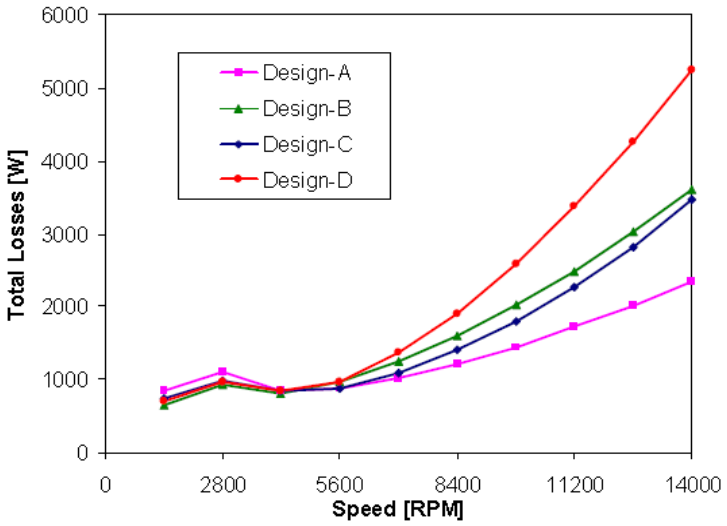


Figure 2.16 - Losses vs. speed for the four designs [43]

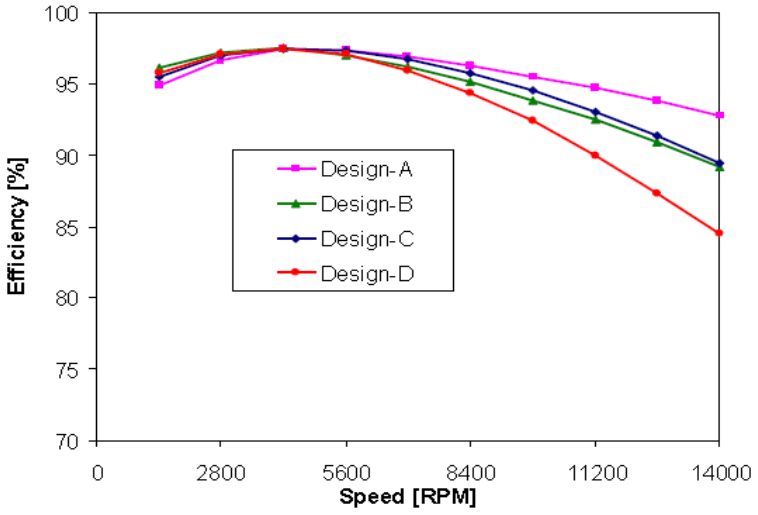


Figure 2.17 - Efficiency vs. speed for the four designs [43]

2.4.4.1 Design Parameters

A lot of the design parameters have not been shown, such as diameters, stack lengths, magnet sizes and air gap size. But it is shown that this machine meets the 35 kg total mass requirement [44].

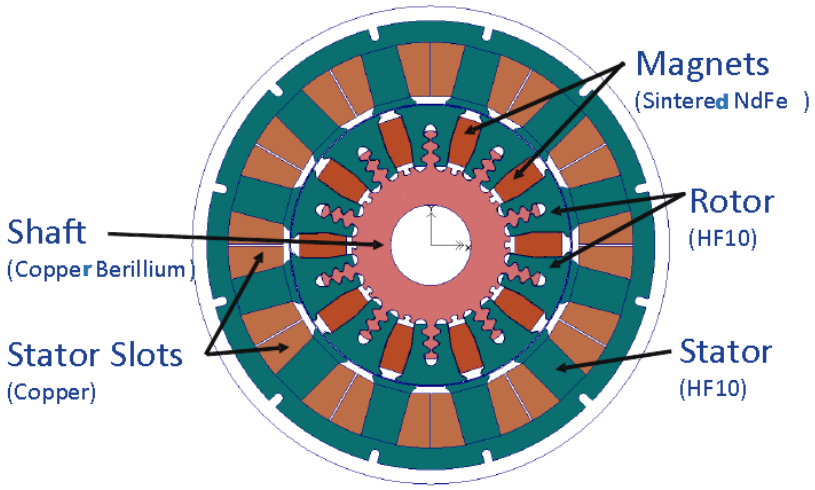


Figure 2.18 - Flux Focusing Machine [44]

2.4.4.2 Results

The machine was constructed and tested experimentally, after being simulated using FEA [44]. Again this machine meets the torque speed characteristic whilst maintaining the voltage and current limit. The efficiency stays higher than 95% until 11000 rpm, and drops to 92.7% at maximum speed (though this does not include mechanical losses) [44]. The maximum temperature at rated load in the machine is 180°C [44], which is just within the limits of the H class insulation.

2.4.4.3 Summary of flux focusing attempt

While this design comes very close to achieving the targets, it also pushes very close to the ultimate boundary of the H class insulation. The amount of magnets used is not stated, but they appear to be large size, this would add quite a lot to the cost of the machine, which was not considered here. And as with the previously shown designs the high speed efficiency has still not been met.

2.4.5 Summary of previous attempts

The main hurdle of all the PM machine design case studies, consulted and presented above, seems to be the efficiency at high speeds. From literature it was perceived that the 95% target is not achievable at these high speeds, with current permanent magnet machines.

Another challenge these papers, and others, have failed to tackle is the cost. NdFeB, a rare earth magnetic material, used in all previous designs costs >$100/kg. The majority of previous designs use over 2kg of magnetic material, leaving very little (to no) budget for other parts, such as steel, copper and construction costs, of the $275 limit.

Chapter 3. Machine Topologies Study

This chapter describes the different technologies and topologies of machines which have been considered in order to reach the FreedomCar 2020 targets. While each type of machine has its advantages and challenges when compared to the others, the comparison is mainly focused on determining which machine topologies would be able to meet both the peak torque and high speed requirements of the FreedomCar targets. References to other works that address the same objectives are included here.

The importance of this section to the design methodology process was not to start the work with any assumptions based on the correct topology to use for the targets. Instead to view the whole range of machine technologies before narrowing down to a single choice.

3.1 Conventional motor types

The 'more conventional' machine types are introduced in this section. Such technologies have been around for a long time, and most have been used in traction applications at some point or other.

3.1.1 Synchronous machine (SM)

Wound field synchronous machines have windings on both the stator and the rotor, as shown in Figure 3.1. The flux produced by the stator and rotor current interact to produce a torque that is only present when properly aligned, i.e. the machine is running at synchronous speed. The field winding gives easy and accurate field flux control, useful for both field weakening and strengthening.

The main challenge resides in supplying the dc field to the rotor. First of all, this will produce extra copper losses, which are harder to remove thermally and reduce the overall efficiency. The other issue is supplying the current to the rotating conductors. Typically this is achieved by implementing brushes or exciters, but they have their drawbacks, particularly at high speeds.

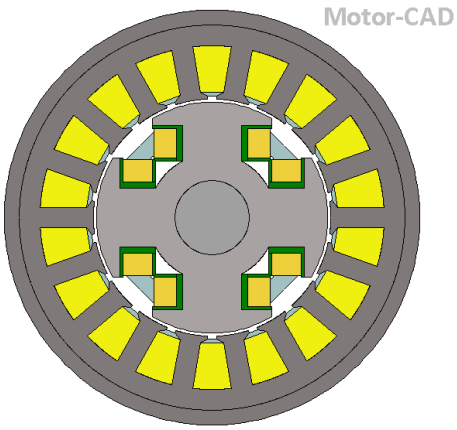


Figure 3.1 - Wound field synchronous machine

As a solution, PMs can be used to produce the field flux, as shown in the following two variations of SMs.

3.1.1.1 Surface mount permanent magnet synchronous machine (SMPMSM)

SMPMSM machines, as the name suggests have PMs on the rotor surface (shown in Figure 3.2), which provide the field flux. Having the PMs as close to the air gap as possible gives the maximum magnet utilisation factor resulting in higher torque densities. However this comes with some disadvantages. The rotor has no saliency and so no reluctance torque is produced, this means that obtaining torque in the field weakening region, whilst maintaining the VA limits is difficult [45, 46]. Also, the PMs require a retaining sleeve to withstand the high centrifugal forces present at high speeds [47].

While this type of machine gives the high power and torque density required, it is unlikely to meet the high speed voltage and efficiency requirements [47]. Also high-performance PMs add considerable cost to machines.

SMPMSMs are commonly used for low speed high torque traction applications, as this is the power node for which they excel. SMPMSMs were used in some of Honda's early hybrid cars [4]. A further example of SMPMSMs being used in traction is green aircraft taxiing where very high torques are needed [48].

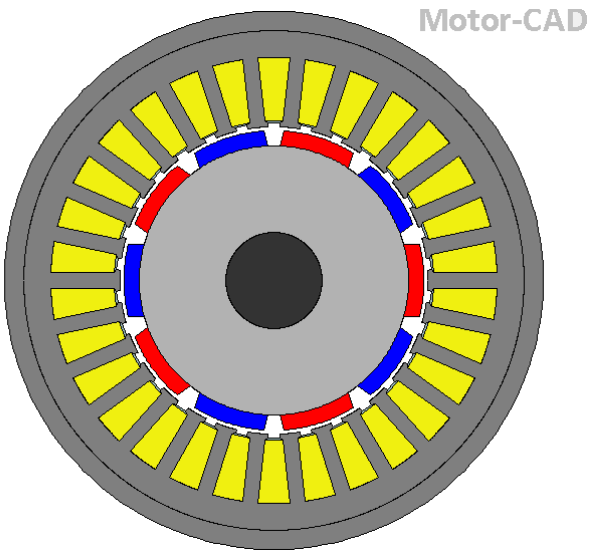


Figure 3.2 - SMPMSM

One documented attempt at using 36 slot 30 pole SMPMSMs for the FreedomCar targets has been found. A major challenge with these designs is that the back EMF usually exceeds the limit, especially at high speeds. The designs slightly exceed the stator diameter limit. Also shown is that for the peak torque the current must exceed the target's limit. Not discussed here is the machine efficiency or iron loss values, but the high pole number and referencing the need to reduce the losses lead to the belief that this target was not met [41].

3.1.1.2 Interior permanent magnet synchronous machine (IPMSM)

The IPMSM machine operates on the same principle as the SMPMSM but has the PMs buried under the surface of the rotor, displayed in Figure 3.3. This gives an almost as good power density and magnet alignment torque density as the SPM [45] and also improves rotor robustness, even at higher speeds, due to the PMs being buried under the rotor steel. The interior magnets also add reluctance torque which helps improve torque density and high speed performance. Although this reluctance value is small compared to some of the topologies shown later [17].

The drawbacks are the requirement for expensive PMs and while it can reach higher speeds than the SMPMSM machine, the performance (in terms of efficiency and torque per amp) is not optimal at these higher speeds.

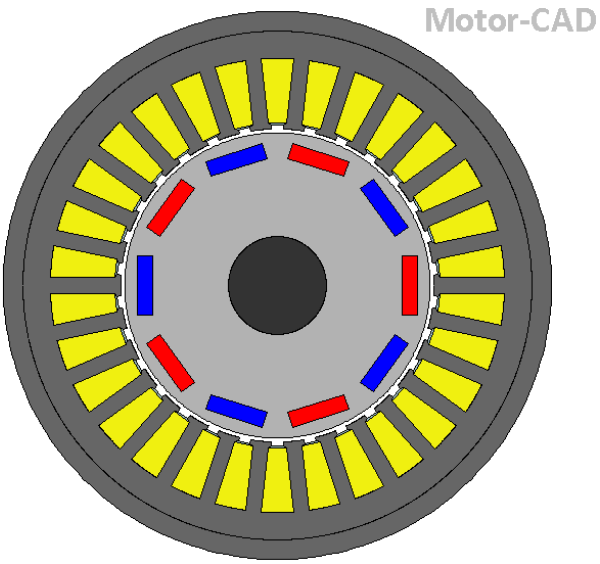


Figure 3.3 - IPMSM

This machine is the current industry standard for automotive traction, as it has high torque density and reasonably good high speed capabilities. IPMSMs are used in many current hybrid vehicle applications, such as many of the Toyota Prius models [4, 15] and CGT's current hybrid traction machine [49].

Due to the torque density and moderate speed range of the IPMSM design, they have been heavily investigated for these targets. The first key example of this is the General Electric (GE) machine [44], which uses radial spoke PMs inset in the rotor. This machine uses a 12 slot 10 pole configuration and meets the majority of the targets, failing on efficiency (92.7%) at maximum speed, although it is not declared what the key loss contributor is here, and it is likely to fail on the cost, as large NdFeB PMs are used [44]. Another example is the V-shape IPMSMs in [43], these designs perform slightly worse than the radial spoke machine, the best dropping below the 95% efficiency target at 10000 rpm and exceeding the back EMF limit [43]. However the V-shape design did use

smaller magnets, so while a cost analysis was not shown for either, the V-shape designs would come closer to this challenging cost target, but both are unlikely to meet the cost requirements.

3.1.2 Brushless direct current machines (BLDCM)

BLDCMs are similar to PM synchronous machines, in that they have a polyphase stator and a rotor with PMs. But in a BLDCM the PMs are designed to give a square wave flux density, which gives a trapezoidal back EMF and requires a square wave armature current, as opposed to the sinusoidal values of these found in the PMSM.

This machine has similar advantages to the synchronous machines, in that it provides high torque with high efficiency [50]. The control of this machine is very easy and generally produces slightly higher torque than the PM synchronous machines.

The sacrifice made for easier control and increased torque is that the torque ripple in the machine is much higher than that of a synchronous machine.

3.1.3 Induction machine (IM)

IMs have existed for over a hundred years and have been used regularly in electric vehicles, particularly larger ones.

IMs use the principles of electromagnetic induction to generate a field flux from electrically conductive rotor bars, shown in Figure 3.4. This keeps one of the significant benefits of PM machines, i.e. that only the stator needs to be supplied with current.

They are cheap, reliable and rugged and can produce traction adequately [51]. One notable advantage of IMs is that the rotor flux can be regulated through field orientated control [52]. This makes them quite competitive against PM machines in the high speed region.

Current flowing in the rotor causes some of the disadvantages, such as high losses and rotor cooling complexity [53]. While IMs are comparable to PM motors at high speed, it is unlikely the same design would be able to meet the peak torque requirement with the current and temperature limits.

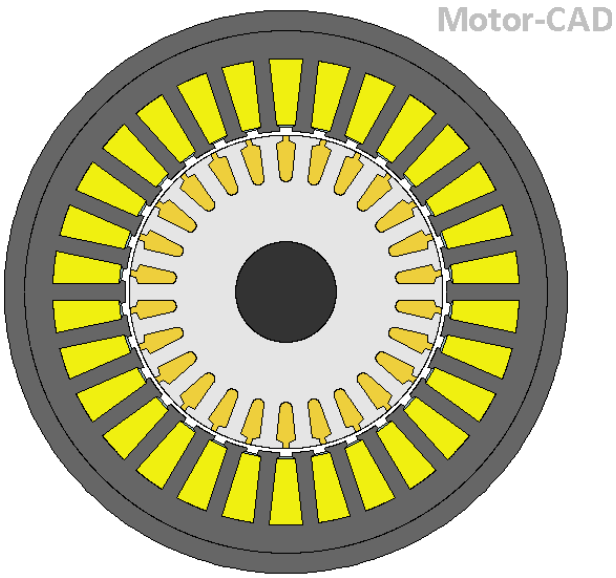


Figure 3.4 - IM

IMs have been previously considered but not implemented for the FreedomCar targets. IMs are commonly seen in hybrid and fully electric vehicle applications from the Tesla Roadster [54] to heavy duty vehicles with high torque, low speed and large mass such as BAE HybriDrive propulsion system and the IMs used by Azure Dynamics for hybrid traction [4].

3.1.4 Switched reluctance machine (SRM)

SRMs produce torque purely based on the reluctance of the rotor. SRMs are defined as having a simple, robust, low cost rotor structure and capability for high-speed rotation [55, 56]; this comes from the rotor being purely made out of laminated steel (with a toothed shape to produce the reluctance) as in Figure 3.5.

The motion is more discretised than other machines and thus gives rise to higher vibrations causing acoustic noise and torque ripple [47, 57]. The simple rotor also means lower power and torque density and so high torque machines need to be very large.

SRMs do not use a standard 3 phase AC stator winding as many of the other machines do, this means they require dedicated power electronics, increasing cost and reducing flexibility [47, 58].

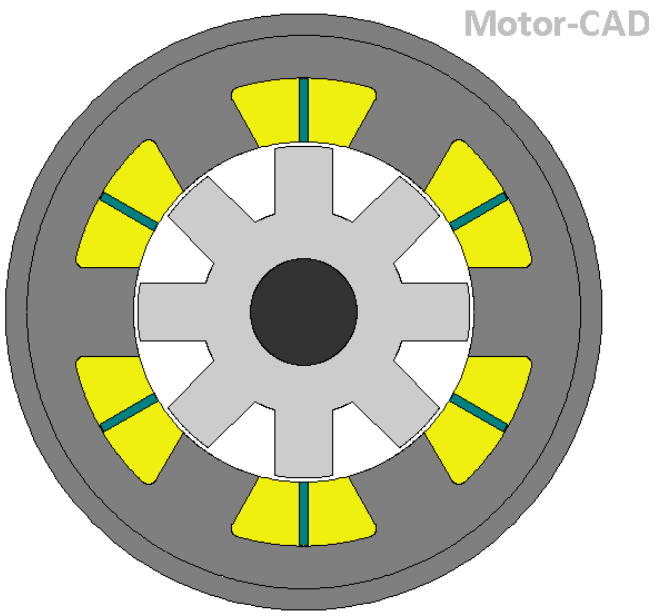


Figure 3.5 - SRM

SRM designs have not previously been considered for the FreedomCar targets. However, high torque low speed machines for full electric vehicles are shown in [54], though the only machines with high enough torque density for the targets have low efficiency, <90%. A similar example of a high torque density but with poor efficiency SRM for EVs is seen in [57]. While the SRMs are optimal for high speed applications, they are also considered where their robustness is important and the vibrations they produce is not an issue such as in off-highway vehicles seen in [4].

3.2 Unconventional flux direction machines

These machines use conventional methods of producing the flux fields in the machine but have the flux travelling in directions other than radial.

3.2.1 Axial flux machines

Axial flux machines have flux travelling in the axial direction. Both the rotor and the stator are annular shaped. Each of the conventional machine types could be made axially, but generally a surface mount or interior PM rotor is implemented, with a synchronous wound stator.

Axial machines generally have a smaller volume for the same power than their radial counterparts. The main benefit of axial flux machines is the extremely high torque density values achievable. However, this is very dependent on the dimensions and the power node being investigated. If the specifications favour the size of the axial flux machine it would be very difficult for a different topology to outperform it. Though, the range of dimensions and power nodes where this superiority would occur is very narrow [59]. The shape of axial machines means they are very suited to applications where the radial room is limited, such as the in-wheel motor shown in [60] .

Because of the shape of axial machines, it is easy to have double stator or double rotor machines. This is seen quite commonly with axial machines [59-62], as seen in Figure 3.6.

These machines are harder to scale than radial machines because the torque is proportional to the cube of the diameter and independent of the stack length, so to increase the torque produced, the diameter must be increased and so different size laminations must be manufactured. This inability to easily scale is a big issue when considering traction machines, which are likely to be produced for a range of different vehicles.

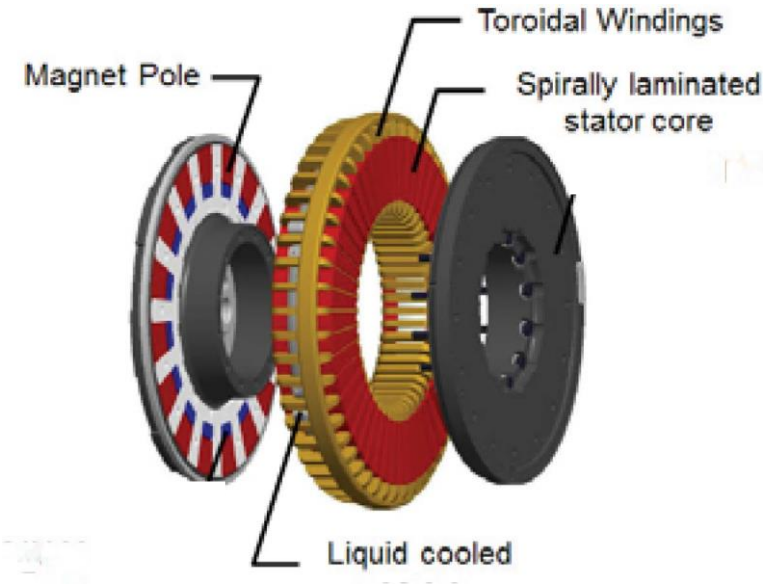


Figure 3.6 - Double rotor axial IPMSM [62]

Axial flux machines are often designed for traction applications due to their high torque density but have not been considered for the FreedomCar 2020 targets. A good example is given in [62], showing a machine designed for strict targets. This is a perfect instance of the axial flux machine being optimal for a specific power and volume node. In this case, the requirements allow a large machine diameter, with a low active length, to produce a large torque at a relatively low speed (2800 rpm).

Another example of axial flux machines being used for traction is given in [61] where such a machine is designed to approximately the same dimensions as that of the Toyota Prius IPMSM machine. It is shown that the axial flux machine can produce over twice the torque of the Prius IPMSM motor, although this is at half the speed. This shows that if the power node can be changed to meet the axial flux optimal point than this machine type can excel.

3.2.2 Transverse flux machines (TFM)

TFMs have flux in the transverse direction. This type of machine uses a homopolar phase winding, a stator core formed by laminated C-cores and a rotor provided with heteropolar PMs [63]. The flux path associated with TFM is shown in the cross-section in Figure 3.7.

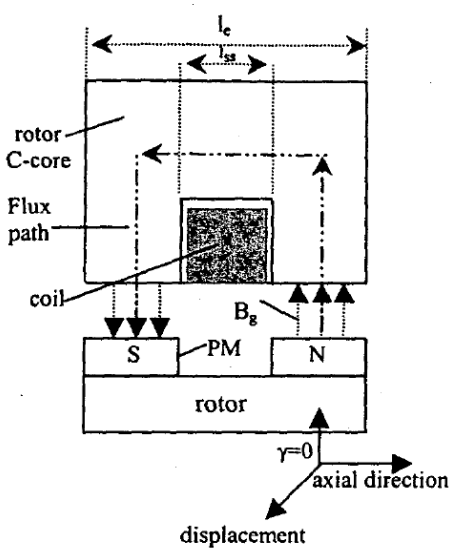


Figure 3.7 - Cross section of a transverse flux machine [63]

Each TFM is single phased, so for multiple phases, multiple machines are needed, a TFM with two phases is shown in Figure 3.8.

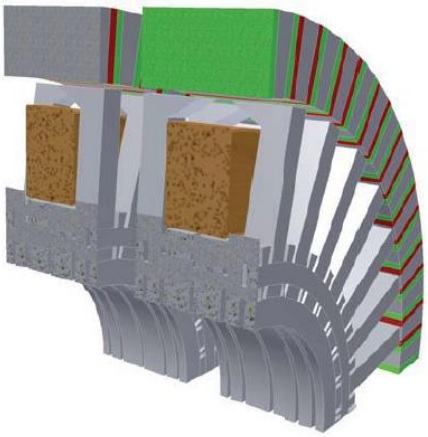


Figure 3.8 - Two phase outer rotor transverse flux machine [64]

The main advantages of TFM are the potential high torque density and high electric loading [52]. Increasing the pole number increases the power and reduces the speed of the machine for a fixed electrical frequency; this means the torque increases by a considerable amount [63]. Each phase is an independent system, giving modularity and increased fault tolerance [65].

The main drawbacks of this machine are that similar to an axial flux machine its construction is very complex and scaling is also problematic. TFMs also have large leakage flux, high winding inductance, and poor power factor resulting in low efficiency and thus a larger power electronics system is needed [52]. TFM are generally best for very high torque at low speed and would be difficult to design for the high speeds required here.

TFMs have been designed for direct drive applications, both with pure reluctance and with PMs. As expected the reluctance machine has a lower torque density than the PM machine, but both are very high, 14KNm/m^3 and 56KNm/m^3 respectively. However, they have a very low maximum speed, 1000 rpm [64]. The machines here, similar to the axial flux machines, have been designed for a specific power node to show optimal performance from the TFMs.

3.3 Unconventional machine topologies

These machines use the conventional radial shape of a machine but have different methods of producing or using the flux. A lot of these machines are a variation of or a hybrid between two of the conventional technologies.

3.3.1 Flux switching machine (FSM)

One of the main benefits of FSMs is that they can be developed to produce the flux purely in the stator, which comprises both the armature windings and the field producing arrangement. The latter can either be PMs (PMFSM) or with a wound field (WFFSM) to produce the field flux, or it could have both. The rotor is usually a similar design to an SRM rotor and so offers the same benefits of robustness and low cost [66].

Using field-windings gives more control of the field flux, but requires a DC current input; an outer rotor machine using this is shown in Figure 3.9. If PMs are used no field current input is required and so fewer losses are produced, however, field weakening will have to be employed at higher speeds in order

to reduce to reduce the field flux to acceptable levels. The advantage of having both PMs and field windings is that the PMs can produce the majority of the flux, but the windings can control this, to strengthen or weaken the field.

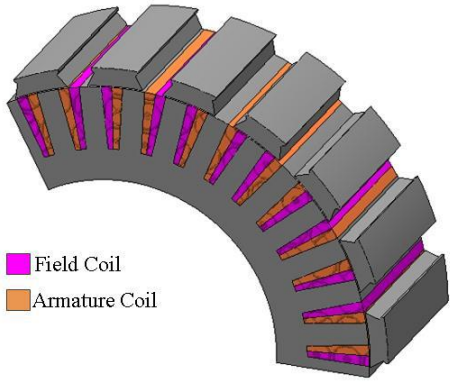


Figure 3.9 - Outer rotor WFFSM [67]

Similar to a conventional PM machine the PMFSM has high air gap flux density [68]. The advantage of this is that the design is less dependent on a small air gap, as SRM are, and this makes the construction simpler.

While the power density of PMFS machines is comparable to that of a PM synchronous machine, the PM utilisation ratio is lower than that of the Toyota Prius IPMSM machine [15]. This results in a larger PM mass being needed to obtain this similar power density to an IPMSM design. However because the PMs would be in the stator, they would be closer to the cooling system, this means less dysprosium (needed to improve the maximum operating temperature of NdFeB) would be required, possibly reducing the overall cost of PM material [69]. Another advantage of the PMs in the stator is there are fewer issues with magnet retention.

Both PMFSM and WFFSM have been designed for the FreedomCar targets [69]. As would be expected, the PMFSM produces higher torque than the WFFSM for the same current supply, but both meet the requirement. The machines do not meet the efficiency requirement across the speed range. The efficiency of the PMFSM machine drops to 85% at maximum speed, due to the high stator and rotor iron losses. The WFFSM machine has a higher efficiency at maximum

speed, but at rated speed fails to meet the target; it has been assumed that this is due to the copper losses from the higher current requirement. Torque ripple is also shown to be an issue, this is somewhat mitigated (from 17% to 7% of average torque) but the targets are still stricter (5%) [69].

A PMFSM has also been designed to the same specifications as the Toyota Prius IPMSM machine, and while the rotor allowed for good mechanical integrity for high speed, and in this case smaller torque ripple, the main drawback was the requirement for a larger magnet mass [15].

3.3.2 Synchronous reluctance machine (SynRelM)

SynRelMs have the same stator as synchronous machines but only produce reluctance torque, based on the saliency of the machine. The rotor is made of laminated steel, with flux barriers placed within the rotor, seen in Figure 3.10, to create a difference in the reluctances of the d and q axis.

Due to the lack of PMs or windings, the rotor of a SynRelM has the benefits of the SRM rotor, in that it is cheap and robust and if designed correctly can go to high speeds [70].

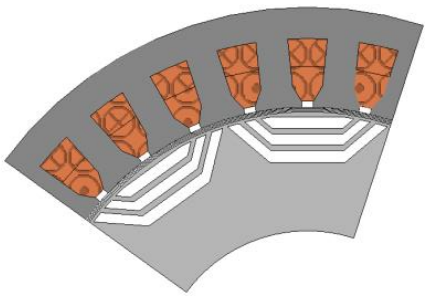


Figure 3.10 - Synchronous reluctance machine

While an acceptable level of torque density can be achieved [70, 71] (considering that it includes no PMs), its performance cannot be compared to that of a PM machine and thus it is improbable that the requirements of the peak and rated torque of the application at hand will be reached. An added complexity of SynRelMs is the required small air-gap, in order to maintain the

require performance, making constructing and maintaining this air gap more difficult than PM machines. Other challenges with these machines include the torque ripple and the power factor. These can be mitigated but are still generally worse than an IPMSM machine [17].

3.3.2.1 Permanent magnet assisted synchronous reluctance machine (PMa-SynRelM)

PMs can be added to create a PM-assisted synchronous reluctance machine (PMa-SynRelM). This increases the torque density of the machine, but also increases the cost and high speed mechanical issues [72]. Compared to an IPMSM, this results in increased reluctance torque, which can be used to reduce supply current or magnet mass requirements for a fixed torque requirement [73].

Figure 3.11 shows a PMa-SynRelM machine where all of the rotor barriers have been filled with ferrite PMs. This design has high saliency and still produces a moderate amount of magnet alignment torque. If cheaper PMs or less NdFeB can be used than in an IPMSM, then a high torque density machine can be made whilst keeping costs low.

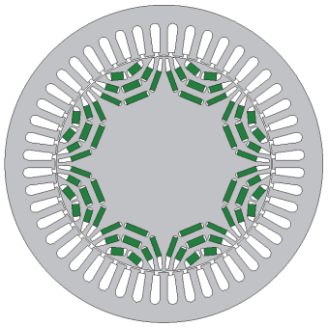


Figure 3.11 - PMa-SynRelM with ferrite magnets [74]

The SynRelM, particularly with PM assistance, has been suggested for HEV and EV applications. A common approach is to use the space within the barriers, by implementing ferrite PMs instead of rare earth. It can be seen in [74], which shows that for similar targets to that of the FreedomCar, that this machine can maintain high efficiencies at high speeds. However when using large quantities

of ferrite PMs at high speed the mechanical issues of these machines become even more critical due to the centrifugal forces [17].

3.3.3 Synchronous–induction hybrid machine (SIM)

SIMs are, as the name states, a hybrid between synchronous machines and induction machines. The main point of these is a synchronous machine that provides torque across a range of speeds, allowing for self-starting [75]. The rotor has both conductive rotor bars and PMs.

Figure 3.12 shows half of an IPMSM SIM. It can be seen that the rotor bars are close to the outside of the rotor, with the PMs under them. This layout gives the highest induction torque. For higher torque at synchronous speed the rotor could be designed with the PMs further out than the rotor bars. Because the magnets are further away from the air gap, there is a lower air gap flux density than an IPMSM. This results in a lower torque density at synchronous speed. Another issue is the large cost and the complex construction. [75]

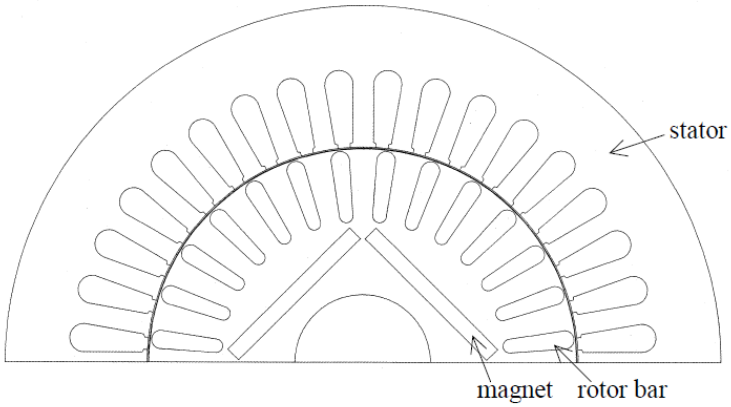


Figure 3.12 – Synchronous-induction hybrid machine [75]

The only advantage of this design over an IPMSM is its ability to self-start without a variable frequency drive. For the application at hand where a variable frequency drive is an option, this type of machine will not be considered further, it was kept in the thesis to show that a full study had been completed of the different machine topologies.

3.3.4 Flux memory motor (FMM)

FMMs are a variant of a radial pole IPMSM machine, using the partial, reversible demagnetisation of the PMs to control the flux flowing through the air gap. This gives a wider field weakening region, resulting in better high speed performances. The rotor usually uses radially placed PMs, with a tangential magnetisation direction [40], such as in Figure 3.13.

The demagnetisation of the PMs must be controlled. This can either be done with very careful control of the d-axis current or by employing a second set of windings (in the rotor or stator). Trapezoidal PMs are used (with the wider area closer to the outer radius of the rotor) because this gives spatial control over the PM demagnetisation [40]. The thinner parts of the PMs are easier to demagnetise, and so the amount of the PM which is demagnetised can be controlled, to manipulate the field flux. This makes the weakening of the flux much simpler and more efficient in this machine compared to a conventional PM machine, but the current control needs to be very precise.

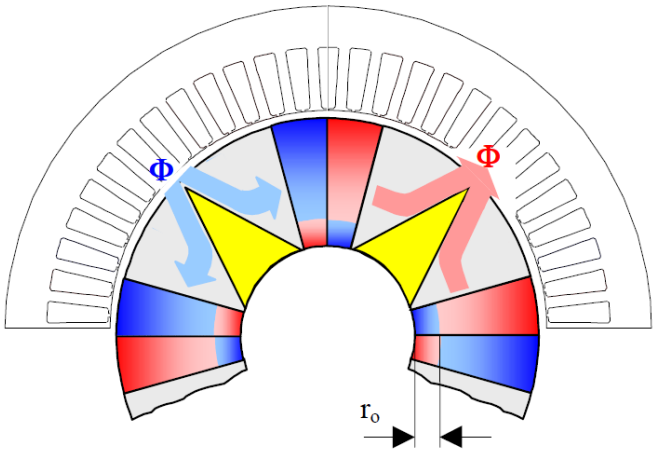


Figure 3.13 - Flux memory motor, partially demagnetised [40]

This machine does not need to use expensive NdFeB PMs, in fact AlNiCo PMs are more suited to this machine, as due to their low coercive force they are easier to demagnetise and remagnetise [40]. Another benefit is that AlNiCo PMs are cheaper than NdFeB.

The major disadvantage of this type of machine is that it is untested at the large scale, so it is unclear whether the benefits would still exist on a larger machine. The main uncertainty resides in whether demagnetisation of larger PMs can be controlled and maintained as easily as for smaller ones.

This type of machine has been suggested for automotive traction applications as an integrated starter generator (ISG) due to the precise flux control and high efficiency of the machine [76]. The machine used for this is low powered, 2.2kW, compared to the DoE targets, so the uncertainty of scaling the magnets is still an issue.

3.3.5 Multi air gap machines

Multi air gap machines are normally based on SMPMSM and IPMSMs but others do exist, such as SRM or IM or combinations between two topologies.

Double stator (DS) machines have a single rotor with PMs and/or saliency on the inside and outside. There is one stator on the outside of the rotor and one on the inside. This allows for a larger armature flux to be set up.

Double rotor (DR) machines have two rotors, which can either be an inner and outer rotor with a stator in between (shown in Figure 3.14) or an inner rotor, then a rotor around this, then an outer stator around this. One advantage of both DR designs, in HEVs, is that one rotor can be connected to an ICE with the other connected to the drive train of the vehicle, this decouples the ICE speed from the wheel speed, allowing the ICE to operate at maximum efficiency [77, 78].

With multi air-gap machines, higher torque densities in terms of Nm/m^3 can be achieved [79], but the improvement in Nm/kg is very limited [80], especially when considering all the extra inactive material required to implement a multi air gap machine. Another drawback of multi air gap machines is increased complexity of design and windings which cannot be easily cooled with conventional water jackets [77].

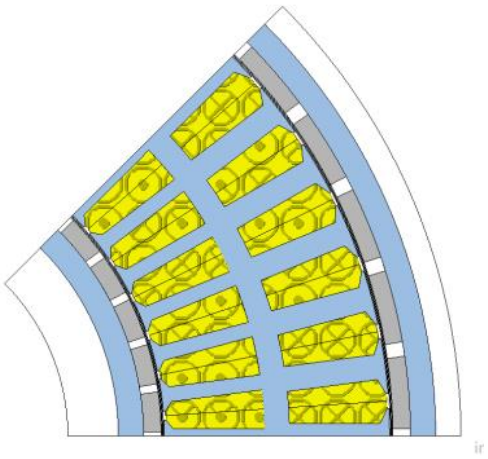


Figure 3.14 - Double rotor SMPMSM [80]

As with other less conventional topologies, these designs have not been considered for the FreedomCar targets but have been designed for traction applications many times. A DR machine has been proposed for traction application, but the low speed and high mass would hold it back when aiming for the FreedomCar targets [77, 78]. DS designs for HEVs are commonly suggested, primarily PM machines [79] but also reluctance machines [54]. These motors are shown to give very high torque per volume, which is very useful for start-up.

3.3.5.1 Double stator switched reluctance machine (DSSRM)

DSSRM has been highlighted because it gives very good torque density whilst using no PMs. Because the teeth of both stators are aligned, and the corresponding windings energise at the same time, the radial forces from the inner and outer stator cancel, and the tangential forces sum, to give a larger overall torque [81].

Figure 3.15 shows a DSSRM, as described above the inner and outer stator teeth and phases are aligned so that the tangential forces sum while the radial forces cancel. The rotor is made of steel, no windings or PMS, and each segment connects at the axial ends of the motor, to give mechanical stability [82].

This has the benefits of an SRM, high speed range and cheap while producing a larger torque [54]. However the design is quite complicated, the two air gaps need to be very small, as with all reluctance machines, and constructing and maintaining this could be difficult, this partially removes the robustness benefit from the SRM. This machine is not very developed, with only a small amount of publications relating to it.

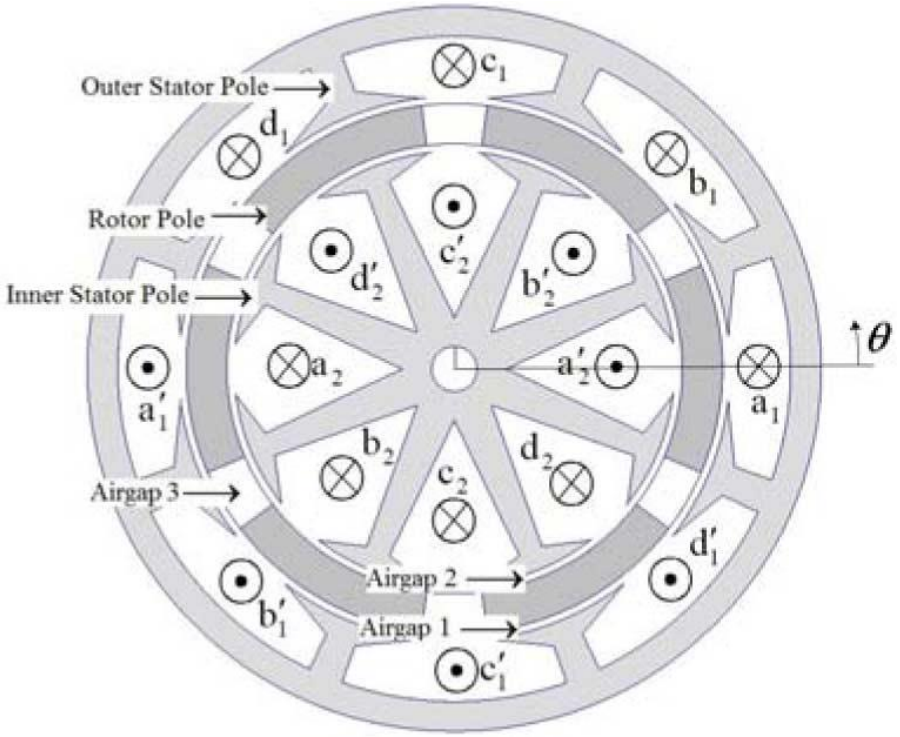


Figure 3.15 - Double stator switched reluctance machine [82]

While DSSRMs have been designed in theory for traction applications they have not been prototyped or practically implemented. The design found has sufficient torque density to meet the FreedomCar 2020 targets, however, it is not rated to the same wide speed range and the maximum efficiency of the design is below the minimum efficiency target [54].

3.3.6 Synchronous homopolar motors

There is a renewed interest in this technology due to the PM free design and precise flux control. The rotor is two sections of salient iron poles rotated 180° electrically from each other [83]. Between each section of the rotor is a toroidal

field winding, held by the stator, this is shown in Figure 3.16. This coil produces an axial field which makes all the iron teeth on one rotor section act as north poles, and the iron teeth on the other rotor section act as south poles. The copper in the stator slots is a standard three phase synchronous machine winding [83].

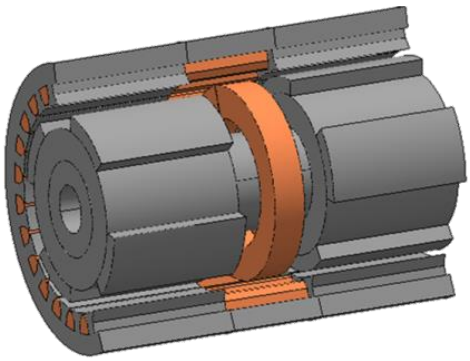


Figure 3.16 - Synchronous homopolar machine

Having no windings or PMs on the rotor gives similar advantages to SRMs [84]. As well as this, it allows for a controllable field excitation [83]. The field excitation coil is simple, reliable and its placement helps protect it from the forces on the rotor [85]

The machine has to be approximately twice as large for the same torque as a conventional synchronous machine [83]. This is due to the length of each pole only being half as long as the whole machine [84]. Because of the uneven rotor surface, the windage losses are higher than that of a smooth rotor machine, which would be more pronounced at higher speeds [84].

An option available for this type of machine is to use a superconductor in the field winding [85]. This would remove the copper losses in this winding and thus increase the efficiency and the maximum field current density [86]. The downside is that this winding must be kept at a very low temperature (the material with highest operating temperature available is 138K), which is very challenging to achieve inside a traction machine.

This technology has never been considered for high torque automotive traction applications but has been designed as a high speed flywheel suitable for hybrid

electric vehicles [87]. While the design shown meets the same power requirement as the FreedomCar targets (30 kW), it is a low torque design, with a much higher speed.

3.4 Comparison of machines technologies

In order to identify the most suited machine technology and topology, relative QIs were set and applied to each technology, qualified by the literature review presented above. Table 3.1 gives the QI of the manufacturability of the machines for this specific application and tabulates these indices by setting a score sheet (with 10 being the maximum) for the 6 key factors that define the production and manufacturing of the machine, along with a weighted total. When assigning the QI values, higher values were always superior i.e. even for volume and mass, a high value refers to a smaller machine (or a higher power/torque density).

The assessment method for these QIs was done via an automated process. Some of the QIs were decided upon by on a series of yes/no checks, for example for scalability, can the machine be lengthened easily to increase torque, or for cost are rare earth PMs used, is the rotor a simple construction. Mass and volume were based on ranking the designs, updating the previous rankings to ensure a proportional spread between 1 and 10.

Some of the machine topologies here covered a small range, such as the FSM referring to both PMFS and WFFS, in this case an average value between the two types of FSM were used.

Some of the machine topologies have been removed due to obvious inabilities. Wound field SM was removed because the complexities of supplying current to the rotating conductors. BLDCM was removed due to it being very similar to the PM SM machines, particularly when considering advantages provided. Also excluded was the SIM, this reduced the performance of an IPMSM while only adding self-starting torque, which is not needed in this application.

Finally, DSSRM was removed due to the complexity and low development of the design.

A weighting system was incorporated to the total to represent which factors were more critical to the comparison. The weighting factor to use for each score was provided by the industrial partner, CGT. The cost was seen as the most critical QI and therefore was given a weighting of 3. Volume and mass were the next most important, as keeping these low is crucial in HEV applications, and so their weighting is 2. The other three QIs were given a value of 1, as they are still significant, but not as much as cost, volume and mass.

Table 3.1- Topology QI scores

Motor Type	Cost	Volume	Mass	Scalability	Equivalent fuel economy	Expected Life	Weighted Total
Weighting Factor	3	2	2	1	1	1	
SMPMSM	5	9	8	8	9	7	73
IPMSM	6	9	9	8	9	7	78
IM	8	7	7	8	6	7	73
SRM	10	3	4	7	4	7	62
SynRelM	9	5	6	8	7	7	71
FSM	7	6	7	7	5	7	66
FMM	5	5	4	4	7	4	48
Homopolar	8	5	6	7	7	7	67
Axial Flux	5	9	8	4	9	6	68
TFM	5	9	8	3	8	6	66
DS PM	4	10	7	6	10	6	68

The same information is shown graphically in Figure 3.17. Each bar represents a machine, with each colour representing how much each QI contributes to the overall score. Here each of the values has already been multiplied by their weighting factor so that the total is correctly displayed.

The cost QI was mainly dependant on materials costs, as expected the topologies that need high amounts of PM (SMPMSM and IPMSM) have a low value for this and the reluctance machines (SRM and SynRelM) have a higher score, this can be seen in both Table 3.1 and Figure 3.17. The volume and mass

QIs were both how small the machine could be and still meet the torque and power requirements, here the PM machines are generally better and reluctance machines score lower. Scalability was how easy it would be to change the power node of the machine, either for a small change to the targets or to produce a range of machines for different sized vehicles, the more conventional machines scored higher at this, with the alternative flux direction machines (axial and transverse) being particularly bad. Equivalent fuel economy was a combination of performance (especially efficiency) and mass, this was won by the PM machines with the alternative flux direction and double stator machines also achieving high scores. Expected life was how long the machine would last in the application and was dominated by the bearing, this gave the same QI values across most the machines, with axial, TFM and DSPM being slightly lower because they required less conventional bearing layouts and FM was low due to the constant de- and re- magnetisation of the magnets.

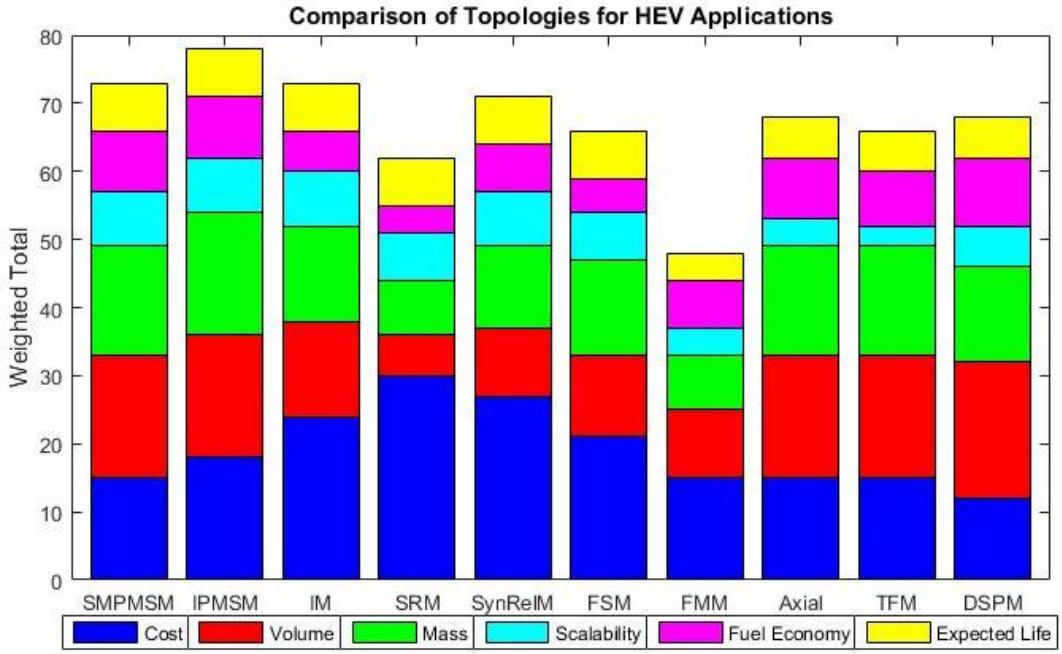


Figure 3.17 - Weighted QI values

Table 3.2 briefly compares the performance of the machines including the potential to reach the peak torque, and the width of the speed range that high efficiency could be maintained for. The optimal performance region of each machine is also displayed in Figure 3.18, with the colour used to represent the

PM mass requirement, with red being high, yellow indicating a small (or optional) PM material amount and green showing that no PMs are required. It is important to note that these measures are a result of published literature.

The alternative flux direction and DS machines have been removed. This was because they would perform similarly to the machines they were based on, but with a lack of scalability and thermal issues respectively which are large disadvantages.

Table 3.2 - Performance comparison of machine topologies

Machine Type	Permanent Magnet Mass	Torque density	Field Weakening Range
SMPMSM	High	High	V. Poor
IPMSM	High	High	Poor
IM	None	Medium	Medium
SRM	None	Poor	Very Wide
SynRelM	None	Medium	Wide
FS	Medium	Medium	Wide
FM	Medium	Medium	Medium
Homopolar	None	Medium	Wide

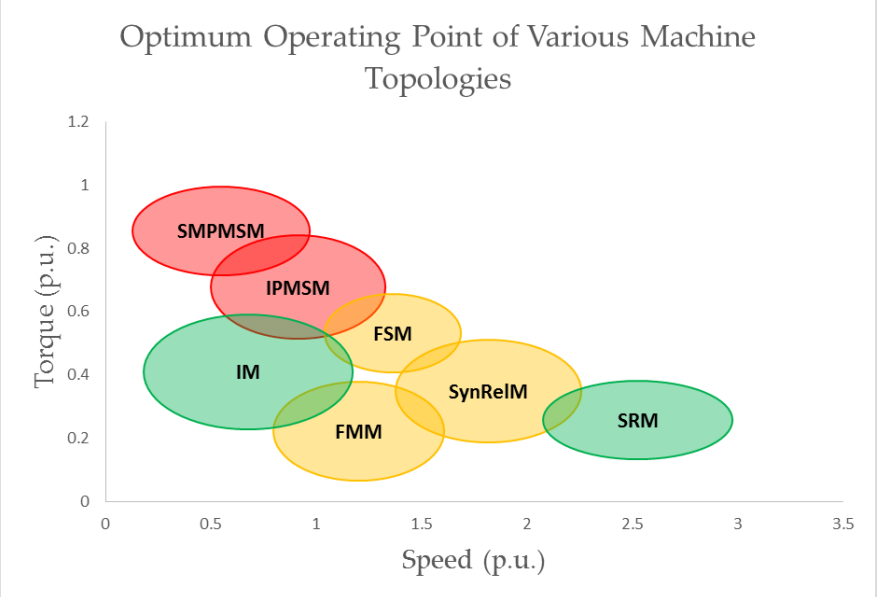


Figure 3.18 – Optimum operating aspects for the range of machine topologies

From Table 3.2 and Figure 3.18, it can be observed how the SMPMSM and IPMSM technologies achieve better torque density performances, but do not perform as well in the extended speed range. As can be expected, the SRM has a low torque density but very high speed capabilities. The remaining technologies give varying results between these two extremes with some positives and some negatives, when considered for the application at hand, covered in [88]

3.5 Optimal machine topology for DoE FreedomCar 2020 targets

From Table 3.1 and Figure 3.17 it was clear that the best choice to use for the FreedomCar 2020 targets was the IPMSM. This was closely followed by the SMPMSM technology, but this did not offer any crucial advantages over the IPMSM. IM scored high, but as stated in the topology section considering it, it would be difficult to design a machine to reach both the high torque density and wide speed range efficiently with the current and temperature limits. The next highest scorer was the SynRelM machine; this was interesting because it offered some benefits over the IPMSM, particularly at high speed.

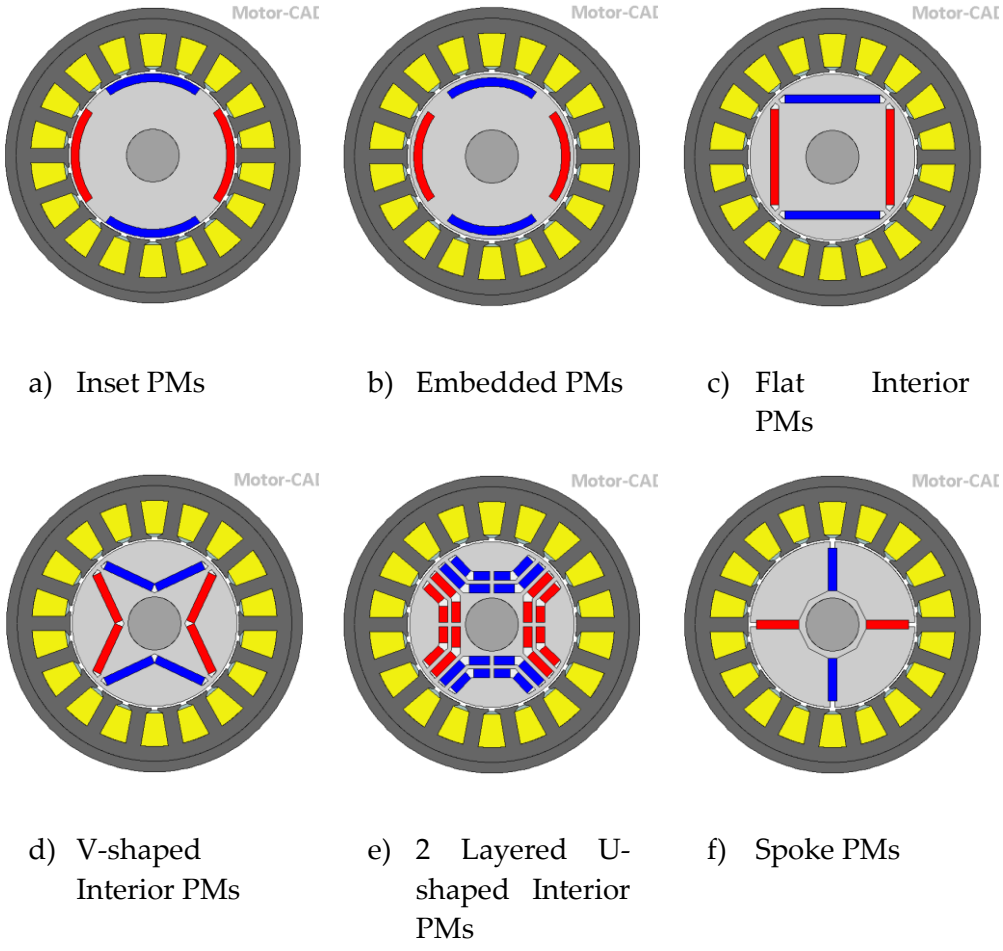
The double stator and the alternative flux direction machines also performed well but these usually had significant drawbacks, such as design complexity, cost and poor scalability, which implied the general superiority of the IPMSM configuration.

As expected the IPMSM machine was the best choice to use for the FreedomCar 2020 targets. It was likely that adding some reluctance to the design, i.e. moving towards a PMa-SynRel topology, would help meet the high speed performance requirements. If the speed range was wider or removal of PMs was a higher priority (such as in similar targets for further in the future) IMs and pure SynRelM machines would be the most promising candidates but there would be some loss of performance associated with these.

3.5.1 IPMSM rotor configurations

Even after and IPMSM had been decided upon there was still a wide range of different layouts the PMs can take, as shown in Figure 3.19.

Inset PMs have the magnets as close to the air gap as possible, this gives the highest magnet alignment torque whilst still having reluctance in the design. However, an inset PM has the same mechanical challenge as a surface mount PM of retaining the magnets at high speed. To overcome this mechanical issue the PMs can be embedded, Figure 3.19b, although this reduces the magnet alignment torque.



a) Inset PMs
b) Embedded PMs
c) Flat Interior PMs
d) V-shaped Interior PMs
e) 2 Layered U-shaped Interior PMs
f) Spoke PMs

Figure 3.19 – Different IPMSM topologies

While arced PMs give lower torque ripple than flat, as in Figure 3.19c, flat PMs are easier and therefore cheaper to produce. V-shaped PMs allow for a higher PM mass to be used in the same pole pitch, and for an increase to the reluctance torque. The U-shape is a further extension of the V shape, allowing for even

more PM mass and reluctance. Spoke PMs are magnetised circumferentially (as opposed to the other topologies which are radial), the flux lines from two adjacent poles push against each other and the resultant is a radial north or south pole between each of the PMs. This allows for the magnet alignment torque to be less dependent on the depth of the PMs, allowing for a mechanically stronger design and an extended area where PM mass can be increased effectively.

Multiple layers, even of different shapes, can be exploited to increase the torque density of the machine. The U shape and V-shaped designs stack particularly well. However, this would increase machining costs (and material costs if more PMs are used) and reduce mechanical strength. The designs can even head more towards a PMa-SynRelM, with only some of the layers occupied by PMs, the rest air barriers. This gives an increase to the reluctance torque without the need for added PM mass.

To begin with option c, flat interior PMs is used. This design is the simplest in terms of mechanical construction and has minimal design parameters to optimise. This gave a good starting point for the machine design. As the design progressed, presented in the next few chapters, the drawbacks of this became clear and thus reluctance was added to improve the high speed performance towards a PMa-SynRelM.

Chapter 4. Initial Machine Design

4.1 Introduction

This section is focused on designing an optimal IPMSM for the FreedomCar 2020 targets, using conventional technology and topologies. Both concentrated wound and distributed wound machines were considered, first independently but then compared against each other. Each started with a trade-off study of a wide range of motor designs, differing from one another primarily based on the number of rotor poles and stator slots [89].

The study then started to focus more towards the final design as the target requirements were introduced in a logical sequence. The final design is then optimised in order to reach the better performing solution. Considering the wide range of initial design candidates, analytical tools were originally used, to quickly evaluate the performance of the machines. As the range of feasible designs narrowed more accurate FEA was implemented into the process.

The overall proposed process, where an efficient balance between computational time and results accuracy was achieved was a highlight of this thesis and a key contribution to knowledge. The process allows for rapid simulation of high numbers of designs, whilst ensuring high accuracy of results on the machines deemed to have a higher potential, whereas traditionally accuracy must be sacrificed for speed.

4.2 Design considerations

4.2.1 Slot pole combination

High pole numbers give higher torque density but increase the frequency requirement. Iron losses are dependent on the frequency and so at high speeds, large pole numbers would lead to higher iron losses. Low pole numbers would need higher currents to reach the same torque and this leads to larger copper

losses and a higher thermal increase [90]. The design exercise explained in this chapter, strived to find the optimum between these two extremes.

To reduce vibrations, the slot number should always be an even number, as this gives more symmetry to the design and thus a higher percent of the radial forces would cancel each other out [91]. The least common multiple (LCM) between slot and pole number was desired to be as high as possible, as this means a high cogging torque frequency, which generally results in a lower cogging torque amplitude. The greatest common divider (GCD) was also wanted as high as possible, as this usually means lower radial forces due to higher design symmetry. The winding factor of a machine is based on the SPP and the closer the winding factor is to 1, the better the machine performance [90].

4.2.2 Concentrated vs. distributed wound

In general, the most common winding configurations for electrical machines are concentrated and distributed windings. Concentrated windings have a coil around each tooth, while windings in a distributed machine span multiple teeth. In this thesis, the term concentrated winding refers to a non-overlapping concentrated winding.

Concentrated windings have smaller end windings and can be constructed with segmented stators, giving higher slot fill factors. This leads to lower copper losses and smaller machines [92].

Distributed windings have higher saliency between the d and q axis, and so produce higher reluctance torque. This is due to both the d and q axis reluctances being proportional to both the winding factor and number of coils over each pole number squared [93]. While each of these can be equal for concentrated and distributed designs, typically these values are higher for a distributed design due to the higher number of slots and integral slots per pole per phase [92, 94, 95]. The windings in these machines are distributed

sinusoidal, this leads to lower leakage flux and therefore lower losses [93, 95, 96].

Concentrated machines are generally better for obtaining high torque density, due to the higher slot fill factor available [97]. Distributed machines perform better in field weakening due to the increased reluctance torque. Because this application requires high torque density and high speed requirements from the same design, it was not immediately clear which type of winding would be most suitable.

4.2.3 Torque production

Eqn. 4.1 gives an estimate of the maximum torque, T, an IPMSM can produce based on the volume, Vol_r, air gap flux density, B_g, and current loading, A_{load}, where k_t is the torque constant. Each of these has their own equation, Eqn. 4.2, Eqn. 4.3 and Eqn. 4.4 respectively. D_r is the rotor diameter and L_{stk} the stack length. B_r is the remnant flux density of the PM, μ_m is the PM relative permeability, L_g is the air gap thickness and L_m is the PM thickness. m is the number of phases, N_t the turns per phase and I_{RMS} the RMS current

$$T = k_t Vol_r B_g A_{load} \quad \textbf{Eqn. 4.1}$$

$$Vol_r = \left(\frac{D_r}{2}\right)^2 \times \pi \times L_{stk} \quad \textbf{Eqn. 4.2}$$

$$B_g = \frac{B_r}{1 + \mu_m \frac{L_g}{L_m}} \quad \textbf{Eqn. 4.3}$$

$$A_{load} = \frac{2mN_t I_{RMS}}{\pi D_r} \quad \textbf{Eqn. 4.4}$$

The above torque (Eqn. 4.1) is the theoretical maximum that can be achieved by an IPMSM. Often maximum torque is not required, such as at high speed or low load; in that case Eqn. 4.5 gives the total torque, T_{tot}, for a specific current input and phase angle. The total torque of an IPMSM is made up of the magnet alignment torque, T_{mag} (Eqn. 4.6), and the reluctance torque, T_{rel} (Eqn. 4.7). The magnet alignment torque is produced from the interaction of the q axis current,

I_q, with the back EMF generated by the coupling between the PMs and the winding. The reluctance torque is based on the difference between the d axis and q axis reluctances, X_d and X_q, and the product of the q axis and d axis current, I_q and I_d. The torque is proportional to the number of pole pairs, p, and inversely proportional to the electrical speed, ω_e, and therefore the electrical frequency, f_e, and mechanical synchronous speed, ω_s, Eqn. 4.8. I_q and I_d are simply the q and d axis components of the total armature current, I_a, based on the phase angle, γ, Eqn. 4.9 and Eqn. 4.10. Eqn. 4.11 and Eqn. 4.12 give the values of the q and d axis reluctances respectively.

$$T_{Tot} = \frac{3p}{2\omega_e}\left[I_q E + I_d I_q\left(X_d - X_q\right)\right] \quad \textbf{Eqn. 4.5}$$

$$T_{Mag} = \frac{3p}{2\omega_e}\left[I_q E\right] \quad \textbf{Eqn. 4.6}$$

$$T_{Rel} = \frac{3p}{2\omega_e}\left[I_d I_q\left(X_d - X_q\right)\right] \quad \textbf{Eqn. 4.7}$$

$$\omega_s = \frac{\omega_e}{p} = \frac{2\pi f_e}{p} \quad \textbf{Eqn. 4.8}$$

$$I_q = I_a \cos\gamma \quad \textbf{Eqn. 4.9}$$

$$I_d = -I_a \sin\gamma \quad \textbf{Eqn. 4.10}$$

$$Xq = j\omega_e L_q \quad \textbf{Eqn. 4.11}$$

$$Xd = -j\omega_e L_d \quad \textbf{Eqn. 4.12}$$

With torque being dependent on the phase angle, Eqn. 4.5 and Figure 4.1, for a specific total current it was clear that there would be an angle which will give the maximum torque. This angle was calculated by rearranging and then differentiating Eqn. 4.5 with respect to γ, giving Eqn. 4.13, and then setting this to zero and rearranging to find the location of the maximum as in Eqn. 4.14. This is called the maximum torque per amp (MTPA) and is the control system used when the voltage required is below the supply limit. When the voltage would exceed the limit, the phase angle must be increased beyond this optimum value, to reduce the voltage.

$$T_{Tot}{}' = \frac{dT_{Tot}}{d\gamma} = \frac{-3p}{2\omega_e}\left[-2\, I_a^2(X_d - X_q)\sin^2\gamma + I_a E \sin\gamma + I_a^2(X_d - X_q)\right] \quad \textbf{Eqn. 4.13}$$

$$\gamma_{Tmax} = \sin^{-1}\left(\frac{E + \sqrt{E^2 + 8I_a^2(X_d - X_q)^2}}{4I_a(X_d - X_q)}\right) \quad \textbf{Eqn. 4.14}$$

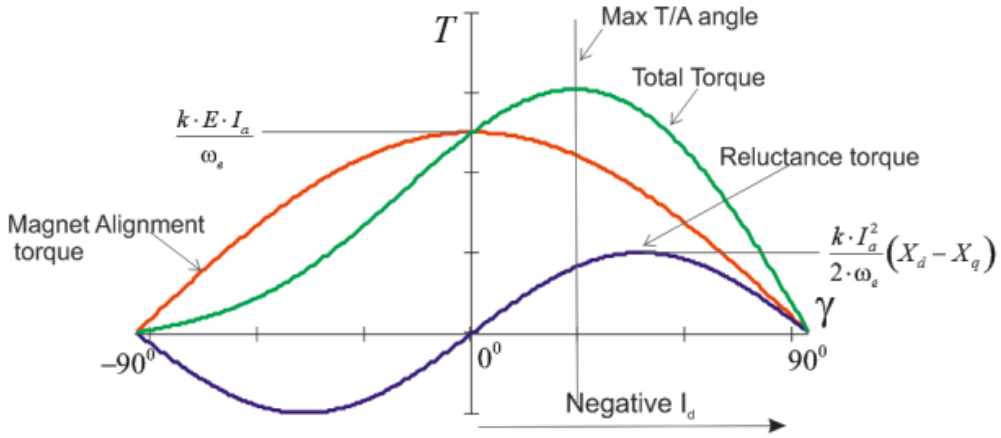


Figure 4.1 - Maximum torque per amp [37]

4.2.4 Phasor diagram

The phasor diagram of the IPMSM is shown in Figure 4.2, where the current, is shown in red, and the total voltages in blue and voltage components in green. The total voltage, V, is the combination of the d-axis voltage, V_d, and the q-axis voltage, V_q, Eqn. 4.15. The q-axis voltage is comprised of the back EMF, q-axis current multiplied by the winding resistance and the d-axis current multiplied by the d-axis reluctance. X_d is a negative imaginary number, as both L_d and ω_e are real positive numbers, Eqn. 4.12, so the multiplication by j in Eqn. 4.16 reverts it back to a positive real number, however, I_d is negative, so the resultant of this expression is a real negative value. The d-axis voltage is the addition of the d axis current multiplied by the winding resistance and the imaginary part of the product of the q-axis current and reluctance, Eqn. 4.17.

$$V^2 = V_q^2 + V_d^2 \quad \textbf{Eqn. 4.15}$$

$$V_q = E + I_q R + jI_d X_d \quad \textbf{Eqn. 4.16}$$

$$V_d = I_d R + jI_q X_q \quad \textbf{Eqn. 4.17}$$

The back EMF is proportional to the electrical frequency of the machine, which results in it increasing linearly with speed. For a fixed phase angle, such as the one that produces the highest torque, it is likely the voltage would exceed the supply limit at high speeds. To counteract this, the phase angle must be increased, decreasing I_q and increasing I_d. This change decreases the second component of Eqn. 4.16 and increases (negatively) the third, reducing V_q. Whether V_d increases or decreases depends on the size of R and X_q and the starting phase angle, however even when it increases the total voltage would decrease. However there is a limit to how much the phase angle can be increased, Figure 4.3 shows the situation where $\gamma=90$ giving $I_d=I_a$, and $I_q=0$. This removes all components dependant on I_q and minimises the voltage. This is the first speed value for which no torque can be produced due to the voltage limit.

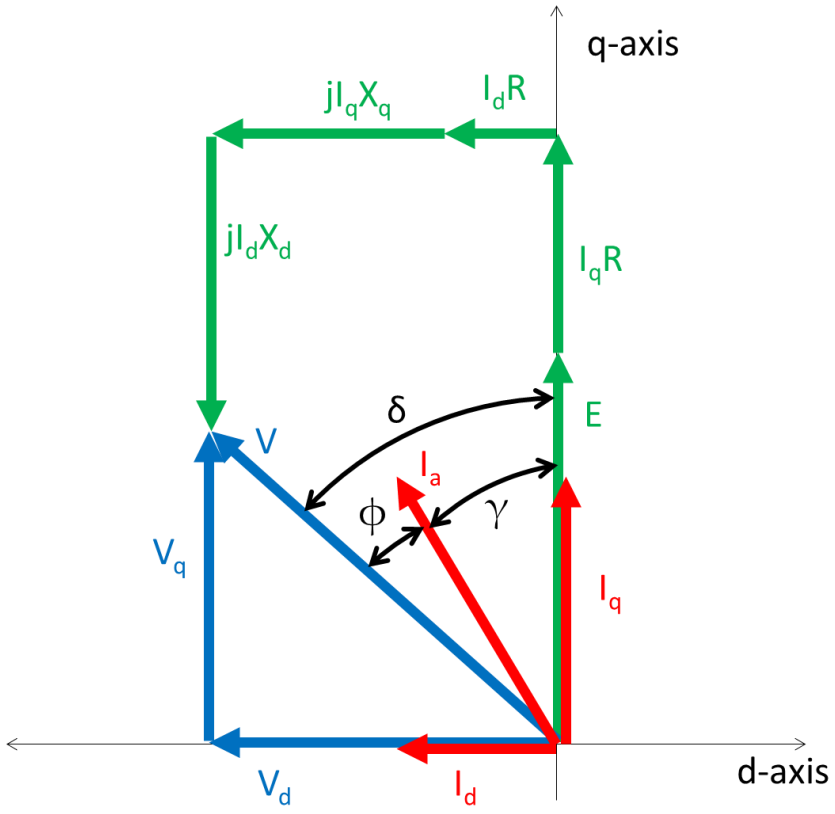


Figure 4.2- Phasor diagram of an IPMSM during normal operation [37]

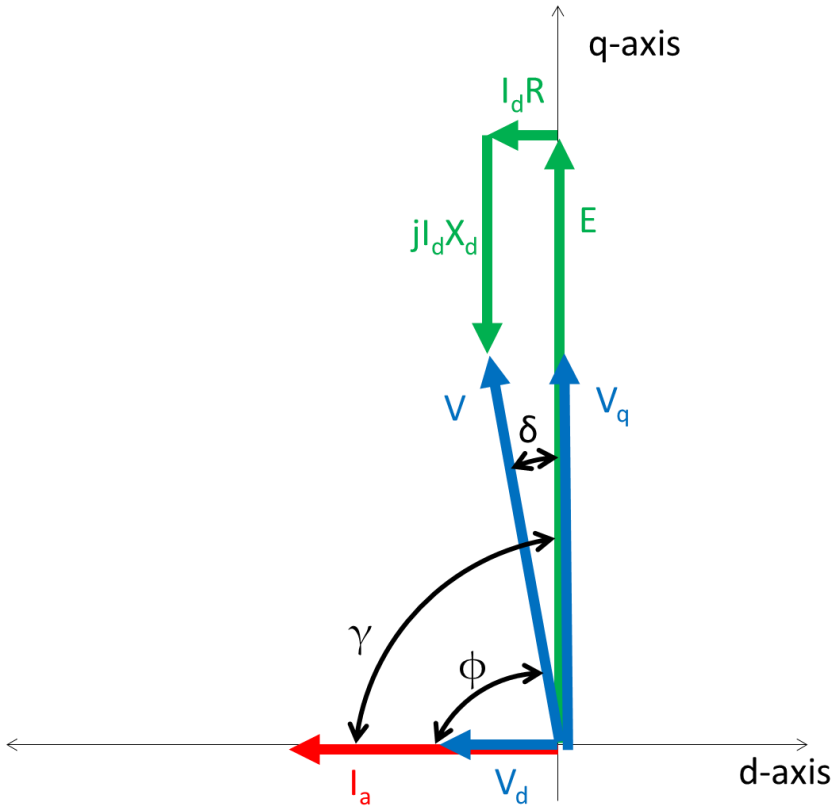


Figure 4.3- Phasor diagram of an IPMSM at maximum speed

4.2.5 Torque ripple

The above equations assumed that torque is a constant value for a given current during operation, but in practice there is always a torque ripple. This ripple is caused by two effects, the space time harmonics and the cogging torque. The torque ripple affects the performance of the machine, creating vibrations and noise, as well as distorting the current waveform.

As seen in Eqn. 4.5 the torque is produced by the product of the current and the back EMF, however the back EMF is typically not purely sinusoidal depending on the slot pole combination, giving rise to harmonics in the back EMF and therefore the torque. This ripple is typically at the same frequency as the harmonics present in the back EMF.

The cogging torque, is present even at no load and is due to the interaction of the flux and reluctance between the PMs and the stator slot opening. The PMs "prefer" being aligned with a stator tooth, moving them away from alignment

requires a force (a negative torque) moving towards them produces a force (a positive torque). The frequency and magnitude are dependent on the least common multiple of the slot (N_s) and pole pair numbers, Eqn. 4.18.

$$f_{cog} = \frac{\omega_r}{2\pi} \times LCM(2p, N_s) \quad \textbf{Eqn. 4.18}$$

The magnitude is more complex, depending on magnet thickness and span, slot opening and pole and slot pitch. These values can be selected to minimise the cogging torque, reducing the overall torque ripple. Or the ripple can be reduced by skewing the rotor or the stator, each section has the same relative ripple but with the ripples slightly out of phase, the overall instantaneous torque averages to a flatter waveform.

4.3 Design process

The detailed design procedure is presented in Appendix B with a brief methodology presented below.

There were two key steps to this process. The first was using the standard machine design equations, Appendix B, to produce a starting point which was independent of the slot pole combination. The next was an automated procedure, which after the input of the range of slot pole combinations, ensured that all the produced designs can meet the peak torque and rated torque speed characteristic whilst maintaining the VA and thermal limits. This procedure has been performed on each of the designs, shown in the next sections of this chapter.

4.3.1 Methodology

Figure 4.4 shows the high level concept of the design procedure, to create the environment, generate the designs and compare them to find the final machine.

4.3.2 Initial designs

Before delving into each of the individual designs, the initial parameters, calculated using the analytical model presented in Appendix B are presented

in Table 4.1. These starting parameters were common for all the designs. These parameters were inputted into the SPEED [98] which performed iterative simulations based on the design process, to determine remaining the geometrical and control inputs parameters.

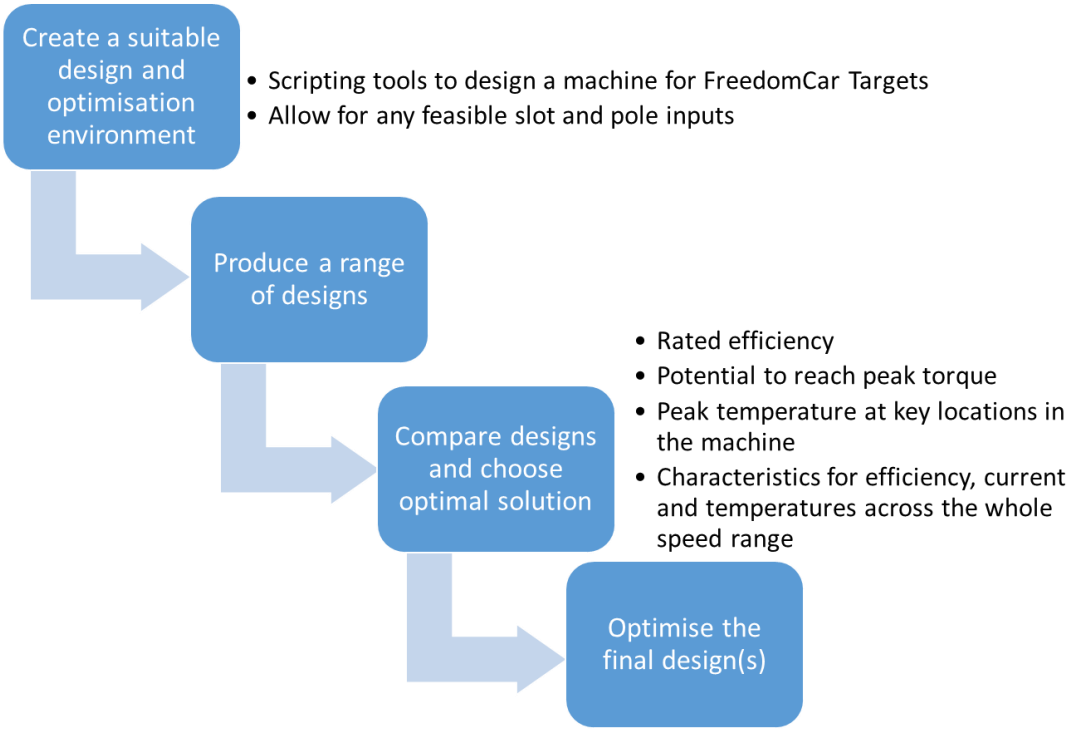


Figure 4.4 – High level design methodology

Table 4.1 – Concentrated design initial parameters for analytical design

Stator outer diameter (mm)	250
Rotor outer diameter (mm)	162.5
Stack length (mm)	200
Air gap length (mm)	1.5
Magnet Thickness (mm)	4.13
Current (A)	130
Torque (Nm)	100

4.4 Concentrated wound designs

This section follows the journey of starting with a wide range of slot pole combinations for a concentrated wound machine and narrowing down to a final design.

4.4.1 Initial range

For the concentrated wound design, pole numbers from 4 to 12 were considered, with slot numbers up to an SPP of 2. Values of SPP greater than 1 were included to check if the reduction in winding factor was outweighed by the extra performance available at high speeds. Because the electrical frequency of the supply was proportional to the pole number, then a number of poles greater than 12 resulted in too high iron losses to achieve the efficiency goal at high speeds. This gave 28 different combinations.

The figures in Table 4.2 show the values of poles and slot numbers that have been simulated for the concentrated wound design, along with the corresponding parameters to each combination.

The design process in Appendix B.2 was completed for each combination. Any combinations that could not meet the basics of the FreedomCar 2020 targets were removed, these were: 12s/4p, 18s/4p, 24s/4p, 18s/6p, 36s/6p, 42s/8p, 48s/8p, 6s/10p, 48s/10p, 54s/10p, 60s/10p, 54s/12p and 72s/12p.

The designs which were removed were mainly the higher slot number machines, this was because as the number of slots increases, the area per slot decreases. Smaller slot areas mean a higher current density, resulting in a higher temperature in the windings. The low pole number machines were also removed, this was due to the currents required exceeding the limits to meet the peak torque.

The only other design to be removed was the 6 slot 10 pole machine. This design was poor because the 6 slot 10 pole machine has a very low winding factor of 0.5, resulting in a large current requirement to reach the target torque. This high current gave high copper losses and thus a high thermal increase in the windings.

Table 4.2 - Concentrated wound slot pole combinations

Poles	4				6		8							
Slots	6	12	18	24	18	36	6	12	18	24	30	36	42	48
SPP	0.5	1	1.5	2	1	2	0.25	0.5	0.75	1	1.25	1.5	1.75	2
LCM	12	12	36	24	18	36	24	24	72	24	120	72	168	48
GCD	2	4	2	4	6	6	2	4	2	8	2	4	2	8
Winding Factor	0.866	0.5	0.328	0.25	0.5	0.25	0.866	0.866	0.617	0..5	0.389	0.328	0.25	0.25

Poles	10										12			
Slots	6	12	18	24	30	36	42	48	54	60	18	36	54	72
SPP	0.2	0.4	0.6	0.8	1	1.2	1.4	1.6	1.8	2	0.5	1	1.5	2
LCM	30	60	90	120	30	180	210	240	270	60	36	36	108	72
GCD	2	2	2	2	10	2	2	2	2	10	6	12	6	12
Winding Factor	0.5	0.933	0.735	0.583	0.5	0.404	0.349	0.307	0.274	0.5	0.866	0.5	0.328	0.25

4.4.2 Comparisons

The remaining designs were compared based on some key performance characteristics across the whole speed range, the results can be seen in Table 3.4. The N/As represent measures that were not met. Although most of the maximum temperatures are greater than the limit, it was felt that this could be improved through optimising the designs further, but this was still a useful comparative value.

From Table 3.4, the best slot number was selected from each pole number. For 4 poles, this had to be the 6 slot design as it was the only one. For 8 poles, 12 slots had the highest minimum efficiency, maintained the >95% efficiency for the widest range and had the lowest winding temperature at maximum speed. For 10 poles, 12 slots this again had the highest minimum efficiency and lowest temperature. For 12 poles, the 18 slot design slightly exceeded the 36 slot one, in terms of highest efficiency and lowest temperatures.

These 4 remaining machines were then more accurately compared against each other.

4.4.2.1 Current and voltage vs. speed

The output power was the same for all designs, so the efficiency was only based on the input power required to obtain this. The input power was reliant on the input current and voltage.

Figure 4.5 shows the current for the remaining 4 machines. The current was not smooth due to the discretisation of the code used, if smaller step sizes and tighter limits on the torque required were used, this would produce a smoother current curve. However this would take much longer to simulate, without the extra data adding significant value to the comparison.

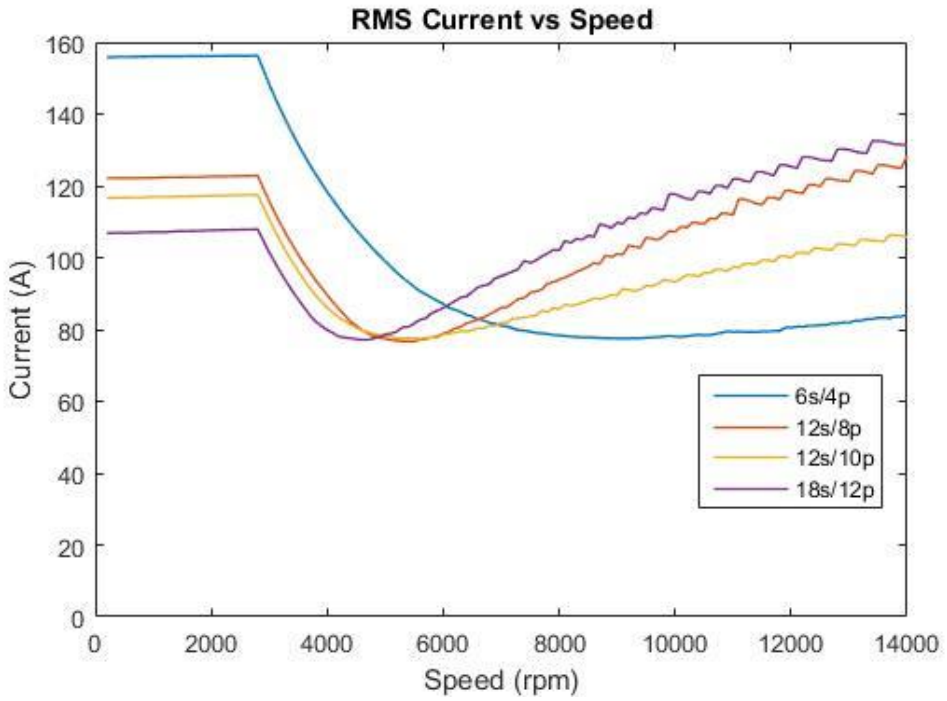


Figure 4.5 – Comparison of the current across the speed range for the analytical concentrated wound designs

It can be seen that while the 18 slot 12 pole machine required the lowest current in the constant torque region, it required a much larger current at high speeds. The 4 pole design, required a low current at high speed, however the rated speed current was very high. The 8 and 10 pole designs were between these two extremes at both ends of the spectrum. The current across the whole range for all the designs was significantly less than the limit of 400A.

Figure 4.6 shows that the voltage was similar for all four machines, linearly increasing with speed to the limit of 132.6V. Once the voltage hit this limit, the script started to increase the advance angle to keep the voltage level.

Table 4.3 – Concentrated designs analytical results summary

Pole	4	8				10						12	
Slot	6	6	12	18	24	12	18	24	30	36	42	18	36
RMS Current (A)	156.2	116.7	128.3	147.2	193.4	116.7	145	161.2	227.9	194.4	207.4	131.4	209.2
RMS Current Density (A/mm2)	2.92	1.7	3.12	5.3	7.25	2.62	5.77	4.08	7.59	7.61	8.89	3.7	8.18
Min Efficiency (%)	90.3	64.7	81.8	76.1	71.2	78.8	75.2	70.3	66.1	63.0	56.6	73.9	61.2
Speed at which eff<95% low (rpm)	200	200	400	1000	1400	400	600	1000	1600	N/A	N/A	400	2000
Speed at which eff<95% high (rpm)	9400	3800	6400	5400	4600	5800	5200	4500	4000	N/A	N/A	5000	3300
Back EMF at Max Speed (rms per phase)	254.5	422.3	377.9	413.0	361.1	402.3	384.9	411.9	333.7	325.3	329.2	442.5	392.6
Temp at max speed (°C)	137.3	232.3	181.2	227.3	267.9	187.5	217.9	259.4	297.6	325.0	370.6	221.7	339.9

Both Figure 4.5 and Figure 4.6 show oscillations in the results, particularly at high speed. This was due to discrete values of advance angle, only integers, being used. In Figure 4.6 when there is a drop in the voltage this was when the advance angle was increased, the voltage then increased linearly back to the limit and dropped again. The effect was more pronounced at high speed where the advance angle must be changed more frequently and by larger amounts. The effect was reversed on the current in Figure 4.5, when the angle was increased there was a distinct step up in current to compensate, which then reduced with the reducing torque requirement.

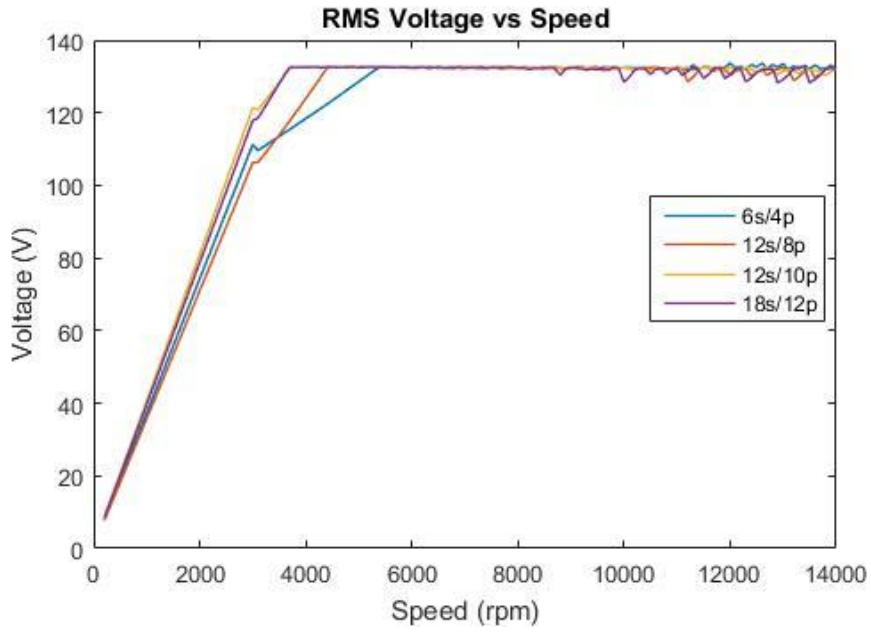


Figure 4.6 – Comparison of the voltage across the speed range for the analytical concentrated wound designs

4.4.2.2 Efficiency vs. speed

The efficiency is the ratio of the output power, P_{out}, over the input power, P_{in}, defined in Eqn. 4.19. Input power can be expressed as the output power plus the losses of the machine. The output power is the mechanical speed multiplied by the torque, Eqn. 4.20. The total losses are the combination of the copper

losses, iron losses, magnetic losses, P_{mag} and frictional and windage losses, P_{mech}, shown in Eqn. 4.21.

$$Efficiency = \frac{P_{Out}}{P_{in}} \times 100\% = \frac{P_{out}}{P_{out} + P_{Loss}} \times 100\% \quad \textbf{Eqn. 4.19}$$

$$P_{out} = T \times \omega_r \quad \textbf{Eqn. 4.20}$$

$$P_{Loss} = P_{cu} + P_{fe} + P_{mag} + P_{mech} \quad \textbf{Eqn. 4.21}$$

As the output power was constant for all the designs in the field weakening range the efficiency was only dependent on the input power, shown in Figure 4.7.

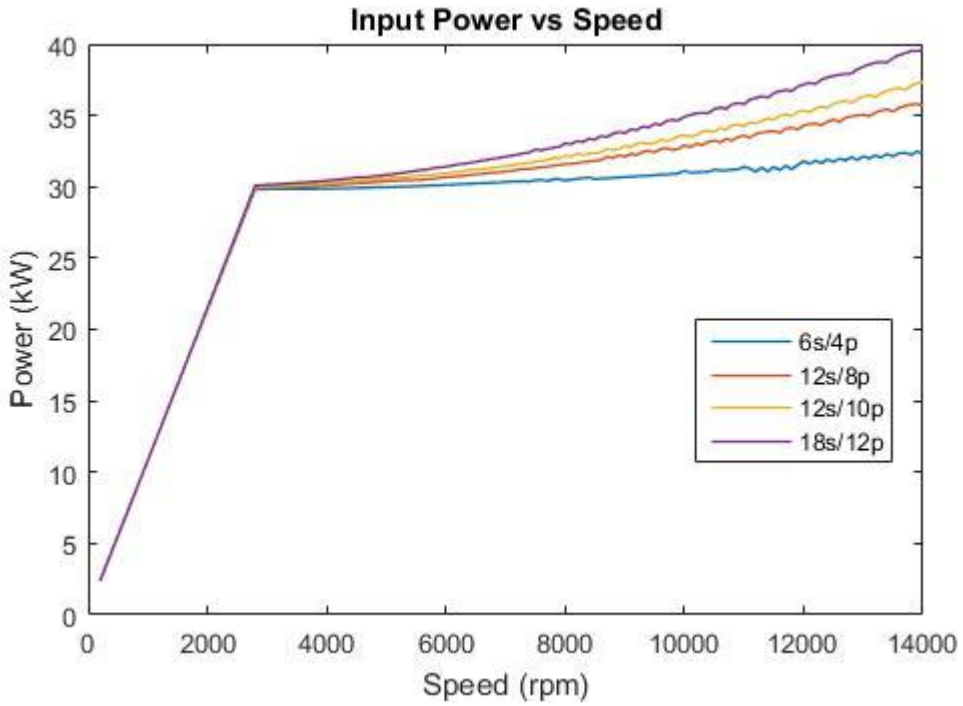


Figure 4.7 - Comparison of the input power across the speed range for the analytical concentrated wound designs

Figure 4.7 shows the input power for the designs across the speed range. Up until rated speed the required power of all four designs was very close. However as the speed increased beyond this, the designs which required the larger current at high speed, Figure 4.5, needed a larger input power.

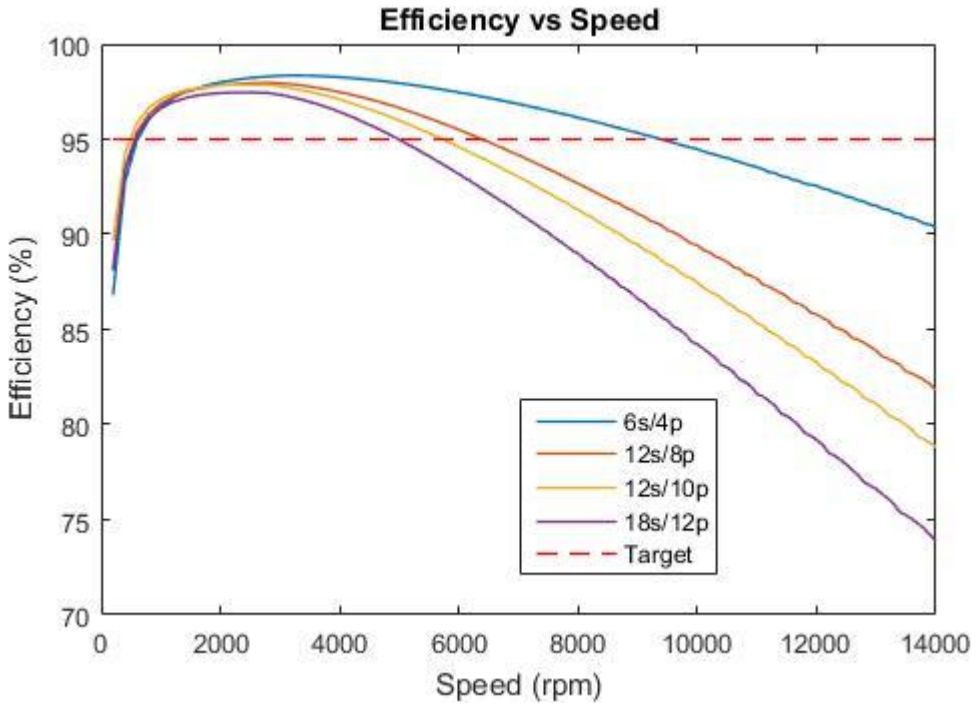


Figure 4.8 - Comparison of the efficiency across the speed range for the analytical concentrated wound designs

Figure 4.8 shows the efficiency of the four designs. The iron losses in all the machines increased proportionally with speed, at a similar gradient, however the designs with higher currents at high speeds had much higher copper losses.

All the machines met the target of >95% for part of the speed range, but they also all failed at high speeds to reach this target. This confirmed that one of the main challenges with the FreedomCar targets was the efficiency objective over the wide speed range.

4.4.2.3 Temperature vs. speed

The final comparison across the speed range was the temperature, calculated in MotorCAD [99]. The temperature shown in Figure 4.9 was the winding temperature as this was both the earliest thermal limit reached and the hotspot of the machine.

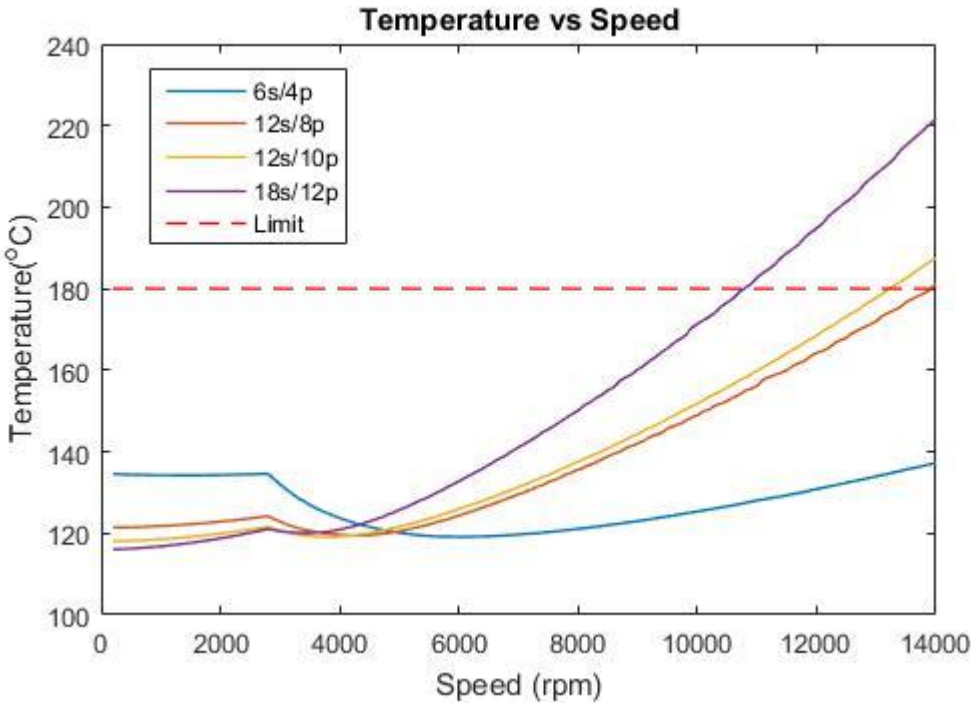


Figure 4.9 - Comparison of the temperature across the speed range for the analytical concentrated wound designs

Figure 4.9 shows, as was expected, that the thermal increase is linked with the current in the machine, as copper losses are the most influential losses on the winding temperature. Although the 4 pole 6 slot machine is the only one to remain below the 180°C limit, the 8/12 and 10/12 designs did not exceed it by much, and it was felt that this can be reduced with further optimisation.

4.4.3 Final concentrated slot pole combination

Table 4.4 shows some key comparative figures of the final four machines.

The efficiencies shown included both stator and rotor iron losses and copper losses (including AC losses and end winding losses). Mechanical losses were assumed to be very similar for the designs and so were not essential for this comparison. The minimum efficiency shown here was at the maximum speed operating point. The designs with the lower poles had higher minimum efficiencies due to the lower current requirement at high speed while the higher pole number designs had lower current requirements at rated torque. The temperature was dependent on the slot width and therefore on the slot number.

Higher slot numbers gave smaller slot areas, leading to higher current densities (for similar current values) and therefore higher copper losses.

Table 4.4 - Comparison of final analytical concentrated design combinations

Poles		**4**	**8**	**10**	**12**
Slots		**6**	**12**	**12**	**18**
Rated RMS Current (A)		155.2	121.8	116.7	107.5
Peak RMS Current (A)		303	236.5	215	209.2
Rated Efficiency (%)		98.3	98.0	97.9	97.4
Rated Speed Losses	**Iron Loss (W)**	194	332	406	494
	Copper Loss (W)	309	270	232	276
Minimum Efficiency (%)		90.3	81.8	78.8	73.9
Rated Copper Temperature (°C)		139.9	130.1	126.2	125.4
Maximum Copper Temperature (°C)		137.3	181.2	187.5	221.7

As can be observed from Table 4.4, the 4 pole design necessitated a significantly higher current to produce the required torque than the other machines, while the 12 pole design somewhat failed in its thermal performance. The goal of this section of the process, to greatly narrow down the number of design, was achieved, reducing the amount from 28 to 4.

These four optimal designs were then taken forward to the next step, using FEA for a more accurate simulation.

4.4.4 Finite element analysis

Up until this point, the simulation process has used the analytical software SPEED. From here the FEA software MagNet from Infolytica [100] has been used to give higher simulation accuracy, although requiring more computational power and time.

4.4.4.1 Differences in result between SPEED and MagNet

There were some noticeable differences in results between the previous analytical results and the initial FEA results that had to be overcome.

4.4.4.1.1 Magnet loss

Magnet loss was underestimated using the analytical equations based on average flux density values in SPEED. Whereas the actual value was found from a much more complex calculation, the introduction of this affected the efficiency of the design. When the models were first exported to FEA this magnet loss was very large, particularly at high speed.

4.4.4.1.1.1 Solution

Segmenting the magnets reduced the losses greatly. The magnets were segmented both circumferentially and axially and could be segmented further if needed. Similar to how laminating the steel reduces losses in the iron, segmenting the magnets made the magnet eddy currents much lower. The formula for how much losses are reduced when circumferentially segmenting the magnets is given in Eqn. 4.22.

$$U = 1 - \left[\frac{\sin\left(\frac{PM_{ang}}{2}\right)}{\frac{PM_{ang}}{2}}\right] \qquad \textbf{Eqn. 4.22 [95]}$$

Where U is the average loss reduction factor and β is the angle of the ratio of the size of the magnet in comparison to the pole pitch, multiplied by 2π.

As an example, this reduced the losses on the initial design from 582W at rated speed and 10.8kW at 14000rpm, to 53W at rated speed and 1.3kW at 14000rpm; this was achieved by segmenting the magnet into 5 parts. This could be reduced further but the improvement would give diminishing returns, each extra segment would decrease the losses a small amount but add complexity to the model and increase simulation times.

4.4.4.1.2 Iron loss

The iron loss was also higher in MagNet, particularly at high speed. This was due to the difference in how SPEED and MagNet estimate the iron losses, with SPEED assuming a constant flux density through the stator components, while FEA calculates a specific value for each element. This is a challenge that cannot

easily be solved, but minimising the iron losses will play a crucial part in the improvement of the machine.

4.4.4.1.3 Change in the operating point of the design

Because of the extra losses, for the same output power, the input power was higher. With a constant current, this meant the voltage was higher. At higher speeds, the values of current and advance angle, found in SPEED to give the desired torque, resulted in a voltage which was over the limits of the targets.

To lower the voltage, the advance angle was increased (and a new current found to produce the desired torque) or when the voltage was significantly above the limit, or the advance angle was already close to 90°, the number of turns was reduced. This meant that the current and advance angles found in SPEED to give the desired torque-speed characteristic could not be used, but were a good starting point when searching for the new values.

4.4.4.2 Four pole machine

When initially moving to FEA, the 12 slot 10 pole design was struggling to meet the targets at the high speed end due to the increase in voltage, so the 4 pole 6 slot machine was also constructed in MagNet. This machine was originally considered worse because of poorer performance at rated speed; however the high speed performance was slightly better in SPEED, with lower iron losses. When this machine was modelled in MagNet it slightly outperformed the 12 slot 10 pole design at high speed, however it performed considerably worse at rated speed and so again the 12 slot 10 pole design was decided to be superior.

4.4.4.3 Thermal

MotorCAD [99] was used to check that the temperature of the windings and magnets do not exceed the limits. While the overall losses increased, this was largely due to the increased iron losses; the copper losses were actually lower. Because the majority of losses had shifted from the copper to iron, the losses were closer to the water jacket and easier to remove. This resulted in lower temperatures in the copper and magnets, reducing them to below their

respective limits. Temperatures exceeding the thermal limit were an issue previously, seen with the losses from the SPEED simulations, which have been overcome.

4.4.4.4 Wider stator teeth

Because the temperature in the windings was no longer near the limits, the machine could be improved by either increasing the current or reducing the slot area. The current already achieved the desired torque, so while increasing this would give higher torque, it was not required. Designing the machine with wider teeth would reduce the slot area (increasing copper losses) but should help reduce the iron losses, which were the main issue at this stage.

4.4.4.5 Improved material

Another issue investigated was the material used. Originally M19 24 gauge was used, because it was a commonly used steel type which was available in both MagNet and SPEED's standard material libraries. Changing this to M235 35A, a steel type with a lower loss profile, greatly reduced the iron losses in the machine.

This was further improved by using very high-end materials, HXT for the rotor and JNHF for the stator. HXT has very high strength so a low rotor bridge thickness can be used and JNHF has low core losses. These materials would be more expensive to use in an actual machine but helped to show the theoretical maximum machine performance available.

4.4.4.6 Loss calculation improvement

While MagNet gave values for the copper and iron losses these are not the definitive values.

Magnet uses the Steinmetz equation to calculate the iron losses. This has been shown to have inaccuracies when the change in flux density is not sinusoidal or large flux density values [95, 101]. On top of this the material constants for the loss equation are the unworked steel, the manufacturing process affects

these values, mainly due to the lamination stamping and cutting [102]. This leads to differences between simulated results and what is actually produced in a real machine unless a building factor is implemented [102-104]. Therefore to ensure that there is not an increase in the iron losses when the machine is prototyped, a building factor of 2 was implemented into the core loss results generated in MagNet.

4.4.4.6.1 End windings

When simulating a design in MagNet the most common solving methods are 2D to decrease the model complexity and solving time. Due to the 2D nature of the model the end windings (the connection from one slot to another) are not considered. The losses in the end windings were calculated post process. The general method was to calculate the resistance of the end windings based on the slot fill factor, slot area, number of turns and an approximate calculation of the length of the end winding. This resistance was then multiplied by the current squared to find the power loss ($P_{cu} = I^2R$). This new power loss was then added to the total copper losses and a new efficiency found.

4.4.4.6.2 AC component of copper losses

Another factor not considered during a typical MagNet simulation was how the resistance of the windings changes depending upon the frequency. The ratio of AC resistance to DC resistance, F_r, is determined in Eqn. 4.23, based on the skin depth, δ, from Eqn. 4.24. This increase in resistance with frequency is due to two phenomena, the first being the skin effect. The skin effect is the tendency for high frequency current density to be the greatest closer to the surface of the conductor. While this skin effect gives a gradually reducing density from the surface to the centre of the conductor, the gradient is dependent on the material and the frequency, it can be approximated as an annulus of constant current density under the surface of the conductor. The depth of the annulus is called the skin depth and can be calculated by Eqn. 4.24. The other influence on the ratio is the proximity effect, due to the interaction of the fields generated by each conductor and the adjacent conductors. The

proximity effect sets up small eddy currents in the conductors effectively increasing the current density and therefore losses in each conductor. Using conductors smaller than the skin depth almost negates the skin effect (as the annulus is the whole conductor), however this will result in a greater number of conductors in parallel which increases the proximity effect. Balancing the conductor diameter, number of parallel conductors per turn and current density to minimise this ratio is difficult but critical when dealing with high frequency machines.

$$\frac{R_{AC}}{R_{DC}} = F_r = 1 + \frac{\pi^2 {N_c}^2 N_t^2 d_{wire}^6}{192\delta^4 W_s^2} \qquad \textbf{Eqn. 4.23 [105]}$$

$$\delta = \sqrt{\frac{2}{\omega_e \mu_0 \sigma}} \qquad \textbf{Eqn. 4.24 [105]}$$

Where N_c is the number of strands per turn, d_{wire} is the diameter of a strand, μ_0 is the permeability of free space and σ is the conductivity of the material, in this case copper.

This gives a ratio which could be used to calculate the copper losses at a given frequency as a post process step. Because copper losses are proportional to the resistance, simply multiplying the copper losses found in MagNet (after including end winding losses) by this value gave the new losses.

4.4.5 Selection of final concentrated wound slot pole combination

At this stage there were the four optimal slot pole combinations found from SPEED, Table 4.4. These designs were inputted into MagNet where the above differences between simulation methods become evident and modifications were implemented.

This lead to the 4 pole design requiring a larger current for peak torque, pushing it above the 400A current limit and 180˚C winding temperature limit.

The 12 pole machine, now with higher iron losses had a significantly lower efficiency at high speed (<70%) and so was also removed as a potential candidate.

This left the 8 and 10 pole machines. The efficiency and current requirement in both machines was similar, minutely favouring the 10 pole at rated speed and 8 pole at high speed. The deciding factor was the distribution of the losses, the 10 pole were higher in the stator core, while the 8 pole losses were greater in the winding.

Considering all the above the 10 pole design was chosen to take forward. The advantage of this over the 8 pole design was the location of the losses, heat generated from winding losses, being further from the water jacket, is more difficult to remove than that from stator iron losses. And looking forward, the next step was to focus on reducing the high speed iron losses, the first method to tackle this was to increase the iron area, reducing the copper area. This change would increase the copper losses further causing a more significant effect, both reducing efficiency and increasing temperatures, in the 8 pole machine.

4.4.6 Final concentrated wound designs

Due to the aforementioned issues with differences between the results from SPEED and MagNet, the imported model's (referred to as "SPEED Design" herein) performance dropped. To overcome this, the tooth shape and PM shape was improved creating the "Wider Tooth Design". The differences between these machines can be seen in Figure 4.10, the overall machine geometry, stator and rotor diameters, stack length and slot pole combination were kept constant. The further similarities and contrasts are presented in Table 4.5.

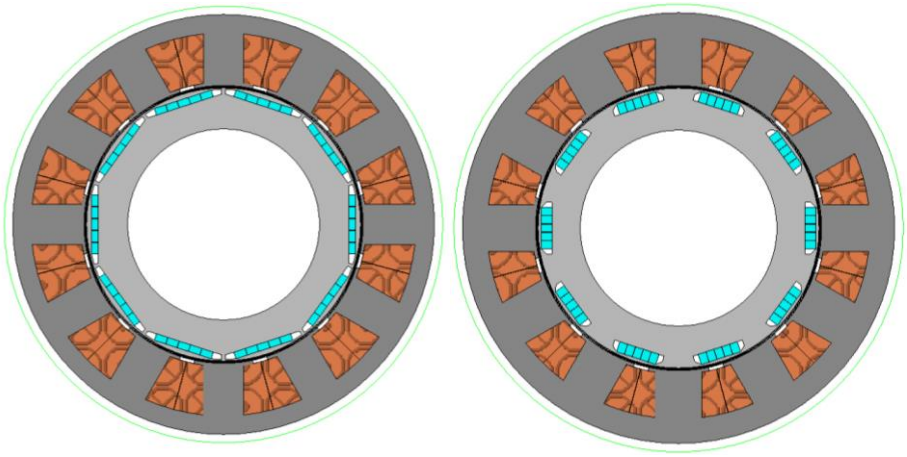


Figure 4.10- a) SPEED design b) Wider tooth design

Table 4.5 – Concentrated Machine Design Parameters

Design		SPEED Design	Wider Tooth Design
Design Parameters	**Poles**	10	10
	Slots	12	12
	Rotor Diameter (mm)	162.5	162.5
	Stator Diameter (mm)	250	250
	Stack Length (mm)	200	200
	Air gap (mm)	1.5	1.5
Magnet Dimensions	**Magnet Thickness (mm)**	4.13	6.2
	Magnet Width (mm)	35.2	24
	Magnet Mass (kg)	2.18	2.23
Stator Dimensions	**Tooth Width (mm)**	23.8	27
	Slot Depth (mm)	29.2	25
Windings	**Turns per phase**	3	5
	Winding Diameter (mm)	1	1
	Number of Strands per Conductor	92	24
	Fill Factor	0.55	0.55
Electrical 2800 rpm	**Rated Current RMS (A)**	169.7	129
	Frequency (Hz)	233	233
	Phase angle (degree)	14	20
Electrical 14000 rpm	**Rated Current RMS (A)**	203.3	90.5
	Frequency (Hz)	1167	1167
	Phase angle (degree)	84	79

It can be seen in Table 4.5 that the overall size of the machines are similar and that the dimensions of the magnets and the slots are the key difference. The number of turns could be increased with the wider tooth design, this lead to lower strands per conductor (for the same fill factor) and a lower current requirement.

Table 4.6 and Table 4.7 show the results across the speed range for both designs. Seven speed values were used to give an adequate spread of the results whilst keeping computational times low. For each speed value a process similar to the methods described in Appendix B.2 was applied to find the optimal current magnitude and phase angle to meet the torque. The losses shown here include the correction factors given earlier in this chapter. To better visualise the differences between the two sets of results the key values have been graphed against each other in Figure 4.11 to Figure 4.14.

Table 4.6 – Operating table - SPEED concentrated FEA Design

Speed	I rms	Ang	T	Iron Loss Rotor	Iron Loss Stator	Copper Loss	Magnet Loss	Pout	Pin	Eff
rpm	A	Deg	Nm	W	W	W	W	kW	kW	%
1000	169.7	14	100	11.46	151.12	146.92	10.2	10.5	10.84	97.1
2800	169.7	14	100	40.74	621.68	154.82	55.2	29.4	30.25	97.1
4000	118.8	11	70	54.45	966.57	80.71	45.7	29.4	30.57	96.2
6000	79.9	11	47	76.83	1665.52	41.78	45.1	29.5	31.30	94.2
8000	78.1	45	35	89.26	2223.63	47.01	49.4	29.5	31.89	92.4
10000	131.5	73	28	116.58	2624.98	158.86	114.9	29.5	32.50	90.7
14000	203.3	84	20	249.93	4046.12	543.20	455.7	29.7	35.03	84.9

Table 4.7 – Operating table – wider tooth concentrated FEA Design

Speed	I rms	Ang	T	Iron Loss Rotor	Iron Loss Stator	Copper Loss	Magnet Loss	Pout	Pin	Eff
rpm	A	Deg	Nm	W	W	W	W	kW	kW	%
1000	134.4	21	99.9	21.4	167.6	330.4	8.5	10.5	11	95.5
2800	134.4	21	99.7	75.7	704.1	343.4	53.6	29.2	30.4	96.1
4000	95.5	19	69.8	78.6	886.3	181.8	49.3	29.2	30.4	96.1
6000	69.3	33	46.6	90.3	1182.5	106.4	50.1	29.2	30.6	95.4
8000	70	55	34.8	137.9	1578.7	123.6	68.1	29.2	31.1	93.9
10000	74.2	66	27.8	204.3	2161.2	160.9	88.5	29.1	31.7	91.8
14000	88	77	20.7	415.4	3932.5	308	136.6	30.4	35.2	86.4

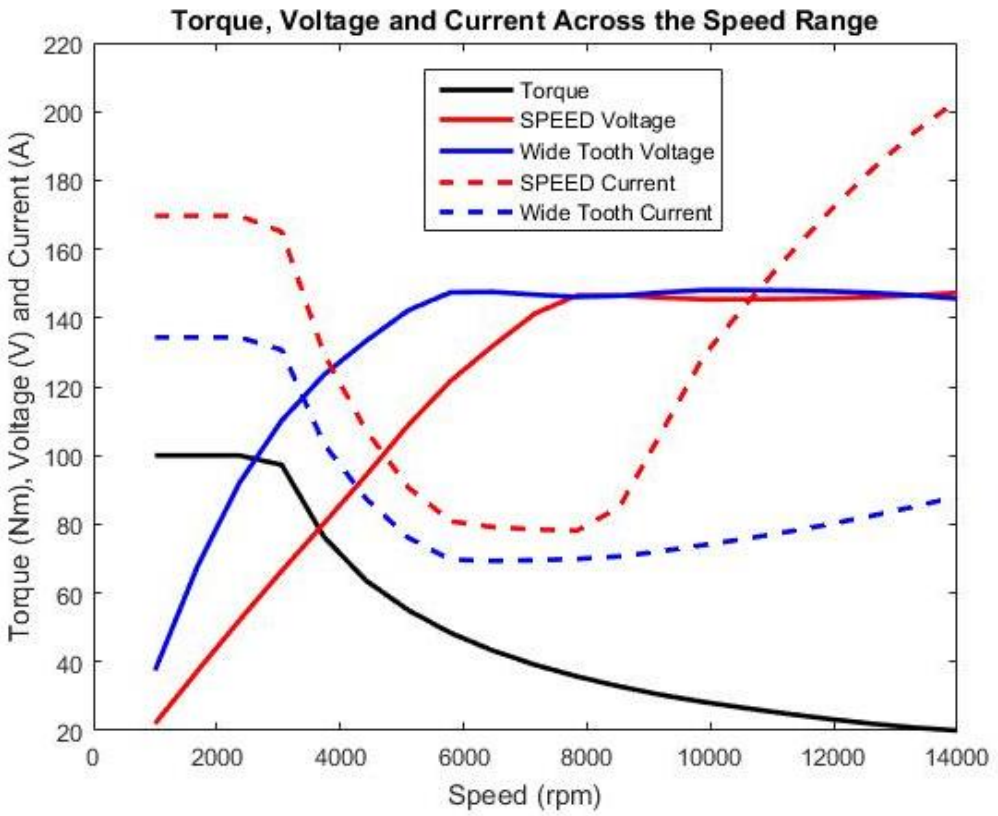


Figure 4.11 - Torque, current and voltage comparison for both concentrated wound IPMSM FEA designs

Figure 4.11 shows the key electrical and mechanical requirements of the two designs. The torque was the same for both designs, meeting the required torque shown with the targets in section 2.2. The voltage requirement of both designs was very similar, increasing with speed to the limit and then staying constant (due to the increasing advance angle). The current of both the designs followed the same pattern, high at low speed to meet the high torques, decreasing when the torque requirement was lower and then increasing again at high speed where higher currents were needed to field weaken.

The SPEED design had a higher current across the whole speed range, but especially at high speed. This was partially what the improved Wide Tooth

design set out to achieve, using a greater number of turns and thicker PMs allowed for a smaller current when producing high torques. The larger iron areas gave lower flux densities (for the same total flux) resulting in lower back EMFs, and therefore lower voltages. A lower voltage means the advance angle can be lower and thus a lower current could be used.

Figure 4.12 shows the power of the machines, both input and output. The output power was the same for both designs, being the required torque multiplied by the speed, giving 30kW in the constant power range. The input power was the output power summed with the total losses. Figure 4.13 compares the efficiency of the two designs, with equal output power this is fully dependent on the input power. It can be seen that, for most of the speed range the wide tooth design had a higher efficiency, the reasoning for this is explained with the losses in Figure 4.14.

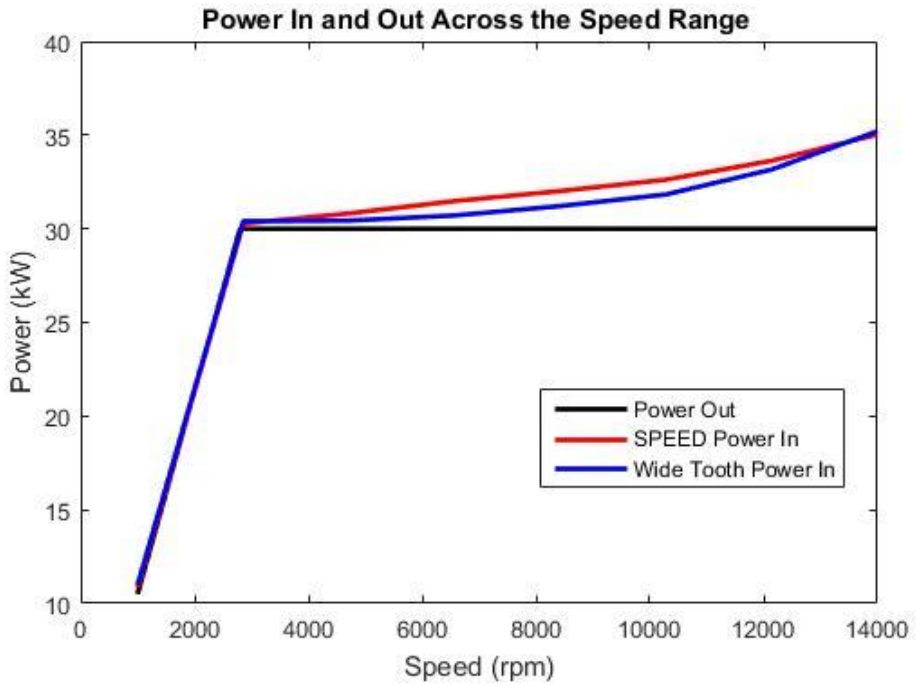


Figure 4.12- Power in and out across the speed range for both concentrated wound IPMSM FEA designs

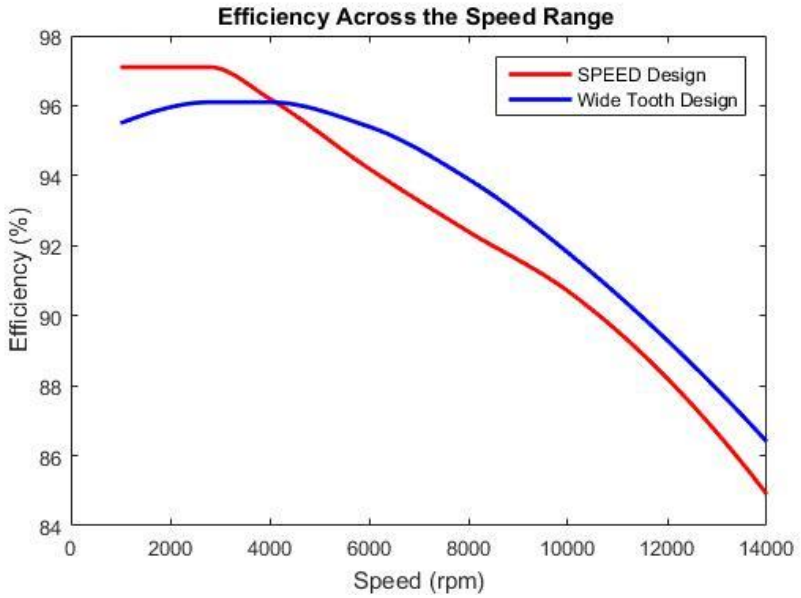


Figure 4.13- Power in and out across the speed range for both concentrated wound IPMSM FEA designs

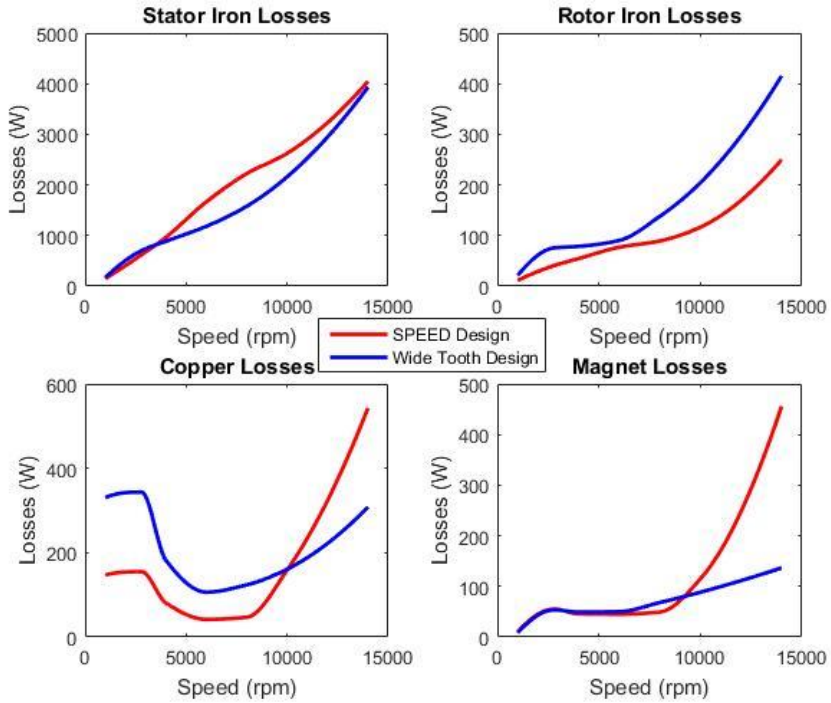


Figure 4.14 – Breakdown of losses across the speed range for both concentrated wound IPMSM FEA designs. a) Stator iron losses, b) rotor iron losses, c) copper losses, d) magnet losses.

Figure 4.14 shows a breakdown of the losses. In Figure 4.14a the stator losses are compared, the wide toothed design was lower for most the range due to the

larger iron areas. This is the opposite of the rotor iron losses which were higher in the wide tooth design, Figure 4.14b, due to the new shape of the PMs. Of note is that the stator iron losses were of an order of magnitude higher than the ones present in the rotor. Because the slot area was smaller in the wide tooth design and the number of turns higher the resistance of the windings was larger, at low speed where the difference in current requirements was not excessive, this produced higher copper losses in the wide tooth design, Figure 4.14c. However as the difference between currents became larger at high speeds this outweighed the higher resistance and the SPEED design had much larger copper losses. Figure 4.14d compares the magnet losses, these are similar until high speeds when they were much higher in the SPEED design, again this was one of the focuses of the improved design.

In addition to reducing the efficiency of the design, a critical issue with losses is that they create a temperature increase in the machine. The temperatures in the key locations of the designs, simulated in MotorCAD, are shown in Table 4.8. These temperatures were the high speed steady state values, shown to be the operating point resulting in the highest thermal increase in Figure 4.9.

Table 4.8 – Temperature comparison of the FEA concentrated wound machines

Design		SPEED	Wider Tooth
Housing		108.1°C	108.1°C
Magnet		125.5°C	142.3°C
Stator Tooth		136.2°C	150.8°C
Copper	Average	132.7°C	162.2°C
	Max	150°C	170.1°C
	Min	111.6°C	153.6°C

Table 4.8 shows that, although the wide tooth design increased the efficiency at high speed, it also increased the temperature in the windings. Whilst this temperature remains below the limit (180 °C) it was still a concern when comparing the designs. Of note is that, as predicted, the maximum operating temperatures dropped significantly from the results when using SPEED, as was shown in Table 4.4.

4.4.7 Concentrated wound IPMSM summary

This section started with a wide range of machines, narrowing down using analytic simulations to find the optimal slot pole combination. A range of designs this comprehensive has not previously been considered for the DoE FreedomCar 2020 targets and thus allowed for a much better understanding of the challenges of these targets and the appropriate designs. From there finite element was used to show that 12 slot 10 pole was the most suitable combination for a concentrated wound flat IPMSM design. An improved design, with wider teeth and thicker magnets, was created; this was shown to be slightly more efficient at high speed.

From what has been simulated, it was clear a flat magnet concentrated wound IPMSM design will not reach the efficiency requirements of the FreedomCar 2020 targets at high speed. The torque, voltage, current, temperature and volume requirements had been met, but the main targets unachieved are the high speed efficiency (currently at 86.4%, specified at >95%) and cost. While the designs could have been improved further, it was probable it would require a large time investment for a very small improvement in design efficiency, likely sacrificing other targets. Because the main issue was the high speed efficiency, a distributed wound design was focused on next, which allowed for a higher reluctance torque, improving the high speed efficiency.

4.5 Distributed wound designs

This section presents a similar story to what has just been shown for concentrated wound designs, but with distributed windings. A group of designs was investigated analytically and then as the design range narrowed FEA was implemented, ending at a final design.

4.5.1 Initial range

The same range of poles was used for the distributed wound designs, as was for concentrated. The slot numbers for the distributed wound machines all had integer SPP numbers, this ensured the LCM was always equal to the slot

number and the GCD was equal to the pole number. An extra consideration, when designing distributed wound machines was whether to use a single or double layered winding per slot. Both have been investigated where applicable, but for odd numbered SPP only the double wind was considered because the single layer wind would need a non-integer number of coils per pole per phase. This study started with 13 combinations (given in Table 4.9) with D referring to a double layer winding only and SD to both single and double layer windings being designed. When both layers of winding were considered, the first winding factor value is for the single layer, while the second is for the double layer.

Table 4.9 - Distributed wound slot pole combinations

Poles	4			6			8		10	12
Slots	12	24	36	18	36	54	24	48	30	36
Layers	D	SD	D	D	SD	D	D	SD	D	D
SPP	1	2	3	1	2	3	1	2	1	1
LCM	12	24	36	18	36	54	24	48	30	36
GCD	4	4	4	6	6	6	8	8	10	12
Winding Factor	1	0.707/ 0.595	0.652	0.866	0.701/ 0.557	0.579	0.866	0.707/ 0.595	0.866	0.866

4.5.2 Comparisons of distributed wound IPMSMs

The range of machines was compared in terms of the torque performance, considering the current required, the efficiencies achieved and the resulting temperature increase, shown in Table 4.10.

Although most of the maximum temperatures were greater than the limit, it has been seen from the previous concentrated wound designs that these are overestimations. So the temperatures shown were a good comparative base, but should not be treated as definitive values. When comparing the machines, the maximum Back EMF was more important than the current, as it was seen in the concentrated designs that the voltage limit is a lot more restrictive than the current limit.

The best slot number was selected from each pole number, to reduce the number of machines for further comparisons. For 4 poles, the 12 slot double layer winding machine was the best, although it had a higher current requirement than the single layer, the full speed back EMF was lower, meaning it would be easier to work within the voltage limit. For 6 poles, the 18 slot single layer winding was optimal, because of the high efficiency and low back EMF. For 8 poles, the single layer winding 24 slot machine appeared to be the best, with the lowest back EMF and highest minimum efficiency. For the 10 and 12 pole motors, there was only one design to choose from for each, the 30 slot and 36 slot respectively. This showed that unity slots per pole per phase performs best for this application. The next step was to compare these machines against each other in more detail.

4.5.2.1 Current vs. speed

The current for each speed value needed to meet the torque requirement is shown in Figure 4.15.

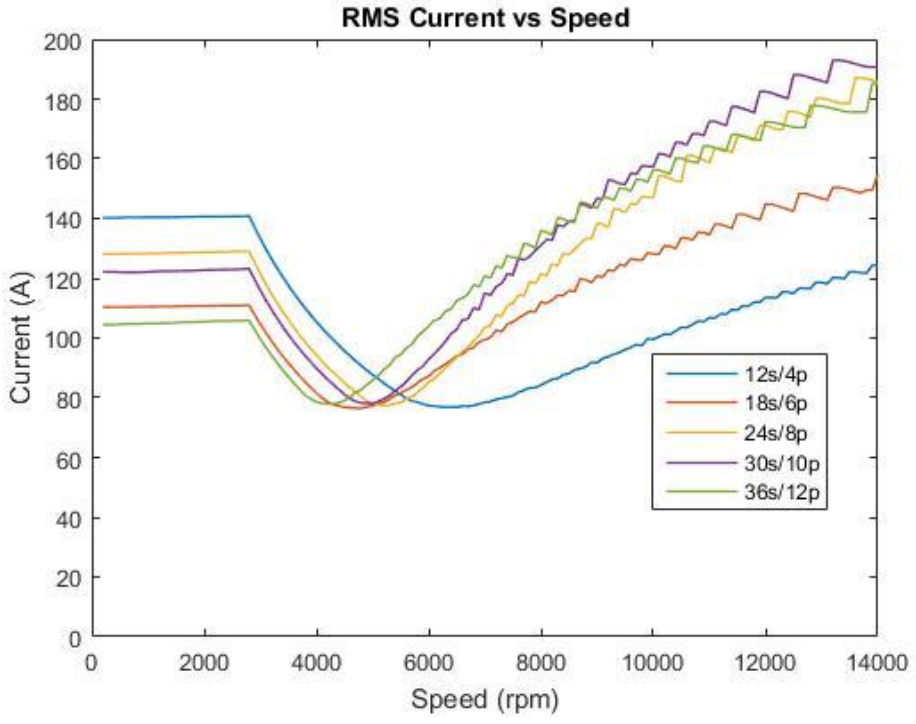


Figure 4.15 - Comparison of the current across the speed range for the analytical distributed wound designs

Table 4.10 - Concentrated designs analytical results summar

Pole	4	8				10						12	
Slot	6	6	12	18	24	12	18	24	30	36	42	18	36
RMS Current (A)	156.2	116.7	128.3	147.2	193.4	116.7	145	161.2	227.9	194.4	207.4	131.4	209.2
RMS Current Density (A/mm2)	2.92	1.7	3.12	5.3	7.25	2.62	5.77	4.08	7.59	7.61	8.89	3.7	8.18
Min Efficiency (%)	90.3	64.7	81.8	76.1	71.2	78.8	75.2	70.3	66.1	63.0	56.6	73.9	61.2
Speed at which eff<95% low (rpm)	200	200	400	1000	1400	400	600	1000	1600	N/A	N/A	400	2000
Speed at which eff<95% high (rpm)	9400	3800	6400	5400	4600	5800	5200	4500	4000	N/A	N/A	5000	3300
Back EMF at Max Speed (rms per phase)	254.5	422.3	377.9	413.0	361.1	402.3	384.9	411.9	333.7	325.3	329.2	442.5	392.6
Temp at max speed (°C)	137.3	232.3	181.2	227.3	267.9	187.5	217.9	259.4	297.6	325.0	370.6	221.7	339.9

In Figure 4.15, a similar pattern appeared to that found in the concentrated wound designs. At low speeds, because torque is proportional to pole number, lower current was needed for higher pole numbers. While at high speeds, high pole numbers result in higher frequency requirements, leading to higher iron losses and AC copper losses, and with higher losses a higher input power (determined by current supply) was needed to meet the same output power requirement. The oscillations at high speed are for the same reason as described in section 1.1.1.

4.5.2.2 Efficiency vs. speed

Figure 4.16 shows the input power for the designs across the speed range. Up until rated speed the power of all five designs was very close. However, as the speed increased beyond this, the higher pole number designs, which required the larger current at high speed, needed a larger input power.

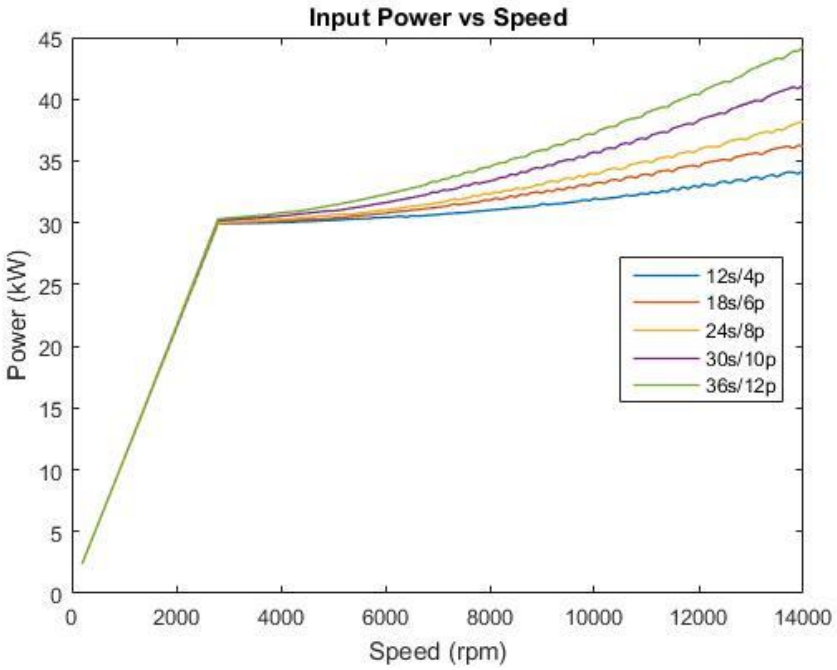


Figure 4.16 - Comparison of the input power across the speed range for the analytical distributed wound designs

Figure 4.17 compares the efficiency of the 5 machines. As expected, the machines with the higher input power had lower efficiency, as the output power was the same for all machines.

All the machines met the target of >95% around the rated speed, 2800rpm. As the speed increased the efficiencies dropped below this target, starting with the 12 pole machine and following in descending pole number order. It was hoped that through optimisation this high speed efficiency could be improved. Although from the study of the concentrated designs, it seemed unlikely a machine will meet the target for the full range; however comparing back to the original efficiency of the concentrated wound machine, Figure 4.8, it is clear the distributed wound designs are an improvement in terms of high speed efficiency.

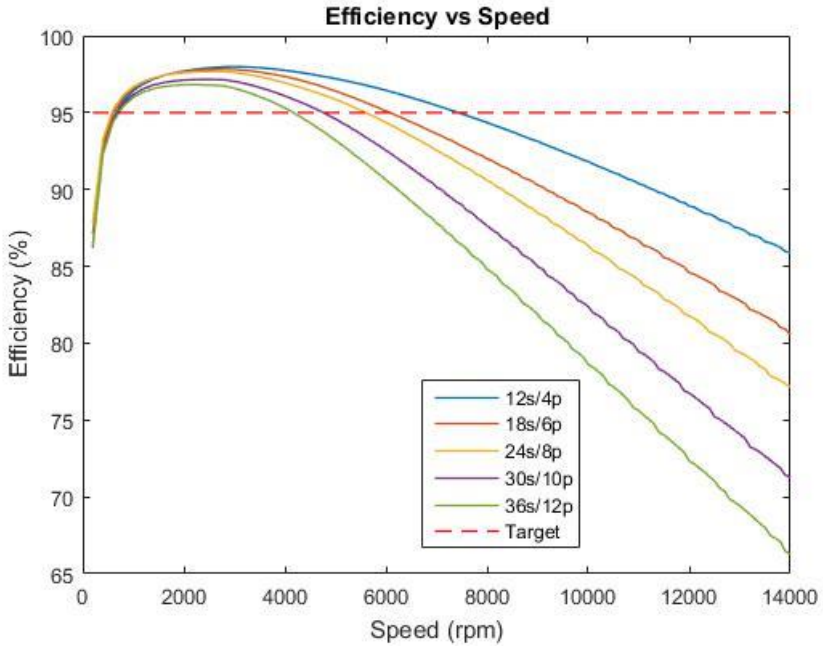


Figure 4.17 - Comparison of the efficiency across the speed range for the analytical distributed wound designs

4.5.2.3 Temperature vs. speed

The final comparison across the speed range is the temperature. The values considered in Figure 4.18 were the temperature in the windings at maximum speed as this was both where the earliest thermal limit is in place and the area with the highest temperature.

Figure 4.18 shows, as was seen previously, that the thermal increase was linked with the current in the machine, as copper losses are the most influential

component on the winding temperature. Although the 4 pole machine was the only one to remain below the 180°C limit, the 6 and 8 pole designs were not much hotter. As shown earlier, when the concentrated wound machines were imported to finite element, the temperatures were found to be a lot lower, so exceeding the limit here was not a significant worry.

4.5.3 Slot pole combination comparison

Here the designs have been moved from SPEED (analytical) to MagNet (FEA), to obtain a higher accuracy simulation of the results.

When looking at the current required to meet the peak torque operating point (200Nm at 2800rpm) it was immediately clear that the 4 and 6 pole designs require very high currents (above 600A) and so they were removed from the comparison. This left the 8, 10 and 12 pole designs to be compared against one another, based on the same parameters considered for the concentrated design exercise, as shown in Table 4.11.

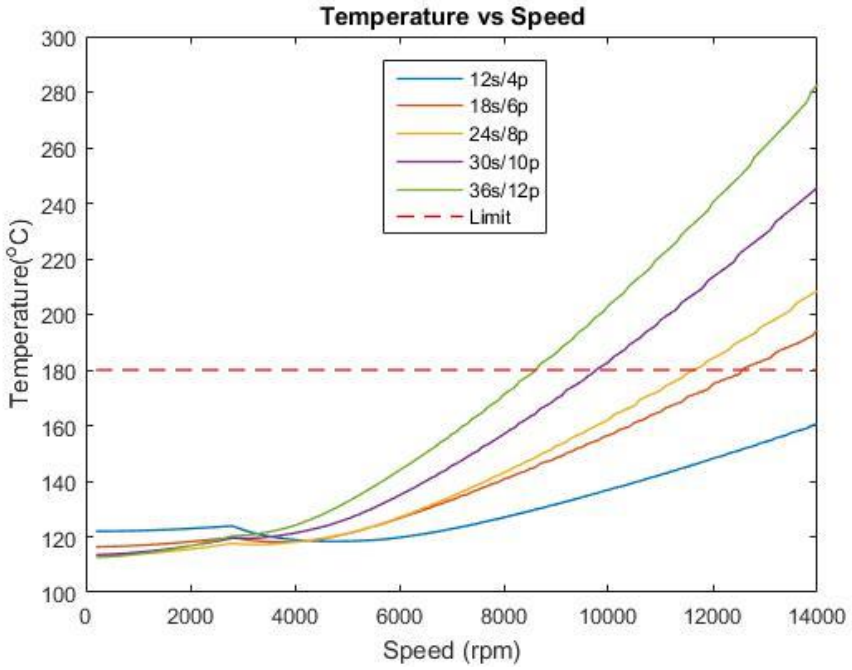


Figure 4.18 - Comparison of the temperature across the speed range for the analytical distributed wound designs

It can be seen in Table 4.11 that at rated speed there was very little difference in the efficiencies. However at the maximum speed (minimum efficiency), it is clear that the 10 pole combination had a higher efficiency than the other two designs. This was mainly due to the 12 pole design having higher iron and magnet losses (higher electrical frequency) and the 8 pole option having a higher current requirement (torque proportional to pole number). So it was decided to focus on the 30 slot 10 pole distributed wound machine. This agreed with the concentrated wound results showing that 10 poles is the best balancing point between iron losses and copper losses.

Table 4.11 - Comparison of final analytical distributed wound design combinations

Poles		**8**	**10**	**12**
Slots		**24**	**30**	**36**
Winding Layers		Double	Double	Double
Rated Current (A)		241.5	232.5	213.5
Peak Current (A)		424	413.5	406.5
Rated Efficiency (%)		97.5	97.1	96.7
Rated Speed Losses	Iron Loss (W)	445	538	659
	Copper Loss (W)	300	321	327
Minimum Efficiency (%)		91	94	93.5
Rated Copper Temperature (°C)		117.5	119.5	120.2
Maximum Copper Temperature (°C)		153.7	181.25	208.4

4.5.4 Final distributed wound IPMSM design

The final design for the distributed wound machine was the 30 slot 10 pole machine. Unlike with the concentrated design, an improved design was not needed when importing to FEA, due to all the differences and potential pitfalls already being known and corrected for. The key design parameters for this motor are given in Table 4.12.

Table 4.13 gives the results across the speed range for the distributed wound machine. The results here are from the FEA with correction to the losses, such as AC copper losses and improved iron losses. These results will be represented graphically, and discussed in more detail, in the next section when they are compared to the results from the concentrated wound machines.

The simulated temperatures of the key points on the machine are given in Table 4.14. The same cooling arrangement as for the concentrated machine has been used. The temperatures stayed below the limit of 180°C and so were acceptable.

4.5.5 Distributed wound IPMSM summary

This section performed the same process that had previously been completed for a concentrated wound machine for a distributed wound machine. The breadth of the design range was again wider than has previously been considered for this application, and allowed for the narrowing down to the optimal combination.

Table 4.12 - Distributed IPMSM design parameters

Design Parameters	Poles	10
	Slots	30
	Rotor Diameter (mm)	162.5
	Stator Diameter (mm)	250
	Stack Length (mm)	130
	Air gap (mm)	2
Magnet Dimensions	Magnet Thickness (mm)	5
	Magnet Width (mm)	25.4
	Magnet Mass (kg)	1.24
Stator Dimensions	Tooth Width (mm)	10.65
	Slot Depth (mm)	25.8
Windings	Turns per phase	3
	Winding Diameter (mm)	1
	Number of Strands per Conductor	20
	Fill Factor	0.45
Electrical 2800 rpm	Rated Current rms (A)	144.6
	Frequency (Hz)	233
	Phase angle (deg)	29
Electrical 14000 rpm	Rated Current rms (A)	126.2
	Frequency (Hz)	1167
	Phase angle (deg)	80

Table 4.13 - Operating table - distributed FEA Design

Speed	I rms	Ang	T	Iron Loss Rotor	Iron Loss Stator	Copper Loss	Magnet Loss	Pout	Pin	Eff
rpm	A	Deg	Nm	W	W	W	W	kW	kW	%
1000	144.6	29	99.9	4.1	138.8	805.9	6.8	11.0	11.9	92.0
2800	144.6	29	99.9	15.6	595.8	829.3	36.3	30.1	31.6	95.3
4000	106.4	25	69.8	16.5	751.8	463.9	26.3	29.9	31.2	96.0
6000	75	25	46.7	18.4	1046.2	248.6	22.4	30.0	31.4	95.7
8000	72.1	50	35.1	20.0	1284.3	254.0	53.4	30.2	31.8	94.9
10000	81.7	65	28.1	26.8	1677.6	365.4	92.6	30.5	32.6	93.4
14000	126.2	80	20.8	76.4	3449.9	1123.6	232.8	32.9	37.7	87.2

Table 4.14 - Distributed wound temperatures from FEA losses

Housing		106°C
Magnet		157°C
Stator Tooth		171.5°C
Copper	Average	173.4°C
	Max	177.5°C
	Min	159.3°C

As opposed to the concentrated wound machine an updated model was not required when transferring to FEA, as the pitfalls and discrepancies were already known.

The study showed a 30 slot 10 pole machine to be optimal when considering efficiency across the speed range, whilst meeting the torque, voltage, current, thermal and sizing requirements. Still the high speed efficiency is an issue, 87.2% when 95% is required.

The next sections compared the two winding topologies against one another to determine which is the more beneficial to progress forwards with.

4.6 Concentrated vs. distributed IPMSM comparison

At this stage there was an optimal concentrated wound IPMSM (12 slot, 10 pole) and a distributed wound IPMSM (30 slot, 10 pole), so the clear next step was to compare them against one another.

4.6.1 Torque, voltage and current

Both machines could meet the torque requirement across the speed range, with the voltage limit. The current they each required to meet the torque is shown in Figure 4.19.

Figure 4.19 shows that the distributed machine needed a higher current than the concentrated machine, across the whole speed range, to reach the torque requirement. The current was higher in the distributed machine for the same torque value due to the shorter machine length and having lower turns per phase than the concentrated machine. This was further pronounced at high speed where more current was needed to deflux the PMs.

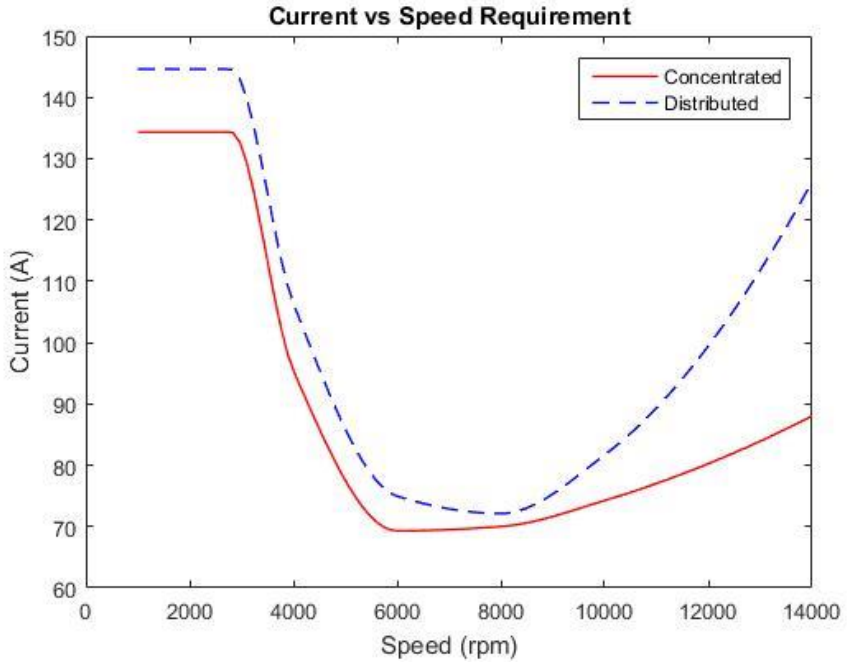


Figure 4.19 – Comparison of current requirement of concentrated and distributed wound IPMSMs

4.6.2 Efficiency

The difference between the two designs in terms of efficiency is shown in Figure 4.20. This was due to the combined losses in the stator iron, rotor iron, winding and PMs.

As the current requirement of the distributed wound machine was higher, the low speed efficiency (where copper losses were dominant) is much lower. However, at higher speeds the increase in current requirement was outweighed by the reduction in the iron losses. This showed the distributed wound machine was more efficient at high speed, which at this stage was the more critical operating point.

4.6.3 Breakdown of Losses

The loss components used to produce the efficiency in Figure 4.20 are given in Figure 4.21.

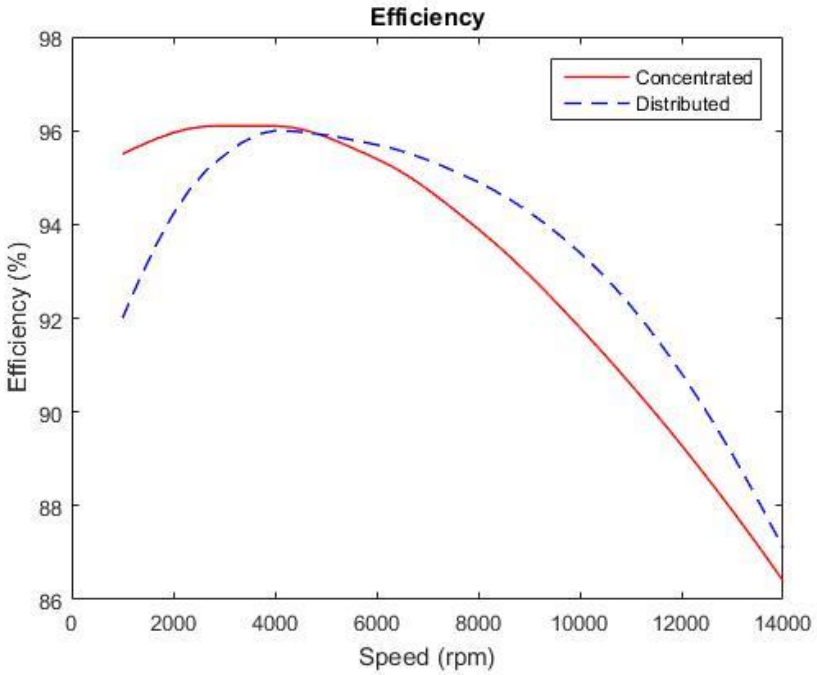


Figure 4.20 - Comparison of efficiency of concentrated and distributed wound IPMSMs

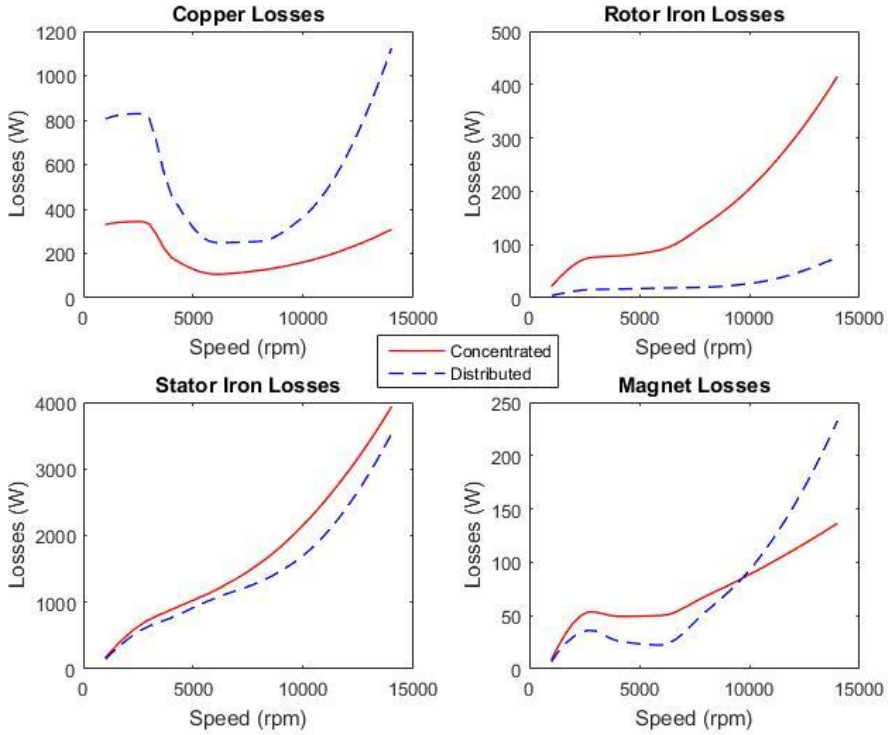


Figure 4.21 - Comparison of loss components of concentrated and distributed wound IPMSMs

As should be expected from the higher current requirement, the copper losses of the distributed wound machine were higher than the concentrated wound, this was further pronounced at the two extremes of speed where higher currents are required. The rotor iron losses were significantly lower in the distributed wound machine, due to the shorter machine length and smaller harmonics due to the winding configuration. The stator iron losses were still the key contributor to the high speed efficiency, while the difference between the two designs was not massive, the fact that the distributed machine is lower here was a huge point in its favour. Finally the PM losses, these were dependent upon current loading, phase angle and frequency and so followed a complex trend. Up until 10000 rpm, the magnet losses are lower in the distributed wound machine due to the smaller PMs. Above this speed is the point where the larger armature current of the distributed design outweighs the smaller PMs giving a larger magnet loss.

4.6.4 Temperature

Although shown separately previously, the simulated temperatures for each of the designs are presented in Table 4.15.

Table 4.15 - Temperature comparison between concentrated and distributed

Winding		Concentrated	Distributed
Housing		108.1°C	106°C
Magnet		142.3°C	157°C
Stator Tooth		150.8°C	171.5°C
Copper	Average	162.2°C	173.4°C
	Maximum	170.1°C	177.5°C
	Minimum	153.6°C	159.3°C

Even though the total losses were higher in the concentrated wound machine, the higher copper losses of the distributed wound machine were more critical, as being further from the cooling source of a water jacket, heat removal is more difficult. However all the temperatures were within the temperature limit.

4.6.5 IPMSM comparison summary

From the above comparison it is clear that both machines met the required torque speed characteristic of the FreedomCar 2020 targets. This was whilst maintaining the limits on the current supply, voltage, winding temperature and physical size.

Where the performance of the machines differed is in the losses and therefore efficiency. The distributed wound machine had a higher current requirement across the whole speed range, leading to higher copper losses. However the iron losses in both the rotor and the stator were significantly lower in the distributed wound machine. This gave the distributed wound machine a higher efficiency at the high speed, which has been shown to be the most challenging specification of the FreedomCar targets. Due to this higher efficiency the distributed wound machine is the superior option for an IPMSM.

4.7 Conclusions

The main conclusion from this chapter, was that it is highly unlikely that a traditional IPMSM will meet the FreedomCar 2020 targets, the most challenging being the high speed efficiency. There were however some other key learnings that have been found from this study. First is that a 10 pole design gave the optimal balance between current requirement and frequency to minimise the combined copper and iron losses whilst remaining within the VA specification. For a concentrated wound design 12 slots, although having high harmonics, gave the best thermal performance and lowest losses. Whereas for a distributed wound machine, 30 slots with a double layer winding was optimal for similar reasons.

While analytical tools such as SPEED are excellent for obtaining a fast estimation of produced torque, geometrical sizing and VA requirements, they were found to be lacking when calculating an accurate value for PM and iron loss. FEA gives a much more accurate representation of the full electromagnetic simulation of the machine but requires a higher amount of computing power, and therefore time.

When comparing the distributed machine against the concentrated it was clear that the increased current requirement of the distributed wound machine resulted in the concentrated wound design being the superior choice at low speed. However the reduced iron losses and increased reluctance of the distributed wound design allowed it to operate with a higher efficiency at high speed. Due to the high speed efficiency being the more challenging to achieve it was decided to focus on a distributed wound design for the remainder of the thesis.

4.7.1 Comparison to the FreedomCar 2020 targets

As the goal of this thesis is to meet the US DoE FreedomCar 2020 targets, each of the designs has been compared against them in Table 4.16. A tick (✓) show that the target has been achieved, a dash (-) that the target has been achieved

but just barely or that there is room for improvement, a cross (×) represents the target has not been met and major alterations would be needed to rectify this.

Table 4.16 – Comparison of IPMSM designs to FreedomCar 2020 targets

Requirements	Target	Concentrated IPMSM Design		Distributed IPMSM Design	
Rated Power (kW)	30	29.9	✓	30.0	✓
Peak Power (kW)	55	58.7	✓	58.6	✓
Peak Torque (Nm)	200	200.2	✓	200.0	✓
Maximum Current (Arms)	400	256.3	✓	269.8	✓
DC Link Voltage (V)	200-450 (325 rated)	325	-	325	-
Max Back EMF at Max Speed (V)	600	608	-	571	✓
Winding Temperature (°C)	180	162	✓	173	✓
Maximum Machine Diameter (mm)	250	250	✓	250	✓
Maximum Machine Length (mm)	200	200	-	130	✓
Maximum Machine Volume (L)	9.7	9.7	✓	6.38	✓
Mass (kg)	35	51.68	×	30.41	✓
Minimum Efficiency (%)	95	86.4	×	87.2	×
Cost	$275	N/A		N/A	

Both machines met the power, torque and current requirements. The distributed wound machine was shorter than the concentrated wound, this meant that after the end windings had been included it would be within the length limit, whereas the concentrated wound machine wound not. This shorter length also allowed the distributed machine to have a lower back EMF at max speed, bringing it under the requirement. The concentrated wound machine was over the mass limit, whereas again the smaller length of the distributed wound machine significantly reduced this. The minimum efficiency of the distributed wound machine was slightly higher than that of the concentrated wound machine. While this difference in efficiency looks small, it clearly shows the superior design was the distributed wound as this efficiency is the key challenge of the targets.

4.7.2 Summary of key findings and contributions

- When considering the FreedomCar targets:
  - 10 poles gave the best balance between torque per amp and high speed iron losses.
  - 12 for concentrated wound and 30 for distributed wound were the optimal slot numbers for minimising losses, current requirements and temperatures.
  - The study covered a much wider range of designs than has been previously considered for these targets.
  - A distributed winding was superior to concentrated wound when the most important factor is the high speed efficiency.
  - A concentrated winding was superior to the distributed winding when considering high torque current requirements.
- The design process of combining analytical tools with FEA to allow for rapid modelling of a high number of designs whilst ensuring accuracy of the simulation results, is in itself innovative.

4.7.3 Next Steps

Overall there were two key challenges remaining in meeting the FreedomCar 2020 targets the first was the high speed efficiency, which in this chapter was proven to be extremely challenging to achieve due to high iron losses. The other was the thermal limits, which define the minimum usable slot area. With less strict temperature limits, such as with an improved cooling system, the current density could be increased, increasing the torque or decreasing the slot area.

In the next chapter, a PMa-SynRelM design will be briefly considered, to show its potential to overcome the high speed iron losses. Improving the thermal management on the machine will be discussed in the following chapter and will have a significant impact on the final design.

Chapter 5. Initial PMa-SynRelM Design

5.1 Introduction

As can be seen from Eqn. 4.5 in Section 4.2, increasing the reluctance component of any machine results in a wider speed range and lower losses at high speed. A less conventional machine family which exploits this very well is the PMa-SynRelM [73, 74]. In this chapter the benefits of using a PMa-SynRelM over an IPM for the FreedomCar targets will be investigated.

Increasing the reluctance of the design allowed for two benefits when considering torque production. First was that based on Eqn. 4.5 the higher the reluctance was, the higher the torque per amp would be, so either the PM size could be reduced (reducing the cost and PM losses) or the current loading could be reduced (reducing the copper losses) or more likely a combination of the two. The other benefit was that, again based on Eqn. 4.5, without reluctance I_d offered no contribution to the torque but was still required to reduce the voltage at high speeds. The higher the reluctance of the design, the lower the drawback of increasing the phase angle and the lower the total current magnitude needed at higher speeds.

To increase the reluctance air barriers were placed behind the PMs of the IPMSM transforming it into a PMa-SynRelM. It has been shown multiple times in literature that higher barriers numbers give higher performance, although with diminishing returns, but that higher numbers also add mechanical issues and decrease the possible thickness of each air gap It has been shown that 3 barriers (including the original with the PM) is usually the optimal amount. [74, 106, 107].

5.2 Design process

An initial PMa-SynRelM design was created, maintaining the stator and PM shape from the 30 slot 10 pole distributed wound machine and simply adding two barriers behind it of the same thickness as the PMs. This design was then

modified with the goal of increasing the high speed efficiency. This involved reducing the PM width and thickness of all 3 barriers, whilst maintaining their general shape, and altering the slot width and depth whilst maintaining the stator outer diameters. The air gap thickness and rotor radius were also modified to optimise the torque production while keeping the back EMF reasonable. The result of this can be seen in Figure 5.1.

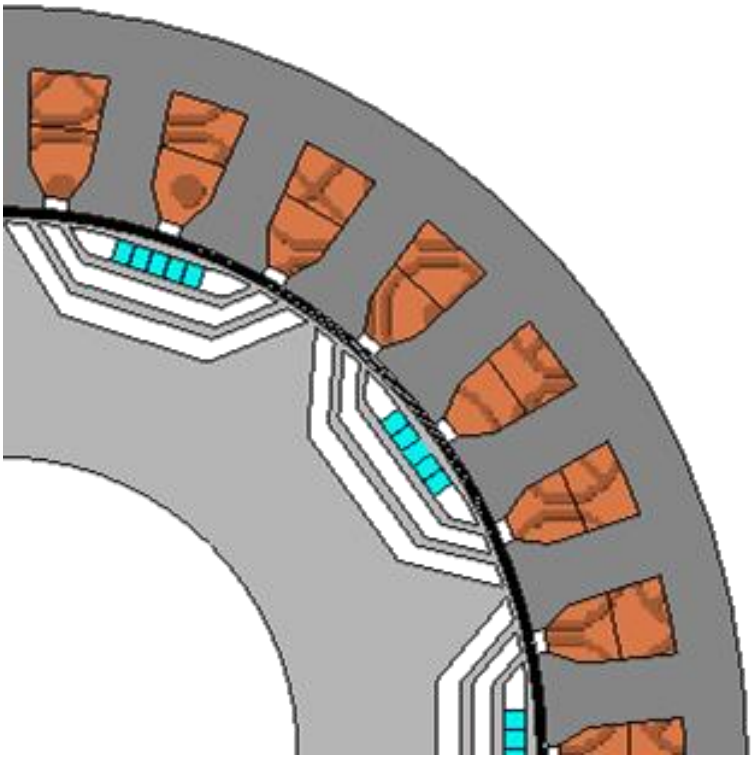


Figure 5.1 - Initial PMa-SynRelM design

5.3 Comparison to IPMSM

The specifications for the new design can be seen in Table 5.1. The general size of the machine has been kept the same with small changes made to improve the high speed efficiency further.

Table 5.2 gives the FEA simulation results for the same spread of speeds as the previous designs. These results will be represented graphically, and discussed in more detail, in the next section when they are compared to the results from the flat IPMSM distributed wound machine.

Table 5.1 – Initial PMa-SynRelM design parameters

Design Parameters	Poles	10
	Slots	30
	Rotor Diameter (mm)	180
	Stator Diameter (mm)	250
	Stack Length (mm)	130
	Air gap (mm)	1.5
Magnet Dimensions	Magnet Thickness (mm)	3.8
	Magnet Width (mm)	15.3
	Magnet Mass (kg)	0.57
Stator Dimensions	Tooth Width (mm)	9.17
	Slot Depth (mm)	20.5
Windings	Turns per phase	3
	Winding Diameter (mm)	1
	Number of Strands per Conductor	20
	Fill Factor	0.45
Electrical 2800 rpm	Rated Current peak (A)	225.2
	Frequency (Hz)	233
	Gamma for Peak (deg)	40
Electrical 14000 rpm	Rated Current peak (A)	80.3
	Frequency (Hz)	1667
	Gamma for Peak (deg)	58

Table 5.2 - Operating table – Initial PMa-SynRelM FEA Design

Speed	I rms	Ang	T	Iron Loss Rotor	Iron Loss Stator	Copper Loss	Magnet Loss	Pout	Pin	Eff
rpm	A	Deg	Nm	W	W	W	W	kW	kW	%
1000	225.2	40	101.6	6.7	116.2	1930	1.46	10.6	12.7	83.8
2800	225.2	40	101.5	26.1	499.1	1963	9.68	29.8	32.3	92.3
4000	172.5	38	71.7	34.3	653.8	1174	9.95	30	31.9	94.1
6000	126.9	36	48	42.5	867.2	666	8.33	30.2	31.7	95
8000	101.1	33	36.1	47.1	1103.7	449.9	6.32	30.3	31.9	95
10000	87.7	42	29	51	1313.8	364.9	6.94	30.4	32.1	94.6
14000	80.3	58	20.9	68	1919.6	364.5	9.53	30.6	32.6	92.8

5.3.1 Current and advance angle

The current requirement was higher for the PMa-SynRelM design for most of the speed range, than the IPMSM, this was incredibly pronounced at low speed, Figure 5.2. This was due to the much smaller PMs, meaning a larger electrical loading was needed for the same torque target. However, at high speed, the

current was actually lower in the PMa-SynRelM design. Referring back to Eqn. 4.5 two effects were in play, first with a higher reluctance I_d had a greater impact on torque, from

Table 5.2 and Figure 5.3 it can be seen that the angle for maximum torque was much higher for the PMa-SynRelM (40°) than the IPMSM (29°). This meant that for larger advance angles the PMa-SynRelM could produce closer to its maximum torque per amp. The other effect was that the PMs are smaller in the PMa-SynRelM, meaning a lower angle was needed at maximum speed (58° rather than 80°) to weaken the field. The lower angle resulted in a higher I_q and thus a lower total supply current was needed to maintain the voltage limit.

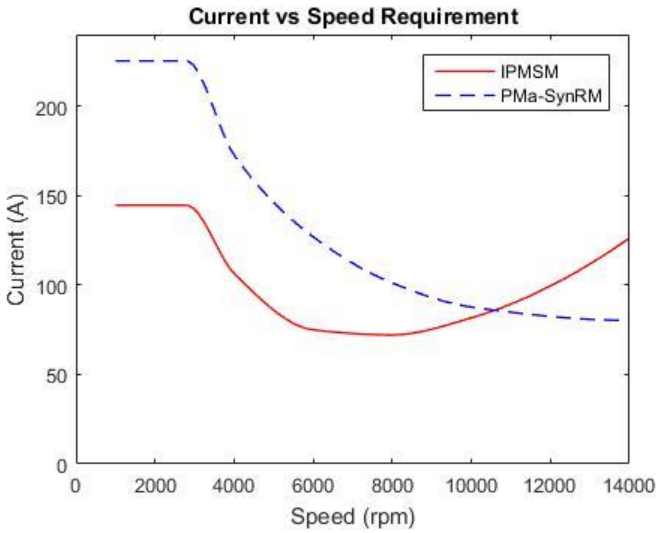


Figure 5.2 - Peak phase current comparison between the IPMSM and initial PMa-SynRelM

5.3.2 Efficiency

As this design was produced to try and improve high speed efficiency the comparison in Figure 5.4, between this and the previous design was crucial. Figure 5.4 and

Table 5.2 show that as designed the PMa-SynRelM had a higher efficiency at high speed, almost obtaining the 95% target. However the low speed efficiency was very poor. While the efficiency only has to be above the target from 10% of the maximum speed, this had not been achieved.

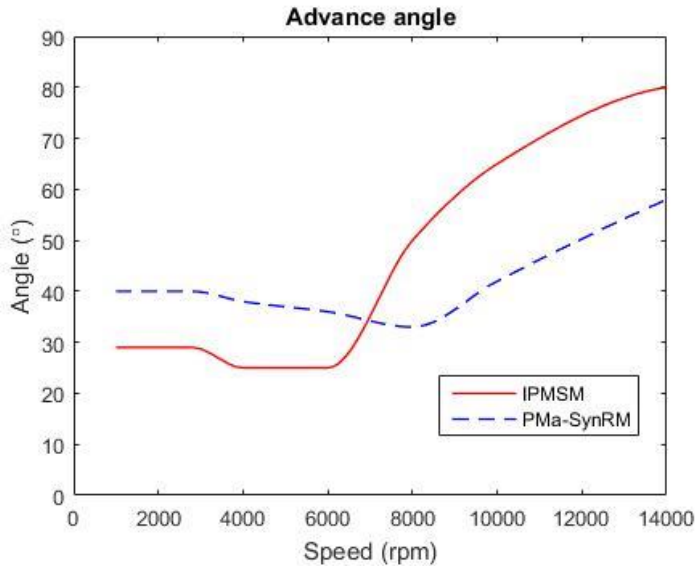


Figure 5.3 - Advance angle comparison between IPMSM and initial PMa-SynRelM

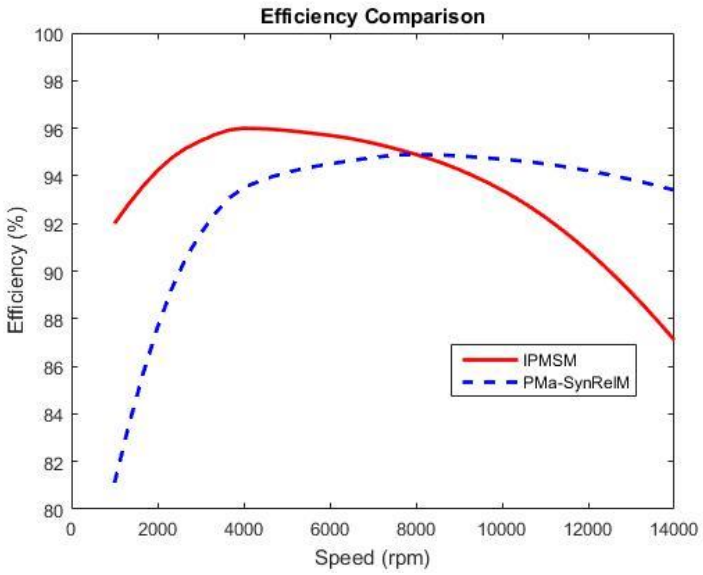


Figure 5.4 - Efficiency comparison between the IPMSM and initial PMa-SynRelM design

5.3.3 Loss break down

With the efficiency target not having been achieved at both the low and high speed ends, a study of the losses helped show where the issues lie. This breakdown of losses is in Figure 5.5, again comparing back to the distributed wound IPMSM design.

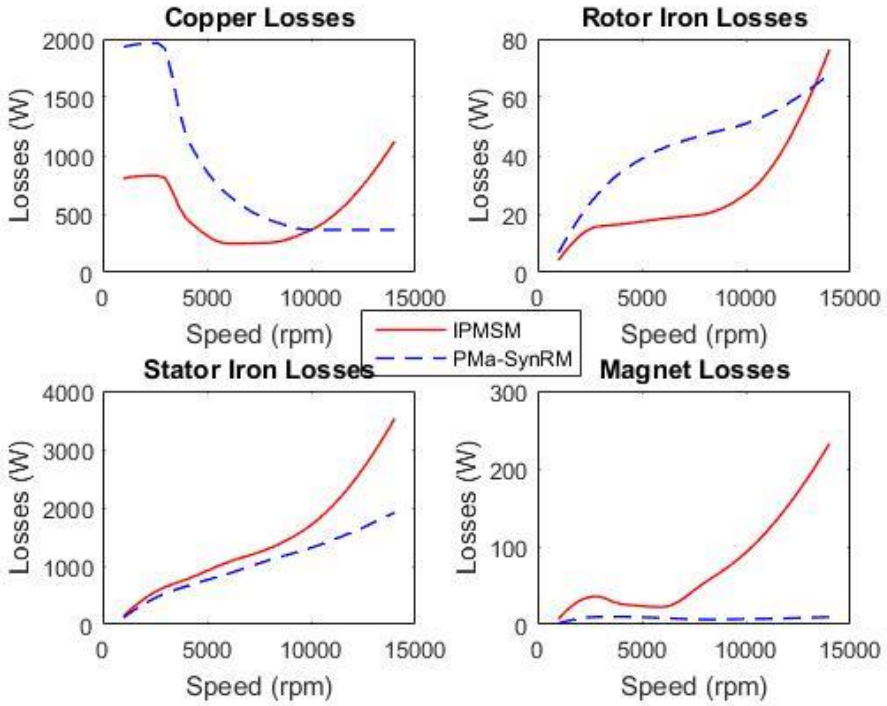


Figure 5.5 - Loss component comparison between IPMSM and initial PMa-SynRelM

With the slot shapes and winding lengths being similar between the two designs, the winding resistances were comparable, this lead to the differences between copper losses following the same pattern as the current requirement, seen in Figure 5.2. The PMa-SynRelM had much higher losses at low speed, but this rapidly decreased until it was below the IPMSM design, and the high speed peak was not seen with the PMa-SynRelM. The rotor iron losses were higher in the PMa-SynRelM design, however they were two orders of magnitude lower than the stator iron and copper losses and so this was not a momentous issue. The stator iron losses were lower in the PMa-SynRelM through the whole speed range, this was especially pronounced at high speed where there was almost a 45% reduction. This was clearly what gave the PMa-SynRelM the advantage over the IPMSM at high speed. Finally, as the PMs were much smaller and the currents were lower at high speed with lower advance angles, the magnet losses of the PMa-SynRelM were much lower through the whole speed range, to the point where they were insignificant compared to the other losses.

5.3.4 Thermal

Finally, the temperature rise due to the losses needed to be considered. In the previous designs, the hottest point was always at maximum speed where the total losses were greatest. Here with the large copper losses at low speed, the peak torque operating point was the most thermally critical, where the increased current must be held for 18 seconds. Table 5.3 compares the temperatures at several points in the machine, at their respective maximum temperature operating points.

Immediately it was clear that this machine would run at higher temperatures than the IPMSM and that it exceeded the 180°C thermal limit of the winding. This was a major drawback of this machine that needs to be overcome.

Table 5.3 - Thermal comparison between the IPMSM and Initial PMa-SynRelM

Topology		IPMSM	PMa-SynRelM
Housing		106°C	107.3°C
Magnet		157°C	143°C
Stator Tooth		171.5°C	194.4°C
Copper	Average	173.4°C	194.6°C
	Maximum	177.5°C	230.9°C
	Minimum	159.3°C	173.5°C

5.4 Conclusion

The initial PMa-SynRelM design was a massive improvement over the previous IPMSM at high speed, however at the high torque operating point the PMa-SynRelM was significantly worse.

The added reluctance ensured that smaller PMs (a reduction of almost 55%) could be used to meet the torque-speed characteristic with the VA limit. The reluctance along with the smaller PMs ensured a lower current and phase angle were needed at high speed, resulting in greater high speed efficiency. However as this machine was optimised to improve high speed performance the low speed, high torque performance suffered. The smaller PMs resulted in larger

current requirements to meet the peak torque and thus overheating due to copper losses.

The work presented in this chapter and the previous resulted in two designs. One, the IPMSM, which performed excellent at low speed but suffered at high speed due to high iron losses. The other, the PMa-SynRelM, achieved a higher efficiency at high speed (although still not quite meeting the target) but very poorly at rated speed.

Meeting the high speed efficiency and minimising the cost requirement have been shown to be the two main challenges of the FreedomCar targets. The PMa-SynRelM has a much greater efficiency at high speed and, due to the reduced PM mass, the materials cost would be lower. And so the PMa-SynRelM was focused on for the remainder of the work.

Two key steps were needed to be made to take this design further. The first was improving the thermal management, allowing for the PMa-SynRelM design to operate at peak torque without overheating, to be covered in Chapter 6. Secondly to further optimise the PMa-SynRelM, of note is that this was only an initial design and with more time a improved design could be created, focusing on reducing the copper losses at the peak torque operating point, whilst maintaining (or hopefully improving) the high speed efficiency, in Chapter 7.

Chapter 6. Implementation of an Improved Thermal Management System

6.1 Introduction

In the previous chapters it has been shown that to improve the design further the high speed iron losses have to be reduced and the thermal management must be improved. Re-designing the stator would allow for a reduction in iron losses, mainly by increasing the iron areas, but this would result in smaller slot areas and thus an even larger thermal issue. However, if the temperature could be significantly reduced it would allow for more freedom to explore the design.

This chapter investigates new cooling methods for the end windings of electrical machines. The thermal limit of the insulation of the windings (H class 180 °C) was the first critical temperature reached in previous designs. Currently the hot spots are in the end winding of the machine, as this had the longest thermal path to the water jacket, as can be seen in Figure 6.1, this is a common occurrence in water jacket cooled machines [108-110]. Because of this, the novel cooling methods considered focused on cooling the end winding more effectively.

These methods could also be applied to other machines and applications as the thermal limit is often a restrictive factor in electrical machines, and so a reduction in temperature would result in the potential for a higher torque density. In general reducing winding temperature has several significant benefits. The easiest advantage to exploit would be that the winding resistance will decrease, reducing copper losses for a given current density. Both this reduction in copper losses and the reduction in winding temperature allows for higher current densities to be used in the windings. Higher current densities result in higher torque densities, either more torque in the same size machine, producing the same torque from a smaller machine, or a combination of the two, giving higher power densities. The other option is to make the slot areas

smaller, giving more space for iron area, reducing saturation and iron losses, or again reducing the machine size.

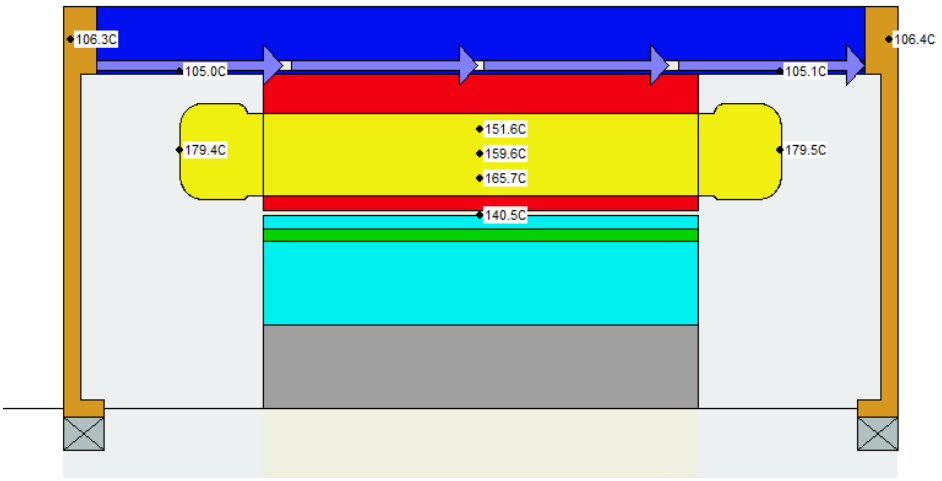


Figure 6.1 - Motor-CAD Thermal simulation

In Figure 6.1 the temperatures in the machine, including the hotspot in the end windings, are shown using Motor-CAD software. This software uses the design dimensions and losses to create a thermal network. While Motor-CAD is quick and easy to use, it is limited to traditional cooling methods, so for the novel ideas a customisable thermal network needed to be created.

6.2 Concepts for improved thermal management

In a water cooled machine, with minimal internal air flow, the hot spot of the machine is often in the end windings, due to the long thermal pathway from the end windings to the water jacket. The ideas proposed here aimed to remedy this by directly cooling the end windings with a range of simple methods.

The basic idea was to run water carrying pipes along the end windings. This was simple to implement and did not affect the active motor design. The key factor to how beneficial this will be, was how much lower the thermal resistances from end winding to the new pipe was, compared to the route through the slot and the stator to the water jacket. This thermal resistance was highly dependent on the contact area and thermal conductivity between the end winding and the added pipe.

During the initial simulations, the experimental work and further thermal simulations the total pumping flow rate was kept constant, not the pumping power. This meant that adding additional flow paths reduces the flow rate of the stator water jacket. In the final results the proportion of the flow through the stator and through the additional flow paths is decided to give the optimal cooling.

6.2.1 Pipe cooling

The obvious choices for pipe material were copper or plastic. The big benefit of a copper pipe was higher thermal conductivity; however, the drawback was poor flexibility and high stiffness. The poor flexibility in the copper pipe would lead to a smaller contact area. A plastic pipe, while having a lower thermal conductivity, could be flexible enough to mould itself to the shape of the end winding when a pressure was applied. Figure 6.2 shows the difference in contact area between a copper pipe and plastic pipe with a flat end winding surface. In reality the end winding surface is likely to be an uneven shape, made up of the circumference of individual conductors; this will give further benefit if a flexible plastic pipe is used.



Figure 6.2 - Plastic and copper pipes attached to the end windings

In Figure 6.2 it can be seen that the copper pipe only had a small localised contact area, while a plastic pipe would be able to obtain a wide contact area, assuming the pipe is malleable enough.

Another consideration was the electrical conductivity of the pipes. While the windings were protected due to their insulation, a fault could occur. If the copper pipes were in contact with this fault they would become electrified, which could lead to serious safety issues if the pipes are not properly grounded

or insulated. The safety factor was increased by including an electrical insulating sheet (such as slot liner) between the end windings and the pipe, but this decreased the cooling potential.

Due to the higher predicted contact area and high electrical insulation, plastic pipes were decided to be the superior option, however both were tested to verify this statement.

The size of the pipe was the next topic. Obviously wider pipes would cover a wider surface area and allow for a higher volume of fluid (at the same flow speed). Smaller pipes generally had thinner walls which mean smaller thermal resistance from fluid to winding.

The solution to this was found in a thin walled (0.5mm) common grade silicon pipe with a moderate diameter (15 mm) characterised by the following features:

- Can be continuously used between -60 °C and 200 °C
- Excellent elasticity, arc resistance, corona resistance, high pressure resistant, high tear resistance
- 40 shore A hardness
- Tensile strength 8mPa.
- Moderate thermal conduction

Figure 6.3 shows a comparison among various rubbers, using natural rubber as a reference. [41]

Silicone rubber withstands high and low temperatures far better than organic rubbers. Furthermore it can be used indefinitely at 150 °C with almost no change in its properties. It withstands use even at 200 °C for 10k hours or more. Silicone rubber can be immersed in any temperature water for long periods with water absorption of about 1%, and with virtually no effect on mechanical strength or electrical properties. [41]

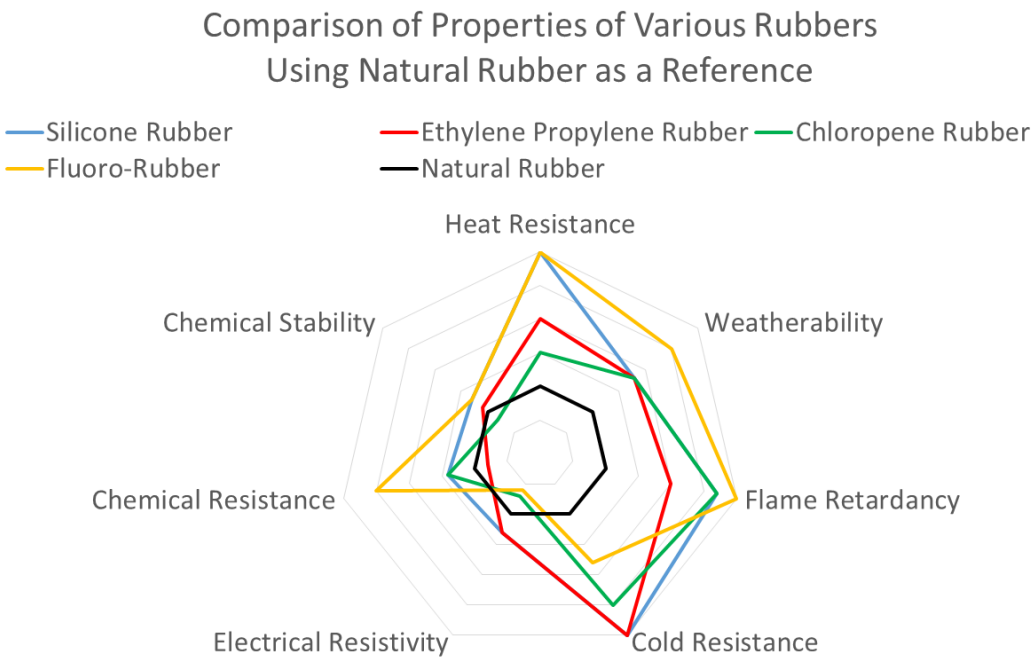


Figure 6.3 - Comparison of properties of various rubbers [41]

Because of all these properties it was the ideal candidate to make flexible pipes from, being easily mouldable to the shape of the end winding. The only downside was that the low hardness limits the pressure of fluid in the pipe. This limited the flow rate to 2.5 lpm, going above this the pipe expanded at an uncontrollable rate.

6.2.2 *Potting compound*

An alternative was to use a potting compound to encase the end windings and a single (or multiple) pipes. The benefit of this was that the contact area is the whole of the end winding bundle. The drawbacks were that the distance from end winding to pipe was likely to be greater, increasing the length of the thermal pathway, and the added cost of the potting compound and mould needed for it. Also, while the thermal conductivity of the compound would be greater than that of air, it was less than that of the thermal paste which was used with the silicone pipe. This thermal conductivity is typically in the range from 0.5W/mK to 5W/mK depending on the material. Figure 6.4 gives a visual representation of this cooling layout.

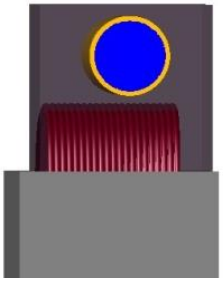


Figure 6.4 - Copper pipe and end windings in a potting compound

Another benefit was that copper pipes could be used here, increasing the pipe thermal conductivity, as there would be no direct contact between the pipe and the end winding, and the flexibility was not critical. The key factors here were the potting compound thermal conductivity and the minimum distance achievable between the pipe and the end winding.

Two potting compounds were used in this work. The first, a standard commercial compound, Robnor Resins PC439XS, with a claimed thermal conductivity of 1.3 W/mK and a max operating temperature of 200°C, which is above the limit of the winding. The other was a high performance compound was Duralco 128, which claimed a thermal conductivity of 4.2 W/mK and a maximum temperature of 260°C.

6.2.3 Altering the pipe position

The easiest way to attach the pipe would be to encircle the end windings with it, as seen in Figure 6.5, so the tension would keep it in place. However, this would directly cool the top of the end windings, the point which is already closest to the water jacket, so would have the least benefit.

The other options were on the outside face of the end winding or the inner radius. The inner radius would have the most benefit but would be the most difficult to hold in place.

In order to identify the optimal position all the above solutions were tested, both in simulation and experimentally to find whether the improved cooling would outweigh the difficulty of placing the pipe underneath the end

windings. The practical experiments shown later also deduced if this perceived difficulty was a real issue or if it was easy to overcome.

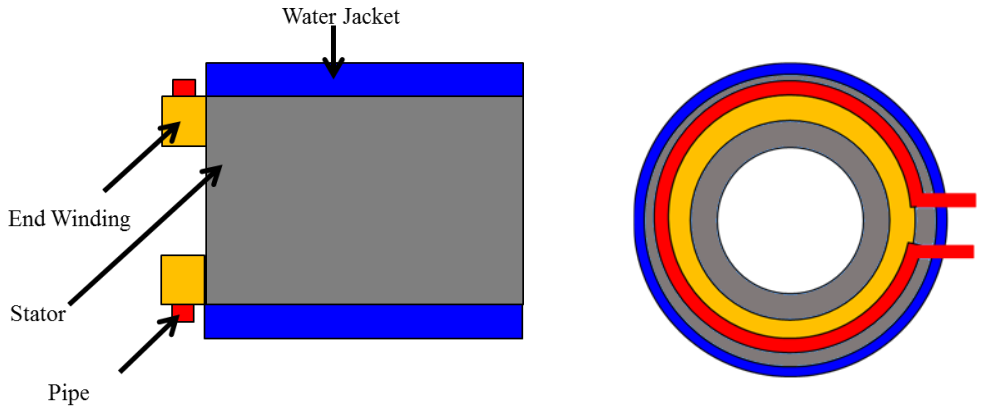


Figure 6.5- a) Pipe over end wind side view. b) Front view

6.2.4 Using multiple pipes

As stated above there were multiple positons to place the pipes on the end winding. A way to profit from this was to have multiple pipes, cooling a higher area of the end windings. Three pipes at 15mm diameter would completely cover the end windings of this design.

This could either have been achieved with the pipes in series or parallel. Assuming a single water supply was used, series would mean the water would follow a longer path in the pipes, heating up more and have less of a cooling benefit later on in its path. Parallel would result in lower pressure in each pipe, meaning lower flow rate and again less of a cooling benefit. Based on the reduced improvement of cooling with each additional pipe it was likely that there was an optimum number of pipes for cooling the end windings, with additional pipes adding higher mechanical complexity to the design without further thermal benefit.

6.2.5 Redesigned end windings

The final idea built off the requirement for improving the surface area between the end winding and the pipe. This investigated into whether if a less optimal winding layout (from an electromagnetic perspective) was used could the

potential cooling be improved, and would this improved cooling outweigh the drawbacks of the winding.

The proposal here was to have a gap running through the end windings which would allow a pipe to be held within it, as shown in Figure 6.6. This increased the end winding length; increasing the overall machine length, required copper mass and end winding copper losses. However this would both vastly increase the contact area achievable with a single pipe and decrease the maximum distance from any point in the end winding to the new cooling system. Through experiments and simulations it has been shown that the benefits of this cooling method outweigh the drawbacks.

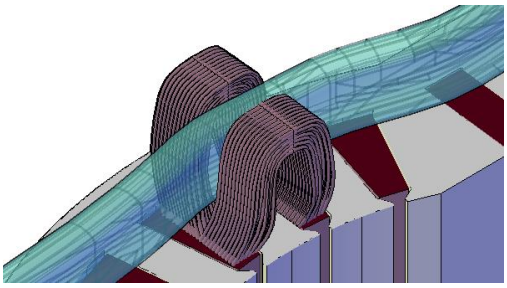


Figure 6.6 - Plastic pipe in end winding gap

6.2.6 *Qualitative comparison to existing solutions*

The current high performance methods for end winding cooling are either spray cooling of the end windings [44, 111, 112] or flooding of the stator [113, 114]. Both these methods produce very high heat dissipation in the end winding, as they allow cooling fluid to be in direct contact with the end windings, lowering the thermal resistance. A downside of both of these methods is that an extra cooling system must be implemented, adding complexity to the design and construction of the machine, and cost to the system. Spray cooling can have reliability and robustness issues due to corrosion and erosion of the intricate interior of spray nozzles and single-point failure as a result of a blockage in the nozzle, and so would be unadvisable for traction applications [115].

There are also methods of improving the thermal path way within the copper. This can either be using in slot cooling flow paths [116] or increasing the thermal conductivity in the slot with high thermal conductivity rigid inserts [97, 114]. The drawback of both these methods is reduction of slot area, increasing the winding resistance. With narrow slots this increase in resistance outweighs the cooling benefit.

All four of these solutions are advantageous when working with large machines. With smaller machines where space and cost are significant limitation factors, they are unfortunately infeasible.

The other common method is using a potting compound to create a thermal pathway from the end windings to the machine frame, axially and radially. This allows the existing cooling, such as a housing water jacket or forced convection on the frame, to further cool the end windings [117]. Typically this method is heavily dependent on the thermal conductivity of the compound, which is directly related to its price. The method involving potting compound suggested here will require a smaller compound volume and thus reduce cost or could be applied in conjunction with the traditional method, further increasing the cooling potential

6.3 Initial thermal simulations

A thermal model was constructed in Simscape (a toolbox of MATLAB [118]) to simulate the different cooling ideas, giving an initial indication of how beneficial the methods would be. This used a network of thermal resistances to create a transient lumped parameter model to calculate the temperature rise in the machine, this technique gave a good balance between accuracy and simulation time [119]. When designing this model previous publications were reviewed for the methods, equations and rules of thumb of using this process [97, 120, 121]. Due to the symmetry of machines in the radial and circumferential directions, only one slot needed to be modelled. The addition

needed here, in comparison to a standard thermal network, is an axial path and modelling of the end windings.

6.3.1 Thermal theory

As described earlier, there is power dissipation in the machine, these losses cause the location they occur in to increase in temperature. The increase in temperature is then transferred to the neighbouring components and spread throughout the machine. The copper losses are localised in the slot and end winding, stator iron losses in the stator teeth and back iron, rotor iron losses in the rotor and magnetic losses in the PMs.

Temperature can be transferred through 3 methods, Figure 6.7, which will be described in more detail below.

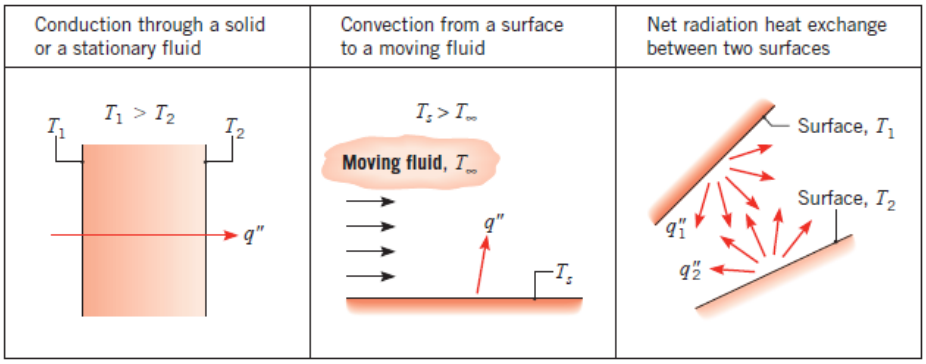


Figure 6.7 - Methods of thermal transfer [122]

While losses cause a temperature increase, higher temperatures also increase the resistance, as can be seen in Eqn. 6.1, which increases the copper losses and a diminishing positive feedback effect is present. In Eqn. 6.1 R is the resistance of the winding at the current temperature ($Temp$), R_0 is the resistance at a reference temperature ($Temp_0$, usually ambient), α is the temperature coefficient of resistance (3.9 x 10^{-3}/°C for copper).

$$R = R_0\left[1 + k_{Temp}(Temp - Temp_0)\right] \qquad \textbf{Eqn. 6.1}$$

6.3.1.1 Electrical analogy

To create a thermal model the specific parameters had to be quantified. The easiest way to understand and create this model (as electrical engineers) was the electrical analogy. This analogy replaces each thermal component with an equivalent electrical parameter and then allows for an electrical network to be modelled and simulated. The temperature rise represents the potential difference and so can be replaced with voltage. The transference of temperature (or voltage) between nodes is the heat flow rate, this can be analogous with current in this model. Electrical resistance simply replaces thermal resistance. The rate of change of temperature is dependent on the thermal mass, or heat capacity, of the component, this is therefore replaced by electrical capacitance. These equivalences are summarised in Table 6.1.

Table 6.1 – Thermal parameters and their electrical equivalent [123]

Electrical	Symbol	Unit	Thermal	Symbol	Unit
Voltage	V	V	Temperature rise	Temp	K
Current	I	A	Heat flow rate	Φ_{th}	W
Electrical Resistance	R	Ω	Thermal Resistance	R_{th}	K/W
Capacitance	C	F	Heat capacity	C_{th}	J/K

6.3.1.1.1 Conduction

The first and most prominent form of thermal transfer is conduction. This is the transfer of temperature through a solid body. Increasing the temperature triggers vibration in the ions of the material which then causes the neighbouring ions to vibrate. This permutation of vibrations allows for heat flow through the material. How easily these vibrations pass through the section is determined by the length, *L*, cross sectional area, *A*, and thermal conductivity of the material, as shown in Figure 6.8 and Eqn. 6.2. The thermal conductivity is based on the material, similar to electrical conductivity those with a denser fill of ions and free electrons (such as metals) have high conductivity while other such as plastics or liquids have poor thermal conductivity.

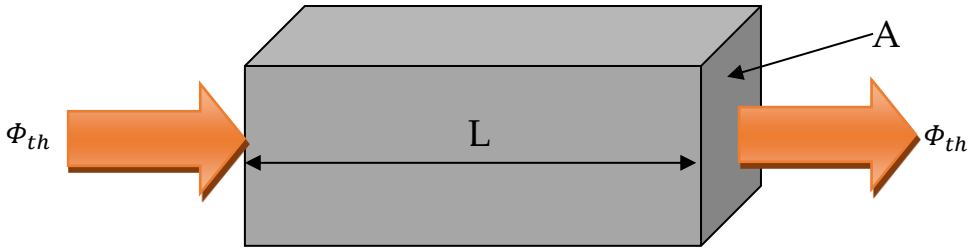


Figure 6.8 – Conduction through block [119]

$$R = \frac{L}{\sigma_{them} A} \qquad \text{Eqn. 6.2}$$

Key areas of conduction in a machine are within the slot, and in the iron areas.

6.3.1.1.2 Radiation

Unless the machine is specifically designed for it, radiation does not play a significant role in the thermal management of the electrical machine. Radiation does not involve the particles of a material and is instead an electromagnetic wave, this means, although not significantly relevant for this application, radiation can occur in a vacuum. Radiation is primarily dependant on the surface area, A, and emissivity, e, as seen in Eqn. 6.3, k_{sc} is Stefan's constant (5.6703×10^{-8} W/m^{2}K^4). The emissivity is dependent on the colour of the surface, with dull and matte blacks giving high emissivities and reflective surfaces giving low [123].

$$R = \frac{1}{e k_{sc} A} \qquad \text{Eqn. 6.3 [123]}$$

Radiation is present on the housing of the machine and in the air gap between the rotor and stator. However its effect is only noticeable when convection is low, such as a natural convection in a machine rotating at low speed. Because this is not the case here, radiation will not be included in the thermal networks.

6.3.1.1.3 Convection

While conduction is the effect which dictates heat transfer throughout the machine, the key effect when removing the temperature from the machine is convection. This is the effect that when a gas or liquid increases in temperature

the particles move faster, expanding the material. Natural convection causes these hotter particles to rise (due to a lower density) and be replaced with cooler ones which in turn heat up, this sets up convection currents cycling in this process of heating up and being replaced. This effect can be even more pronounced when forced convection is applied, this is where a liquid or gas is forced to flow over a surface of the machine transferring the heat away at a much quicker rate. The effect of convection is down to two parameters, seen in Eqn. 6.4, again the surface area, A, and the convective heat transfer coefficient, h_c. The heat transfer coefficient is dependent on the flow rate and fluid and whether it is a turbulent or laminar flow [119].

$$R = \frac{1}{h_c A} \qquad \textbf{Eqn. 6.4 [119]}$$

Convection is present anywhere in the machine there is air, such as the air gap, end areas or the outer of the housing. Forced air can be used in the machine, through the air gap or specifically designed paths, or on the outer of the housing. Liquid cooling can be applied to the machine in a range of methods, either in an axial or spiral water jacket in the housing, spray cooling or a flooded stator or using the methods described in this chapter.

6.3.1.1.4 Heat capacity

Heat capacity or thermal mass is what determines how quickly a body can increase in temperature. Higher thermal masses require more energy to heat up and so for the same losses would increase in temperature at a slower rate. The heat capacity, C_{th}, is based on the specific heat capacity of the material used, c_p and the mechanical mass of the body shown in Eqn. 6.5 [124]

$$C_{th} = c_p * mass \qquad \textbf{Eqn. 6.5 [124]}$$

6.3.2 Lumped parameter thermal network

When discussing the direct pipe cooling, the location of the pipes used was either on top, side or bottom of the end windings. This refers to the cooling sources on the graphical representation of the thermal network in Figure 6.9.

The model was designed such that each position of the potential cooling can be switched off or on to allow for one model to represent multiple cooling configurations. The interface material (green) represents several possibilities of substance between the pipe and the end windings, included are thermal pastes, potting compounds, air or direct contact (no interface material).

A potential cooling spot not shown here is the pipe in the gap between the end windings. This could not be effectively modelled before experiments as there were too many uncertainties in the winding design and thermal pathways.

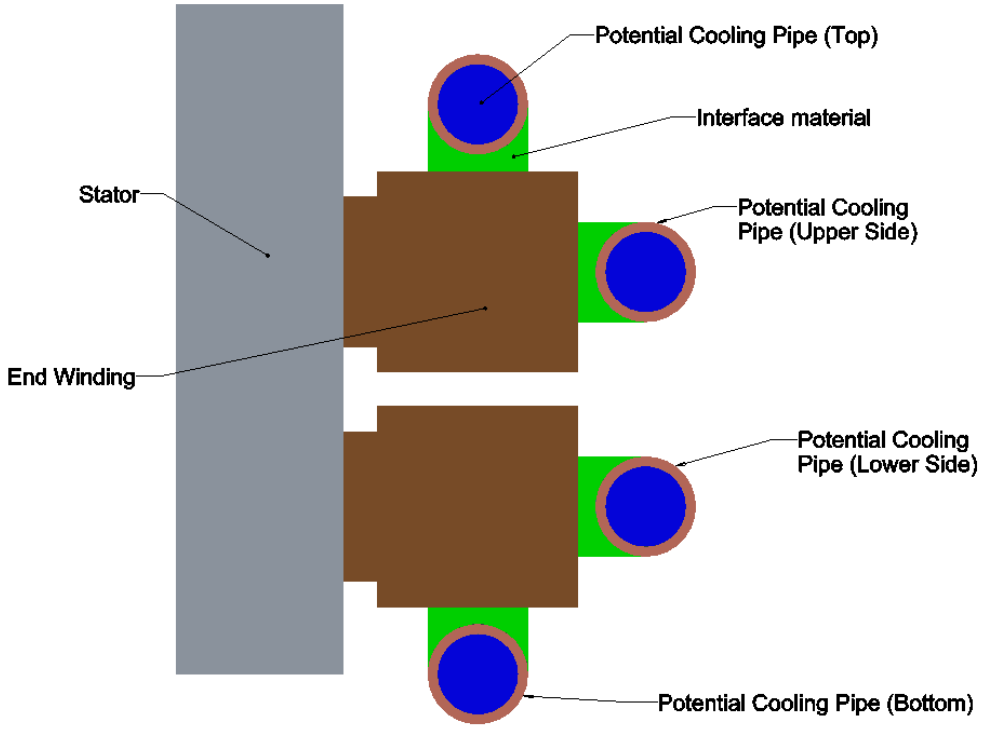


Figure 6.9 - Location of cooling source

A goodness factor used is the potential contact area between the pipe, interface and end winding. This goodness factor was dependent on how well the pipe could be compressed onto the windings and what contact area would be created, with 100% goodness factor being when half of the surface area of the pipe was in contact with the windings. This extreme was unlikely to be achievable but gave a best case scenario value to aim for. Contact areas with low and high goodness factors (with no interface material) are shown in Figure

6.10 on the left and right respectively. At this stage this goodness factor was used to give a range of results, however after the experimental work it was one of the variables used to calibrate the model.

6.3.2.1 *Slot thermal model*

The model used in the slot is standard and can be seen multiple times in literature [93, 97]. A basic diagram of the slot is shown in Figure 6.11, with the resistance network shown over laid on a version scaled to allow for better representation of the nodes in Figure 6.12. The resistances shown in Figure 6.12 and any new parameters introduced are included in Appendix C, Table C.1 and Table C.2

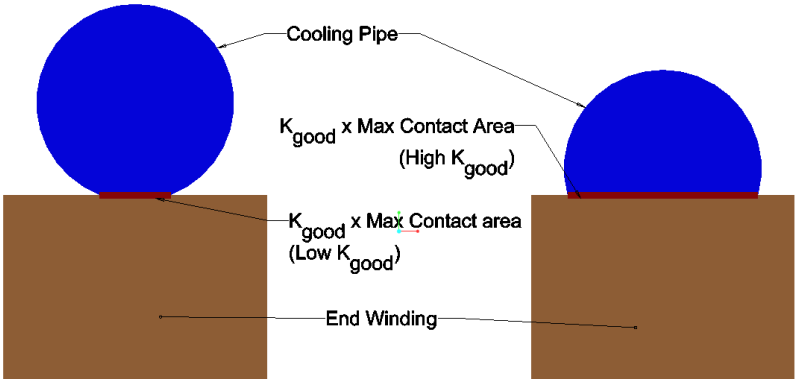


Figure 6.10 - Comparison of contact area with different goodness factors

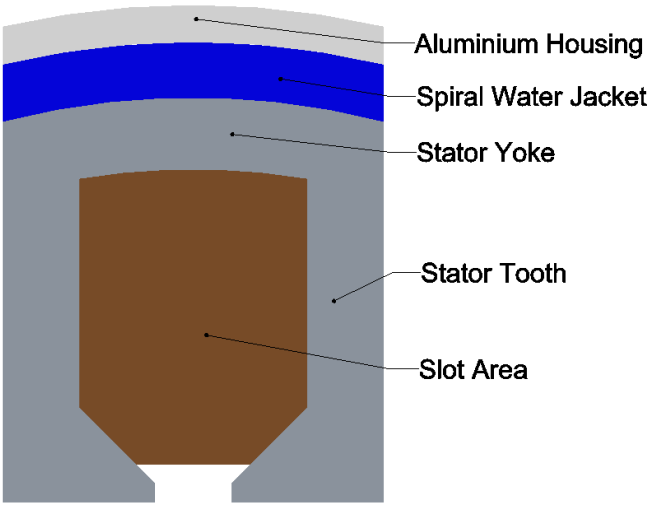


Figure 6.11 - Slot diagram

While the diagram in Figure 6.12 shows a single node in the slot, for increased accuracy the full thermal model used 18 nodes in the slot. The full thermal network of the slot used can be seen in Appendix C, Figure C.1 and Figure C.2.

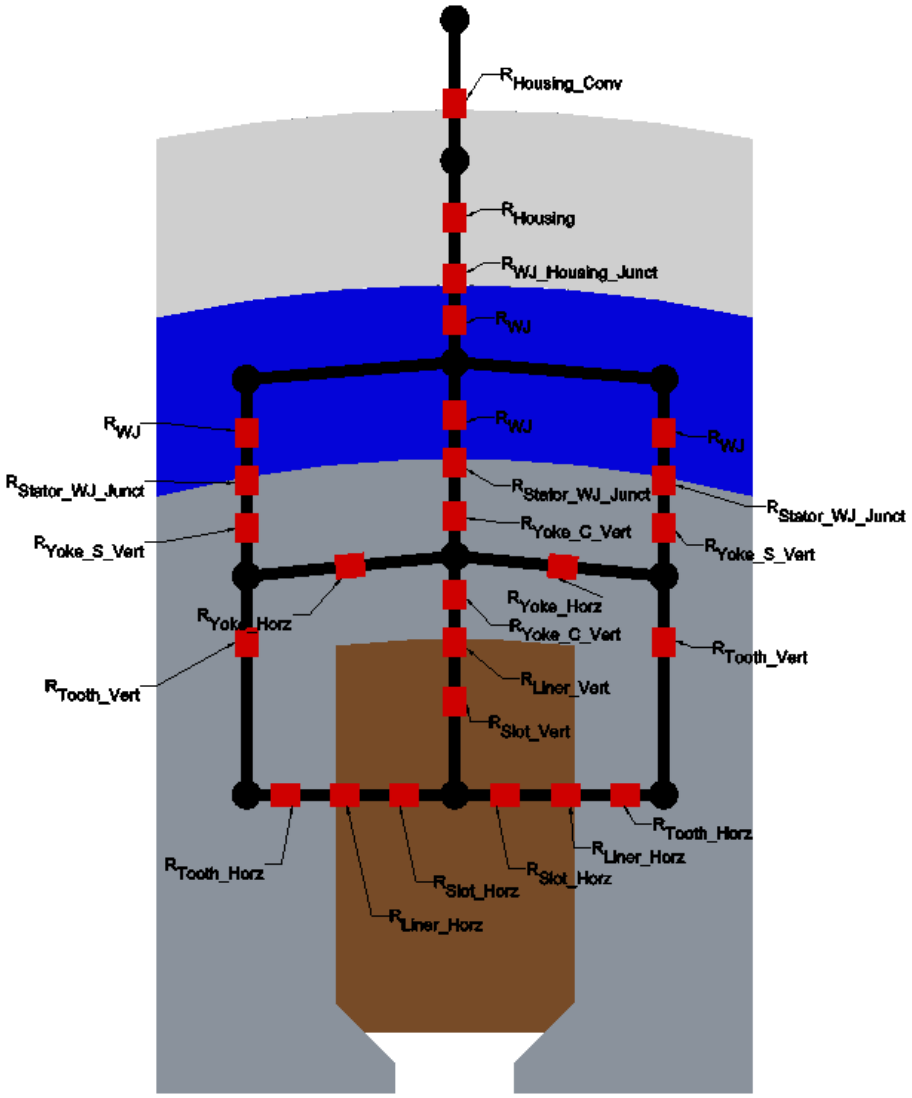


Figure 6.12 - Slot thermal network diagram

6.3.2.2 *End winding model*

An interesting addition was the section of the model to allow the end winding cooling to be applied, as is shown in Figure 6.13. This represents the same area as Figure 6.9, but the dimensions of the components have been varied to give an understanding of where the thermal resistances lay. Here one thermal path

way (to a cooling pipe on the top) is shown, but similar paths were implemented for the other 3 potential cooling points.

The equations for each component and explanation of any new variables of the end winding resistance network are given in Appendix C, Table C.3 and Table C.4.

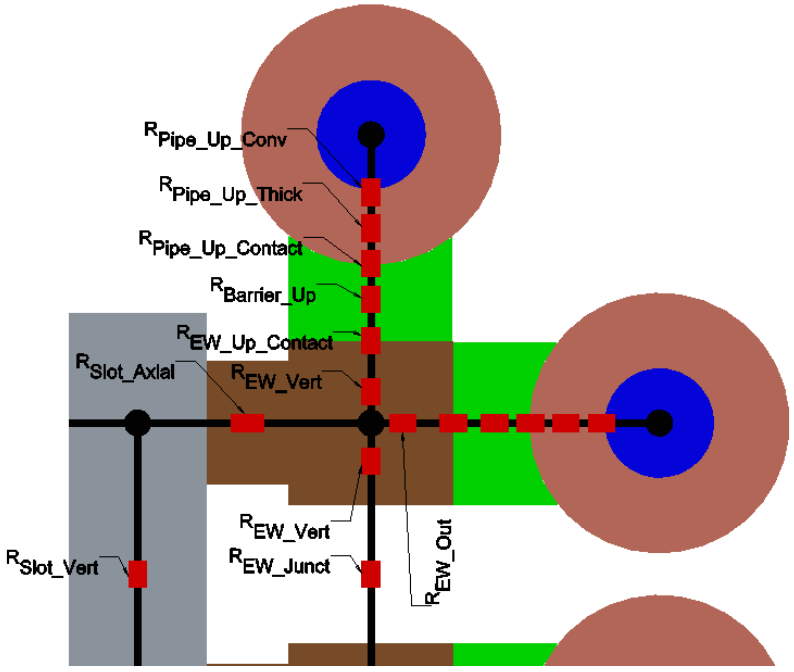


Figure 6.13 - End winding cooling thermal network

Figure 6.13 refers to the values for a network with a low number of nodes. In reality, as with the slot, a much higher discretisation was used to allow for more accurate models and distribution of losses and cooling, shown in Appendix C, Figure C.3 and Figure C.4.

6.3.3 *Results*

The initial temperatures calculated using the thermal network are given in Table 6.2. The values are the hotspot of the machine, for the majority of the simulations this value was the end winding, with the higher goodness factor values this was within the slot. The simulated electromagnetic losses, used as current source inputs to the thermal model, and the final temperatures were an

iterative process, until the difference between one simulation and the next was less than 1% [125].

In these simulations when the goodness factor was high enough that a pipe would cover the whole of the corresponding edge of the end windings, the remaining pipe area covered the adjacent edge(s). The side position shared the goodness factor between the upper and lower end winding bundle. The two pipe model simulated a pipe on both the top and bottom position, and with high goodness factors both extending onto the side positions, Figure 6.9.

Table 6.2 - Initial thermal simulation results

Goodness factor	No Pipes (°C)	One 15mm pipe (°C)			Two 15 mm pipes (°C)	Potting Compound (°C)
		Top	Side	Bottom		
10%	178.2	167.8	160.3	155.9	154.8	137.3
25%		166.5	158.2	150.9	148.6	
50%		165.6	154.3	147.5	144.9	
75%		165.2	151.8	146.1	143.4	
100%		165	150.6	145.3	142.5	

It can be seen in Table 6.2 that having a pipe on the top did not give a major benefit over no pipes. This was because this section of the end windings was already the closest to the water jacket in terms of thermal path ways. The potting compound model gave the lowest temperature. However this simulation assumed a distance between the pipe and end winding of 3 mm and a potting compound thermal conductivity of 1.2 W/mK. Until tests had been performed it was uncertain if these were attainable values. Also shown is that the single pipe at the bottom was almost as effective as the double pipe. As stated earlier, the bottom of the end windings was the hottest spot, so after ensuring this point is cooled adding any extra pipes had diminishing returns.

6.3.4 Uncertainties

While the thermal network has been compared against Motor-CAD there were still several variables that were uncertain. The main ones were, what goodness factor and contact areas are achievable, where the pipe could be attached, the

convection coefficients to the water (in both the water jacket and pipe) and to the surrounding air and the thermal conduction in the slots.

Because of these uncertainties in variables, practical tests had to be done to allow for validation of the thermal models.

6.4 Experimental validation

Experimental tests were needed to prove the cooling benefit of the proposed methods and validate the thermal networks, particularly when the models have novelty and so could not be fully based on previously documented results [121, 126]. These tests were performed on a motorette, which was a 6 slot section of a stator. To increase the temperature in the windings a DC current was passed through the conductors. Using a DC current ensured the only losses are DC copper losses, which were easily and accurately calculable. This guaranteed that the total power converted to thermal energy was known exactly, which will be useful in later sections when the results were used to validate thermal models.

The temperature was determined using thermocouples at various key spots, such as in the slot, the end windings, the stator tooth and the input and output of the cooling fluid. In the critical areas, such as the end windings, multiple thermocouples were used to obtain a temperature map, and to ensure the hot spot was observed.

The wound motorette, with water jacket and thermal insulation to the surface, but no additional cooling method, is shown in Figure 6.14. The rest of the equipment used and set up of the experiments is given in Appendix D.

6.4.1 Tests

To test the temperature increase, a range of current values were used for each cooling method to give a spectrum of results. Each current value was tested multiple times to ensure repeatability. The DC current produced copper losses which then increased the temperature in the dummy stator, in particular the

winding. The temperature was measured using thermocouples in the slots, on the end windings, on the stator and one to measure the ambient temperature.

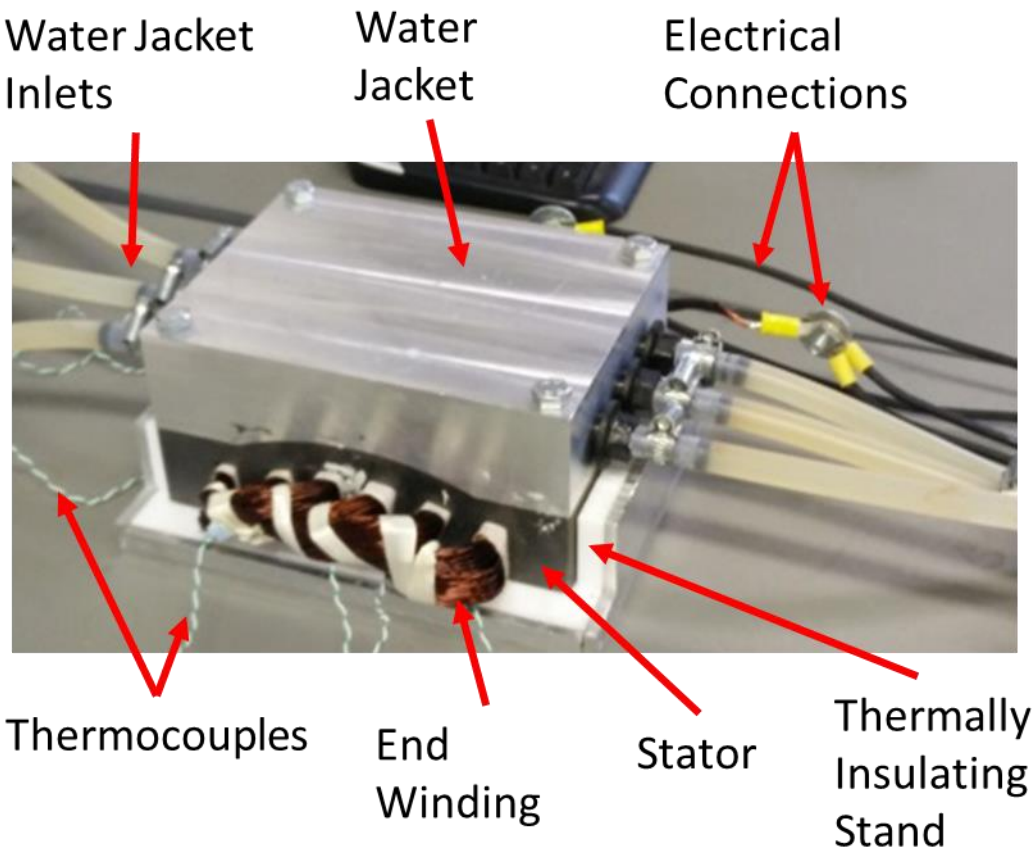


Figure 6.14 - Photo of dummy stator without additional cooling methods

For the experiments flow rate measurement and control hardware was implemented for the cooling fluid paths.

The first tests were without any cooling, from the water jacket or extra pipes. High currents could not be used here as the windings would overheat. However low current tests were completed to give a good idea of the convection coefficients, through the stator, water jacket and end windings. Next, tests were done using the water jacket to cool but without any added pipes yet. This gave a base line to compare the novel cooling methods back to.

When testing the silicone pipe, it was added in incremental steps. First the optimum position of a single pipe was found. Then the pipe was folded back on itself to represent the double pipe in series layout. Finally the best double

pipe layout was attached with thermal paste, with a thermal conductivity of 1.1 W/mK. Adding the thermal paste increased the contact area and thermal conductivity but was difficult to remove, so could only be added after the best pipe configuration was decided. Tests were also performed with just the pipe cooling; no fluid in the water jacket, to give an idea of how much of an effect this novel method could be, used by itself. A similar process was followed for the other cooling configurations.

Between each cooling method, the motorette had to be rewound, due to the thermal paste or potting compound being difficult to remove or the winding layout needing to be modified. This meant that before each cooling method was implemented, the motorette had to be retested with just the water jacket cooling to obtain a baseline for comparisons of the next cooling method implemented.

6.4.2 Experimental results

6.4.2.1 Silicone pipe on end winding surface

Table 6.3 shows the peak temperature found when cooling the dummy stator with a range of silicone cooling pipe layouts on the surface of the end winding bundle.

Table 6.3 - Silicone pipe dummy stator results

Cooling Method	Current (A)	Peak Temperature (°C)	Temperature Reduction (°C)
Water Jacket	100	78.9	N/A
	120	100.7	
	130	115.3	
Singular Pipe	100	76.4	5.0
Two Pipes	100	74.2	7.4
Two Pipes with Thermal Paste	100	73.9	8.1
	120	95.6	8.3
	130	109.9	9.4

It can be seen from Table 6.3 that there was a small decrease in temperature with the silicone pipes. This reduction increased as the contact area increased; by folding the pipe back on itself to attempt to double the contact area, and by adding thermal paste to the junction between the pipes and end winding.

There was a limitation in this set of tests, in that the winding resistance was very low, as it was designed to match the winding pattern of a full machine. This meant that the maximum temperature was limited by the maximum current of the supply used instead of the wire insulation. While these results did not push the wire to its thermal limit, there was still sufficient data to use to validate the thermal networks. In the re-winds of the dummy stator the number of turns was increased and parallel paths per turn decreased, keeping the slot fill factor constant whilst increasing the resistance.

Later, tests were done using the silicone pipe on a winding with a higher resistance so a higher baseline temperature could be tested. While other tests focus on maximising the cooling, these tests focus on emphasising the positioning of pipe. The results for these tests are shown in Table 6.4, where *WJ* refers to the baseline of only water jacket cooling, *Pipe* is with the pipe applied and *Diff* is the reduction between the two. For these tests a range of thermocouples were used in the windings and Table 6.4 shows the reduction in the thermocouple closest to the cooling and the one farthest away, with the others falling somewhere between. Two pipe locations were used, one on the side and one on base of the end winding.

From Table 6.4 it can be seen that high reductions were produced near the application of the pipe, but this did not penetrate well to other sections of the end windings. This was due to the very low turn to turn thermal conductance as no impregnation was used on the windings, this was even more problematic in the end windings where the conductors are less densely packed. The difference was even more noticeable when considering the reductions in the slot were usually larger than the furthest point in the end winding, the much higher thermal conductance of the conductors along their path accounted for

this. Higher reductions were seen in the side position due to the thermocouples being much closer, in fact being in direct contact with the pipe, whereas the closet thermocouple to the pipe placed on the base was about 10 mm away.

Table 6.4 – Silicone pipe difference in end winding temperature reduction

Pipe Location	Current (A)	End Winding Temperature					
		Closest Thermocouple to Pipe (°C)			Farthest Thermocouple from Pipe (°C)		
		WJ	Pipe	Diff	WJ	Pipe	Diff
Side	40	144.1	127.5	16.6	154.6	150.8	3.8
	41.3	163.4	143.7	19.7	152.2	148.5	3.7
Bottom	40	156.0	148.4	7.6	164.0	161.6	2.4
	41.3	166.0	150.6	15.4	174.2	171.5	2.8

Pipe Location	Current (A)	Slot Temperature (°C)		
		WJ	Pipe	Diff
Side	40	97.0	92.9	4.1
	41.3	101.3	98.8	2.5
Bottom	40	97.0	91.3	5.7
	41.3	101.3	97.0	4.3

Again, the results in Table 6.4 were not a definitive proof of how much cooling was possible with this method, as cooling a specific point was not beneficial if other points in the end winding remain hot spots. However, the results from this, in particular the difference in temperature between the different thermocouples in the end winding, were used to calibrate the thermal models.

6.4.2.2 Copper pipe on end winding surface

The results from the copper pipe test are shown in Table 6.5. The tests completed for this were, a baseline test with just a water jacket to be used for comparison and tests with the copper pipe cooling the end winding, as shown in Figure 6.15.

Only a single copper pipe was used for these tests as the size of the pipe connectors would not allow for more than one pipe. However, more pipes in series or parallel could be modelled once the thermal network was calibrated.

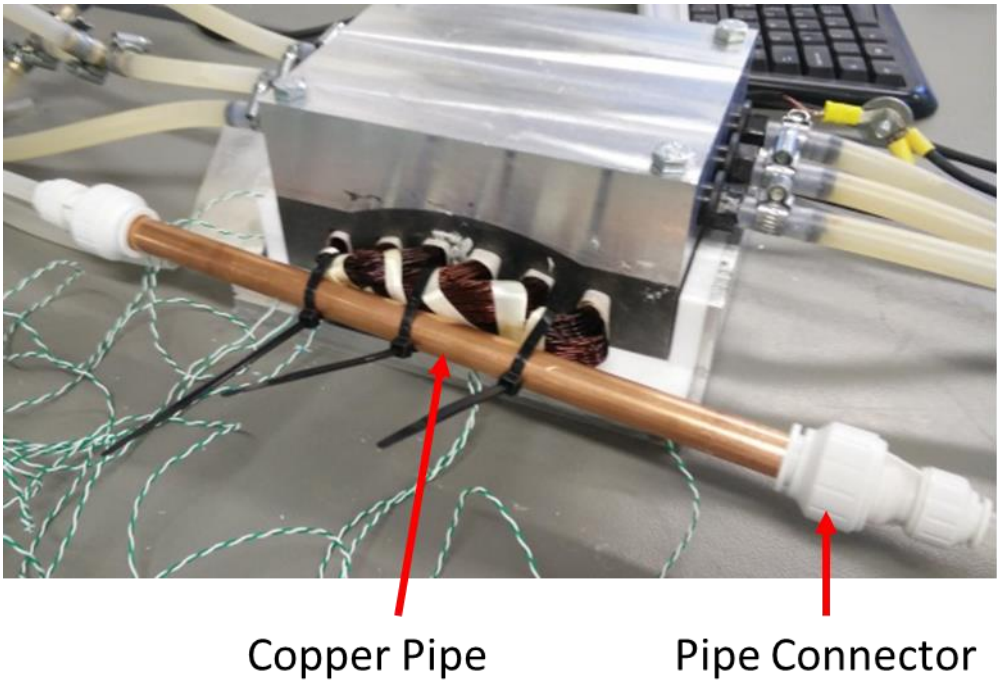


Figure 6.15 - Photo of dummy stator with copper pipe cooling end windings

Table 6.5 shows that as expected the copper pipe cooled the end windings, and the reduction increased with increasing temperature. Again a small reduction in the peak end winding temperature can be seen.

Table 6.5 - Copper pipe dummy stator results

Cooling Method	Current (A)	Peak Temperature (°C)		Temperature Reduction (°C)	
		Slot	End Winding	Slot	End Winding
Water Jacket	45	74.2	131.7	N/A	
	50	88.2	160.1		
	52.5	98.7	178.2		
Water Jacket and Pipe	45	79.4	127.6	-5.2	4.1
	50	95.0	155.6	-6.8	4.5
	52.5	99.5	172.4	-0.7	5.8

Of note is that while the end winding temperature reduced the slot copper temperature actually increased. This increase was due to the reduced flow rate through the water jacket. There was less flow through the water jacket as the copper pipe was connected to the same fluid network in parallel.

Flexible copper pipes and square copper pipes were also used to try and improve the contact area between the pipe and end winding. However the further thermal reduction was minimal. This reduction was not worth the increased cost of the pipe (for the flexible pipe) or fittings (for the square pipe).

The reductions in temperature here were lower than with the silicone pipe, even from the higher initial temperatures. This emphasised that contact area was the critical component that needed to be increased.

6.4.2.3 Commercial potting compound

The next stage to be shown here is presented in Table 6.6, which shows the benefit of encasing the end windings and cooling pipe in a potting compound. The compound used here was a moderately priced commercially available product with a claimed thermal conductivity of 1.3 W/mK, Robnor Resins PC439XS.

The end winding encased in the potting compound with a copper pipe passing through is shown in Figure 6.16. Of note is the gap between the compound and the stator, this ensured all the additional cooling came from the pipe not due to an increased conduction to the water jacket. This was useful to be able to use the results to calibrate thermal models accurately, on a real machine the compound would also touch the stator to allow for this extra cooling path. During the tests, it was clear that the potting compound also added thermal mass to the end winding, due to the thermal increase being less rapid, even without water flowing through the pipe, although the same steady state temperature was reached.

In Table 6.6, the reduction in temperature from this method is shown. As with the previous two methods, the cooling effect increased as the current, and therefore temperature, increased.

Here the temperature in the slot has also been reduced; this is because the increased cooling on the end windings outweighs the reduced cooling from the water jacket due to the reduced flow.

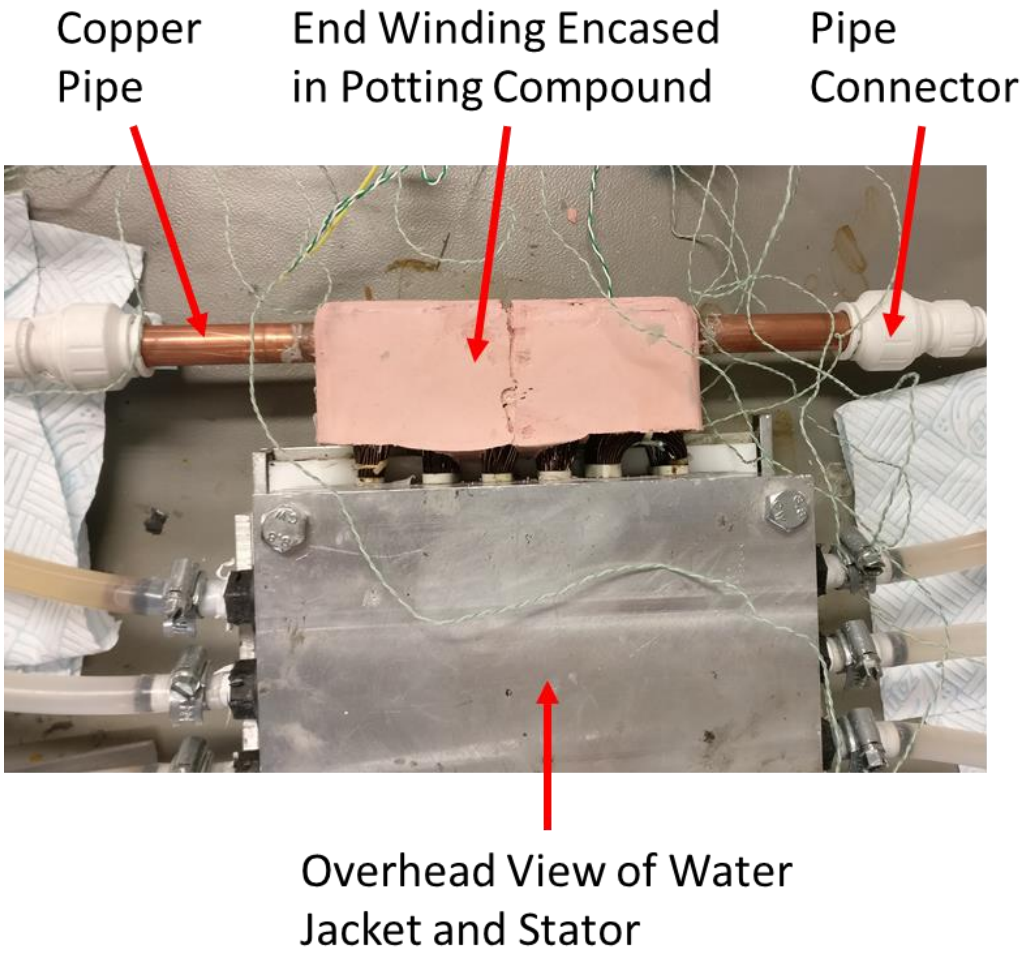


Figure 6.16 - Photo of dummy stator with potting compound

Table 6.6 - Commercial potting compound dummy stator results

Cooling Method	Current (A)	Peak Temperature (°C)		Temperature Reduction (°C)	
		Slot	End Winding	Slot	End Winding
Water Jacket	35	80.9	120.7	N/A	
	40	101	155.2		
	42.7	117.6	179.8		
Water Jacket and Pipe	35	77.5	111.6	3.4	9.1
	40	98.1	145.7	2.9	9.5
	42.7	115.2	169.6	2.4	10.2
	43.8	120.3	178.3	N/A	

The reductions in temperature here were comparable to the silicone pipe, but with the added cost of the compound and set up time with the mould.

6.4.2.4 *High performance potting compound*

The potting compound tests were repeated, this time with a compound, Duralco 128, with a higher thermal conductivity (4 W/mK), although at an increased cost.

Table 6.7 - High performance potting compound dummy stator results

Cooling Method	Current (A)	Peak Temperature (°C)		Temperature Reduction (°C)	
		Slot	End Winding	Slot	End Winding
Water Jacket	35	92.4	121.4	N/A	
	40	117.5	157.5		
	42	133	179.5		
Water Jacket and Pipe	35	88.8	111.1	3.6	10.3
	40	111.6	144.5	5.9	13
	42	124.5	164.6	8.5	14.9

Table 6.7 shows an increase in the reduction possible compared to the commercial compound in Table 6.6. However with triple the thermal conductivity and almost ten times the cost, the increase in cooling was disappointing. This could have been down to the high performance compound having much higher viscosity which may have prevented it from flowing between the conductors as completely.

6.4.2.5 *Silicone pipe with modified end windings*

The final type of cooling applied to the dummy stator is that shown in Figure 6.6, where the silicone pipe used previously was passed through a gap in the end windings, referred to as 'modified end windings' method herein. Obviously this required some changes to the winding design to create this gap. Previously all the designs had been distributed wound in a double layered pattern, here a concentrated winding was implemented with a single coil per slot. This was to allow for this gap to be created which could not be achieved with standard winding methods with a distributed winding. Adding the gap

also increased the winding length beyond what is expected of a standard concentrated winding by 50%, increasing the copper losses for a given current and temperature. The results for these tests are shown in Table 6.8.

Table 6.8 - Modified end windings dummy stator results

Cooling Method	Current (A)	Peak Temperature (°C)		Temperature Reduction (°C)	
		Slot	End Winding	Slot	End Winding
Water Jacket	35	95.4	126.1	N/A	
	40	124.8	163.2		
	41	132.2	172.7		
Water Jacket and Pipe	35	75.2	94.6	20.2	31.5
	40	96.8	122.5	28	40.7
	41	102.3	129.8	29.9	42.9

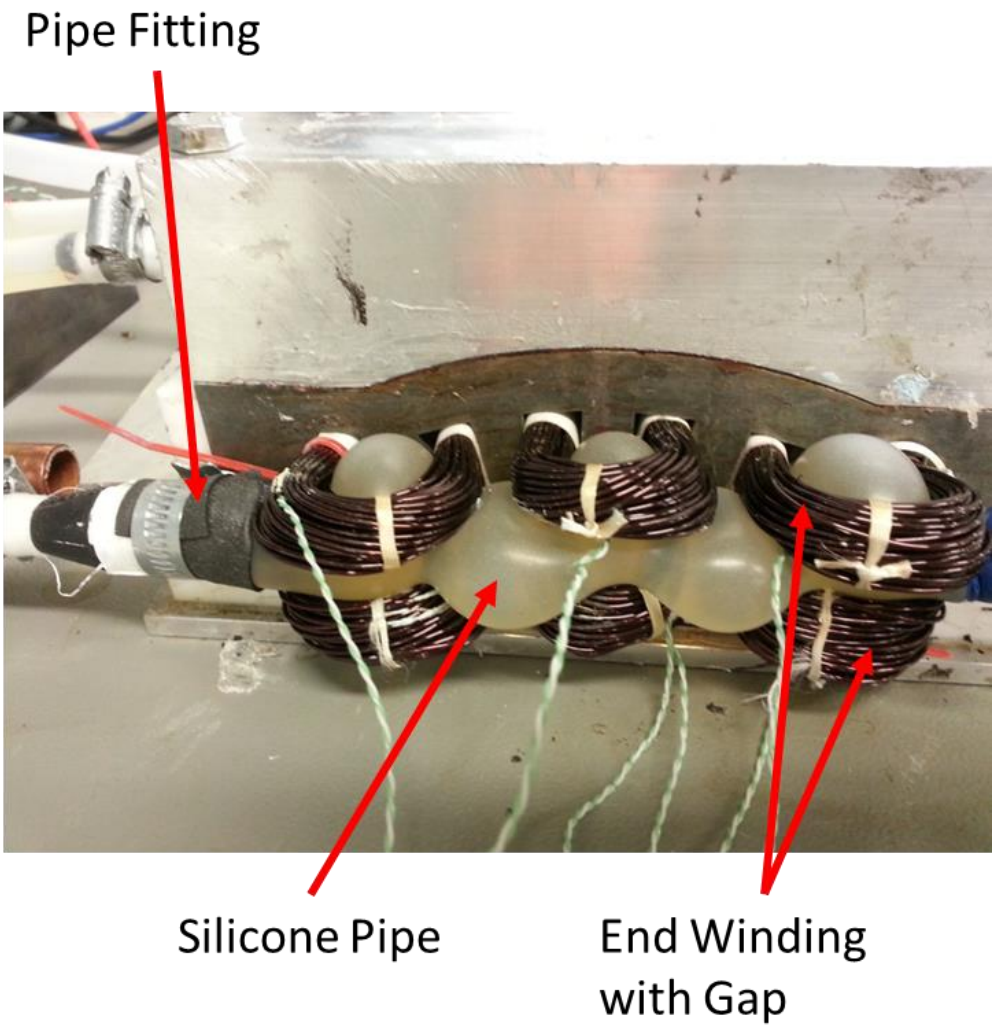


Figure 6.17 - Pipe expanding within the modified end windings

It is obvious from Table 6.8 that this cooling method was extremely effective, even with the increase in copper losses. This was due to the pipe expanding with the pressure of the flowrate into the gaps between the coils, as seen in Figure 6.17; this gave a massive increase in contact surface area when compared to the same pipe on traditional windings.

6.4.3 Comparisons

Multiple cooling methods have been tested. A comparison of the cooling potential, cost and complexity of these methods is given in Figure 6.18. While the temperature reduction and additional cost are quantitative values, the complexity is a relative comparison between the methods on a score out of 10.

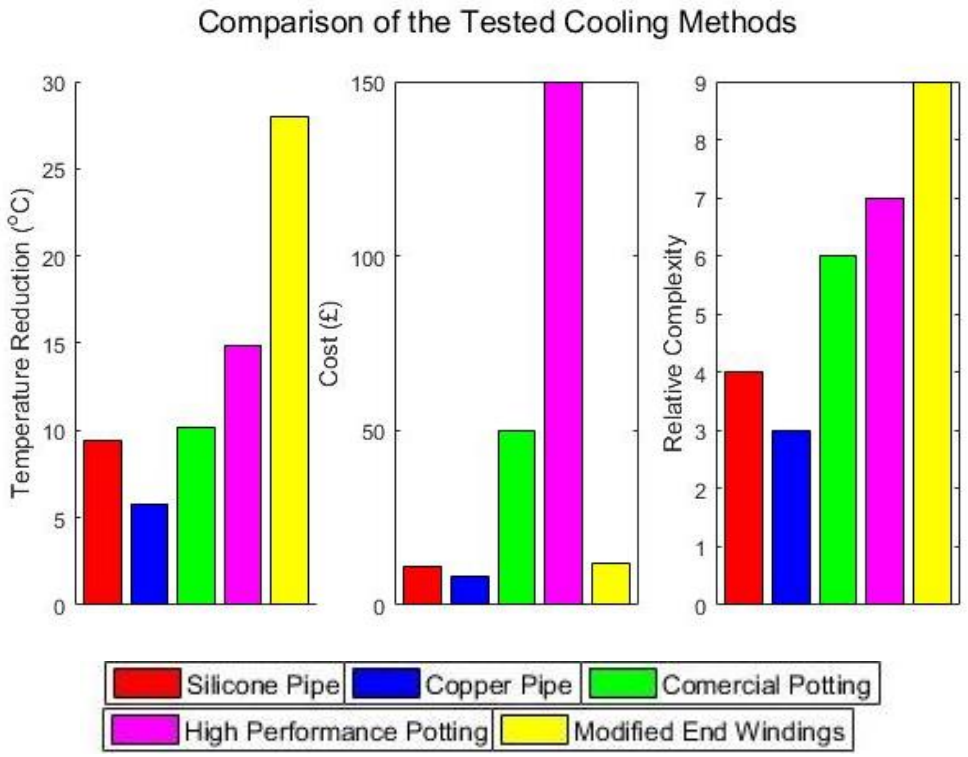


Figure 6.18 - Temperature reduction, cost and relative complexity of the cooling methods

When using a traditional end winding and no potting compound, the silicone pipe gave a higher reduction than the copper pipe for a similar cost and complexity. Of note is that the larger temperature reductions from the plastic pipe were at a lower baseline temperature. This means it is likely the reduction would be even greater at 180°C, and the next sections aimed to show what is

achievable. Also shown during these tests was that, as would be expected, without impregnating the windings the thermal conduction through them was poor and any cooling was very localised.

The potting compound results showed a slight improvement in the temperature reduction than that for the plastic pipe. However this came with the added requirement of having to cure the compound in a mould, usually for 24 hours, during assembly. This added time and complexity to the construction of the cooling system. How effective the cooling is depended on the thermal conductivity of the compound which is related to the cost. This was not a linear increase, materials with double or triple the conductivity typically have a cost an order of magnitude higher, as can be seen comparing the two potting compounds in Figure 6.18.

The cooling method which showed the most promise was the silicone pipe with the modified end windings. This was also one of the cheaper methods. The main disadvantage came from the limitation in the winding. Unless an innovative method is discovered for a distributed winding, this idea is only applicable to concentrated wound machines. Creating this gap in the end windings also increased the end winding length and the complexity of the winding process, reducing the slot fill factor.

6.5 Calibration of thermal networks

As stated earlier, the aim of the dummy stator experiments was to use the results to validate the thermal networks. This was accomplished by producing a thermal network that matched the dummy stator. The majority of the required parameters (lengths, areas, conductivities) could be measured from the dummy stator or found from look up tables online [127]. There were some remaining parameters that were uncertain, such as slot conductivity, junction resistances and, most critically, contact area between pipes and end windings.

6.5.1 Dummy stator thermal model

Because the dummy stator had only 6 slots and was approximately cuboid shaped instead of a full cylinder, symmetry could not be used to simplify the design, and so a more complex thermal model was constructed, Appendix C, Figure C.6 to Figure C.9. The full model was not just a slice of the active material but also included the end winding connections between the slots, as well as the thermal path ways between the different end winding layers.

At this stage this thermal network had the same uncertain parameters as were present in the full model. The results from the experiment were then used to calibrate these parameters.

6.5.2 Optimisation

The method used for calibrating these uncertain parameters was to input reasonable values for them into the thermal network and find the difference between the simulated results and the experimental temperatures. Minimising this difference would give the correct values for these unknown factors. The variables of this optimisation were the previously stated uncertain variables, which were detailed for each cooling layout, with constraints keeping them within a feasible range. For example, the contact area between the pipe and the end winding could not be higher than the smaller of half the surface area of the pipe and the applicable surface area of the end windings. The objective function to be minimised was the sum of the difference between the simulated and experimental temperature for multiple comparison points across a range of tests at different current values. The optimisation compared the results across the whole time range, but it was weighted to give extra consideration towards the steady state value, as this was the most critical point to match.

As with the testing, each cooling layout was separated, so to begin with the no cooling model was validated and then the cooling method was altered and validated in steps. Both genetic algorithm and pattern search optimisation methods were used. Two different methods were used to ensure the global

optimum was found. Pattern search was used because it is simple to understand and follow the optimisation process, this meant it could be easily monitored to ensure the optimum is found. Genetic algorithm was also chosen because with the added randomness of the mutations and a large enough population in each generation, it ensured that any global minima were not missed, as pattern search occasionally resulted in a local minimum.

It was clear during these optimisations of the uncertain variables that the more effective the cooling the easier it was to minimise the difference. This was due to the complexity of natural air convection coefficients, particularly with the open stator faces and end windings having irregular shapes. While convection was obviously relevant to the cooling from the additional pipes, the contact conduction was much more critical.

The results from the calibration of the thermal models are given in Appendix E.

6.6 Application to a full machine

The uncertain parameters that have been validated could then be used in a thermal network modelling a full machine with the full array of losses. This gave an accurate representation of how much cooling would be possible during an actual machine's operation. For each cooling method a range of possible options are presented when applicable. The temperatures were calculated for a case study. The case study used was the previously designed distributed wound IPMSM machine for the FreedomCar 2020 targets. The input to the thermal model was the losses were calculated the peak torque operating point. The temperature reduction values shown are the difference from the model without end winding cooling.

6.6.1 Silicone pipe on the end winding surface

When implementing pipes, the goodness factor of both the end winding and pipe surface areas was considered, as shown in Table 6.9. These same goodness

factors were applied as an estimate for the goodness factors in a full machine. The contact area was then the goodness factor multiplied by the available surface area. The minimum of the calculated copper contact area and pipe surface area was used.

It can be seen that having the pipes and thermal paste as they were in the dummy stator experiments did not give a significant decrease in temperature. However as extra pipes are added and the thermal paste application was improved, a much more impressive reduction occurs.

Considering that for this model the water jacket, pipe fluid and ambient temperature were 105°C, the 22.7 °C decrease represents a 30% reduction in thermal increase.

Table 6.10 shows the different cooling available from three silicone pipe layouts. The differences were in the positioning of the pipes, the quantity of pipes and the quality and thickness of the thermal paste applied. While a wide range of combinations were possible, the three stages represented here were: a conservative level (using the exact values found from the dummy stator experiment), a realistic level (using slightly improved values that are still reasonable) and an ideal level (using the optimal possible values).

Table 6.9 – Comparison of experimentally achieved goodness factors

Amount of Pipes	**Single**	**Single**	**Double**	**Double**
Position	**Top**	**Side**	**Top**	**Side**
Total Possible Winding Area (mm^2)	400	475	400	475
Total possible Pipe Area (mm^2)	512	768	512	768
Found No Paste (NP) (mm^2)	300	385	183.9	111.6
Found with Paste (WP) (mm^2)	N/A	N/A	261.7	396.1
Goodness factor NP EW (%)	75	81.1	46	23.5
Goodness factor WP EW (%)	N/A	N/A	65.4	83.4
Goodness factor NP Pipe (%)	58.6	50.1	35.9	14.5
Goodness factor WP Pipe (%)	N/A	N/A	51.1	51.6

It can be seen that having the pipes and thermal paste as they were in the dummy stator experiments did not give a significant decrease in temperature. However as extra pipes are added and the thermal paste application was improved, a much more impressive reduction occurs.

Considering that for this model the water jacket, pipe fluid and ambient temperature were 105°C, the 22.7 °C decrease represents a 30% reduction in thermal increase.

Table 6.10 - Validated Plastic Pipe Simulation Results

Level	Conservative	Realistic	Ideal
Pipe Amount	Single	Double	Triple
Pipe Location on end windings	Side	Side and bottom	Top, side and bottom
Winding Contact Area Goodness Factor Side (%)	85	83	90
Winding Contact Area Goodness Factor Bottom (%)	-	65	75
Thermal Paste Conductivity (W/mK)	1	3	6
Thermal Paste Thickness (mm)	3.5	1.5	0.5
Temperature Slot (˚C)	169.5	155.7	150.9
Temperature End Winding (˚C)	175.2	157.7	151.5
Slot Reduction (˚C)	5.2	19	23.8
Slot Reduction (%)	7.5	27.3	34.1
End Winding Reduction (˚C)	5.2	22.7	28.9
End Winding Reduction (%)	6.9	30.1	45.2

While the dummy stator experiments showed good localised reductions but poor penetration of the cooling, in this simulation it was assumed the windings had been impregnated with a standard varnish, bringing the thermal conductivity from 0.41 W/mK to the range of 3 to 4 W/mK. While the reduction was still most prominent where the pipe is applied, this allowed for a better spread of this cooling benefit.

6.6.2 Copper pipe in potting compound

The results of both potting compound calibrated models were combined to create a single model. A similar method as with the plastic pipe model was used, where three possible levels of cooling were proposed. Here the differences were the thermal conductivity (and cost) of potting compound and the gap between the pipe and the end winding edge. The results for this are given in Table 6.11.

The effect of the thermal conductivity and distance between the end winding and pipe is shown in Table 6.11. Low conductivity values and large gaps showed a very small change in temperature, whilst improved compounds and small gaps give a significant reduction. Showing that this method of cooling could be very beneficial, but was heavily dependent upon the cost spent and precision of pipe placement and end winding regularity.

Table 6.11 - Validated potting compound simulation results

Level	Conservative	Realistic	Ideal
Potting Compound Conductivity (W/mK)	1.0	1.5	4.5
Distances between Pipe and End Winding (mm)	10	5	2
Temperature Slot (˚C)	165.7	159	151.4
Temperature End Winding (˚C)	166	156.5	145.6
Slot Reduction (˚C)	9.0	15.7	23.3
Slot Reduction (%)	12.9	22.5	33.4
End Winding Reduction (˚C)	14.4	23.9	34.8
End Winding Reduction (%)	19.1	31.7	46.2

Of note was another benefit of the potting compound, it added a significant thermal mass to the windings. While this did not affect the steady state temperatures it did affect how quickly it would be reached. This gave a benefit when the 18s peak torque is required, as the steady state was not reached during this short time.

6.6.3 Silicone pipe with modified end windings

The final method to apply to a simulated full machine was the silicone pipe in the modified end windings. This required a different electromagnetic design and thus different losses and starting temperatures to the previous two machines. Here the remaining uncertain variable was the increase in length in the end winding to allow for the gap and pipe. As well as what was mechanically possible when winding the machine, it was interesting to see which had a greater effect when increasing the length, a higher cooling due to the larger contact area, or the increase in copper losses. The results for this are shown in Table 6.12. The column showing no increase in end winding length was not a feasible option in reality, but gives an interesting comparative point.

From Table 6.12 a balancing point between the contact area and increase in losses is shown to be a 66% increase in the end winding length. However there was only a slight benefit over the 33% and this provided a smaller increase to the overall machine length.

Table 6.12 - Validated silicone pipe with modified end windings results

Increase in end winding length	None (0%)	Small (33%)	Medium (66%)	High (100%)
Temperature Slot (˚C)	146.4	145.6	145.4	145.4
Temperature End Winding (˚C)	153	151.1	150.9	151.5
Slot Reduction (˚C)	17.4	18.2	18.5	18.5
Slot Reduction (%)	29.6	31	31.5	31.5
End Winding Reduction (˚C)	27.4	29.3	29.5	28.9
End Winding Reduction (%)	36.3	38.9	39.1	38.3

6.6.4 Comparison

The reductions from a silicone pipe with modified end windings were even higher than three silicone pipes completely covering the surface of the end windings. The method with the modified end windings gave more cooling for a lower cost and pipe network complexity than pipes on the surface. However it had restrictions in winding topologies it can be applied to, mainly that it can only be used with concentrated designs.

The amount of cooling provided by a copper pipe in potting compound was very dependent on the potting material used. When standard compounds were used the silicone pipe with modified end windings was superior. However if very high performance compounds were used then this is the optimal cooling method, although the least cost effective.

The decision on which to use for an application would come down to cost limits, whether the winding has already been created or if a distributed winding is a requirement, and how much additional cooling is actually desired.

6.7 Conclusion

The improved cooling presented here allowed for a simple addition to the machine design to give a significant reduction in the maximum winding temperature.

Initially the idea of cooling the end windings with pipes was described, discussing the different materials usable for the pipe. Next initial simulations were performed, which led to the need to do experimental tests to verify the simulations. These tests were performed on a dummy stator, using DC currents to increase the temperature. The dummy stator tests showed that the improved contact area achievable by the plastic pipe (9.4°C reduction) was more beneficial than the higher thermal conductivity of the copper pipe (5.8°C reduction), but that using a copper pipe in a potting compound was superior to this (14.9°C reduction). It was also shown that modifying the end windings to increase the contact area was hugely beneficial, giving a 40.7°C temperature reduction in the end windings. The results from the dummy stator tests were then used to fine tune thermal models, matching the simulated results with the experimental results. The improved models then were simulated with the losses associated with a full machine.

The results from using the improved models showed that a realistic value for the achievable reduction in end winding temperature rise was 30% with a standard distributed winding or 40% with the modified concentrated.

A key area of interest when applying these methods to full machines was how much extra current density and torque this allowed for, presented in Table 6.13.

Table 6.13 - Potential increase in current density and torque with the new thermal limits

Winding	Cooling	Current Density		Torque	
		Value (A/mm^2)	Increase (%)	Value (Nm)	Increase (%)
Distributed	Standard WJ	11.4	N/A	94.6	N/A
	Two pipes on EW Surface	12.9	13.2	106.6	12.7
	Moderate Performance Potting Compound	13.7	20.2	113.2	19.7
Concentrated	Standard WJ	10.4	N/A	144.2	N/A
	Modified End Winding	12.8	23.1	175.4	21.6

What was seen with all these methods is a general saturation in the amount of cooling obtainable. A small reduction is easy to obtain, but when improving these methods further larger reductions become increasingly difficult.

It was decided that the potting compound method was most suitable for this application. It has already been shown that a distributed winding was the best option for the FreedomCar targets, so the pipe in a modified end winding was not feasible here. While the potting compound method and silicone pipe on the end winding surface gave similar temperature reductions, the benefit of the potting compound was the increased thermal mass for during the peak torque transient.

The improved cooling allowed for a higher current density to be applied before the thermal limits are reached. This gave more options in the design optimisation to allow for smaller slot areas or higher currents. And so, in the next chapter, further optimisation will be presented on the PMa-SynRelM design, with these less strict thermal limits, to allow it to meet the FreedomCar targets.

Chapter 7. Final Machine Design

7.1 Introduction

As well as the application of the improved thermal management the PMa-SynRelM design needed to be further optimised. There were several goals of this final optimisation, in descending order of importance:

1. Ensure the torque speed requirement could be met with the VA and thermal limit
2. Minimise the losses to reach the 95% efficiency requirement
    - Focusing on the high speed and rated speed operating points
3. Minimise the PM mass to minimise the cost

Based on the results shown in the previous chapters the design taken forward was a PMa-SynRelM 30 slot 10 pole distributed wound design.

7.2 Optimisation of PMa-SynRelM design

As a final step towards achieving the best design for the FreedomCar targets, optimisation procedures using genetic algorithms were incorporated into the machine design process.

7.2.1 Maximising reluctance torque

To use the minimal amount of PM mass and obtain the maximum torque per Amp, the reluctance torque must be maximised. Reducing the PM mass reduces the material cost of the design significantly. Increasing the torque per Amp reduces current requirements, in turn reducing the copper losses, which always play a significant role in respecting the thermal limits of the machine.

To achieve this goal, the objective function of the optimisation algorithm was maximisation of torque performance in a rotor with zero PM mass. The considered variables for optimisation are shown in Figure 7.1, $\alpha 1$ to $\alpha 3$ are the angles to the tip of each air barrier and $b1$ to $b3$ are the thickness of each barrier. This gave 6 parameters to be optimised. In parallel to this, analytical mechanical

constraints were implemented to ensure the rotor could withstand the stresses at high speed. Figure 7.2 and Figure 7.3 show the results from this optimisation.

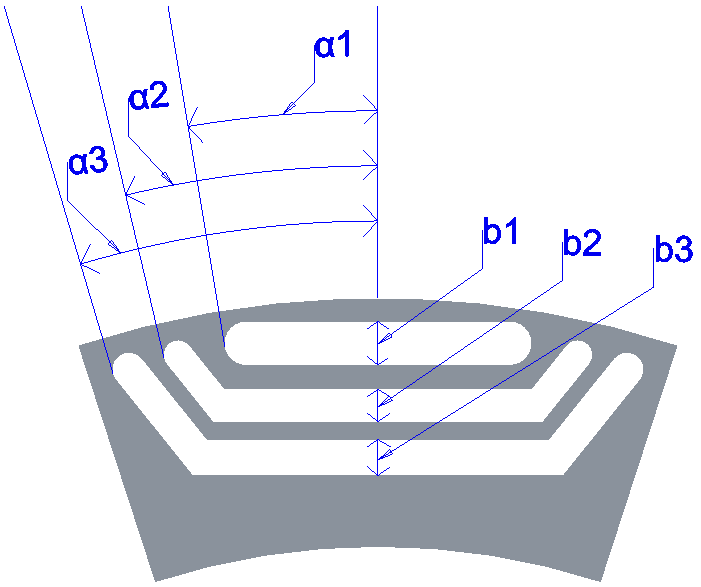


Figure 7.1 – PMa-SynRelM rotor geometry parameters

In Figure 7.2 it can be seen that as a general rule the reluctance torque increased with cumulative barrier thickness and total arc span, excluding a small trough that appears at 10 mm thickness. However when both values were at their maximum geometrical limit, this resulted in very narrow paths along the rotor q-axis, thus saturating the rotor flux paths and reducing the torque, giving a drop in the graph when both of these values are high. The maximum torque here was achieved with the maximum combined barrier thickness, 12mm and a total span of 14°.

The combined barrier thickness shown in Figure 7.2 had to be distributed between the three air gaps in an optimal ratio, the search for this is shown in Figure 7.3. A distinct ridge of maximum torque is presented in Figure 7.3, showing a range of ratios that complemented one another, with the peak of this being a ratio of 1:0.5:0.8 (*b1:b2:b3*).

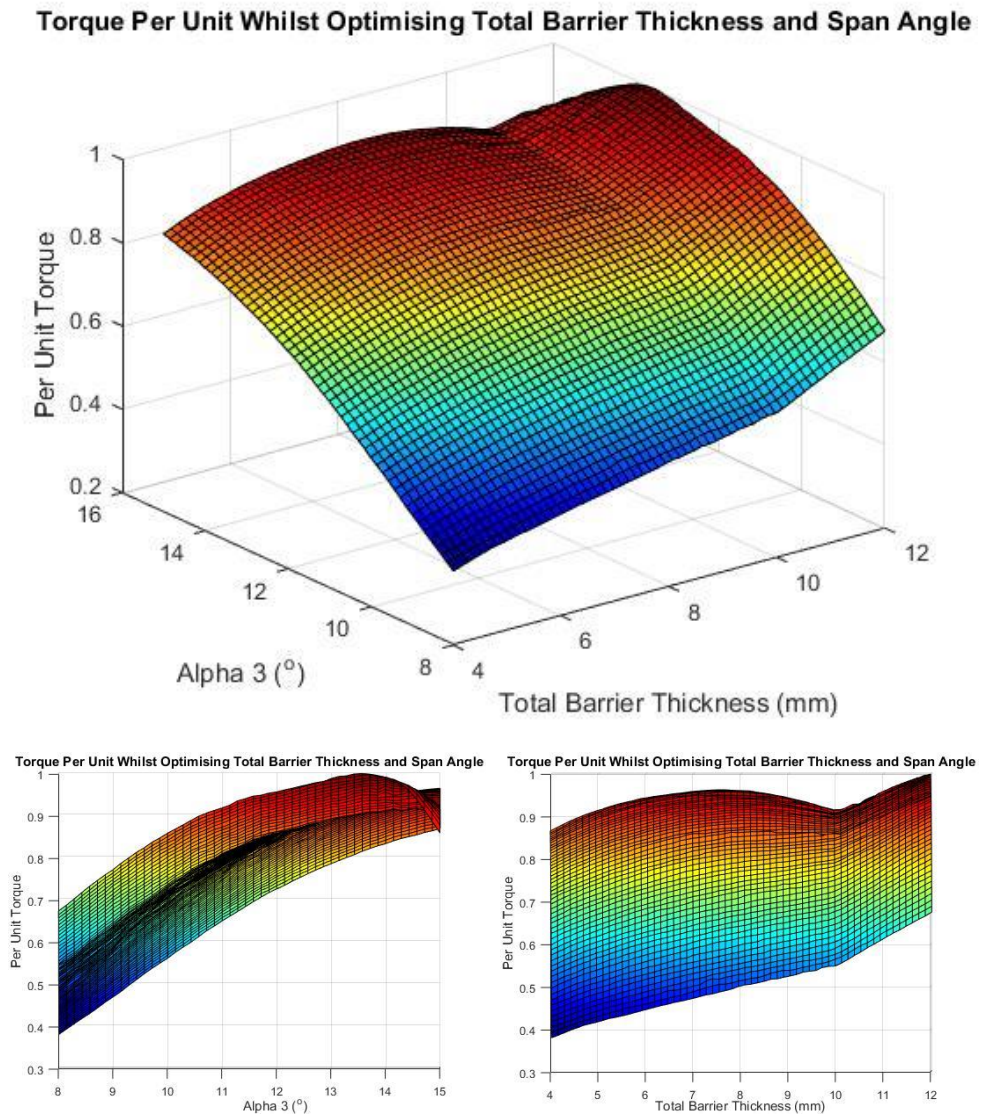


Figure 7.2 - Reluctance torque based on total barrier angle and cumulative barrier thickness

7.2.2 Minimising magnet mass

In order to keep the lowest value possible in terms of NdFeB mass, the PMs were only added to the top barrier in such a manner as to fill the gap in the radial and axial directions as shown in Figure 7.4. With this consideration, the optimisation process could be focused on increasing the magnet span until the optimal value of PM mass against current requirements was found. For each magnet span the temperature was compared to the thermal limit of the winding insulation (180°C) [99].

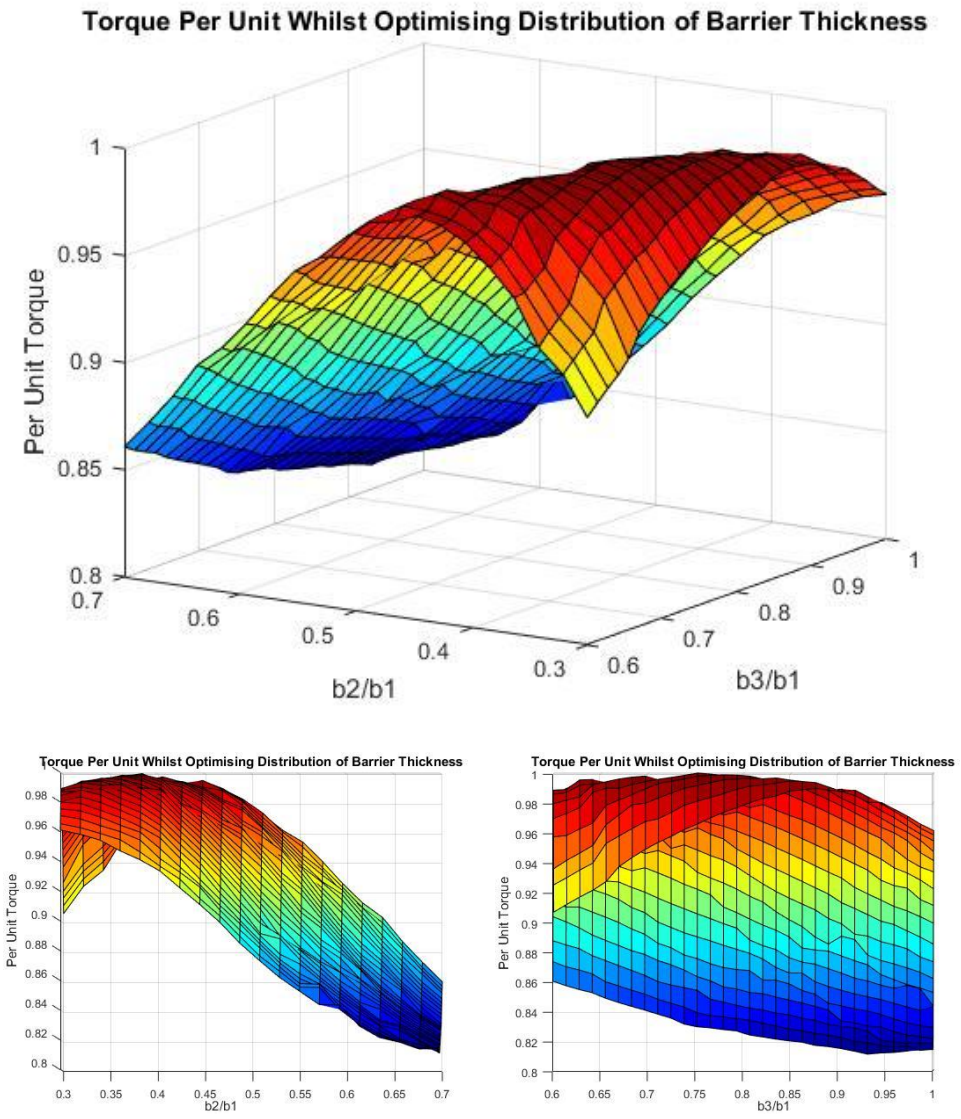


Figure 7.3 – Reluctance torque based on the distribution of total barrier thickness between the three barriers.

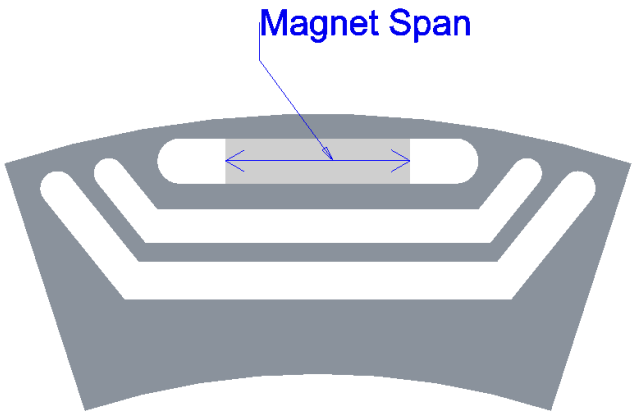


Figure 7.4 – Rotor geometry with added PM.

The results from this optimisation are represented in Figure 7.5, showing that the minimum magnet span percent was within both the current and thermal limit from just below 80%. The greater of these, and thus the more critical, was the current requirement which was within the limit for a magnet span greater than 79%.

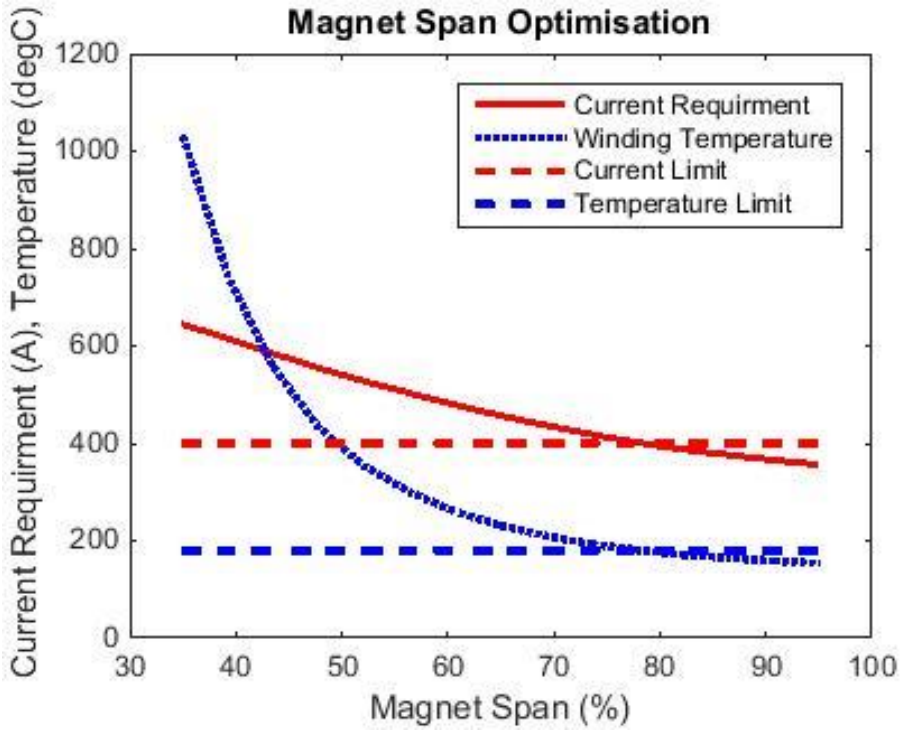


Figure 7.5 – Current and winding temperature for the feasible range of magnet spans

7.2.3 Minimising losses

In order to achieve the optimal efficiency characteristic, a genetic algorithm was used with a more complex objective function. The function minimised the losses at the high speed operating point, until the efficiency was greater than the 95% target. Once the high speed efficiency had been achieved, the function switched to minimising the losses at the peak torque operating point.

The variables for this were based around the tooth and slot shape shown in Figure 7.6. A fixed area (one slot pitch) was shared between each tooth and slot. Larger iron areas gave lower iron losses while larger copper areas resulted in lower copper losses. Slot width and depth, along with tooth tip shape and yoke thickness were adjusted to balance these losses. Constraints were used to

ensure that the required torque values were met; with the VA and thermal limit not exceeded.

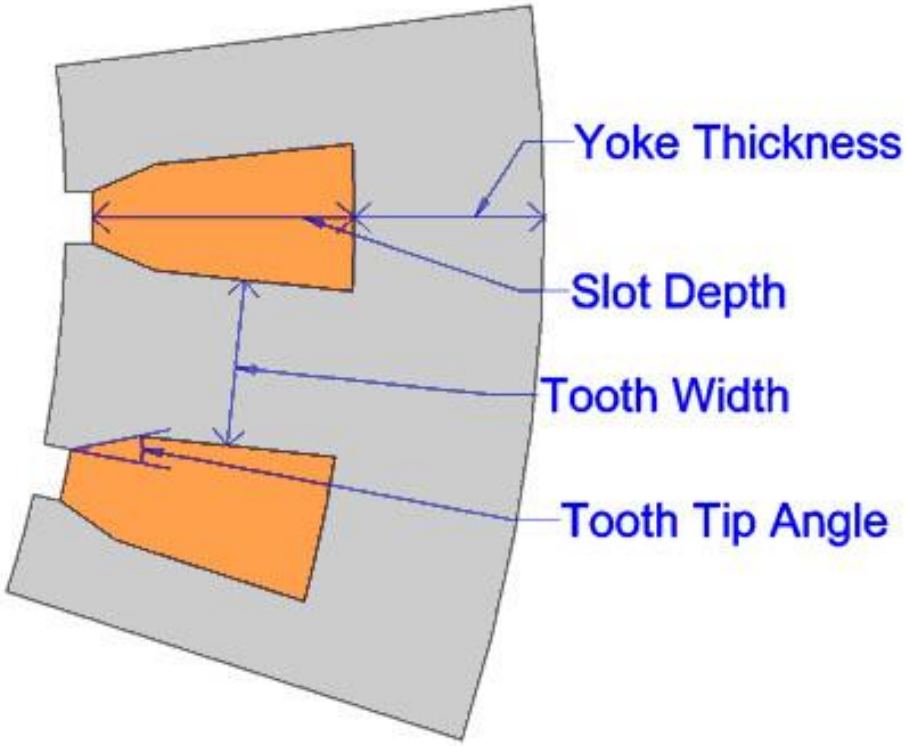


Figure 7.6 – Stator geometry parameters

Figure 7.7 to Figure 7.12 show the results for this optimisation. For both maximum speed and rated speed, the copper losses, stator iron losses and total losses (combination of the previous two, and rotor iron losses and PM losses) are displayed in surface plots, with additional angles to provide pseudo 2D plots.

At rated speed, Figure 7.7 shows that copper losses decreased with increasing slot area, either via larger slot depth or smaller tooth width. The relationship with slot depth can be seen as linear, while tooth width appeared to be more quadratic. At very small tooth widths the copper losses actually started to increase, this was due to the iron area saturating and higher currents being required to meet the rated torque.

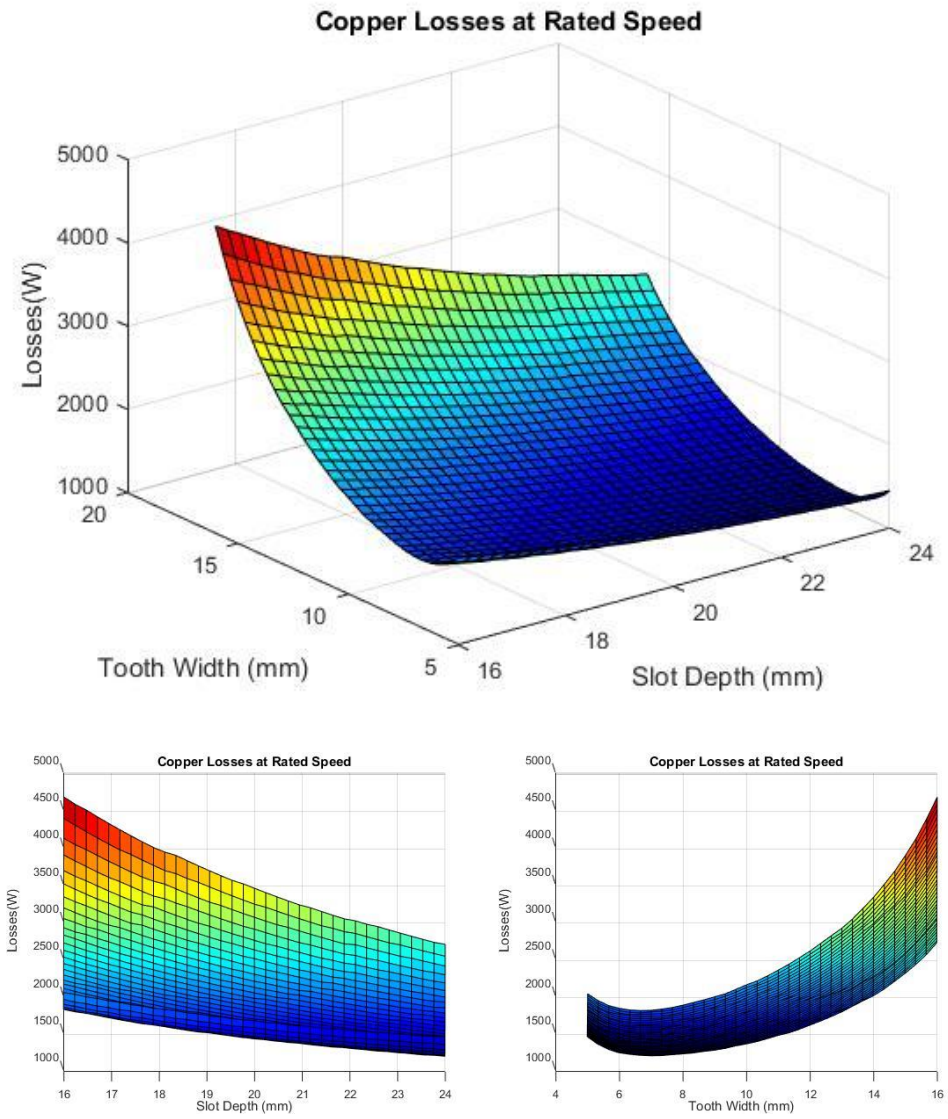


Figure 7.7 - Variation in copper losses due to slot depth and tooth width at rated speed

The rated speed iron losses, Figure 7.8, followed a more complex relationship. While the correlation with slot depth was still linear, higher slot depth meant smaller yoke and thus higher iron losses, the link with tooth width was less clear. A decrease in iron losses between 8mm and 15mm could be seen, due to larger iron areas decreasing flux density. Below 8mm the iron losses decreased due to the teeth saturating, while this was bad from a torque production point of view, it meant the flux density was constant in a decreasing iron mass, and iron losses are proportional to the iron mass as well as flux density. At the high end of tooth width, >15 mm, again an increase was seen, because of the increase

in mass of the tooth section outweighing the decrease in flux density in the iron loss equation.

Figure 7.9 gives the total losses at rated speed, it can be seen from this (and the scales on the previous two figures) that at rated speed the copper losses were dominant. Thus the total losses followed the same patterns as the copper losses, albeit with a more significant increase with low tooth width values.

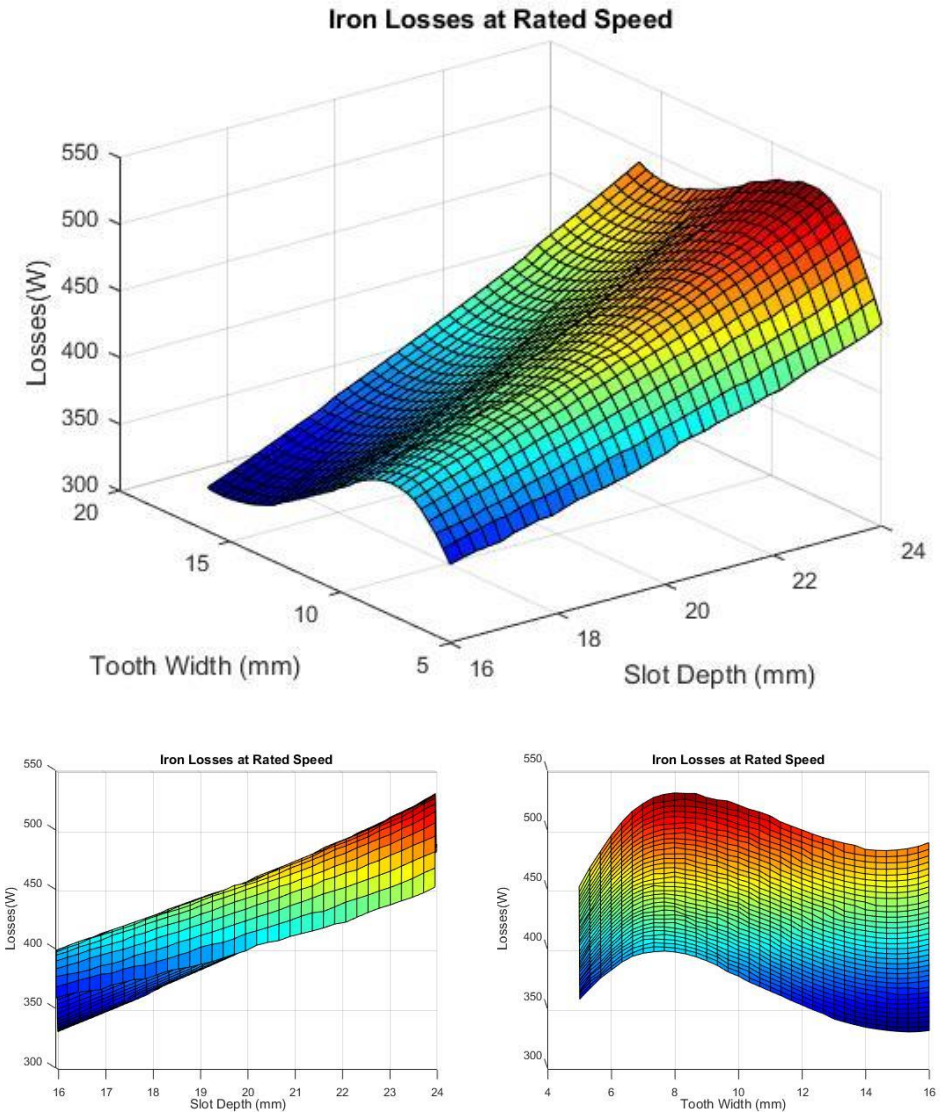


Figure 7.8 - Variation in iron losses due to slot depth and tooth width at rated speed

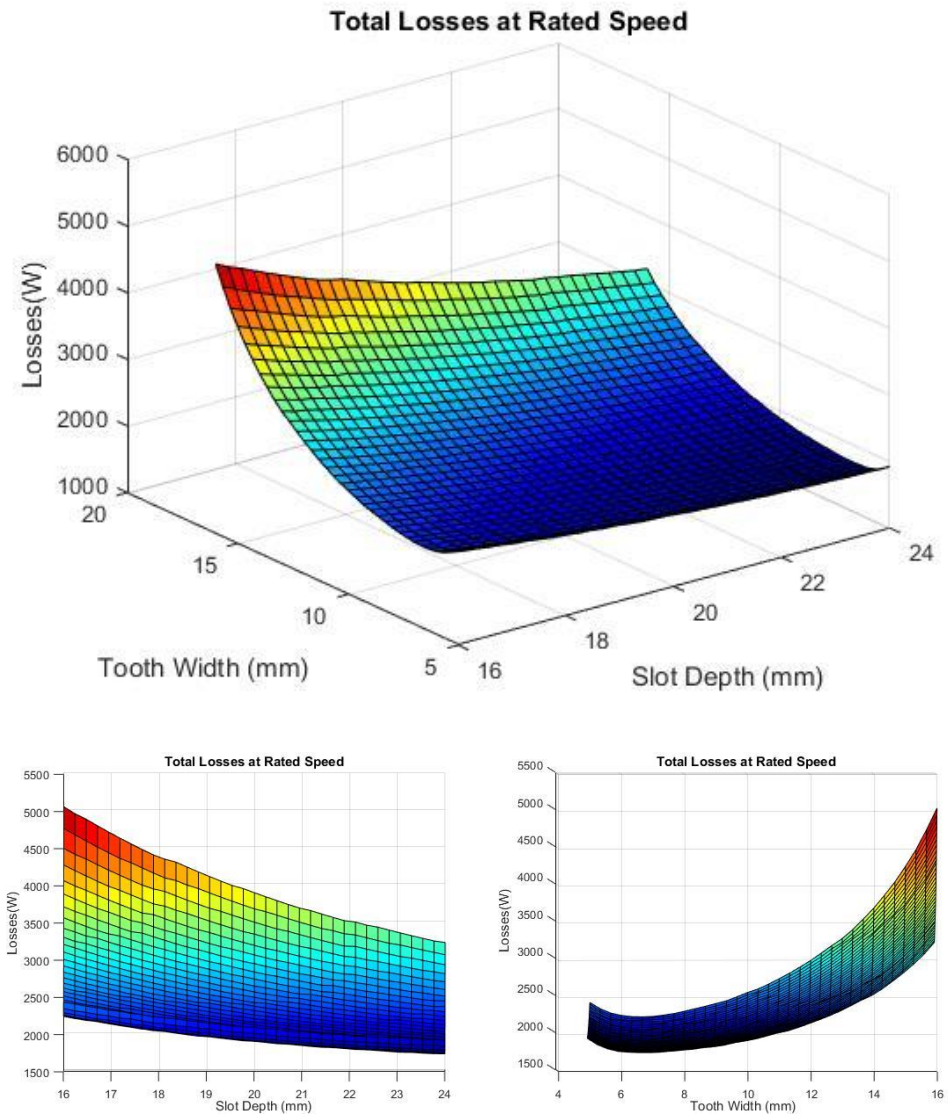


Figure 7.9 - Variation in total losses due to slot depth and tooth width at rated speed

At high speed the same relationship with copper losses increasing with increasing tooth width (decreasing slot width) is seen, Figure 7.10, however the change with slot depth showed some spikes, although the general trend of decreasing with increasing slot depth was still there. These spikes were the points where an extra layer of windings had been added to the slot. While extra layers allow for more conductors per turn reducing the DC resistance of the winding, this increased the proximity losses, which were a larger factor at high speed. However it can be seen that this effect was only prominent at large tooth widths, which were unlikely to be selected due to the high copper losses at rated speed, Figure 7.7.

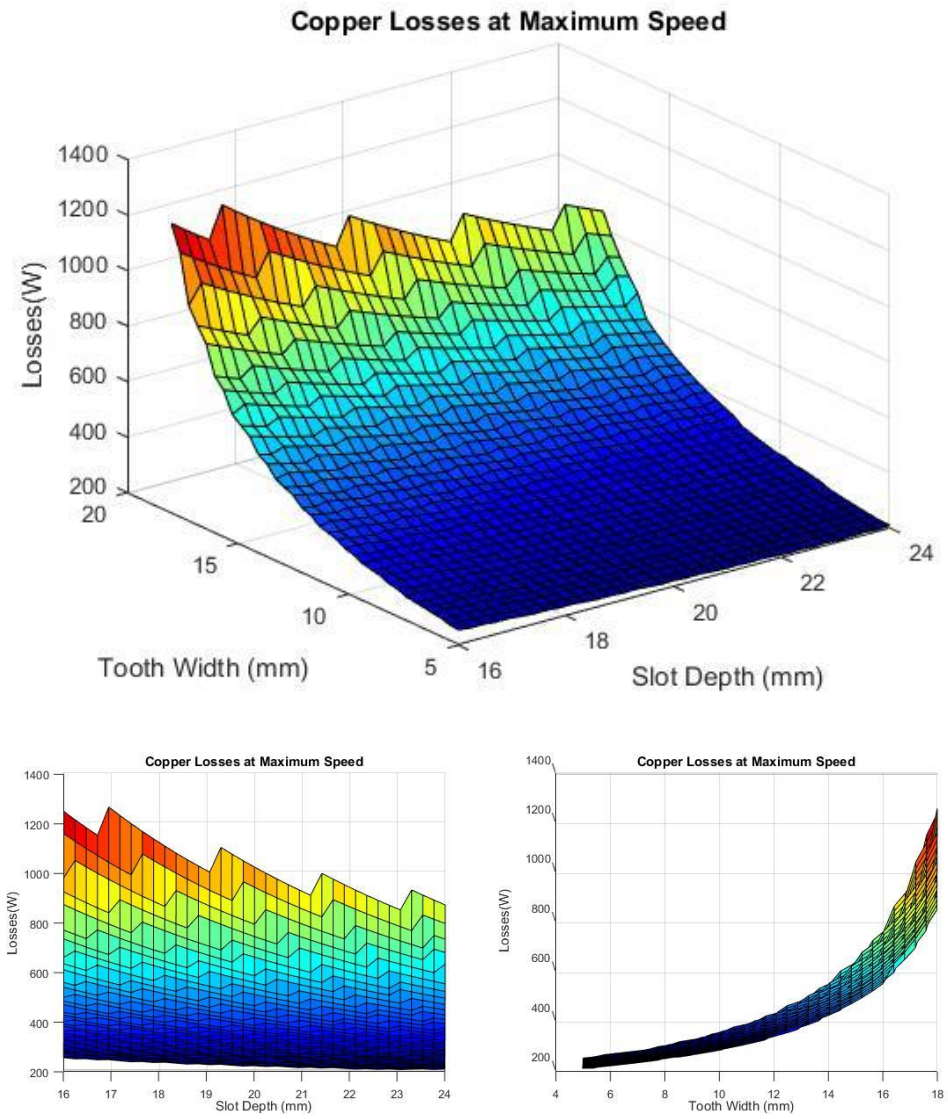


Figure 7.10 - Variation in copper losses due to slot depth and tooth width at maximum speed

The iron losses at high speed, Figure 7.11, followed the expected result of increasing with reduced iron areas. With the frequency being much higher at this speed, the iron losses were significantly larger. This was noticeable in the total loss at maximum speed, Figure 7.12, which follows the trend of the iron losses for the most part, except when tooth widths were high (high copper loss, low iron loss).

7.3 Final design geometry

The final geometry is shown in Figure 7.13, with the general sizing parameters in Table 7.1. The overall sizing parameters such as rotor and stator parameters,

stack length and air gap size were fixed before the above optimisation process by the work done in Chapter 3. To ensure the optimal value for each of these had not changed, each was varied and re-simulated.

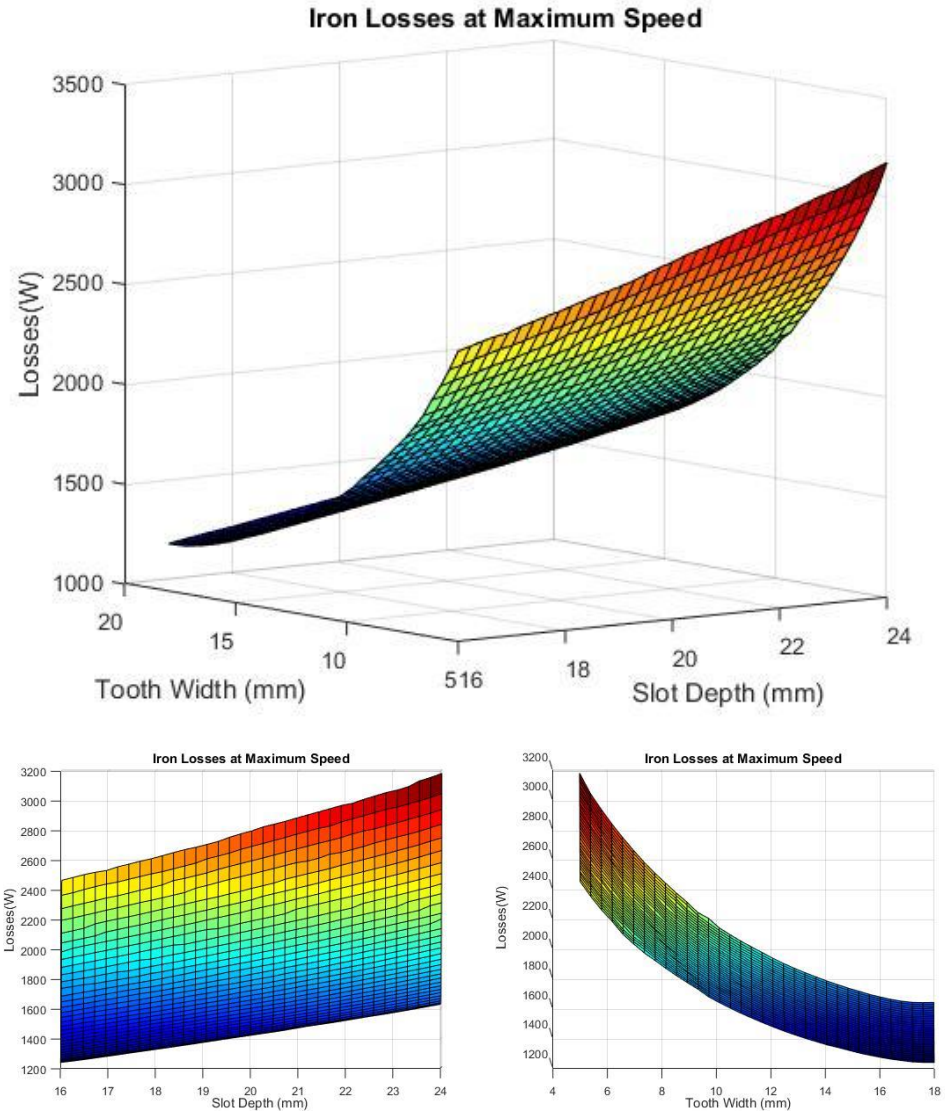


Figure 7.11 - Variation in iron losses due to slot depth and tooth width at maximum speed

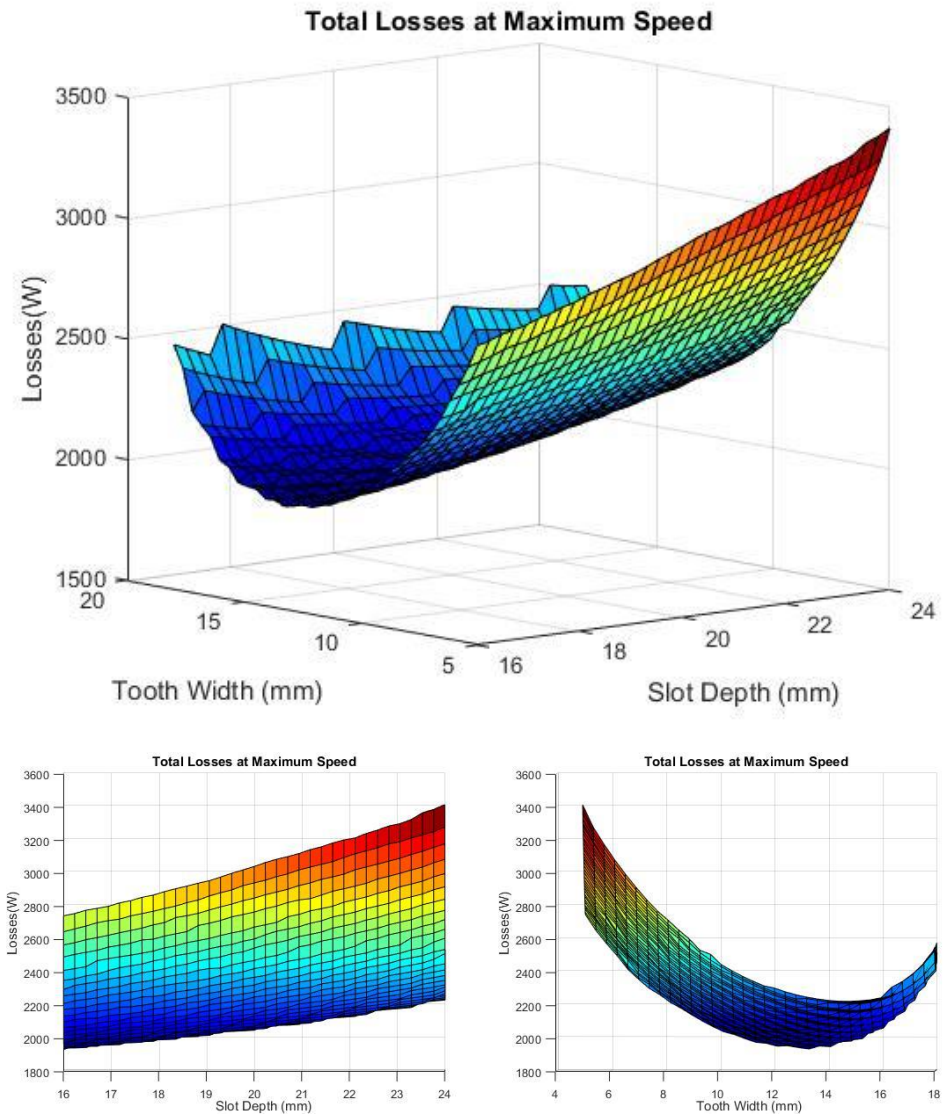


Figure 7.12 - Variation in total losses due to slot depth and tooth width at maximum speed

When the air gap was made larger, the torque density decreased, when made smaller, the back EMF and high speed iron losses were too large. Smaller stack lengths required higher current densities which led to overheating, longer gave higher back EMFs and would require more machine mass. The stator outer diameter was at the maximum of the specs, decreasing this would either reduce slot area, increasing copper losses, or back iron area, increasing copper losses. The rotor diameter was the right level to balance torque per amp with increasing back EMF, which both increase with rotor diameter.

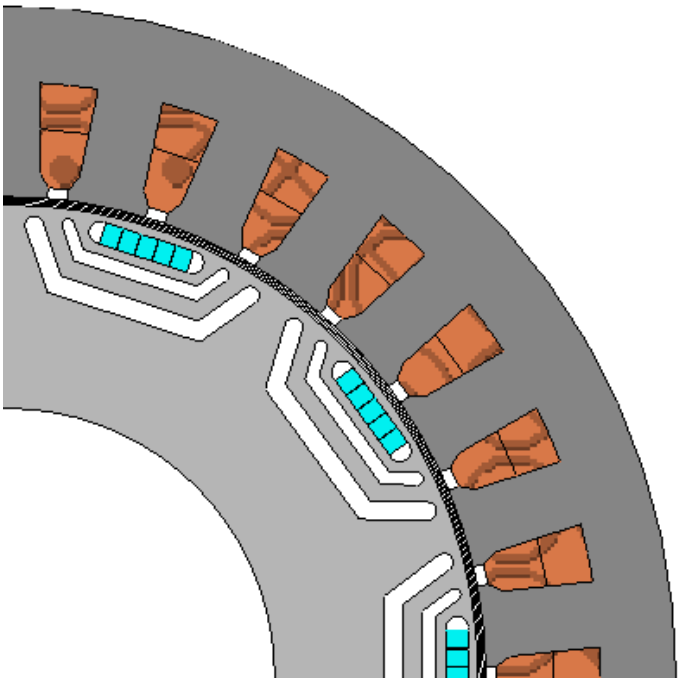


Figure 7.13 – Final machine geometry

Table 7.1- Final machine general parameters

Topology	PMa-SynRel
Slots	30
Poles	10
Winding Layout	Distributed, double layer
Active Length	130 mm
Stator Outer Diameter	250 mm
Stator Inner Diameter	179 mm
Air Gap Thickness	1.5 mm
Rotor Outer Diameter	176 mm
Rotor Inner Diameter	100 mm

7.3.1 Rotor geometry

The final rotor parameters are given in Table 7.2, detailing the materials used and shape of each barrier, the results were taken from the above optimisation process. HXT from Nippon Steel was used for the rotor design for its high tensile strength, decreasing the maximum bridge size (between the air gap and the barrier) before there are mechanical issues, allowing for the PMs to be placed closer to the air gap. NdFeB was used for the PM material for the reasons given in section 2.3.3.3, it has high remnant flux density and coercive force

without being as expensive as SmCo. The sizing and shaping of the barriers came from the optimisation in section 7.2.1.

The PM material filled the whole first barrier radially, the width of the PM was determined by the optimisation in section 7.2.2. This gave the minimal PM mass required whilst keeping the current low enough for the current and thermal limits at peak torque. The total PM mass was 0.79 kg, this was considerably lower than the 1.24 kg in the IPMSMs in section 4.5.4 and the 2kg + of the previous attempts in section 2.4. This reduction in PM mass would help to keep the costs low.

The rotor was skewed into 5 sections, with a 2.4° shift between each section. The goal of this was to reduce the torque ripple. This skewing can be seen in, Figure 7.14, where the rotor steel has been made partially transparent, showing the offset in the PMs in each layer.

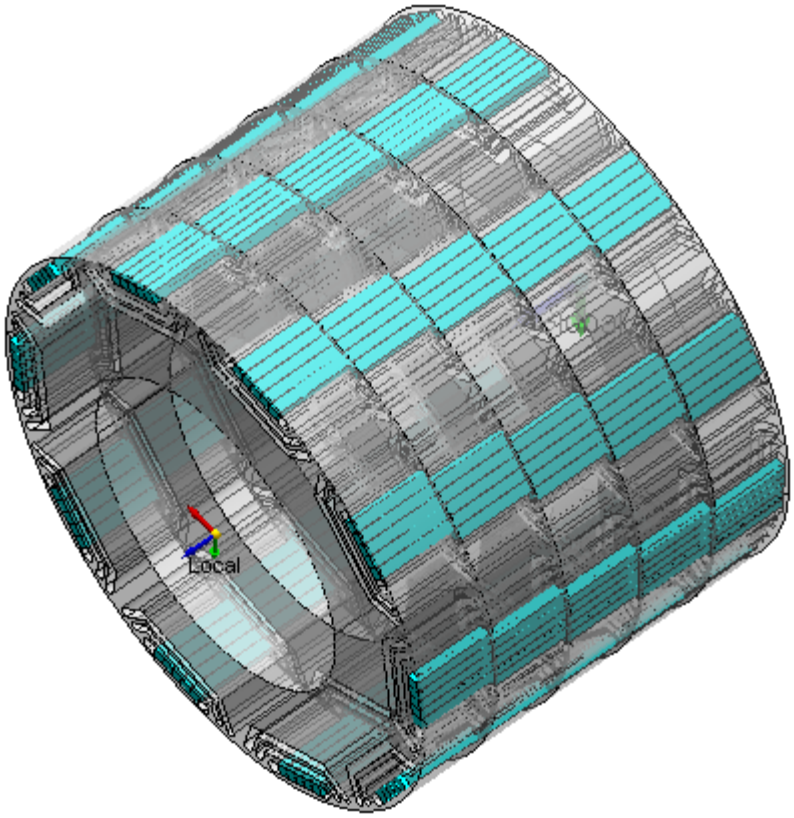


Figure 7.14 – Final machine rotor skew

Table 7.2 – Final machine rotor parameters

Rotor Material		HXT – Nippon Steel
PM Material		Neodymium Iron Boron: 32/16
Skew		5 slices totalling 12° shift
Rotor Barrier 1	Thickness	3.9 mm
	Depth on x axis	2.1 mm
	Span Arc	7.9°
	Width	15.9 mm
Rotor Barrier 2	Thickness	2.9mm
	Depth on x axis	8.3 mm
	Span Arc	12°
	Width	35.4 mm
Rotor Barrier 3	Thickness	3.3mm
	Depth on x axis	12.8 mm
	Span Arc	15°
	Width	44 mm
PM	Thickness	3.6mm
	Width	11.4mm
	Percent of Barrier 1 Flat Width	79 %
	Volume per Pole	$1.05 \times 10^{-5}\ m^3$
	Total Volume	$1.05 \times 10^{-4}\ m^3$
	Mass per Pole	0.08 kg
	Total Mass	0.79 kg

A check that had to be made with the rotor design is if it had sufficient mechanical strength to withstand the centrifugal forces from the PM mass during maximum speed rotation. The calculation process for this is shown in Eqn. 7.1 to Eqn. 7.4. Where r_R is the rotor radius, *RPM* is the max rotational speed in rpm, the area specified is the smallest bridge thickness to the outer barrier multiplied by the stack length and the yield point is specified by the material, 659 N/mm^2. A safety factor was included, to allow for both the possibility of inaccurate speed control during operation and discrepancies between analytical and experimental results. The safety factor value of 5 was provided by the industrial partner CGT as their standard for this.

$$Rotational\ Accelration = \frac{Peripherial\ Speed^2}{r_R} \quad \textbf{Eqn. 7.1}$$

$$= \frac{\left(2\pi \times r_R \times \frac{RPM}{60}\right)^2}{r_R}$$

$$= \frac{\left(2\pi \times 0.088 \times \frac{14000}{60}\right)^2}{0.088} = 189145\ m/s^2$$

$$Force = PM\ mass\ \times Rotational\ Acceleration = 0.08\ \times 189145 \quad \textbf{Eqn. 7.2}$$

$$= 15.1kN$$

$$Stress = \frac{Force}{Area} = \frac{15.1 \times 10^3}{0.001 \times 0.13} = 116.4M\ N/m^2 = 116.4\ N/mm^2 \quad \textbf{Eqn. 7.3}$$

$$Safety\ Factor = \frac{Yield\ Point}{Stress} = \frac{659}{116.4} = 5.66 \quad \textbf{Eqn. 7.4}$$

7.3.2 Stator geometry

The parameters for the geometrical design of the stator are given in Table 7.3, while the values for the winding are given in

Table 7.4. JNHF was used for the stator steel, again from Nippon Steel, due to its low loss profile, the windings were standard copper. The tooth width, slot depth (and thus slot width and yoke depth) were found from the optimisation in section 7.2.3. The slot opening was designed to minimise the torque ripple.

The number of turns is based on the balance between lowering current requirements whilst keeping high speed voltages from being excessive. The wire diameter and conductors per turn were chosen to keep the fill factor between 0.42 and 0.45, any higher would be difficult to achieve in practice, lower would increase copper losses and reduce thermal conductivity. The diameter and number of conductors were then varied to minimise the combination of the skin effect, more prominent in larger diameters, and the proximity effect, more prominent in higher numbers of conductors. The winding pattern is shown in Figure 7.15 and a more detailed section in Figure 7.16, this was the same winding layout as was determined to be optimal in Chapter 3.

Table 7.3 – Final machine stator parameters

Stator Material	JNHF – Nippon Steel
Tooth Shape	Parallel Tooth
Tooth Width	11.9mm
Tooth Tip Depth	2 mm
Tooth Width at Opening	14.9 mm
Slot Opening Width	3.75 mm
Slot Opening percent of Slot Pitch	20 %
Yoke Depth	16.7mm
Slot Width	9 mm
Slot Depth	17mm

Table 7.4 – Final machine Winding Parameters

Turns/phase	3
Conductors/turn	13
Wire Diameter	0.8128 mm (AWG 20)
Winding Throw	2
Slot Fill Factor	0.4254

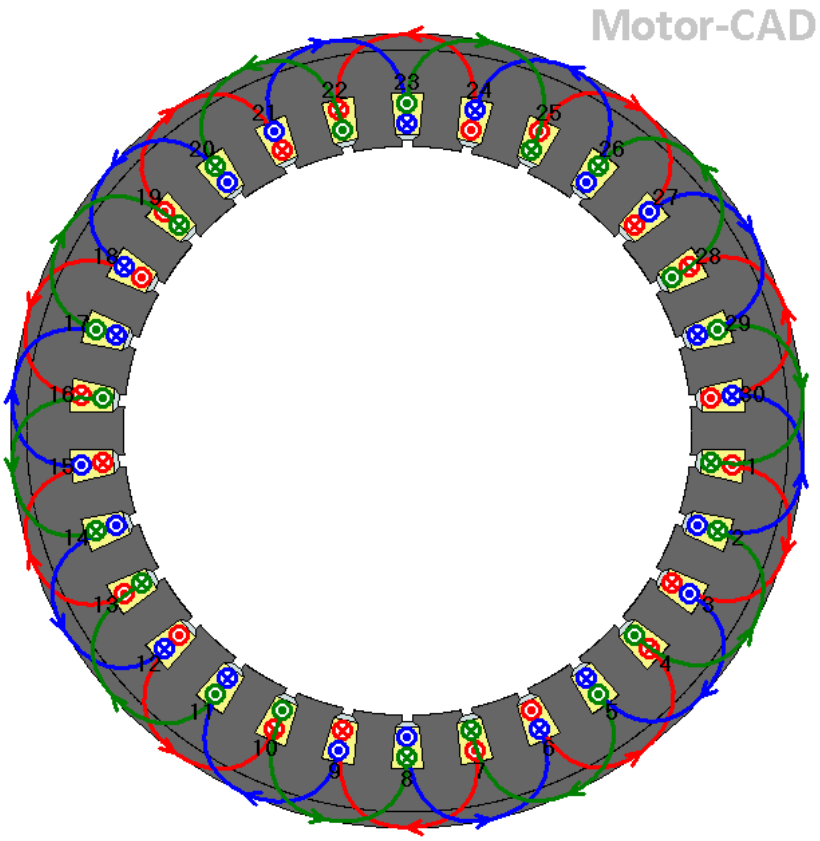


Figure 7.15 – Final machine winding pattern

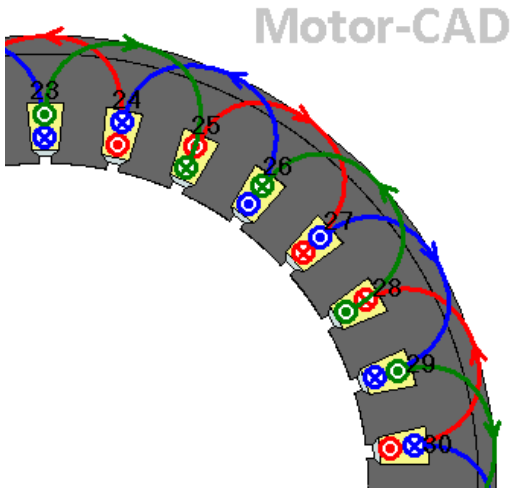


Figure 7.16 – Section of final machine winding pattern

7.4 Finite element results

The current and advance angle required to meet the rated torque, along with the losses these produced and the calculated efficiency from them are given in Table 7.5. The current, voltage and torque are then displayed in Figure 7.17, where the continuous lines are requirements to meet the rated torque with the crosses representing the requirements for the peak torque operating point. This shows the machine could meet the specified torque speed characteristic with the current and voltage supply limits. These results will be compared against the previous machines in the next section.

Table 7.5 – Operating table for final machine

Speed	I rms	Ang	T	Iron Loss Rotor	Iron Loss Stator	Copper Loss	Magnet Loss	Pout	Pin	Eff
rpm	A	Deg	Nm	W	W	W	W	kW	kW	%
1000	205.8	39	102.3	3.2	47.0	1222.7	1.1	10.7	12.0	89.4
2800	205.8	39	102.3	16.9	270.2	1248.2	7.2	30.0	31.5	95.1
4000	158.4	38	71.6	27.4	411.0	832.5	8.1	30.0	31.3	95.9
6000	115.3	34	47.7	41.6	642.8	508.9	6.8	30.0	31.2	96.2
8000	91.2	37	35.8	47.8	816.4	343.3	5.3	30.0	31.2	96.1
10000	78.8	45	28.6	53.6	998.2	280.4	6.2	30.0	31.3	95.7
14000	70.4	59	20.5	65.4	1292.8	227.9	6.9	30.0	31.6	95.0
2800	365.6	46	200.0	26.4	498.2	3939.7	22.7	58.6	63.1	92.9

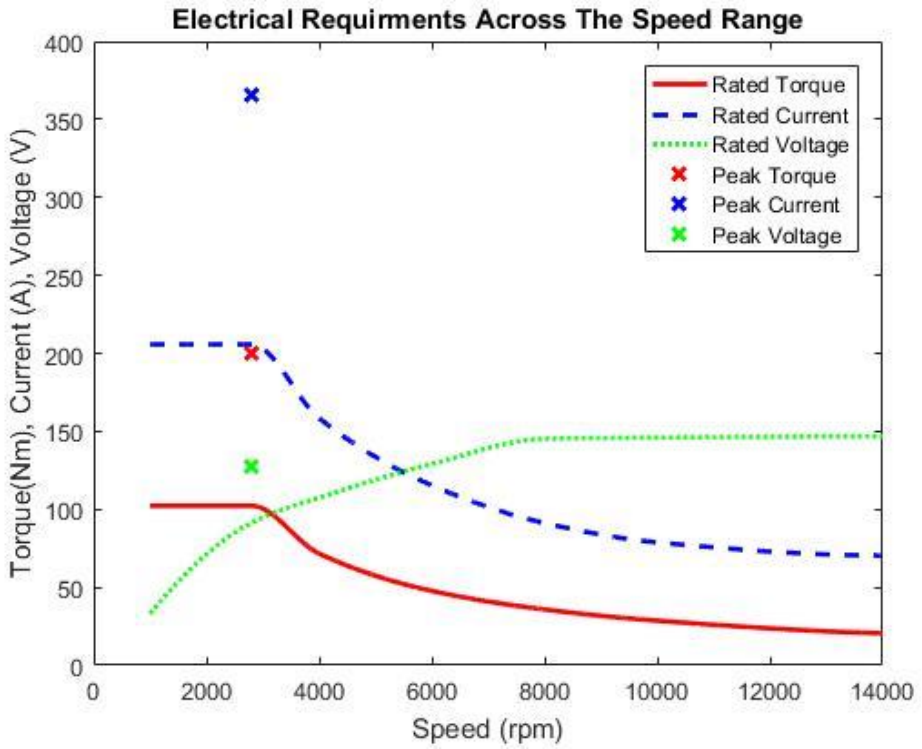


Figure 7.17 - Torque, current and voltage vs speed for the final machine

Figure 7.18, Figure 7.19 and Figure 7.20 show the instantaneous torque of one electrical cycle for the peak torque, rated torque at rated speed, and max speed operating points respectively. Each of these figures shows the contribution of each of the 5 skewed slices, as shown when discussing the rotor design, and then the summed value below. It can be seen that there was a larger ripple in the first millisecond, because of the sudden switch on of the current. In practice this would be ramped up and this would not be a major issue.

Table 7.6, Table 7.7 and Table 7.8 give the numerical values of the same results, displaying average torque values and ripple magnitudes. It can be seen that the percentage torques were very high without skew, however with the skewing implemented these were reduced significantly. The reduction was dramatic as, although the non-skewed ripple is large, it was very sinusoidal and thus easier to cancel. After skewing, each operating point was shown to be within the 5% torque ripple limit of the specifications. In each of the tables there is also the

skewed results ignoring the start-up ripple. Reducing torque ripple was not part of the optimisation, instead being countered by skewing the rotor. It would be of interest to reduce the torque ripple of each section so less skewing is needed.

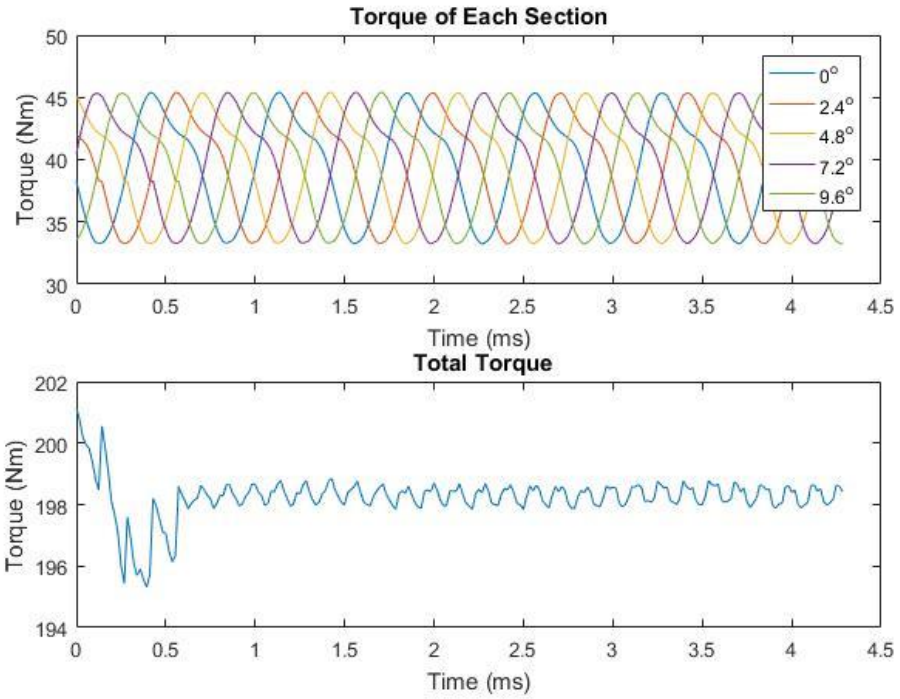


Figure 7.18 - Instantaneous skewed torque at peak torque, rated speed

Table 7.6 - Peak torque values

Value	Section	Skewed Total	Steady State Skewed Total
Mean Torque (Nm)	40	200.03	200.12
Minimum Torque (Nm)	33.57	197.12	199.64
Maximum Torque (Nm)	45.76	202.93	200.64
Pk to Pk Torque Ripple (Nm)	12.18	5.82	1.00
Pk to Pk Torque Ripple (%)	30.45	2.91	0.50

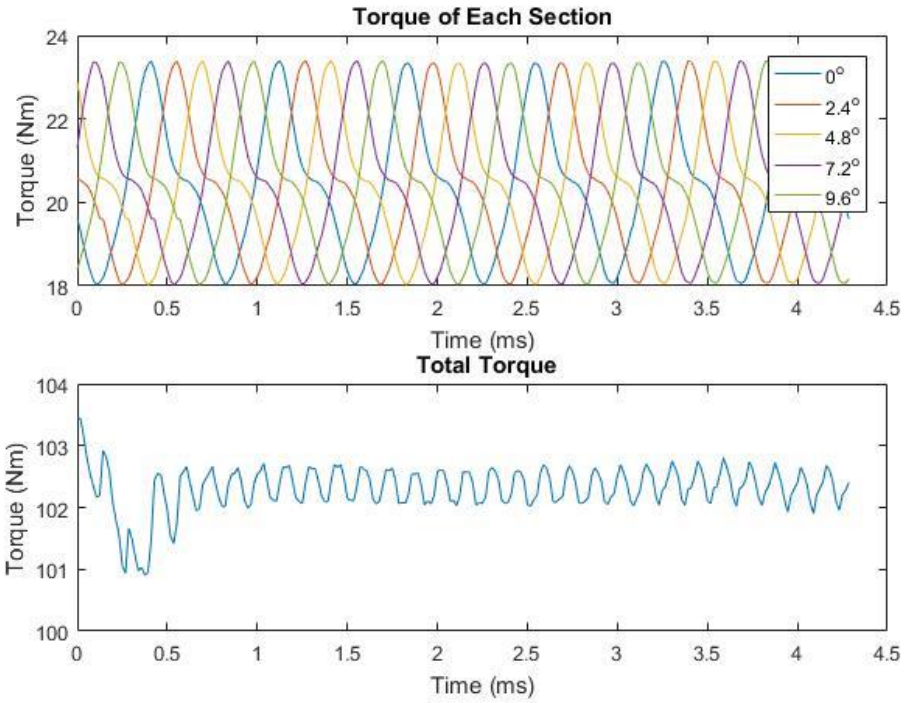


Figure 7.19 - Instantaneous skewed torque at rated torque, rated speed

Table 7.7 - Rated torque values

Value	Section	Skewed Total	Steady State Skewed Total
Mean Torque (Nm)	20.46	102.31	102.36
Minimum Torque (Nm)	18.02	100.91	101.9
Maximum Torque (Nm)	23.39	103.45	102.8
Pk to Pk Torque Ripple (Nm)	5.37	2.54	0.9
Pk to Pk Torque Ripple (%)	26.26	2.48	0.88

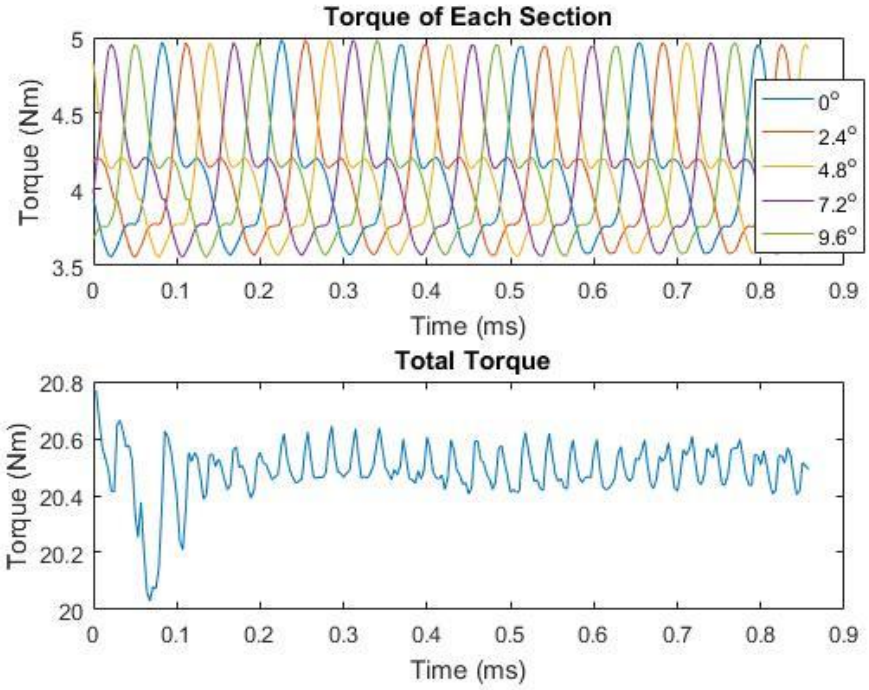


Figure 7.20 - Instantaneous skewed torque at rated torque, max speed

Table 7.8 – Max speed torque values

Value	Section	Skewed Total	Steady State Skewed Total
Mean Torque (Nm)	4.1	20.49	20.5
Minimum Torque (Nm)	3.56	20.03	20.39
Maximum Torque (Nm)	4.98	20.77	20.64
Pk to Pk Torque Ripple (Nm)	1.43	0.74	0.25
Pk to Pk Torque Ripple (%)	34.85	3.61	1.24

Figure 7.21 shows that except at very low speeds the efficiency was above the required 95%. The maximum efficiency is achieved at 6000rpm. From a loss perspective, this can be considered as the 'point of balance' between the higher copper losses at low speed and the higher iron losses at high speeds. The cross shown here is the efficiency at the peak torque operating point.

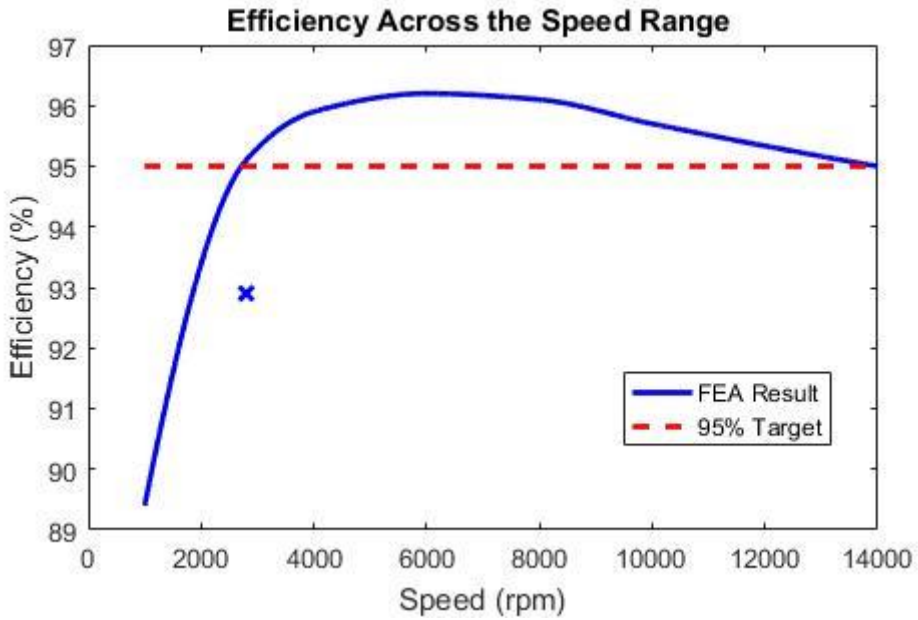


Figure 7.21 – Final machine efficiency vs speed

Figure 7.22 shows the thermal increase in the machine if only water jacket cooling was implemented, with Table 7.9 giving the key values from this. The simulation allowed for the machine to reach a steady state temperature using the rated torque losses, then the peak torque losses were inputted for 18 seconds, and finally the rated torque losses were inputted again for the temperatures to return to the steady state values. This was the 'worst case scenario' i.e. the machine has reached its maximum temperature from continuous operation before the peak torque was required.

From Figure 7.22 and Table 7.9 it can be seen that the slot winding and end winding both exceed the 180 ˚C limit even before the peak torque losses are applied. It is also shown that the winding temperature was much more susceptible to the additional losses than the stator. The stator had a higher thermal mass, restricting the change in temperature, and the iron losses are not as significantly increased as the copper losses are for the peak torque.

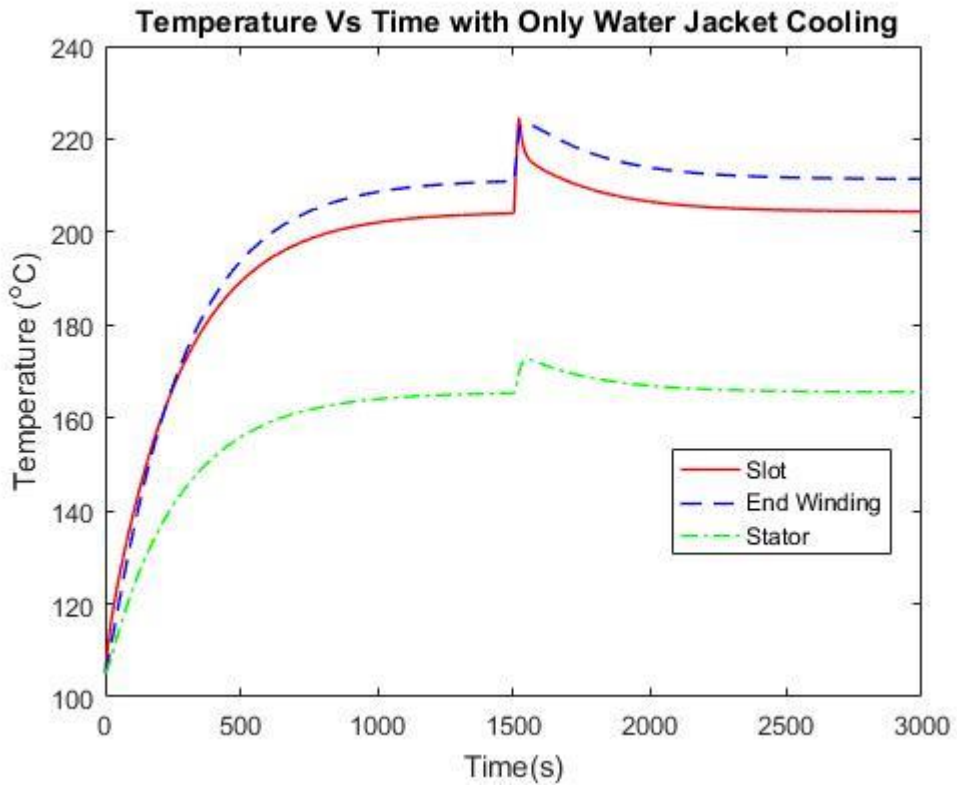


Figure 7.22 - Final machine thermal response with only water jacket cooling

Table 7.9 – Peak temperature based on machine location, with only water jacket cooling

Location	Steady state (˚C)	Peak (˚C)
Slot	204	224.6
End Winding	210.9	223.4
Stator	165.3	1725

Figure 7.23 and Table 7.10 show the same losses applied to the model with the additional pipe in a potting compound cooling. This thermal management method kept the temperatures within the winding limit, showing both the machine design and cooling arrangement were valid. Of note is that with the additional thermal mass of the potting compound, the end winding temperature was not as vulnerable to the increased loss spike, increasing less and ending below the slot temperature.

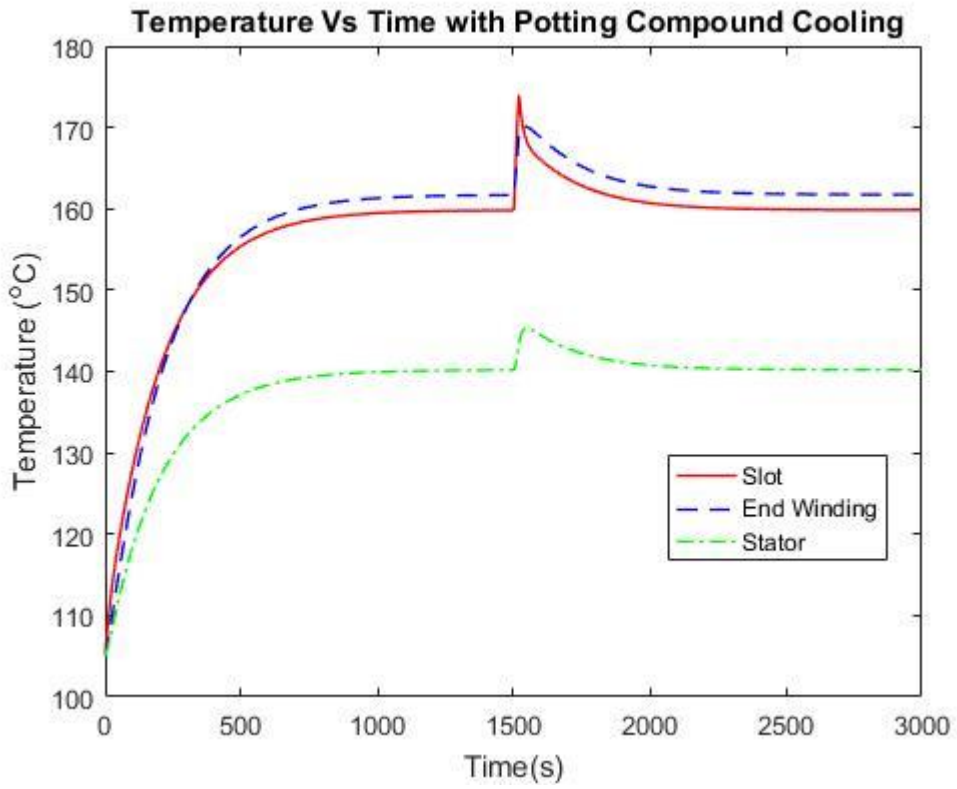


Figure 7.23 - Final machine thermal response with potting compound cooling

Table 7.10 – Peak temperature based on machine location, with only water jacket cooling

Location	Steady state (˚C)	Peak (˚C)
Slot	159.8	174
End Winding	161.7	170
Stator	140.2	145.3

7.4.1 3D Finite Element Results

Up until this stage only 2D FEA had been used. For improved accuracy three dimensional FEA was also employed. Due to the dramatic increase in solving time for 3D FEA only a few operating points were considered instead of the full speed range. The model used for the 3D FEA is given in Figure 7.24, with the rotor skewed as in Figure 7.14.

Figure 7.25 shows the waveform of the torque at rated speed and rated power for both the 3D and 2D FEA, the specific values for this are given in Table 7.11. It can be seen there is a slight drop in mean torque and increase in torque ripple from the skewed design. These changes are due to the interaction of the

different layers of the rotor skew which could not be modelled with 2D FEA methods.

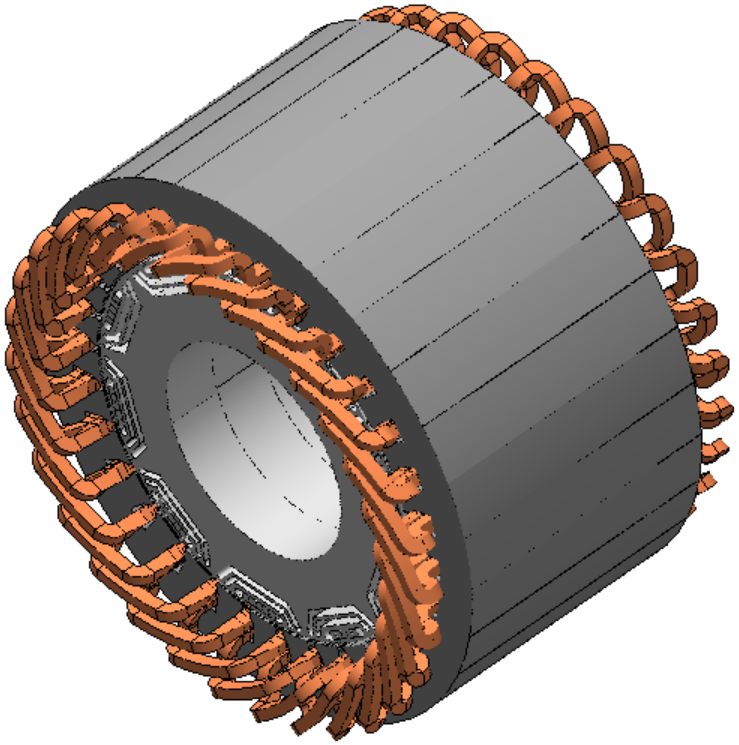


Figure 7.24 – 3D FEA Model

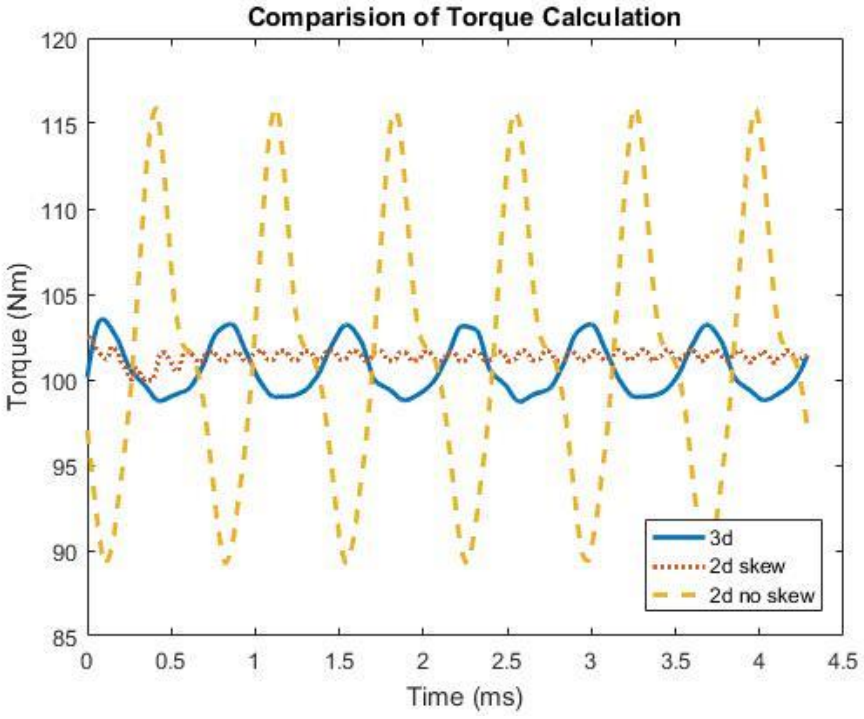


Figure 7.25 – 3D FEA Torque results for rated torque rated speed

Table 7.12 compares the losses between the 2D and 3D methods for the three key operating points. The difference in copper losses is due to the analytical estimation of the end winding length used for the 2D model is longer than the 3D model end winding. The iron losses were lower in the 3D model due to the 2D simulation assuming a fixed flux density through the axial length, which was higher than the average found during the 3D FEA.

Table 7.11 – Mean and ripple torque comparison of 2D and 3D FEA

Method	Target	2d No Skew	2d Skew	3d
Mean (Nm)	100	102.3	102.3	100.6
Ripple (%)	5	26.3	2.48	4.84

Table 7.12 – Loss comparison of 2D and 3D FEA

		2D	3D
Rated Power, Speed	Core Loss	287	263
	Copper Loss	1248	1160
Peak power	Core Loss	525	502
	Copper Loss	3940	3664
Max speed	Core Loss	1358	1298
	Copper Loss	228	212

7.5 Comparison to previous designs

From the previous section it appears that the new design is meeting all of the targets that the previous machine designs failed on. To investigate the differences in performance between the designs this section will compare the key operating characteristics between this final PMa-SynRelM design, the initial PMa-SynRelM design and the distributed wound IPMSM.

The current required to meet the torque speed characteristic for each machine is given in Figure 7.26. The final PMa-SynRelM design required a current value between the IPMSM and initial PMa-SynRelM design at low speed. At high speed, while the IPMSM required current significantly increases, both PMa-

SynRelM designs continued to decrease in current requirement with increasing speed. The IPMSM had larger PMs, so required lower current to meet high torques, but more current to field weaken at high speeds, this is shown in Figure 7.27, where the advance angle of the IPMSM was much higher at high speeds, but started lower at slow speeds. The final PMa-SynRelM had a similar trend in advance angle to the previous PMa-SynRelM, however the current requirement of the final design was lower across the whole speed range due to the final design having slightly larger PMs and higher reluctance torque.

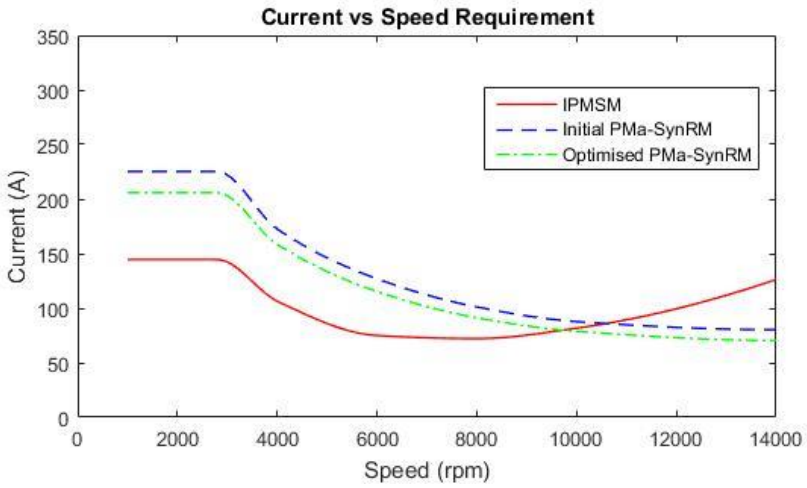


Figure 7.26 – Comparison of current requirement of the final machine vs earlier designs

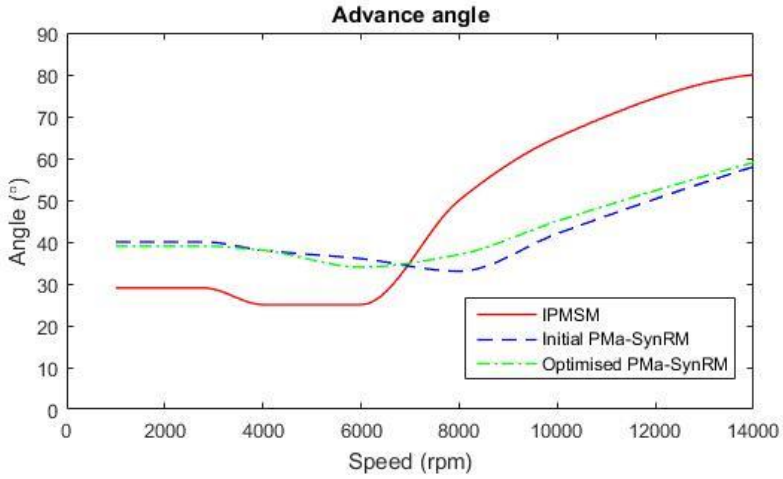


Figure 7.27 – Comparison of advance angle of the final machine vs earlier designs, needed to maintain the voltage limit

Figure 7.28 gives the four major loss components for each of the designs. The copper losses followed the same pattern as seen in Figure 7.26, with the slot sizes not changing dramatically the resistance stayed around the same level, and so the main difference between the copper losses was the variation in current requirements. These differences were expanded due to the copper losses being proportional to the current required squared. The stator iron losses were considerably lower in the final PMa-SynRelM, this was the major result of the optimisation process, particularly at high speeds. The main contributing factors to this were the larger stator iron area, reducing flux density for the same total flux, and higher reluctance torque, reducing flux requirement. This increase of stator iron area required the reduction of the slot area, which was made possible by the innovative cooling methods. The rotor iron losses and PM losses of the final PMa-SynRelM were similar to the initial PMa-SynRelM, and again these values were small enough compared to the copper and stator iron losses that they are not significant.

The final comparison is the efficiency based on these losses, shown in Figure 7.29. As can be expected from the losses in Figure 7.28, the initial and optimised PMa-SynRelM designs followed the same trend with the optimised one having a higher efficiency across the whole speed range. The IPMSM had a higher efficiency at low speeds due to the lower copper losses, however while the efficiencies of the PMa-SynRelM designs were almost static at higher speeds, the IPMSM fell off sharply. The IPMSMs poor high speed efficiency was due to both the iron loss and copper loss increasing with speed. While only the iron losses increased with speed in the PMa-SynRelM designs, and this was not as rapid of an increase as in the IPMSM.

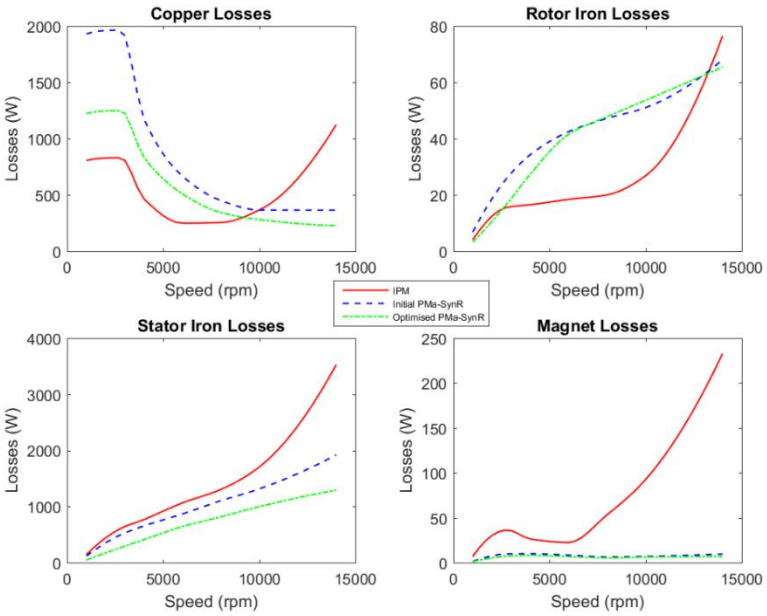


Figure 7.28 - Comparison of the four major loss contributors of the final machine vs earlier designs

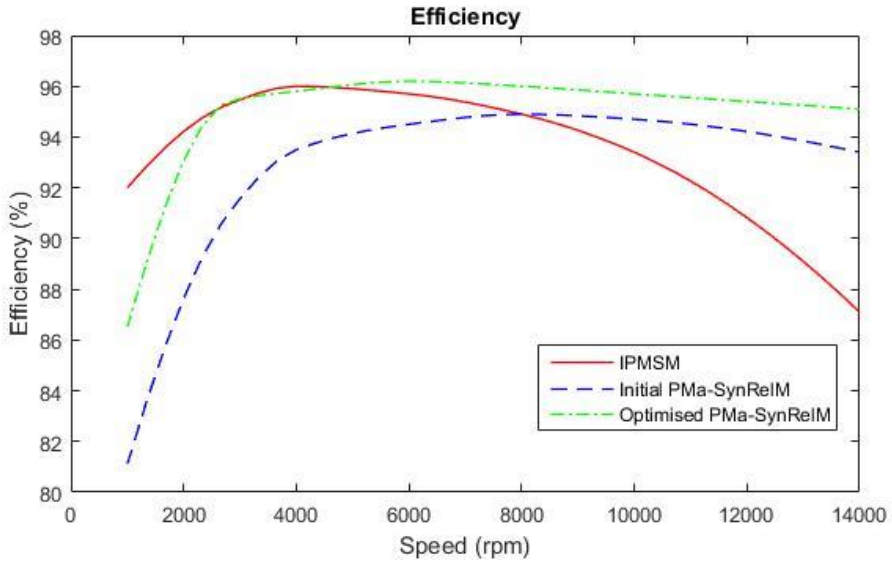


Figure 7.29- Comparison of efficiency of the final machine vs earlier designs

7.6 Comparison to attempts by others

As well as comparing each of the design stages against one another and the original targets, the final design was also evaluated against the machines proposed by others presented in Section 2.4. This comparison is shown in Table 7.13. The column numbers refer to:

1. The SPMSM machine from Section 2.4.1, [41]
2. The IPMSM machine from Section 2.4.2, [42]
3. The V-shaped IPMSM, design A from Section 2.4.3, [43]
4. The flux focusing IPMSM from Section 2.4.4, [44]

Table 7.13 – Comparison of against previous attempts at the FreedomCar 2020 targets

Requirements	Target	Final design	1	2	3	4
Rated Power (kW)	30	30	30	30	30	30
Peak Power (kW)	55	58.6	55	55	55	55
Peak Torque (Nm)	200	200	200	200	N/A	200
Maximum Current (Arms)	400	365.6	390	400	N/A	Met
DC Link Voltage (V)	200-450 (325 rated)	325	325	325	325	325
Max Back EMF at Max Speed (V)	600	375	666	800	910.3	950
Winding Temperature (°C)	180	174	N/A	90	N/A	180
Maximum Machine Diameter (mm)	250	250	300	237	N/A	280
Maximum Machine Length (mm)	200	130	65	85	82.4	80
Maximum Machine Volume (L)	9.7	6.38	4.6	3.74	N/A	4.93
Mass (kg)	35	33.6	N/A	27	41.9	Met
Minimum Peak Efficiency (%)	95	95	<95	91	93	85
Cost	$275	1	2	3	4	5

Design 1 gave a higher torque and power per volume than the proposed design. While design 1's outer diameter was larger than the specs, the length was much smaller, bringing it within the volume limits. The mass and temperature were not considered. The other main downfalls of this machine are the maximum back EMF exceeding the limit and while the efficiency had not been explicitly stated, it was mentioned it did not meet the 95% requirement. [41]

Again design 2 had a higher torque and power density, both in terms of volume and mass. This design had a reasonable machine diameter, but the back EMF was much larger, well above the limit. While the winding temperature appears low, this was tested from 20˚C with rated losses. Assuming the same thermal increase from the specified ambient of 105˚C, would give 175˚C, and this is before the increase in copper losses with temperature or the peak torque losses are taken into account. The efficiency of 91% is a FEA result, they also presented an experimental result of 87.5%. The FEA result was used for a fair comparison to the design from this thesis. [42]

Design 3 did not consider the peak torque requirement or the thermal limit. The volume and outer diameter were not provided, but the mass is exceeding the limit. Again the back EMF is well above the target and minimum efficiency below what is required. [43]

For design 4, in addition to the already referenced paper a more recent update was found which focused on mechanical and thermal issues but also compared the design back to the targets, [128]. For some of the targets the paper only stated that they were achieved, not what the specific value was. As with the other designs the back EMF is above the limit, and while the efficiency met the target for a large section of the speed range it harshly dropped well below the requirement at high speed. [44]

Thus, all this confirms that the proposed design of this work, compares excellently and in many points even exceeds the results of other works and previous attempts.

7.7 Construction

Time constraints limited the option to build and prototype the machine, the mechanical drawings were constructed, a selection of these are shown in Appendix F. Appendix F also shows what the machine would look like when housed. While this could not be part of this thesis, the procurement and construction is currently underway and will be tested as part of the postdoctoral work.

7.8 Conclusion

This section detailed the optimisation of a PMa-SynRelM design. This started with designing the rotor without PMs to maximise reluctance torque, and then adding the minimum amount of PMs to meet the torque density and thermal requirements. After this, the stator was optimised to meet 95% efficiency at maximum speed and then minimise losses at rated speed.

The final design that this optimisation process produced was detailed, showing all the geometrical parameters and the results of the electromagnetic and thermal simulations. The performance was compared back to the previous two designs, the IPMSM and the initial PMa-SynRelM, showing that although the IPMSM was still better at low speeds, the new design was the preferable design past rated speed and superior to the previous PMa-SynRelM overall. The only drawback in comparison to the previous PMa-SynRelM is an increase in PM mass.

Of course, as always the main objective is the FreedomCar2020 targets, in Table 7.14 the parameters for the each of the targets are analysed. It can be seen that all the targets have been met. The only remaining target that could be improved is the DC link voltage. 325V is the average value, so machine performance would drop when the battery is close to depletion. Cost has also not been considered here but it will be discussed in the next chapter. Overall, this machine has been shown to be the optimal option for reaching these targets, thus achieving the overall aim of the thesis.

Table 7.14 - Final machine comparison to FreedomCar 2020 targets

Requirement	Target	Result
Rated Power (kW)	30	30
Peak Power (kW)	55	58.6
Peak Torque (Nm)	200	200
Maximum Current (Arms)	400	365.6
DC Link Voltage (V)	200-450 (325 rated)	325
Max Back EMF at Max Speed (V)	600	375
Winding Temperature (°C)	180	174
Maximum Machine Diameter (mm)	250	250
Maximum Machine Length (mm)	200	130
Maximum Machine Volume (L)	9.7	6.38
Mass (kg)	35	33.6
Minimum Peak Efficiency (%)	95	95

The design was also compared to the attempts at the FreedomCar targets made by others in the past. It was shown that for the targets the design machine is superior to them all, with the main reasons being it was designed with the size

limits in mind, it used a reduced amount of PM mass and had an improved high speed efficiency.

Chapter 8. Conclusion

8.1 Project summary

This thesis focused on the design of an electromagnetic machine to achieve the highly challenging US DoE FreedomCar 2020 targets for PHEV traction.

To this end, first a wide range of all applicable machine technologies were considered and evaluated against one another with a set of defined QIs. This comparison found that an IPMSM was the optimal starting point. When high speed performance became an issue, this study was referred back to, showing that a PMa-SynRelM would be the best option to overcome this challenge. If it had been the case that the peak torque was difficult to reach, the study showed an SPM would be the way to go. Other designs such as the IM and double air gap machines showed promise but had known drawbacks highlighted in Chapter 2.

From here a range of IPMSM designs were considered, varying based on the slot pole combination and winding configuration, the collection is shown in Chapter 3. A best configuration for both concentrated wound (12 slot, 10 pole) and distributed wound (30 slot, 10 pole) were selected and then compared against each other. This evaluation showed that distributed designs required less current and produced lower losses, both copper and iron at high speed. At rated speed the concentrated wound machines required less current and therefore had lower copper losses. Both machines struggled to meet the efficiency requirements at high speed, and that the iron losses were the predominant reason for this. However, the distributed wound machine was affected less by this high speed weakness and so was decided upon to be the superior design for these targets.

Two routes were established to improve upon this design, the first was adding reluctance to create a PMa-SynRelM design. This initial PMa-SynRelM design was shown to have the potential to have severely reduced high speed losses,

however due to the smaller PMs a higher current was required, overheating the machine during peak torque operation.

The other route to improving the design was to improve the thermal management. To achieve this, an innovative cooling method was devised and investigated experimentally. The key idea behind this method was direct cooling of the end windings with a fluid carrying pipe and possibly applying potting compounds to improve the thermal conduction between the two. The full range of cooling methods can be found in Chapter 6. During the experimental result, temperature reductions of up to 14.9˚C were seen. These experimental results were then used to calibrate thermal models, which showed that in a full machine a hot spot reduction of 23.9°C would be achievable. Considering the fluid temperature is 105°C and previous peak was 180.4°C, this is a reduction of 31.7% of the thermal increase. It is clear that this is a hugely successful thermal management system, but most of all it allowed for more freedom in the machine design before the new thermal limit was reached.

The final step was to optimise the final PMa-SynRelM design. This firstly focused on maximising the reluctance torque and minimising the PM mass whilst meeting the torque requirements with the current supply and thermal limits. The stator slot designs were optimised to meet the efficiency target across a wide a speed range as achievable. The results from this optimisation along with the final design are detailed in Chapter 7.

8.2 Key findings and contributions

The two main aims of the project were to meet the US DoE FreedomCar 2020 targets and to prove the effectiveness of the thermal management method proposed. These have both been achieved.

8.2.1 Performance enhancement methodology

The methodology used for the machine design itself was original. This involved using fast analytical methods to simulate a huge range of designs rapidly and combining this with FEA for the more promising designs. The FEA allowed for more accurate modelling of the localised flux densities and therefore back EMF and iron losses. Incorporated into this design process was thermal modelling, using both commercial software and validated thermal networks. The iterative process of cycling between electromagnetic modelling and thermal analysis allowed for convergence on both the temperature dependant electromagnetic factors (such as copper losses) and final temperature.

Included into this cycle of analytical, FEA and thermal modelling was a genetic algorithm optimisation based on minimising losses to ensure that the final design produced was the optimal choice.

Throughout this thesis, this process and the results has been shown in steps, which were the stages it was developed in. However by the end of the project this methodology was fully automated from the original comparisons down to the final design.

8.2.2 FreedomCar 2020 targets

Throughout the thesis, four main stages of development for the machine have been proposed and compared to the FreedomCar targets, this comparison is summarised in Table 8.1. A tick (✓) show that the target has been achieved, a dash (-) that the target has been achieved but just barely or that there is room for improvement, a cross (×) represents the target has not been met and major alterations would be needed to rectify this. For the cost, a simple ranking system was used between the four, with higher numbers being more expensive to produce.

All four of the machines managed to meet the power and torque requirements with the current limit. However the initial PMa-SynRelM design was on the very edge of these limits, the rated current would need to be slightly increased

to meet the power, and there was room to decrease the peak torque. For all four designs the rated DC link voltage was used, at the minimum the machine would still operate, just at a lower efficiency. The back EMF of the PMa-SynRelM designs was well within the limit, the distributed wound IPMSM was still below the limit but much closer to it and the concentrated wound machine exceeded the limit. The only machine with thermal issues was the initial PMa-SynRelM, however if the final PMa-SynRelM did not have the improved thermal management system it would also be above the thermal limit.

Table 8.1 – Comparison of four designs to the FreedomCar 2020 targets

Requirements	Target	Concentrated IPMSM Design		Distributed IPMSM Design		Initial PMa-SynRelM		Final PMa-SynRelM	
Rated Power (kW)	30	29.9	✓	30.0	✓	29.7	-	30	✓
Peak Power (kW)	55	58.7	✓	58.6	✓	59.2	✓	58.6	✓
Peak Torque (Nm)	200	200.2	✓	200.0	✓	202	✓	200	✓
Maximum Current (Arms)	400	256.3	✓	269.8	✓	394.2	-	365.6	✓
DC Link Voltage (V)	200-450 (325 rated)	325	-	325	-	325	-	325	-
Max Back EMF at Max Speed (V)	600	608	-	571	✓	356	✓	375	✓
Winding Temperature (°C)	180	166	✓	162	✓	194.6	×	174	✓
Maximum Machine Diameter (mm)	250	250	✓	250	✓	250	✓	250	✓
Maximum Machine Length (mm)	200	200	-	130	✓	130	✓	130	✓
Maximum Machine Volume (L)	9.7	9.7	✓	6.38	✓	6.38	✓	6.38	✓
Mass (kg)	35	51.68	×	30.41	✓	31.8	✓	33.6	✓
Minimum Peak Efficiency (%)	95	86.4	×	88.0	×	92.3	×	95	✓
Cost Rank	$275	4		3		1		2	

All four machines used the maximum machine diameter. The concentrated wound IPMSM also used the full machine length, hence why the back EMF was larger, this was not fully achieving the length target as this was only the active length and the target includes end winding. The other three machines had a shortened length, which meant even with the end windings, and additional cooling, they were within the length limit. As all machines met the maximum diameter and length, they were within the volume limit. Again due to its longer length, the concentrated wound IPMSM did not meet the mass requirements, while the other three designs did.

Efficiency has been the main challenge throughout the project, particularly at high speed. It was seen that an IPMSM could not achieve this target, although the distributed wound came closer than the concentrated wound. The initial PMa-SynRelM design almost met the high speed efficiency but sacrificed the performance at lower speeds to achieve this. Lastly the final PMa-SynRelM design met the efficiency requirement at both high speed and rated speed.

While a full cost analysis has not yet been performed, the designs can be ranked against one another. The main cost components are, the PM material and the high end stator and rotor steel. The concentrated IPMSM design, being the longest required the highest quantity of both PM and steel. The distributed IPMSM had a smaller PMs and a smaller stack length and so would be cheaper. The initial PMa-SynRelM had the smallest quantity of PMs and so would be the cheapest. The final PMa-SynRelM had more PM mass than the initial PMa-SynRel and a larger iron mass, and so would cost more, but not as much as the distributed wound IPMSM.

8.2.3 Thermal management method

The other key aim was to investigate an innovative cooling method. This involved directly cooling the end windings, which were previously the hotspot and limiting factor in the machine. A summary of the results of these methods is given in Table 8.2, where each method is given a rating for the four key comparative factors. An expansion on this, showing quantitative results to justify these values was given in Chapter 6.

All the methods without potting compound would be cheap to implement. Due to the low contact area of the copper pipe, only a small thermal reduction was seen, the flexibility of the silicone pipe improved upon the contact area and therefore the cooling potential. Placing the silicone pipe in the specifically created gap in the modified end windings increased this contact area even further and reduced the temperature even more. However this modification to the end winding significantly increases the complexity of the machine winding,

also increasing the length of the machine. The pipes on the end winding surface are simple to implement and while the copper pipe adds a fixed size to the machine length, the silicone pipe is compressible and so the additional length can be small.

Table 8.2 – Summary of thermal management methods

Method	Cooling Potential	Cost	Complexity	Additional Machine Length and Mass
Silicone Pipe on End Winding Surface	Medium	Low	Low	Low
Copper Pipe on End Winding Surface	Low	Low	Low	Medium
Silicone Pipe with Modified End Winding	High	Low	High	Low
Commercial Potting Compound	Medium	Medium	Medium	High
High Performance Potting compound	High	High	Medium	High

The potting compounds cost considerably more, particularly when using the very high performance materials. However the cooling provided increases with the expense of the material (although not at a linear rate). Producing the required mould and curing time add some complexity to the design. The cured compound adds significant mass to the machine and will also increase the machine length more than the other methods.

The overall best depends on a number of factors. If cost and additional mass are not an issue the high performance potting compound gives the best cooling. If the winding can be concentrated wound and be designed to have the required gap then the silicone pipe with the modified end windings is optimal. Otherwise the silicone pipe on the end winding surface is the best compromise between cost, simplicity and thermal reduction.

8.2.4 Literature review

A still important yet less critical target of the work, was the literature review, apart from gaining an understanding of the industrial relevance and previous

attempts at the targets, this was aimed at comparing different machine topologies for the FreedomCar targets. Figure 3.17 was a key grasaphic summarising this comparison. This took the weighted QIs described in Chapter 2 to show that the IPMSM was the optimal choice, with the SPMSM, IM and SynRelM as high scoring alternatives.

8.2.5 Publication of work

The final objective of this project was the dissemination of the high quality work. The publications produced as part of this work are listed below.

- "A Topology Selection Consideration of Electrical Machines for Traction Applications: Towards the FreedomCar 2020 Targets" *EVER 2015*. A. Walker, M. Galea, C. Gerada, A. Mebarki, and D. Gerada
- "Design Considerations for High Performance Traction Machines: Aiming for the FreedomCar 2020 Targets" *ESARS 2015* A. Walker, M. Galea, C. Gerada, A. Mebarki, and D. Gerada
- "Development and Design of a High Performance Traction Machine for the FreedomCar 2020 Traction Machine Targets" *ICEM 2016,* A. Walker, M. Galea, C. Gerada, A. Mebarki, and D. Gerada, N. Brown
- "Design of a Short Term Duty Electrical Machine for an Extreme Environment" *IEEE Transactions on Industrial Electronics,* P. Arumugam, A. Walker, C. Gerada. Submitted and in the second stage of review
    - On the transient thermal increase of windings due to high losses for a short amount of time, here the losses produced when producing peak torque for 18s.
- Patent application:
    - The range of cooling methods are also currently being proposed for a patent application.
    - Due to the confidentiality of the patenting process, the submission of two journal papers which are already compiled

and completed has been postponed until after the work is patented. The patent application is already in progress.

8.3 Future work

Due to the time constraints of the project there are several avenues of further research that will still be investigated as further projects.

First is the torque ripple, this is typically large in any SynRelM machine and was overcome here by skewing the rotor. Skewing adds complexity to the machines construction and so it would be beneficial if the necessity for it can be removed or reduced. During the optimisation process, torque ripple was not a target as the efficiency target was more pressing. Now that the efficiency has been met, time can be spent improving the torque ripple whilst attempting to keep the losses constant.

Throughout the designs of this project the rated value for the DC voltage supply was used (325V), the actual specifications stated a range of values depending on the charge of the battery (from 450V at full to 200V at minimum). Time will be spent exploring the effect this has on the machine performance. The lower voltages will require higher field weakening at high speed, and thus will reduce efficiency, with higher voltages having the opposite effect.

The thermal management ideas presented have been shown to significantly reduce the temperature of the windings in this application. However there are still routes to explore to exploit these ideas further. The immediate routes to continue this thermal work are focusing on improving the contact area and thermal conduction between the pipe and the end winding conductors. For the silicone pipe this could be increasing the gap size in the end winding, adding multiple gaps or redesigning the end winding completely to maximise contact area. For the potting compound, new materials can be investigated, either higher thermal conductivities or with a lower viscosity to allow for a better flow between the conductors during the curing process. Another direction is to look into combining these methods, such as having a silicone pipe through a gap

and another on the bottom of the end winding, or having a copper pipe in a larger gap and encasing in potting compound. Approaches into how to apply the current methods more effectively will be also investigated. Concentrating on if the gap in end windings can be applied to distributed windings and how to minimise the added machine length for all the proposed methods. The ultimate goal is applying the same methods to alternative machines and applications, it has been proved to work here but it would be useful to show its effect on other machines to enhance its potential industrial impact.

The final objective to round off the project is to prototype the final machine and ensure that it matches the simulations. Procurement and manufacturing procedures are on-going at the time of writing this thesis. Both the electromagnetic and thermal performance are crucial to proving that this machine can meet the FreedomCar 2020 targets in practice as successfully as it has in simulations. During the construction a cost analysis will be performed, including identifying areas that significant savings could be made during mass production.

Appendix A. Technical Skills

Technical skills, both software and experimental, had to be learnt to complete the project. While time was spent learning these skills, the training will not be covered directly in this thesis, but a general high level overview is included as follows.

A.1 Software

A.1.1 MATLAB [118]

MATLAB was used primarily for analytical modelling and for automation related to the commercial software packages introduced below. This automation derived from using MATLAB was essential in order to maximise simulation efficiency.

A.1.2 Infolytica MagNet [100]

MagNet is a FEA software which allows for accurate modelling of electromagnetics with respect to motion, time and electrical input. This was the primary commercial software used in this project, producing detailed simulations of electrical machine models.

A.1.3 MotorCAD [99]

The commercial package MotorCAD was mainly used for thermal analysis. From machine geometry, cooling method and loss inputs MotorCAD builds a thermal network which is then used to predict what temperatures the machine will reach.

Recent upgrades of the MotorCAD package allowed for FEA of the electromagnetic performance of the machines under investigation, later in the project. While this does not have the flexibility of MagNet, it was faster, easier to use and allowed for easy iteration between the thermal and electromagnetic simulations.

A.1.4 SPEED [98]

SPEED is an analytical machine design tool, with a built-in FEA solver to calibrate models. This gave very fast simulations allowing for a vast range of machines to be quickly compared.

A.1.5 Simulink

Simulink is a subprogram within MATLAB that allows for system networks to be built. The section of this subprogram heavily used in this project was Simscape, which models physical systems. Simscape was utilised to build and model thermal networks which involved novel ideas, which could not be simulated with MotorCAD.

A.2 Experimental

A.2.1 Electrical machine testing

Before they were required to be used on any novel machines, practical skills for testing electrical machines were learned by testing on machines with known results. This involved how to set up test rigs and experiments, running the associated programs, how to obtain the results and how to deal with any errors.

A.2.2 Thermal experiments

Good practice aspects of thermal management experiments were also considered. This involved the health and safety around high currents, high temperatures and hazardous materials (potting compounds). The power supply used was a high current DC supply, and the only measurement apparatus was to read the temperature from thermocouples.

Appendix B. Design Equations and Procedure

The basic analytical sizing equations and design procedure used in Chapter 4 is detailed in this appendix. The first part is the equations used to produce the initial design. The second is the procedure used with SPEED and MagNet to design the machine for each slot pole combination.

B.1 Design equations

B.1.1 Machine size

The first step was the overall size of the rotor and stator, based on Eqn. 4.2 and Eqn. B.1.

$$D_r = D_s \times r_{split} \quad \textbf{Eqn. B.1}$$

The stator diameter, D_s, was the maximum from the targets, 250mm. The split ratio, r_{split}, is the ratio between the rotor and stator diameters and was initially set to be 65%. The initial length was the maximum stack length from the targets, 200mm.

B.1.2 Torque estimation

To ensure the machine could produce the desired torque both the magnetic loading and the electrical loading needed to be appropriate values based on Eqn. 4.1. The rated torque value from the targets was 100Nm.

B.1.3 Electrical loading

To calculate the required electrical loading, Eqn. 4.1 can be rearranged to give Eqn. B.2.

$$A_{load} = \frac{T}{k \times B \times Vol} \quad \textbf{Eqn. B.2}$$

In this case B, the magnetic loading of the air gap, which can be calculated using Eqn. 4.3, was targeted at half the saturation value of the steel used in the stator

teeth, 1.8T. This was then used to give a target for A_{load}, by rearranging Eqn. 4.4 gives Eqn. B.3 and Eqn. B.4.

$$N_{Total\ turns} = \frac{A_{load} \times \pi \times D_r}{2 \times I} \quad \textbf{Eqn. B.3}$$

$$N_{Turns\ per\ slot} = \frac{N_{Total}}{m \times N_s} \quad \textbf{Eqn. B.4}$$

$N_{TotaltTurns}$ is the total number of turns in the whole machine, $N_{turns\ per\ slot}$ is the number of turns per phase in each slot, and this number was then rounded as turns are physical objects and cannot be a non-integer amount.

From Eqn. B.2 the required electrical loading could be found, using Eqn. B.3 this lead to the total number of turns per phase and Eqn. B.4 then gave the turns per slot.

B.1.4 Magnetic loading

The desired value of magnetic loading had already been determined at this stage, but the PM size needed to be calculated. The thickness was found from Eqn. B.5, a rearrangement of Eqn. 4.3 which is a standard machine design equation.

$$L_m = \frac{\mu_r L_{ag}}{\frac{B_r}{B_{ag}} - 1} \quad \textbf{Eqn. B.5}$$

After the thickness of the PMs had been determined, the PM width needed to be calculated, this could be achieved with Eqn. B.6.

$$W_m = 2 \times \left(\frac{D_r}{2} - L_{Bridge}\right) \times \sin\left(\frac{\frac{360}{2 \times p} \times M_{percent}}{2}\right) \quad \textbf{Eqn. B.6}$$

W_m is the width of the magnets. L_{Bridge} is the rotor bridge, how deep the magnets are buried. $M_{percent}$ is the percent of the pole pitch the magnet covers, 70% was initially used.

B.1.5 Stator dimensions

The two main remaining dimensions of the stator, with the outer and inner diameter and stack length already determined, were the tooth width and slot depth, determined using Eqn. B.7 and Eqn. B.9 respectively.

$$W_t = \frac{B}{B_t} \times \lambda_s \quad \textbf{Eqn. B.7}$$

$$\lambda_s = \frac{\pi \times D_r}{N_s} \quad \textbf{Eqn. B.8}$$

W_t is the tooth width, to be calculated. B_t is the saturation value of flux density of the teeth, 1.8T. λ_s is the slot pitch calculated in Eqn. B.8.

$$W_y = \frac{B}{2 \times B_{core}} \times \lambda_p \quad \textbf{Eqn. B.9}$$

$$\lambda_p = \frac{\pi \times D_r}{4 \times p} \quad \textbf{Eqn. B.10}$$

W_y is the thickness of the stator yoke. B_{core} is the saturation value of flux density of the core, usually the same value as the teeth. λ_p is the pole pitch, calculated in Eqn. B.10. If the stator yoke was deemed too thick (over half the total stator depth or over double the tooth width) the yoke thickness is reduced, this was to give adequate slot depth to avoid the coils overheating, though this would reduce the flux in the stator.

After the yoke thickness and various stator diameters had been determined the slot depth can be calculated, Eqn. B.11.

$$SD = \frac{D_s}{2} - W_y - \frac{D_{s\,inner}}{2} \quad \textbf{Eqn. B.11}$$

SD is the slot depth, the distance from the slot opening to the stator back iron, radially. D_s is the outer diameter of the stator. $D_{s\,inner}$ is the inner diameter of the stator, based on the rotor outer diameter and the air gap thickness.

The final parameter to initially size for the stator was the slot opening width Eqn. B.12, which has a large effect on the torque ripple of the machine.

$$SO_w = D_{s\,inner} \times \pi \times \frac{SO_R}{N_s} \qquad \textbf{Eqn. B.12}$$

SO_w is the width of the slot opening, to be calculated. SO_r is the ratio of slot opening to tooth, originally chosen at 0.2. This is a known ratio to provide low torque ripple.

B.1.6 Winding layout

To determine the winding layout for each phase, a 'star of slots' diagram was drawn. An example of this, for a concentrated wound 9 slot 4 pole machine is given in Figure B.1.

The star of slots was determined by the number of poles and slots. Eqn. B.13 gives the electrical angle from one slot to the next.

$$Angle = p \times \frac{360}{N_s} \qquad \textbf{Eqn. B.13}$$

From here the star of slots could be drawn, by drawing an arrow for every rotation by this angle as in Figure B.1, and slots electrically close grouped together.

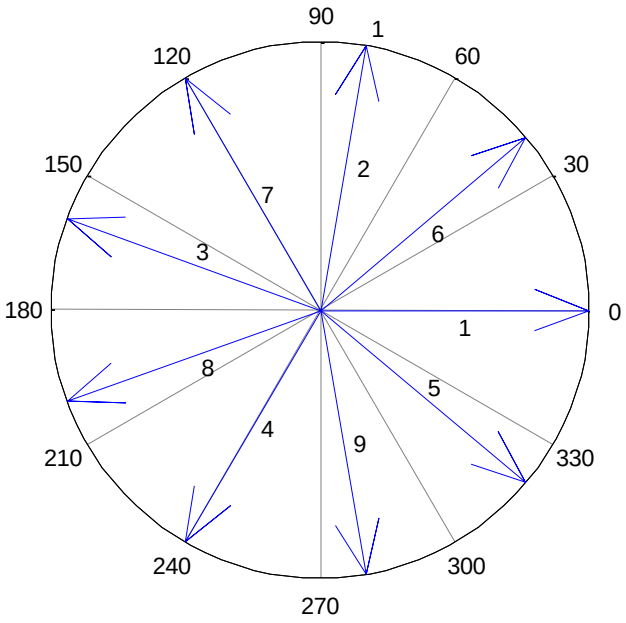


Figure B.1 - Star of slots for 4 pole 9 slot machine

This is done via a script and the first stage is to make sure the slot pole combination was viable. For the combination to be viable, it needed: an even number of poles, a number of slots divisible by three (the number of phases) and an integer offset, the number of slots between one phase and the next, calculated from Eqn. B.14.

$$Offset = \frac{4}{3}\frac{N_{slot}}{p} + 4n\frac{N_{slot}}{p} \quad \textbf{Eqn. B.14}$$

Where n is an integer, starting from 0 and increasing by 1 until the offset was also an integer. The only time this is not viable is when the number of slots per pole was an integer but not a multiple of three (e.g. 12 slots /12 poles and 12 slots / 6 poles).

The script then grouped the slots. Each angle was calculated as if it were between 0° and 360° (e.g. 400° becomes 40° and 1000° becomes 280°) and compared to the borders given in Table B.1. Each slot number was then be equated to a specific phase and connection.

Table B.1 – Star of slot group limits

Angle of Slot	Phase
330° - 30°	A positive
30° - 90°	C negative
90° - 150°	B positive
150° - 210°	A negative
210° - 270°	C positive
270° - 330°	B negative

B.2 Simulation process

The following sections detail the steps of the analytical simulations using SPEED.

B.2.1 Determine the required current

The first simulation was to find the advance angle where the torque was the maximum, as in Eqn. 4.14, and find what value of average torque the initial design produced.

The advance angle was then set to the maximum torque point and then the model was run again. If the average shaft torque is less than 99.5Nm, the current is increased; if it was greater than 100.5Nm the current is decreased. The magnitude of the change in the supply current was based on how large the difference between the simulated toque and the target range was. This process is repeated until the shaft torque was within the given tolerance.

This step was needed because, while the initial design would be close to providing the desired torque and an estimate of the maximum torque angle can be calculated, it would not be perfect. This discrepancy was due to losses not being considered in the original calculation and the change in inductance with loading, which cannot easily be corrected for without an accurate calculation of both these effects.

B.2.2 Determination of the appropriate number of turns

A tight constriction on the design was the voltage limit, and because of the high speed requirement, the back EMF was quite large. To reduce this large back EMF, low numbers of turns were needed. If the voltage was above the limit at maximum speed, the number of turns per slot per phase is reduced and the above process for finding the current is used again. This process was repeated until the full torque-speed characteristic could be met with the VA limit. Occasionally a design had a voltage which was significantly lower than the limit, in this case, the number of turns was increased and again the current required for 100Nm would be modified accordingly.

B.2.3 Achieve a reasonable slot fill factor

Because of the low number of turns in these designs, the slots at this point had a very low fill factor and high current density. To correct this, the number of strands per turn was increased; this effectively increases the diameter of the conductor, without having to use larger wires. This was increased until the slot fill factor reached a reasonable amount (45% for distributed wound, 55% for concentrated).

B.2.4 Determine the optimum tooth width

The next step was to find the optimum tooth width for the design, this meant finding the highest efficiency design, while not exceeding the temperature limit (180 °C for H class insulation). To achieve this, a range of tooth widths were considered, from 25% to 75% of the slot pitch, any widths smaller or greater than this were assumed to be too extreme and would saturate at too low a tooth flux value (for <25%) or have too high current density (for >75%). For each tooth width a similar process to above was used, where the number of strands was changed to get the same slot fill factor and then the current was altered to obtain 100Nm. The important value to find here was the efficiency and losses for each tooth width.

B.2.4.1 Peak torque

The various tooth width designs needed to be compared based on temperature. While a comparison between machines could be done with rated loads, to check the temperature did not exceed the limit, the thermal extreme must be considered. The peak torque operating point required a higher current and higher flux densities than the rated load, and so would run at a higher temperature, due to higher losses.

For each tooth width, the current was increased until the torque produced was 200Nm. Each design was then checked to ensure that the current and voltage were still below the limits of 400A and 132.6V (Conversion of 325V DC supply to possible AC supply, $325/\sqrt{(3 \times 2)}$) respectively and the peak losses were recorded.

B.2.4.2 Thermal check

Thermal analysis of the models at this stage was done using the commercially available software MotorCAD. MotorCAD and SPEED can be linked to rapidly pass designs back and forth.

B.2.4.2.1 The water jacket

A simple script added the water jacket to the MotorCAD design before the thermal equivalent circuit was produced. The maximum flow rate of the water jacket is given in the DoE targets of 10L/min.

The original water jacket had channels 5mm deep, with 2.5mm walls above and below the channels, giving an added 20mm to the diameter of the machine. The sections separating each channel were chosen to be 10mm thick, with the channels being 20mm in width; this gave 28 channels with a flow area of 200 mm^2 each. The pressure of the coolant fluid was found to be 29.3 kPa (4.26psi) well below the limit of 20 psi.

Both the ambient and the fluid inlet temperature were set to 105°C, as this is the maximum temperature for the water jacket (given in the targets) so this was considering a worst case scenario.

B.2.4.2.2 Temperature calculation

The maximum temperature in the machine occurred when the peak torque was required after the machine had already been running at rated load for a long enough time to reach a steady state temperature. The peak was only required for 18 seconds.

To calculate this with MotorCAD, first, the design was analysed statically with the rated load losses to find the rated load steady state temperatures. These temperatures were then used as initial conditions for an 18s transient analysis with the peak load losses. The temperatures at the end of this transient analysis were the maximum temperatures the windings would reach during operation.

B.2.4.3 Optimum tooth width

The tooth width with the highest efficiency at rated load was chosen. The peak winding temperature for this width was then compared to the limit. If it was too high, this width was then ignored and the second highest efficiency was chosen and then compared to the temperature limit. This is then repeated until

the optimum tooth width with a maximum copper temperature below 180°C was found.

If none of the tooth widths gave a copper temperature below this level, then this slot pole combination was removed from the comparisons.

B.2.5 Producing the torque-speed characteristic

As well as at rated speed, the designs had to be compared across the whole speed range. The target torque speed characteristic, including output power, is shown in Figure 2.7.

B.2.5.1 Constant torque region

The constant torque region is the range of speeds from 0rpm to rated speed, 2800rpm. For this region, the current was varied very slightly to keep the torque at 100Nm across the range. Though the current should have been constant for the constant torque region, there was a slight increase required due to the increasing iron losses and AC copper losses with speed.

B.2.5.2 Field weakening region

The field weakening region is the range of speeds from the rated, 2800rpm, to the maximum 14000rpm. For this region, the speed was increased whilst the output power is kept constant, at 30kW.

For each speed value, the target torque was rated power divided by the speed; the current was reduced until the torque was at this value. The voltage was then checked and if it was too high the advance angle was increased and the current was calculated again. This process repeats itself until the voltage was below the limit and then until each value of speed had been covered, producing the torque-speed characteristic shown in Figure 2.7.

Appendix C. Thermal Networks

C.1 Thermal resistance parameters

This part of the appendix details each of the thermal resistances shown in section 6.3.

Table C.1 - Slot thermal network resistances

R_{Slot_Vert}	$k_{eq_S}\frac{SD/2}{SW \times L_{Slot}}$
R_{Slot_Horz}	$k_{eq_S}\frac{SW/2}{SD \times L_{Slot}}$
R_{Liner_Vert}	$k_{Liner}\frac{L_{Liner}}{SW \times L_{Slot}}$
R_{Liner_Horz}	$k_{Liner}\frac{L_{Liner}}{SD \times L_{Slot}}$
R_{Tooth_Horz}	$k_{steel}\frac{W_t/2}{SD \times L_{Stk}}$
R_{Tooth_Vert}	$k_{steel}\frac{SD/2 + W_y/2}{W_t \times L_{Stk}}$
$R_{Yoke_C_Vert}$	$k_{steel}\frac{W_y/2}{SW \times L_{Stk}}$
$R_{Yoke_S_Vert}$	$k_{steel}\frac{W_y/2}{W_t \times L_{Stk}}$
R_{Yoke_Horz}	$k_{steel}\frac{W_t/2 + SW/2}{W_y \times L_{Stk}}$
$R_{Stator_WJ_Junct}$	$k_{Junct}\frac{L_{\text{Stator_WJ_Junct}}}{(\pi \times D_s)/(N_s \times 3) \times L_{Stk}}$
R_{WJ}	$\frac{1}{h_{WJ} \times (\pi \times D_s)/(N_s \times 3) \times L_{Stk}}$
$R_{WJ_Housing_Junct}$	$k_{Junct}\frac{L_{\text{WJ_Housing_Junct}}}{\left(\pi \times (D_s + 2 \times L_{WJ}\right)/N_s \times L_{Stk}}$
$R_{Housing}$	$k_{al}\frac{L_{House}/2}{\left(\pi \times \left(D_s + 2 \times L_{WJ} + L_{House}\right)\right)/N_s \times L_{Stk}}$
$R_{Housing_Conv}$	$\frac{1}{h_{air} \times \left(\pi \times \left(D_s + 2 \times L_{WJ} + 2 \times L_{House}\right)\right)/N_s \times L_{Stk}}$

Table C.2 - Parameters for slot thermal network

k_{eq_S}	Slot equivalent thermal resistivity (mK/W)
k_{Liner}	Slot liner thermal resistivity (mK/W)
k_{Steel}	Stator Steel thermal resistivity (mK/W)
k_{al}	Aluminium thermal resistivity (mK/W)
k_{junct}	Junction thermal resistivity (mK/W)
h_{WJ}	Convection coefficient of water flow in water jacket (W/m^2K)
h_{air}	Convection coefficient of air to housing (W/m^2K)
SD	Slot Depth (m)
SW	Slot Width (m)
W_t	Tooth Width (m)
W_y	Yoke thickness (m)
D_s	Stator outer diameter (m)
N_s	Number of slots
L_{stk}	Active length (m)
L_{Liner}	Slot Liner Thickness (m)
$L_{Stator_WJ_Junct}$	Junction thickness between stator and water jacket (m)
$L_{WJ_Housing_Junct}$	Junction thickness between water jacket and housing (m)
L_{WJ}	Water jacket radial thickness (m)
L_{House}	Housing radial thickness (m)

Table C.3 - End winding thermal network resistances

R_{Slot_Vert}	$k_{eq_S}\frac{SD/2}{SW \times L_{Stk}}$
R_{Slot_Axial}	$k_{copper}\frac{L_{stk}/2}{N_t \times N_c \times \pi \times \left(\frac{d_{wire}}{2}\right)^2} + k_{eq_EW}\frac{L_{EW_H}/2}{L_{EW_V} \times W_{EW}}$
R_{EW_Vert}	$k_{eq_EW}\frac{L_{EW_V}/2}{L_{EW_H} \times W_{EW}}$
R_{EW_Out}	$k_{eq_EW}\frac{L_{EW_H}/2}{L_{EW_V} \times W_{EW}}$
$R_{EW_Up_Contact}$	$k_{Contact}\frac{L_{Contact_Cu_Barrier}}{K_{good} \times L_{EW_H} \times W_{EW}}$
$R_{Barrier_Up}$	$k_B\frac{L_{Barrier}}{K_{good} \times L_{EW_H} \times W_{EW}}$
$R_{Pipe_Up_Contact}$	$k_{Contact}\frac{L_{Contact_pipe_Barrier}}{K_{good} \times L_{EW_H} \times W_{EW}}$
$R_{Pipe_Up_Thick}$	$k_{pipe}\frac{L_{pipe}}{\pi \times (d_{pipe} - L_{pipe}) \times W_{EW}}$
$R_{Pipe_Up_Conv}$	$\frac{1}{h_{pipe} \times \pi \times (d_{pipe} - 2 \times L_{pipe}) \times W_{EW}}$
R_{EW_Junct}	$k_{junct}\frac{L_{junct}}{L_{EW_H} \times W_{EW}}$

Table C.4 - Parameters for the end winding thermal network

k_{copper}	Copper thermal resistivity (mK/W)
k_{eq_EW}	End winding equivalent thermal resistivity (mK/W)
$k_{contact}$	Thermal resistivity of contact between two materials (mK/W)
k_B	Interface material thermal resistivity (mK/W)
k_{pipe}	Pipe thermal resistivity (mK/W)
k_{junct}	End winding junction thermal resistivity (mK/W)
N_t	Number of turns
N_c	Number of parallel conductors per turn
d_{wire}	Wire diameter (m)
L_{EW_H}	Horizontal (axial) length of end winding bundle (m)
L_{EW_V}	Vertical (Radial) length of end winding bundle (m)
W_{EW}	Width (circumferential length) of one slot pitch of the end winding bundle (m)
$L_{Contact_Cu_Barrier}$	Contact thickness between the end winding and interface material (m)
$L_{Contact_Pipe_Barrier}$	Contact thickness between the pipe and interface material (m)
d_{pipe}	Pipe outer diameter (m)
L_{pipe}	Pipe wall thickness (m)
h_{pipe}	Convection coefficient of water flow in pipe (W/m^2K)
L_{junct}	Length of gap between top and bottom end winding bundles (m)

C.2 Thermal network models

The remainder of this appendix is figures of the thermal models. In the figures orange blocks represent the copper area, yellow is slot liner, grey is stator, blue is housing and water jacket and red are losses. Green is an interface, either between the top and bottom end winding layers or to the implemented cooling.

To include the full model at this scale it is very difficult to make out any specific components so a more "zoomed in" section is also shown for each figure.

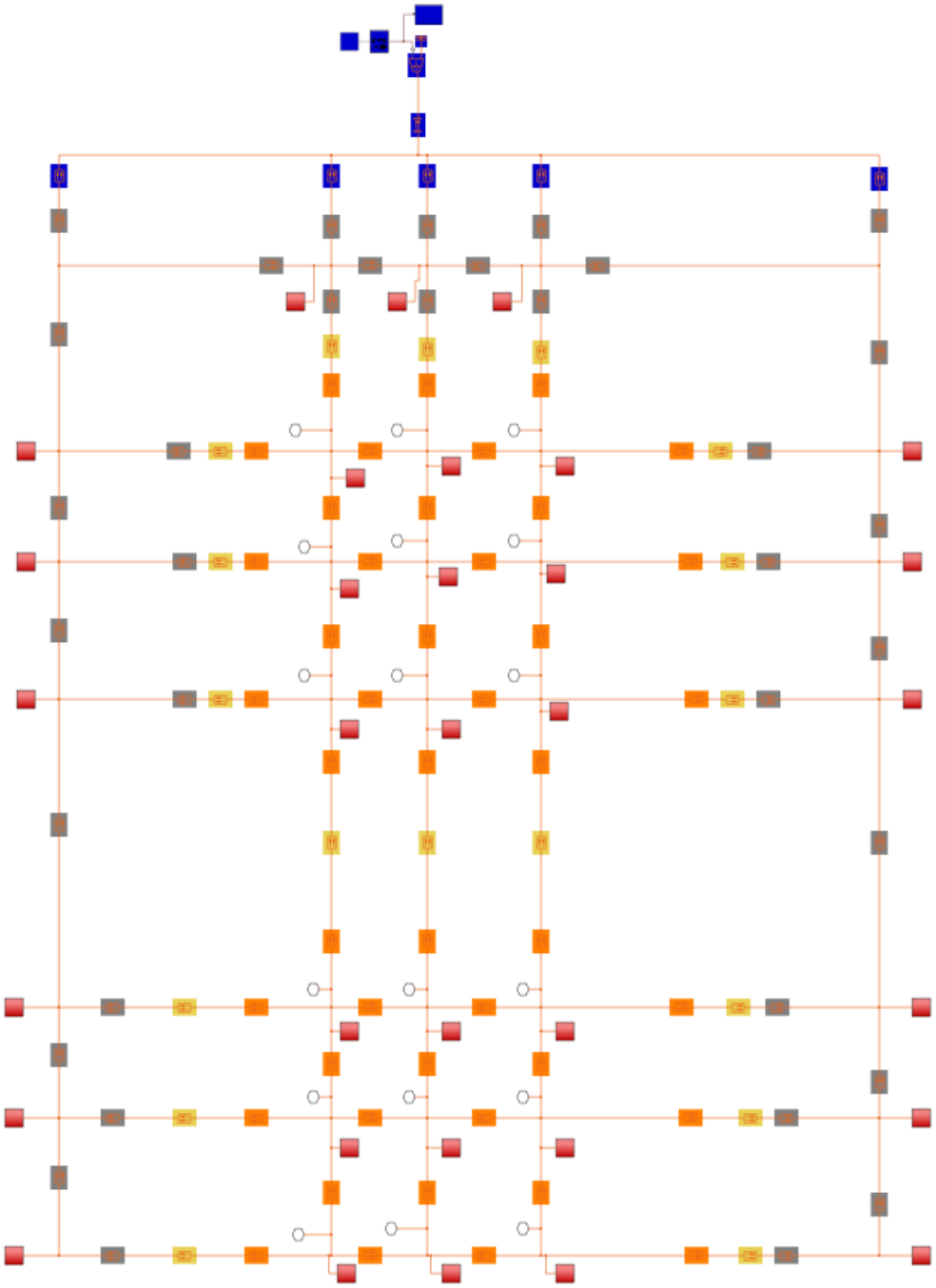


Figure C.1 - Full slot thermal network

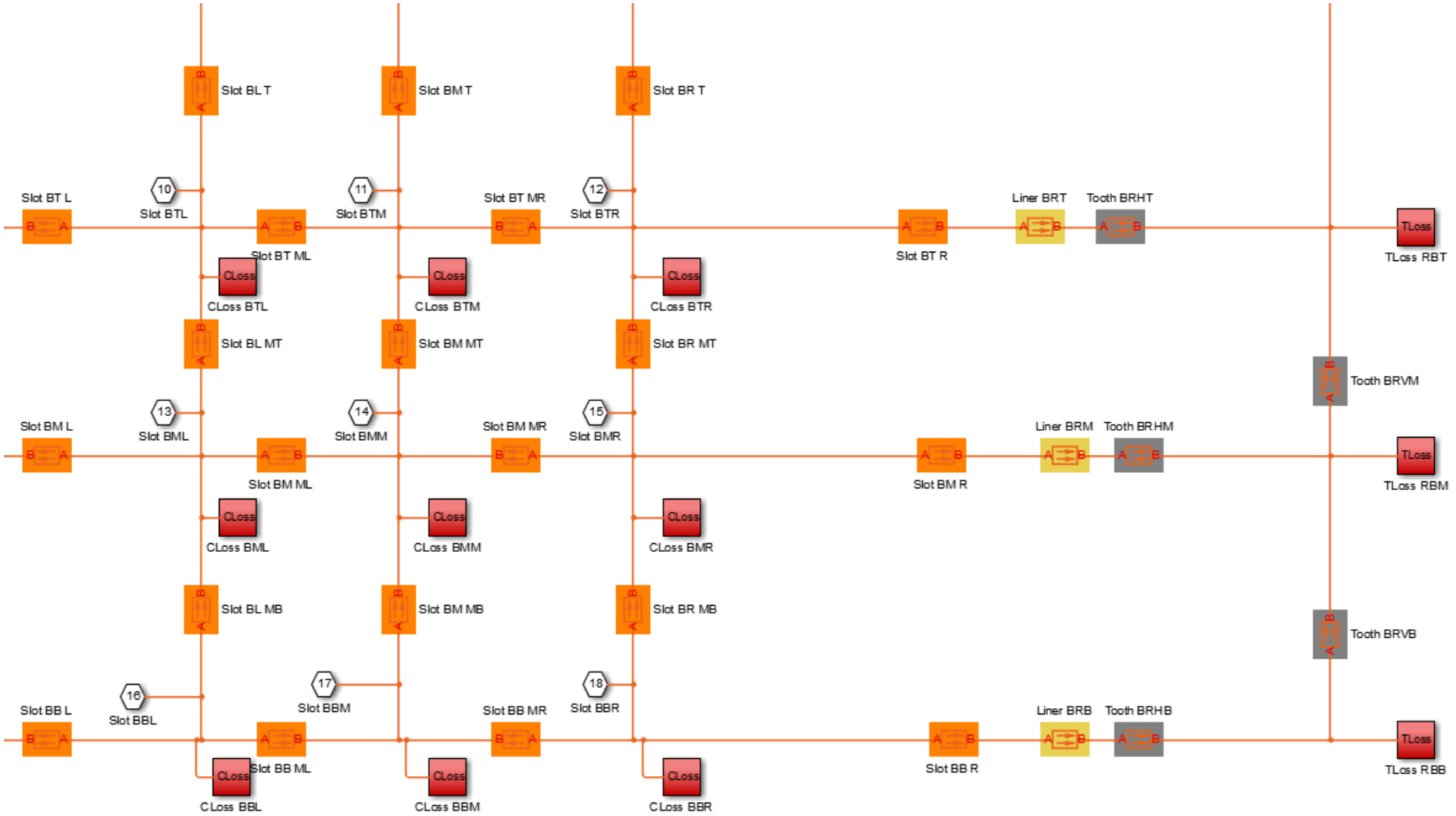


Figure C.2 - Detailed slot thermal network

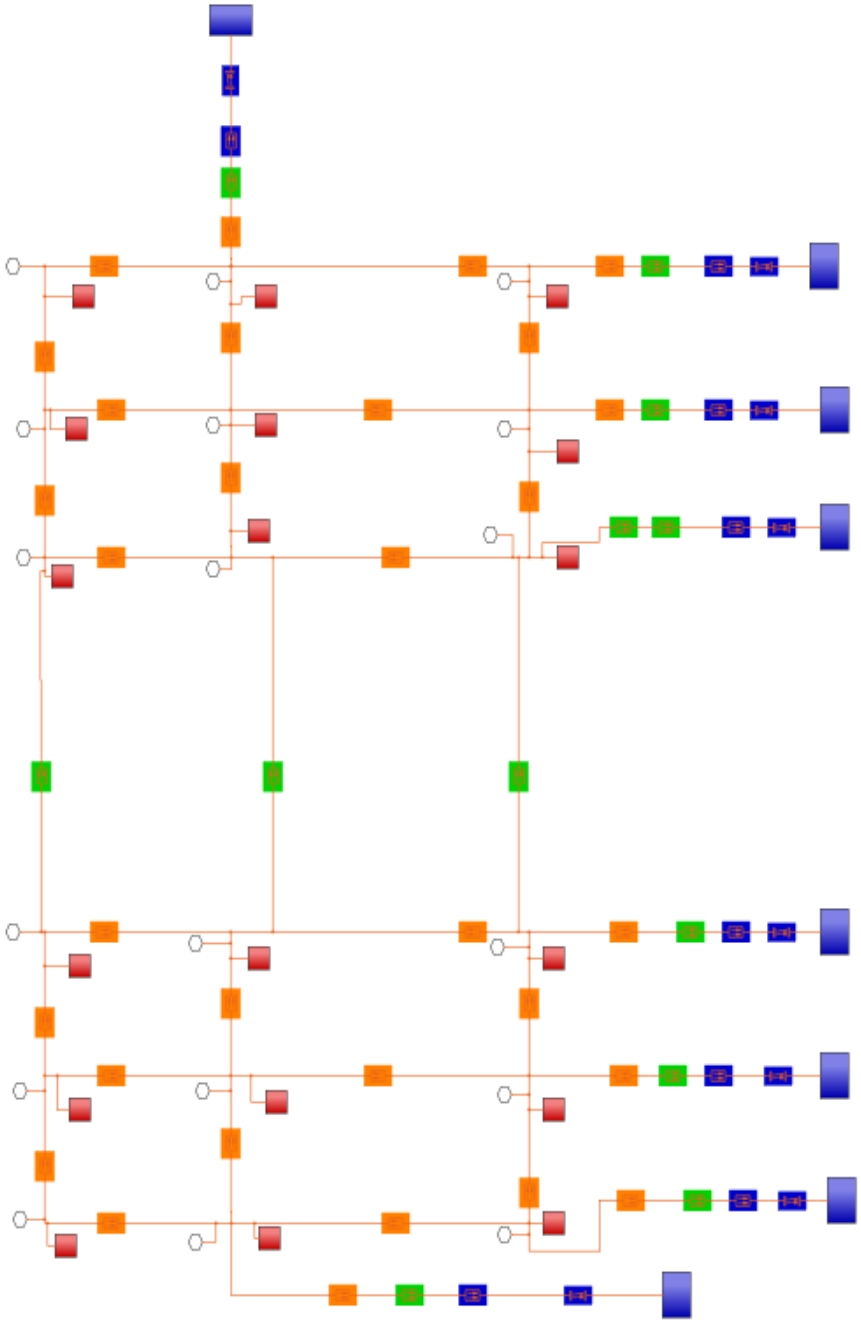


Figure C.3 - Full end winding thermal network

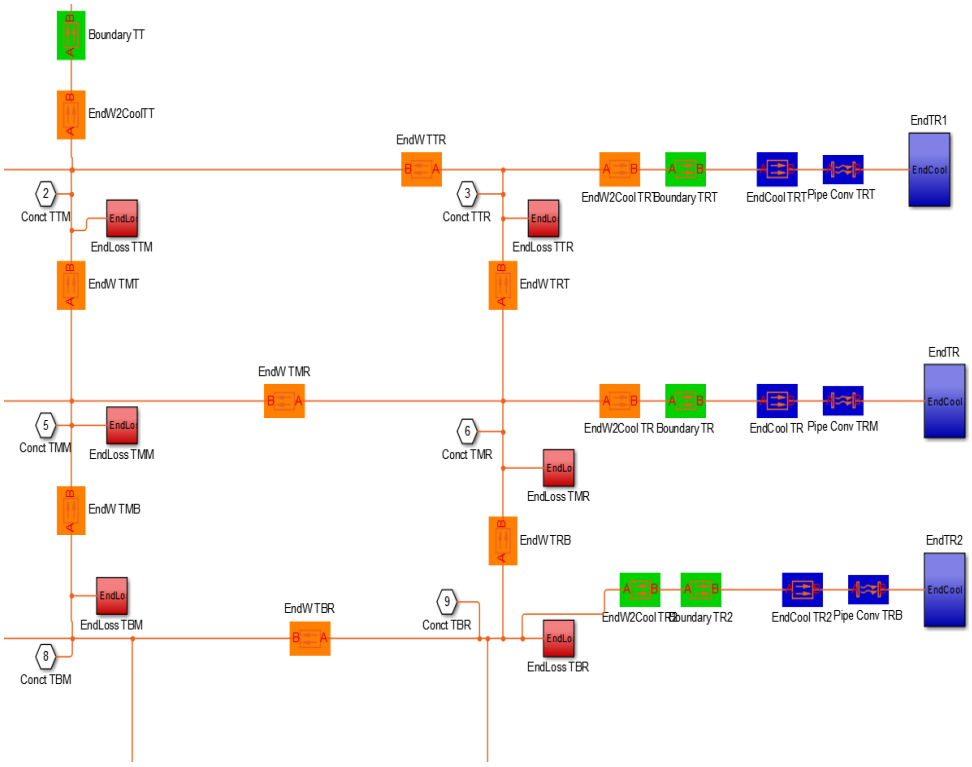


Figure C.4 - Detailed end winding thermal network

Both the slot network (Figure C.1 and Figure C.2) and the end winding network (Figure 6.13 and Figure C.3) are used as subsystems in the model. They are connected as can be seen in Figure C.5, with the central block being the slot subsystem, and the upper and lower being the two end windings. The orange blocks are the axial paths in the conductors. It was assumed that the temperature within the active length of the machine did not deviate a great deal axially and so only one slice was needed.

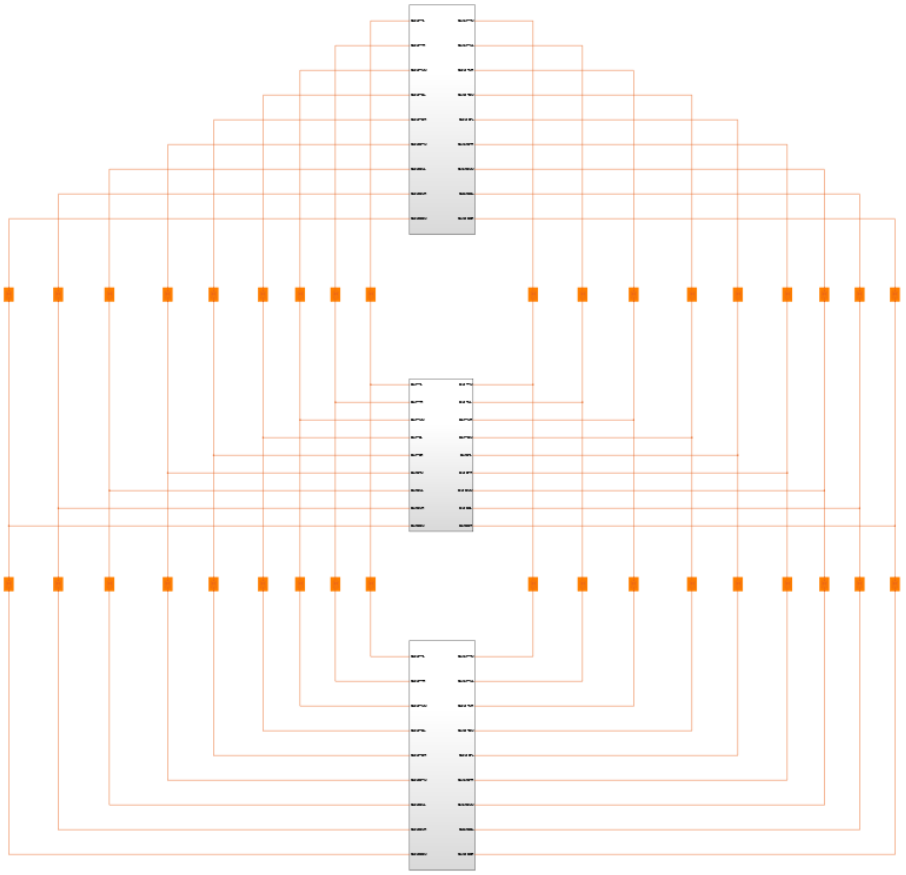


Figure C.5 - Connection between thermal network sections

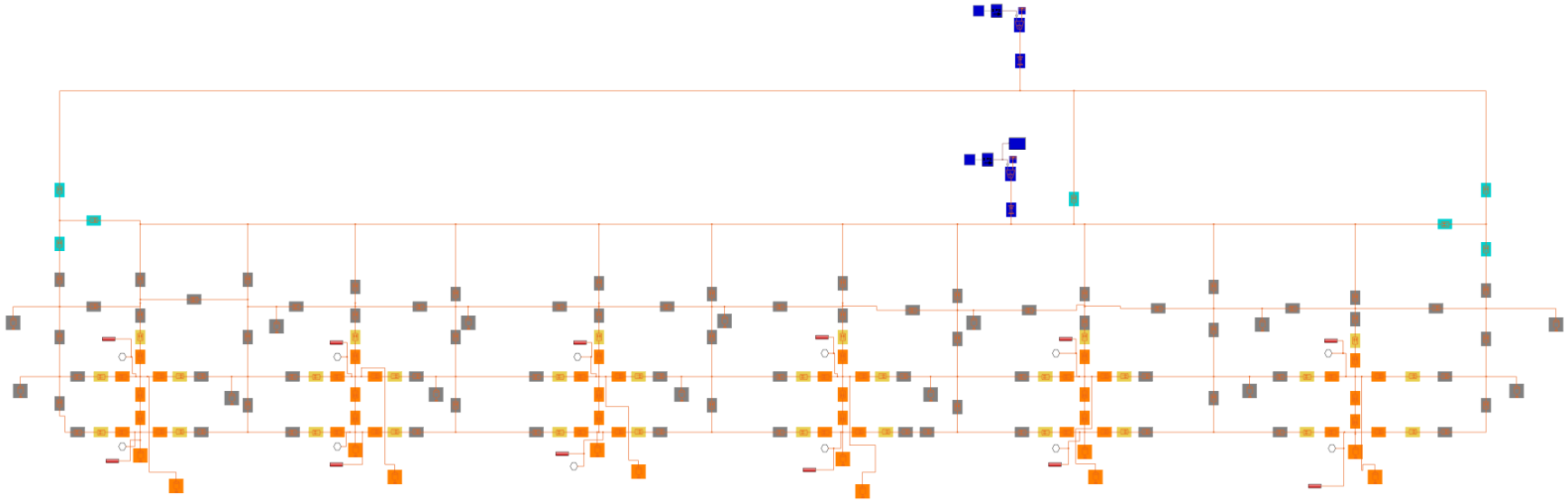


Figure C.6 - Dummy stator full slot model

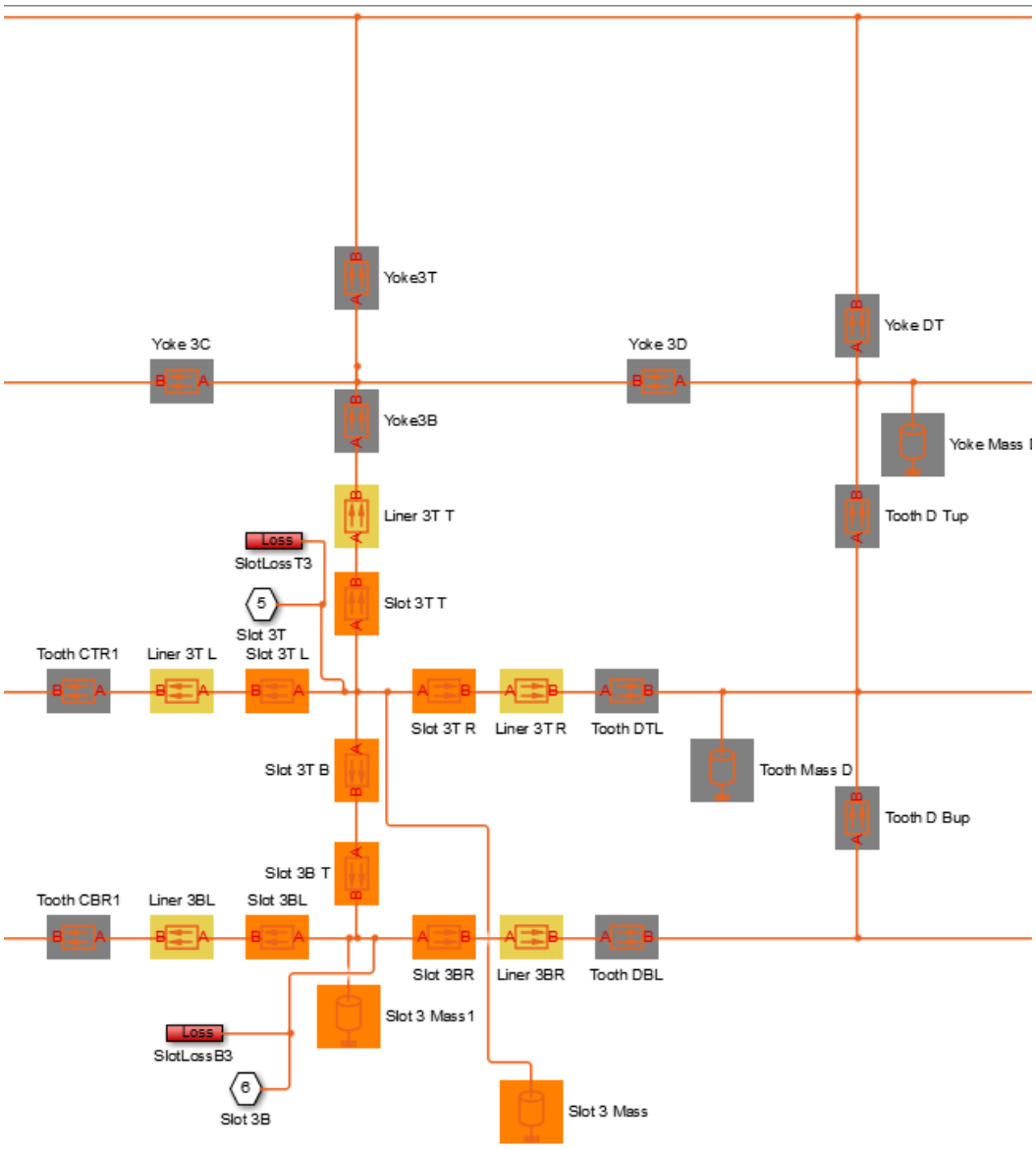


Figure C.7 – Dummy stator detailed slot model

The dummy stator slot model seen in Figure C.6 and Figure C.7 was used as a sub system in the full model shown in Figure C.8.

On the top side, which is uncooled, the natural convection blocks can be seen in blue, while on the bottom the potting compound can be seen in black and pipe cooling in blue. Again it is difficult to represent the model on this scale so a zoomed in section of the cooled end winding is shown in Figure C.9.

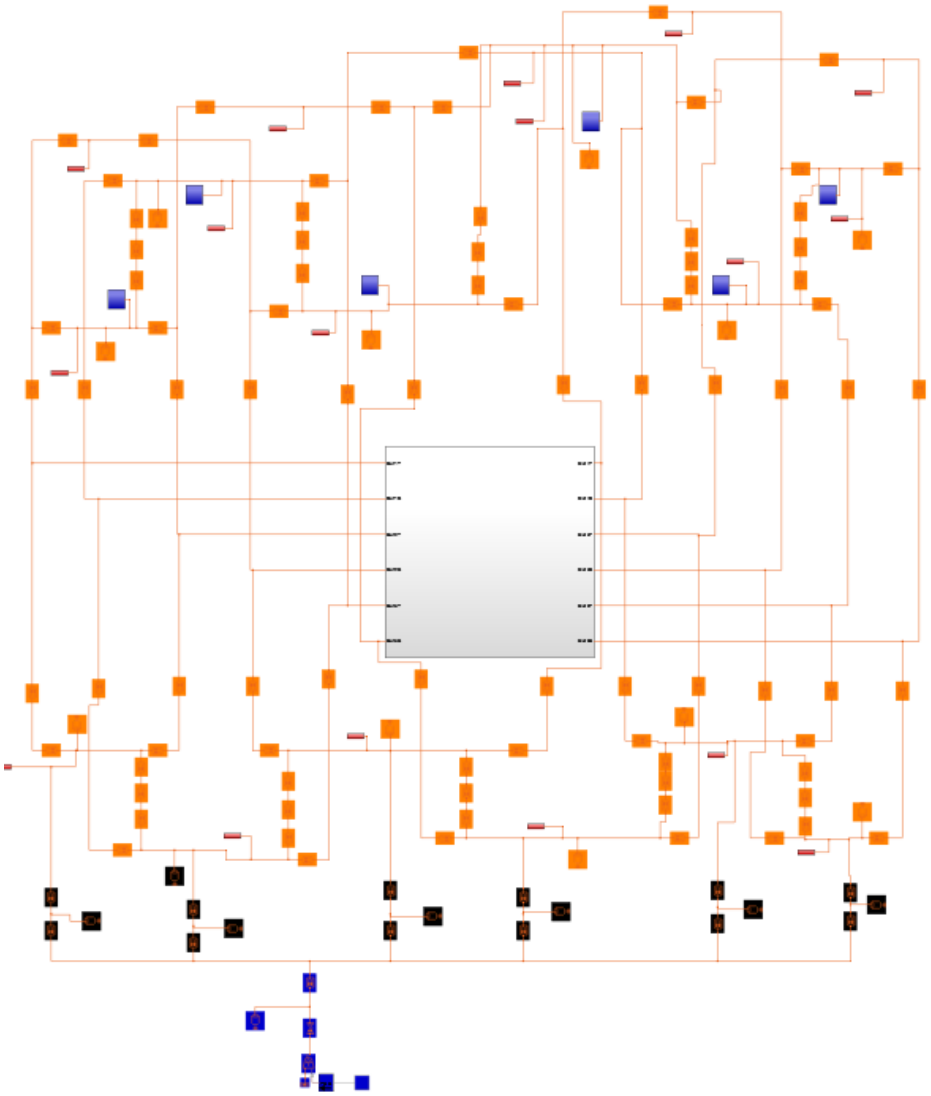


Figure C.8 - Dummy stator full end winding model with potting compound

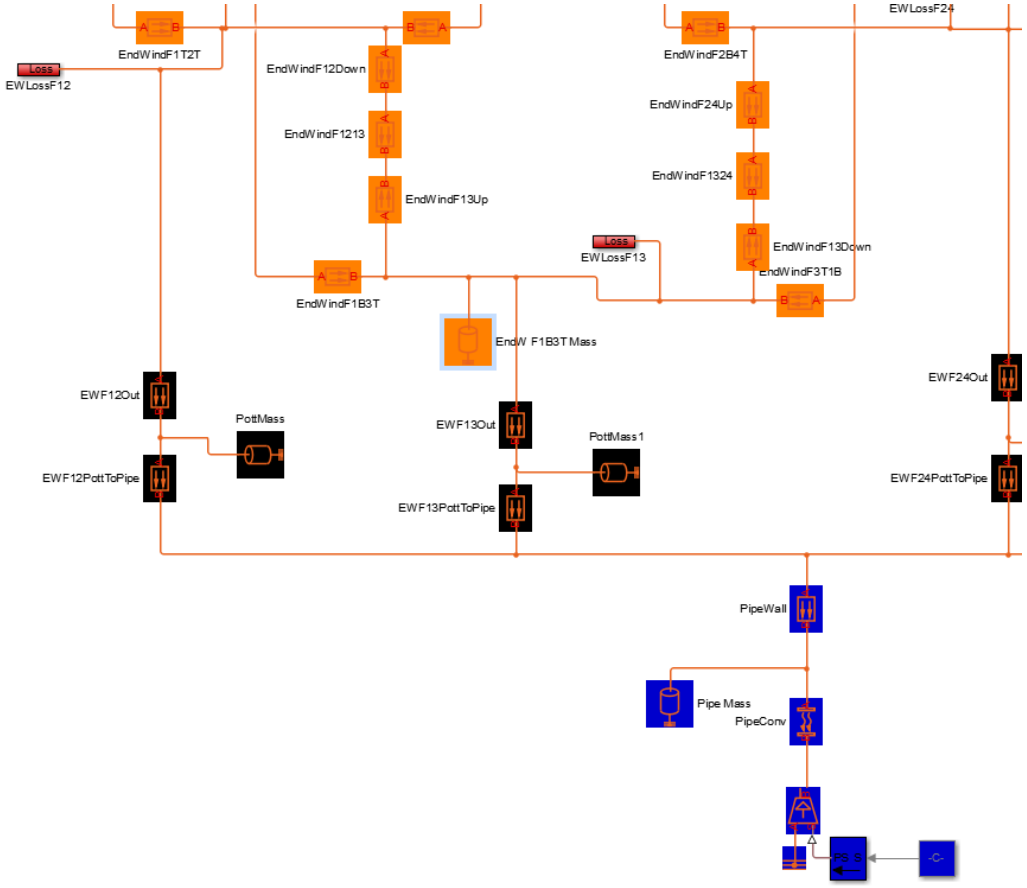


Figure C.9 - Dummy stator detailed end winding model with potting compound

Appendix D. Thermal experimental setup

This appendix details the setup of the thermal experiments detailed in Section 6.4.

The shape of the four central slots was based on the current stator design at that point. The motorette also included two extra larger slots, one on either side of the four. This meant that the desired winding configuration could be created in the four central slots, with any windings that would use any other slots in the configuration using these two extra slots. The design can be seen in Figure D.1. The stator was made out of non-laminated mild steel. This was cheaper and quicker to produce than a laminated stator and, because only DC currents were used, iron losses were not an issue.



Figure D.1 - Dummy stator design model

An aluminium water jacket was designed and created. This consisted of a single wide channel running circumferentially across the stator, with three inlets and outlets to distribute the water evenly. Figure D.2 shows the water jacket, with the base facing upwards. An O-ring was used to ensure there was a tight seal between the stator and water jacket.

A stand was built for the dummy stator to rest on. This was an aluminium frame used to support a thick layer of PTFE (yellow) on the base and sides of the dummy stator; the full model is shown in Figure D.3. The reasoning for the PTFE is that it has a very low thermal conductivity, removing the convection from the sides and conduction through the surface it was placed on, that would not be present in a full machine.

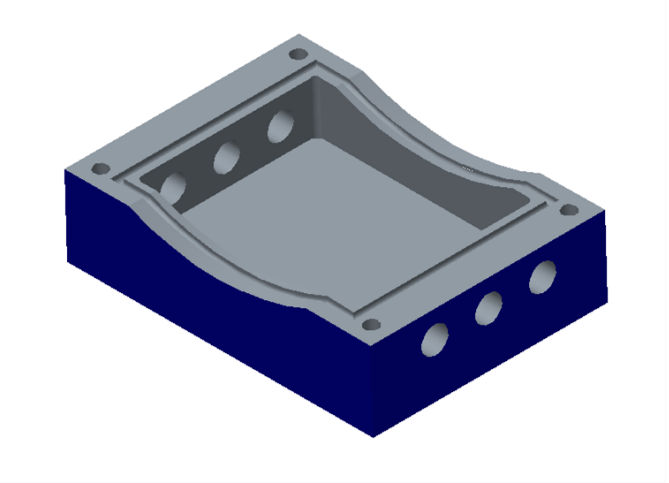


Figure D.2 - Water jacket model

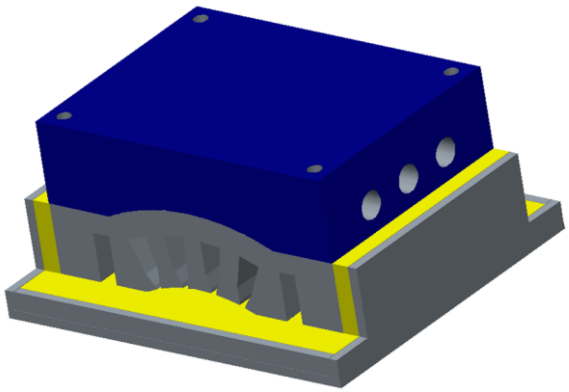


Figure D.3 - Complete dummy stator model

A network of pipes was used to allow one pump to supply water to all three inlets (and receive it from the three outlets). This pump also included a reservoir and cooling system. In the pipe network a tap was used to control the flow rate and also as a means to measure the inlet water temperature.

The winding was designed as if the dummy stator was a 3 phase 30 slot machine with a double layered distributed winding. Each coil was then connected in series to form a continuous path to allow for a single supply to be used to power the whole winding.

D.1 Materials

The stator was constructed from solid steel. Laminations were not required as only DC currents were used, so no iron losses were present. The windings were standard 1mm diameter copper conductors with H class insulation. When copper pipes are used these are standard copper, typically used for plumbing applications. The interesting material was the plastic pipe, what this actually refers to is the very thin walled (0.5mm) common grade silicone pipe detailed in section 6.2.1.

Different potting compound materials were considered to show the effect of the thermal conductivity on the cooling potential. To use this potting compound a mould had to be made, which allowed for the end windings and a pipe to be encased in the compound.

Appendix E. Thermal Model Calibration

This appendix gives the results of the optimisation of the difference between the thermal model and the experimental results detailed in Section 6.5

E.1 No cooling applied

With the test without any forced cooling, the main variables of interest were the heat transfer coefficients for the housing and end winding convection, documented values of air convection vary in a wide range even with analytical calculations [123]. There are also documented ranges for thermal conductance of the windings in slots, however these assume a very high fill factor and resin impregnated between the windings, which would have higher conductivity than the air between windings used here, and so this was included as a variable [123]. The area and thickness of the thermal paste used to connect the thermocouples to various parts of the dummy stator effected the recorded temperature, while not affecting the actual temperatures in the machine. The results for these variables are given in Table E.1.

Table E.1 - No cooling validation parameters

Variable	Result
Copper Thermal Conductance in slot (W/m^2K)	0.411
End winding convection heat transfer coefficient (W/m^2K)	2.56
Aluminium housing convection heat transfer coefficient (W/m^2K)	134
Thermocouple Thermal paste contact area (mm^2)	226.6
Thermocouple Thermal paste contact thickness (mm)	1.5

Table E.2 shows the steady state values and how small of an error was achieved. Typically, thermal models have some inaccuracy so anything below 3% has been deemed acceptable.

As can be seen in Table E.2, the simulated final values were within 1.7% of the experimental values, this was acceptable to consider this model validated. Of note was how low the copper thermal conductance was, this was due to the aforementioned low slot fill factor and lack of resin between the conductors.

The heat transfer coefficient from the housing was quite high; due to this also including the convection from the sections of the stator which were open to the air.

Table E.2 - Comparison of results - no cooling

Steady State Values	End Winding	Stator
Experimental (°C)	93.37	50.85
Simulation (°C)	91.82	50.98
Error (°C)	1.55	0.13
Error (%)	1.66	0.256

E.2 Water jacket cooling

Adding the water jacket cooling to the thermal network, there was only one new uncertain variable and that was the heat transfer coefficient for the convection of the water in the jacket. Again an idea of this could be obtained from literature but the specific value needed to be investigated [123]. The value found for this is shown in Table E.3.

Table E.3 – Water jacket validation parameters

Variable	Result
Water jacket convection heat transfer coefficient (W/m^2K)	5670

The differences between the experimental and simulation results for this are shown in Table E.4. The end winding temperature was almost perfect; however the stator temperature is less accurate. This was thought to be due to the surface temperature of the stator being measured whilst the centre was simulated, in further simulations this would be taken into account. However, because the stator was much cooler than the end windings, its temperature, while still important, was less critical.

Again the final values from the validation were very close to the experimental values for the end windings, with only small errors (less than 1%) as seen in Table E.4.

Table E.4 - Comparison of results water jacket

Steady State Values	End Winding	Stator
Experimental (°C)	78.85	32.29
Simulation (°C)	79.01	35.17
Error (°C)	0.16	2.88
Error (%)	0.203	8.92

E.3 With silicone pipe on the end winding surface

As described in Chapter 6, there were several different silicone pipe cooling layouts, so the variables had to be considered for each, however for the sake of brevity only the final layout (double pipe with thermal paste) will be analysed here. This had the pipe folded back on itself to create two contact areas in series, one on the top of the end windings and one on the outside. Thermal paste was then added between the pipe and end winding to increase the conduction between the two.

The variables considered here were the contact area for the pipe on the side and top of the end winding, the thickness of the thermal paste layer and the thermal conductivity of the thermal paste. As well as the conductivity of the silicone and the heat transfer coefficient to the pipe water. It was assumed that the thermal paste was the same thickness across all the contact areas, so the value in Table E.5 is an average thickness value.

Table E.5 – Double silicone pipe with paste validation parameters

Variable	Result
Pipe Contact Area Top (mm^2)	261.7
Pipe Contact Area Side (mm^2)	396.1
Pipe water heat transfer coefficient (W/m^2K)	280
Pipe Thermal Conductivity (W/m^2K)	80
Thermal Paste Thickness (mm)	3.5
Thermal Paste Conductivity (W/m^2K)	0.998

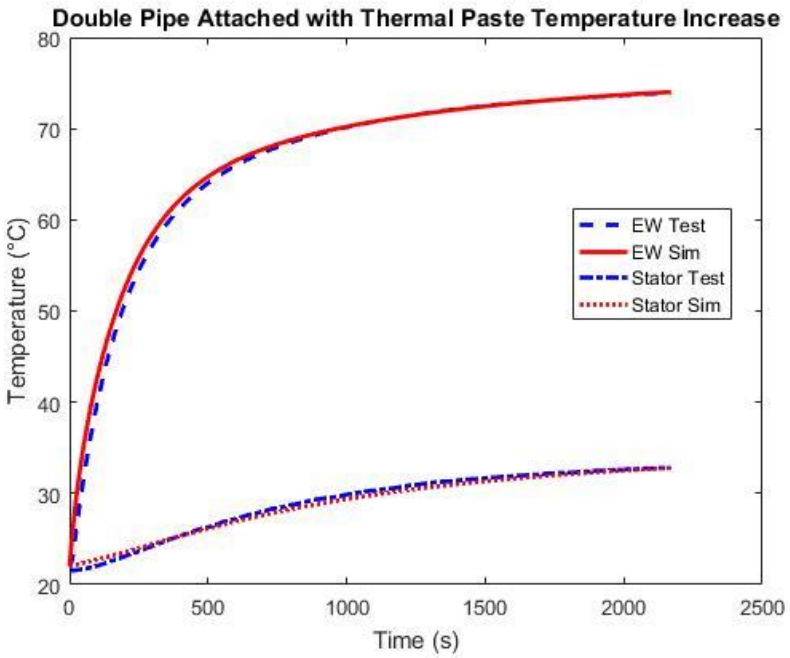


Figure E.1- Comparison of practical and simulation of double silicone pipe with paste cooling test

Figure E.1 shows the difference between the experimental temperatures and validated simulated results. The steady state values are compared further in Table E.6.

Table E.6– Comparison of Results Double Pipe with Paste

Steady State Values	End Winding	Stator
Experimental (°C)	73.93	32.82
Simulation (°C)	74.02	32.8
Error (°C)	0.09	0.02
Error (%)	0.12	0.06

Here, Figure E.1 and Table E.6, the values were very close, at steady state about 0.1% error for end winding temperature and lower than 0.1% error for stator temperature. Figure E.1 also shows that the difference was very small during the transient response.

E.4 Commercial potting compound

The first potting compound used was Robnor Resins PC439XS, with a claimed thermal conductivity of 1.3 W/mK and a max temperature of 200°C, which was

above the limit of the winding. The key factors to search for here, were the distance between the end winding and the pipe (calculated as an average), the actual thermal conductivity of the potting compound, and the heat transfer coefficient of the pipe. The results are given in Table E.7

Table E.7 –Commercial potting compound validation parameters

Variable	Result
Average Distance from Pipe to End Winding (mm)	17.1
Potting Compound Thermal Conductivity (W/mK)	0.92
Pipe water heat transfer coefficient (W/m²K)	1260

How well these values allowed the simulation to match with the experimental tests are given in Figure E.2 and Table E.8. These show a very good correlation between both steady state temperatures and the transient of the simulation. While there was still some difference in the slot result, it was within the expected limits of the model.

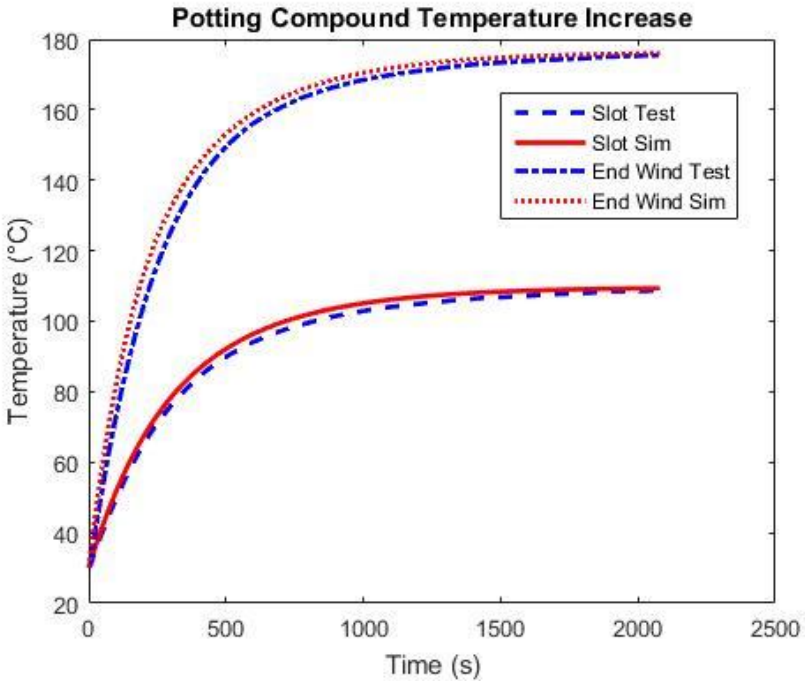


Figure E.2- Comparison of practical and simulation of commercial potting compound

To note here is the relatively large gap between the winding and the pipe, this was due to two issues. First the hole placement (for the pipe) in the mould was

not perfect, giving some distance between the windings and the pipe, this was the first mould used and so it was preferential to be further from the windings rather than too close (and therefore impossible to insert the pipe). The other was that the edge of the end windings had a curve to its surface, so while some points were closer, others were further away (this is an average value) this curve would typically be less prominent in a full machine. In addition, the thermal conductivity was below the specified amount, the specified values are often tested in perfect conditions for a small regular shape, and its ability to fill all the crevasses within the end windings would affect its perceived conductivity.

Table E.8– Comparison of results for commercial potting compound

Steady State Values	Slot	End Winding
Experimental (°C)	105.2	177.21
Simulation (°C)	107.56	177.35
Error (°C)	2.36	0.14
Error (%)	2.24	0.08

E.5 High performance potting compound

The high performance compound was Duralco 128, which claimed a thermal conductivity of 4.2 W/mK and a maximum temperature of 260°C. As this was based on the same set up as the commercial compound, only with a different compound, the same 3 parameters were investigated, with the results in Table E.9.

Table E.9 – High performance potting compound validation parameters

Variable	Result
Average Distance from Pipe to End Winding (mm)	16.1
Potting Compound Thermal Conductivity (W/mK)	1.62
Pipe water heat transfer coefficient (W/m^{2}K)	1260

The difference between the simulation and the experimental tests has been presented both graphically, in Figure E.3, and as steady state values in Table

E.10. Again a good match was seen between the two, particularly at steady state.

The same two issues occurred with this compound as with the commercial one. A significant distance between the end winding and pipe and that the potting compound did not meet the specified thermal conductance value in practice. The heat transfer coefficient was found to be the same as with the commercial compound, this correlation strengthened the certainty of this value.

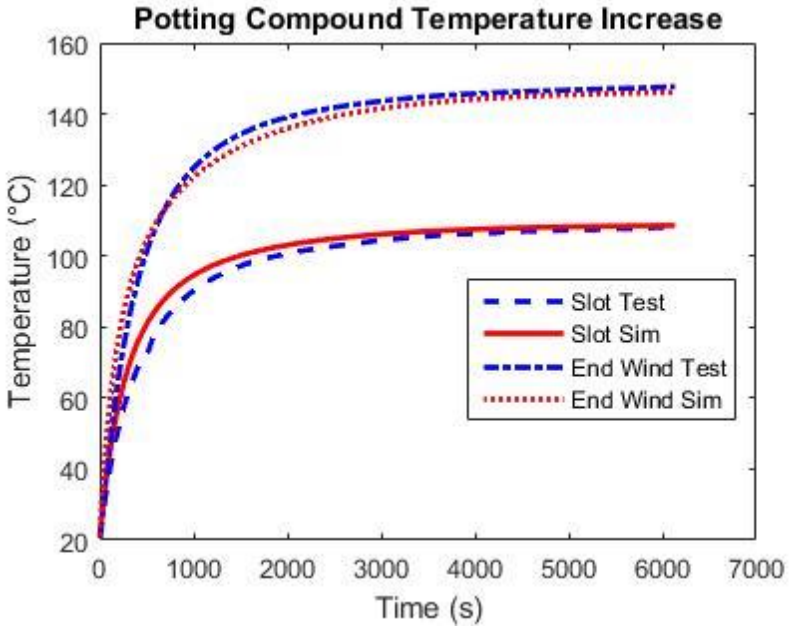


Figure E.3- Comparison of practical and simulation of high performance potting compound

Table E.10– Comparison of results for high performance potting compound

Steady State Values	Slot	End Winding
Experimental (°C)	126.8	163.5
Simulation (°C)	127.4	164.5
Error (°C)	0.6	1
Error (%)	0.47	0.611

E.6 Silicone pipe with modified end winding

The final method was the silicone pipe with modified end windings, this was tested without any thermal paste, just direct contact. This left three variables, the heat transfer coefficient of the pipe, and the contact areas, between the pipe

and the parallel surfaces of the gap and between the pipe and any additional perpendicular surfaces it expands to (called 'winding edge' in the table). The results for these are given in Table E.11.

Figure E.4 and Table E.12 give the comparisons with experimental results, again matching up within the accuracy tolerances.

Table E.11 – Silicone pipe with modified end windings validation parameters

Variable	Result
Pipe Contact Area Gap Surface (mm^2)	499
Pipe Contact Area End Winding Edge (mm^2)	162
Pipe water heat transfer coefficient (W/m^2K)	280

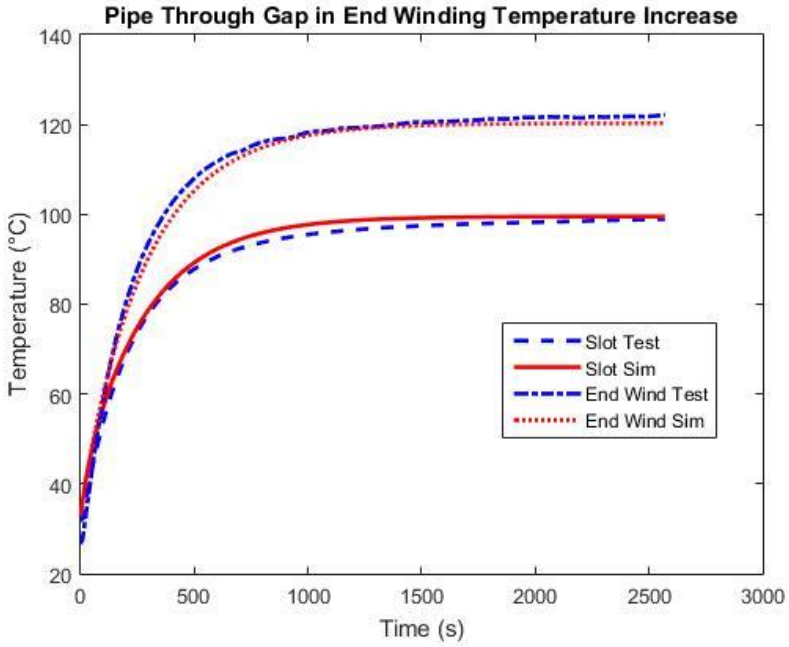


Figure E.4- Comparison of practical and simulation of the silicone pipe with modified end windings

Table E.12– Comparison of results for silicone pipe with modified end windings

Steady State Values	Slot	End Winding
Experimental (°C)	98.94	122.25
Simulation (°C)	99.53	120.28
Error (°C)	0.59	1.97
Error (%)	0.6	1.61

While the pipe expanded into more areas than was originally intended, the actual contact area produced by these was only one third of the contact area in the intended region. So while pictures such as Figure 6.17, show the benefit of the pipes expansion, it was not as significant as it appeared.

Appendix F. Machine engineering drawings

This appendix shows the technical drawings of the final machine including the housing. The colours are used to differentiate between the different components, (the housing will not actually be green), otherwise the majority of the components would be similar shades of grey.

Figure F.1 shows views of the full machine, while Figure F.2 is an axial cross section showing inside the machine. Figure F.3 gives radial cross sections showing the rotor and stator inside the housing layers. Both Figure F.4, another axial cross section, and Figure F.5, another outer view, show references to each component that has to be constructed, with names in

Table F.1. There are also components that are not labelled such as the bearing, pipes and spring rings, as these would be purchased and so did not have their own drawings that needed referencing.

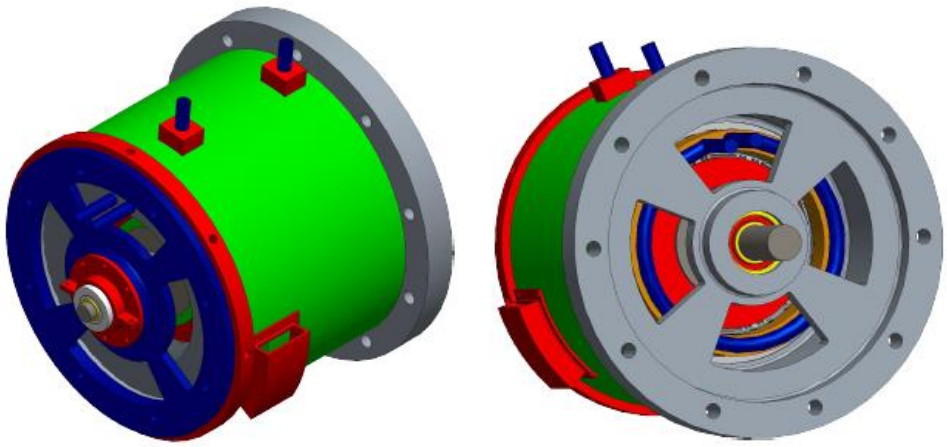


Figure F.1 - View of the full housed machine

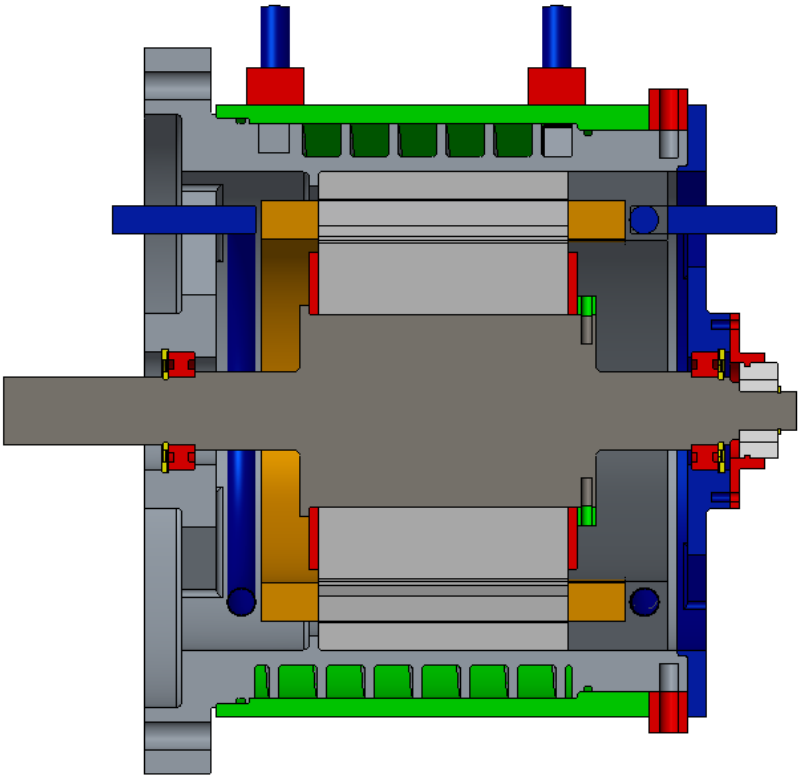


Figure F.2 - Coloured axial cross section of the final machine

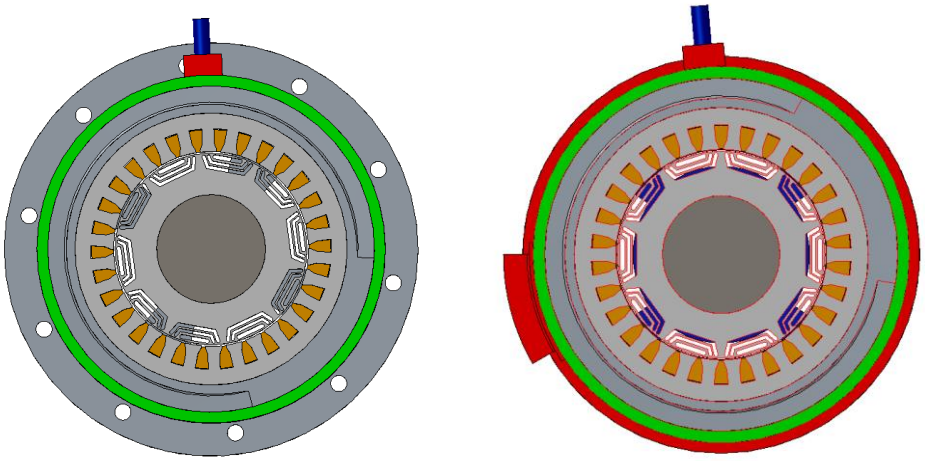


Figure F.3 - Radial cross sections of the final machine

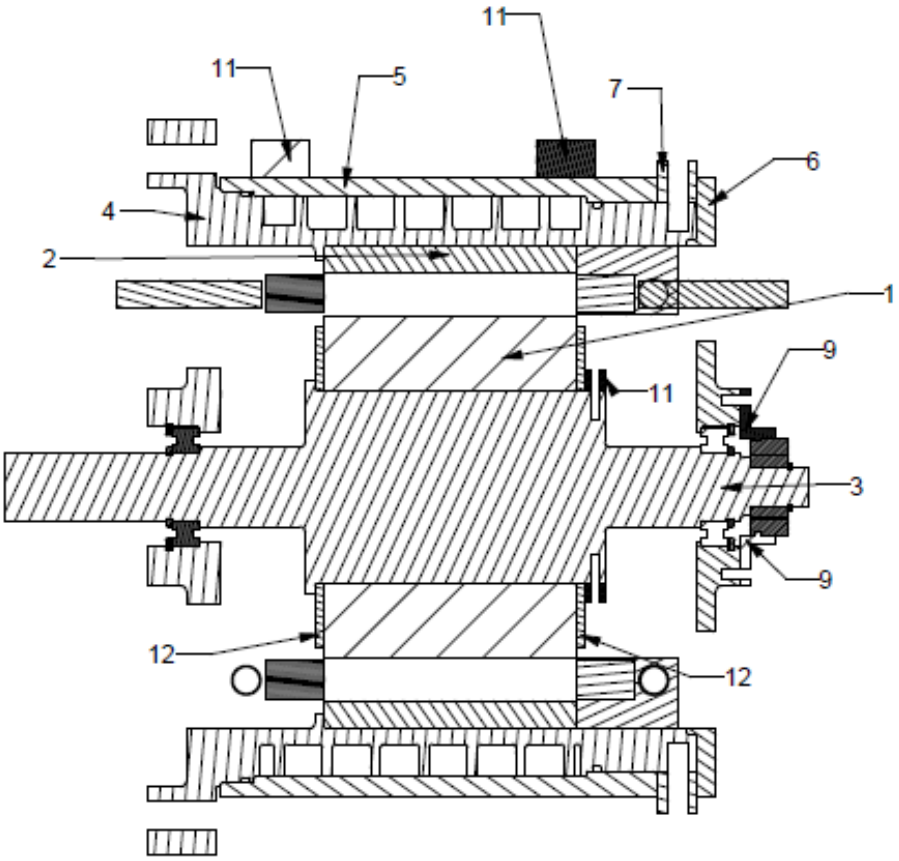


Figure F.4- Labelled axial cross section of the final machine

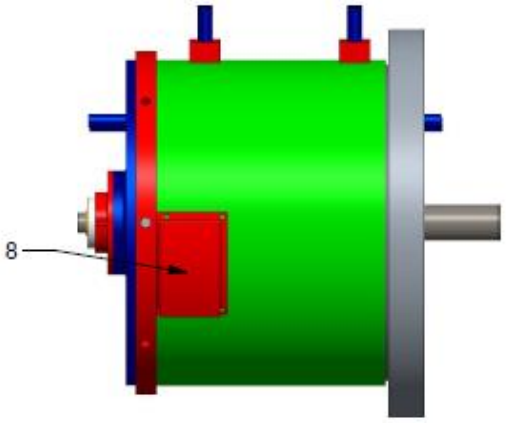


Figure F.5 - Labelled outer housing of the final machine

Table F.1 – Final machine component names

Number	Part
1	Rotor
2	Stator
3	Shaft
4	Housing Inner
5	Housing Outer
6	End Plate
7	Housing Ring
8	Winding Box
9	Resolver Housing
10	Rotor Ring
11	Water Jacket Inlet Block
12	Rotor Plate

The rotor and stator described in Chapter 7 are shown in Figure F.3, with Figure F.2 showing the end winding, along with the potting compound and the pipe, the potting compound is not shown on the left hand side to allow the pipe and end winding to be viewed easier. The shaft was designed to hold the rotor in place axially, to be able to withstand the mechanical forces and be sized for the appropriate bearings.

The inner and outer housings were designed to allow for an axial spiral water flow. The two steps in diameter are to allow for very tight tolerance around the O-rings with laxer control over the longer ribbed section, as fluid escaping into the adjacent channel is undesirable but not as catastrophic as it escaping past the O-rings. The left hand side of the housing, on Figure F.2 and Figure F.4, is a lip to allow the machine to be mounted to a plate, with holes in the centre to allow for access for thermocouples and viewing during operation as this was a prototype. The other axial end, right hand side, is open. To cover this there is the end plate, to be attached after the active part of the motor has been assembled, which has the same holes for access as the housing. Between the

outer housing and end plate there is the housing ring, to rigidly hold the outer housing in place, while the end plate is not attached. On the outside of the outer housing there is the winding box, to contain all the electrical connections, and the water jacket inlet pipes with blocks to allow for a welded connection.

The shaft has a lip to hold the rotor in place from one end, the other has a rotor ring which will be screwed in place. Between the rotor and these two structural components, there are rotor plates, to allow for the removal of material to balance the rotational section after completion. At either end of the shaft there are the bearings and on the very right hand side (Figure F.2 and Figure F.4) is the encoder, in its own separate housing. The encoder rotor, and bearings are held in place axially by carefully selected spring rings.

The rotor to shaft, stator to inner housing and inner housing to outer housing are all designed to use interface fittings. This is a slight overlap in the diameters, which causes the pressure between the two to hold the components in place.

Bibliography

[1] (2016). *The Price of Fuel - PetrolPrices.com*. Available: https://www.petrolprices.com/the-price-of-fuel.html

[2] i. j. n. JohnHenry.net. (2016). Available: http://www.racfoundation.org/data/uk-pump-prices-over-time

[3] M. A. Rahman, "Recent status on IPM traction drives for plug-in and hybrid electric vehicles," in *Power and Energy Society General Meeting, 2010 IEEE*, 2010, pp. 1-6.

[4] A. M. El-Refaie, "Motors/Generators for Traction/Propulsion Applications: A Review," *Vehicular Technology Magazine, IEEE*, vol. 8, pp. 90-99, 2013.

[5] (2016). *Reducing CO2 emissions from passenger cars - European Commission*. Available: http://ec.europa.eu/clima/policies/transport/vehicles/cars/index_en.htm

[6] edking_Ch. (2015). *Falling battery prices boost outlook for electric vehicles | Climate Home - climate change news*. Available: http://www.climatechangenews.com/2015/03/23/falling-battery-prices-boost-outlook-for-electric-vehicles/

[7] N. Denis, M. R. Dubois, K. A. Gil, T. Driant, and A. Desrochers, "Range prediction for a three-wheel plug-in hybrid electric vehicle," in *Transportation Electrification Conference and Expo (ITEC), 2012 IEEE*, 2012, pp. 1-6.

[8] M. Yilmaz and P. T. Krein, "Review of Battery Charger Topologies, Charging Power Levels, and Infrastructure for Plug-In Electric and Hybrid Vehicles," *Power Electronics, IEEE Transactions on*, vol. 28, pp. 2151-2169, 2013.

[9] (2016). *Here's How Electric Cars Will Cause the Next Oil Crisis*. Available: http://www.bloomberg.com/features/2016-ev-oil-crisis/

[10] M. Farhadi and O. Mohammed, "Energy Storage Technologies for High-Power Applications," *IEEE Transactions on Industry Applications*, vol. 52, pp. 1953-1961, 2016.

[11] P. Keil, M. Englberger, and A. Jossen, "Hybrid Energy Storage Systems for Electric Vehicles: An Experimental Analysis of Performance Improvements at Subzero Temperatures," *IEEE Transactions on Vehicular Technology*, vol. 65, pp. 998-1006, 2016.

[12] F. A. Rusu and G. Livint, "Study of hybrid power sources for electrical vehicles," in *2016 International Conference on Development and Application Systems (DAS)*, 2016, pp. 176-179.

[13] R. Gu, P. Malysz, and A. Emadi, "A novel battery/ ultracapacitor hybrid energy storage system analysis based on physics-based lithium-ion battery modeling," in *Transportation Electrification Conference and Expo (ITEC), 2015 IEEE*, 2015, pp. 1-6.

[14] U. S. Department of Energy, "FY 2011 Vehicle Technologies Program Wide Funding Opportunity Announcement Funding Opportunity Number: DE-FOA-0000239," ed, 2011, pp. 17-18.

[15] C. Ruiwu, C. Mi, and C. Ming, "Quantitative Comparison of Flux-Switching Permanent-Magnet Motors With Interior Permanent Magnet Motor for EV, HEV, and PHEV Applications," *Magnetics, IEEE Transactions on,* vol. 48, pp. 2374-2384, 2012.

[16] Y. Amara, L. Vido, M. Gabsi, E. Hoang, A. Hamid Ben Ahmed, and M. Lecrivain, "Hybrid Excitation Synchronous Machines: Energy-Efficient Solution for Vehicles Propulsion," *Vehicular Technology, IEEE Transactions on,* vol. 58, pp. 2137-2149, 2009.

[17] J. Yun-Ho, K. Kwangdeok, K. Yong-Jae, P. Byung-Sup, and J. Sang-Yong, "Design characteristics of PMa-SynRM and performance comparison with IPMSM based on numerical analysis," in *Electrical Machines (ICEM), 2012 XXth International Conference on*, 2012, pp. 164-170.

[18] Intemag. (2015, 16/05/16). *Rare Earth Ore Prices Stable*. Available: http://www.intemag.com/uploads/Rare%20Earth%20Pricing%20Bulletin.pdf

[19] (2016). *New standards for rare earth sector - People's Daily Online*. Available: http://en.people.cn/90001/90778/90860/7253040.html

[20] CeciliaJamasmie. (2016). *Rare earths prices rise as China builds reserves, tackles illegal mining | MINING.com*. Available: http://www.mining.com/rare-earths-prices-rise-as-china-builds-reserves-tackles-illegal-mining/

[21] (2016). *WTO | dispute settlement - the disputes - DS431*. Available: https://www.wto.org/english/tratop_e/dispu_e/cases_e/ds431_e.htm

[22] (2016). *Top 10 EVs With the Longest Range - Autotrader*. Available: http://www.autotrader.com/best-cars/top-10-evs-with-the-longest-range-221440

[23] (2015). *11 Electric Cars With Most Range*. Available: http://evobsession.com/electric-car-range-comparison/

[24] U. S. D. o. Energy, "Fuel Economy Guide," D. o. Energy, Ed., ed, 2016.

[25] U. S. D. o. Energy. (2017). *Chevrolet Spark EV Equivalent Fuel Economy*. Available: http://www.fueleconomy.gov/feg/Find.do?action=sbs&id=33640

[26] U. S. D. o. Energy. (2017). *BMW i3 Equivalent Fuel Economy*. Available: http://www.fueleconomy.gov/feg/Find.do?action=sbs&id=36030&id=37222&id=38229&id=38001

[27] U. S. D. o. Energy. (2017). *Nissan Leaf Equivalent Fuel Economy*. Available: http://www.fueleconomy.gov/feg/Find.do?action=sbs&id=37066&id=37067&id=34918&id=34699

[28] P. Kulkarni, "Review of Hybrid Electrical Vehicles," *International Journal of Emerging Research in Management &Technology*, vol. 4, pp. 24-31, March 2015 2015.

[29] ERTRAC, "European Roadmap - Hybridisation of Road Transport " ERTRACJune 2011 2011.

[30] (2016). *Department for Transport - GOV.UK*. Available: https://www.gov.uk/government/organisations/department-for-transport

[31] L. CVP, "Transport Roadmaps - A guide to low carbon vehicle, energy and infrastructure roadmaps," D. o. Transport, Ed., ed, 2015.

[32] "Renewable Energy Directive (Directive 2009/28/EC)," *Official Journal of the European Union* vol. 52, pp. 16-62, 23 April 2009 2009.

[33] (2016). *Advanced Propulsion Centre*. Available: http://www.apcuk.co.uk/

[34] (2016). *Horizon 2020 - European Commission*. Available: https://ec.europa.eu/programmes/horizon2020/

[35] E. Commission. (2016). *H2020-GV-2016-2017*. Available: https://ec.europa.eu/research/participants/portal/desktop/en/opportunities/h2020/calls/h2020-gv-2016-2017.html#c,topics=callIdentifier/t/H2020-GV-2016-2017/1/1/1/default-group&callStatus/t/Forthcoming/1/1/0/default-group&callStatus/t/Open/1/1/0/default-group&callStatus/t/Closed/1/1/0/default-group&+identifier/desc

[36] Z. A. Needell, J. McNerney, M. T. Chang, and J. E. Trancik, "Potential for widespread electrification of personal vehicle travel in the United States," *Nature Energy*, vol. 1, p. 16112, 08/15/online 2016.

[37] M. Degano, "Advanced Electrical Machines H64AEM Lecture Slides," ed. University of Nottingham, 2016.

[38] D. Gerada, A. Mebarki, R. P. Mokhadkar, N. L. Brown, and C. Gerada, "Design issues of high-speed permanent magnet machines for high-temperature applications," in *Electric Machines*

and Drives Conference, 2009. IEMDC '09. IEEE International, 2009, pp. 1036-1042.

[39] D. Gerada, A. Mebarki, N. L. Brown, C. Gerada, A. Cavagnino, and A. Boglietti, "High-Speed Electrical Machines: Technologies, Trends, and Developments," *IEEE Transactions on Industrial Electronics,* vol. 61, pp. 2946-2959, 2014.

[40] V. Ostovic, "Memory motors-a new class of controllable flux PM machines for a true wide speed operation," in *Industry Applications Conference, 2001. Thirty-Sixth IAS Annual Meeting. Conference Record of the 2001 IEEE*, 2001, pp. 2577-2584 vol.4.

[41] W. L. Soong, P. B. Reddy, A. M. El-Refaie, T. M. Jahns, and N. Ertugrul, "Surface PM Machine Parameter Selection for Wide Field-Weakening Applications," in *Industry Applications Conference, 2007. 42nd IAS Annual Meeting. Conference Record of the 2007 IEEE*, 2007, pp. 882-889.

[42] P. B. Reddy, A. M. El-Refaie, H. Kum-Kang, J. K. Tangudu, and T. M. Jahns, "Comparison of Interior and Surface PM Machines Equipped With Fractional-Slot Concentrated Windings for Hybrid Traction Applications," *Energy Conversion, IEEE Transactions on,* vol. 27, pp. 593-602, 2012.

[43] J. K. Tangudu and T. M. Jahns, "Comparison of interior PM machines with concentrated and distributed stator windings for traction applications," in *Vehicle Power and Propulsion Conference (VPPC), 2011 IEEE*, 2011, pp. 1-8.

[44] A. M. El-Refaie, J. P. Alexander, S. Galioto, P. Reddy, H. Kum-Kang, P. de Bock*, et al.*, "Advanced high power-density interior permanent magnet motor for traction applications," in *Energy Conversion Congress and Exposition (ECCE), 2013 IEEE*, 2013, pp. 581-590.

[45] A. Vagati, G. Pellegrino, and P. Guglielmi, "Comparison between SPM and IPM motor drives for EV application," in *Electrical Machines (ICEM), 2010 XIX International Conference on*, 2010, pp. 1-6.

[46] K. T. Chau, C. C. Chan, and L. Chunhua, "Overview of Permanent-Magnet Brushless Drives for Electric and Hybrid Electric Vehicles," *Industrial Electronics, IEEE Transactions on,* vol. 55, pp. 2246-2257, 2008.

[47] J. B. Bartolo, Z. He, D. Gerada, L. De Lillo, and C. Gerada, "High speed electrical generators, application, materials and design," in *Electrical Machines Design Control and Diagnosis (WEMDCD), 2013 IEEE Workshop on*, 2013, pp. 47-59.

[48] M. Galea, T. Hamiti, and C. Gerada, "Torque density improvements for high performance machines," in *Electric*

Machines & Drives Conference (IEMDC), 2013 IEEE International, 2013, pp. 1066-1073.

[49] Cummins Generator Technologies. (2012, 31/10/2014). *Cummins Motor Generator with CorePlus™ Technology*. Available: https://www.cumminsgeneratortechnologies.com/www/en/referenceapplications/hybrid/CumminsMotorGenerator_Brochure.pdf

[50] M. Norhisam, A. Nazifah, I. Aris, H. Wakiwaka, and M. Nirei, "Effect of magnet size on torque characteristic of three phase permanent magnet brushless DC motor," in *Research and Development (SCOReD), 2010 IEEE Student Conference on*, 2010, pp. 293-296.

[51] M. Jalalifar, A. F. Payam, B. Mirzaeian, and S. M. S. Nezhad, "Dynamic Modeling and Simulation of an Induction Motor with Adaptive Backstepping Design of an Input-Output Feedback Linearization Controller in Series Hybrid Electric Vehicle," in *Power Electronics, Drives and Energy Systems, 2006. PEDES '06. International Conference on*, 2006, pp. 1-6.

[52] X. Wei, Z. Jianguo, G. Youguang, W. Shuhong, W. Yi, and S. Zhanghai, "Survey on electrical machines in electrical vehicles," in *Applied Superconductivity and Electromagnetic Devices, 2009. ASEMD 2009. International Conference on*, 2009, pp. 167-170.

[53] D. Gerada, D. Borg-Bartolo, A. Mebarki, C. Micallef, N. L. Brown, and C. Gerada, "Electrical machines for high speed applications with a wide constant-power region requirement," in *Electrical Machines and Systems (ICEMS), 2011 International Conference on*, 2011, pp. 1-6.

[54] W. Wang and B. Fahimi, "Comparative study of electric drives for EV/HEV propulsion system," in *Electrical Systems for Aircraft, Railway and Ship Propulsion (ESARS), 2012*, 2012, pp. 1-6.

[55] K. Nakamura, K. Murota, and O. Ichinokura, "Characteristics of a novel switched reluctance motor having permanent magnets between the stator pole-tips," in *Power Electronics and Applications, 2007 European Conference on*, 2007, pp. 1-5.

[56] J. B. Bartolo and C. Gerada, "The electromagnetic design of a high speed, 45kW, switched reluctance machine having a novel rotor geometry for aerospace application," in *Electrical Machines (ICEM), 2014 International Conference on*, 2014, pp. 2513-2519.

[57] K. Watanabe, S. Aida, A. Komatsuzaki, and I. Miki, "Driving force characteristics of 40kW switched reluctance motor for electric vehicle," in *Electrical Machines and Systems, 2007. ICEMS. International Conference on*, 2007, pp. 1894-1898.

[58] B. Bilgin, A. Emadi, and M. Krishnamurthy, "Comprehensive Evaluation of the Dynamic Performance of a 6/10 SRM for Traction Application in PHEVs," *Industrial Electronics, IEEE Transactions on*, vol. 60, pp. 2564-2575, 2013.

[59] P. Giangrande, D. Ronchetto, G. Pellegrino, F. Cupertino, C. Gerada, and M. Sumner, "Hybrid sensorless control of axial flux permanent magnet motor drives, including zero speed," in *Power Electronics and Applications (EPE 2011), Proceedings of the 2011-14th European Conference on*, 2011, pp. 1-8.

[60] C. Versele, Z. De Greve, F. Vallee, R. Hanuise, O. Deblecker, M. Delhaye, *et al.*, "Analytical design of an axial flux permanent magnet in-wheel synchronous motor for electric vehicle," in *Power Electronics and Applications, 2009. EPE '09. 13th European Conference on*, 2009, pp. 1-9.

[61] T. Arakawa, M. Takemoto, S. Ogasawara, K. Inoue, O. Ozaki, H. Hojo, *et al.*, "Examination of an Interior Permanent Magnet Type Axial Gap Motor for the Hybrid Electric Vehicle," *Magnetics, IEEE Transactions on*, vol. 47, pp. 3602-3605, 2011.

[62] A. Mebarki, D. Gerada, and N. L. Brown, "Analysis of an axial PM flux machine with field weakening capability for engine integration," in *Power Electronics, Machines and Drives (PEMD 2014), 7th IET International Conference on*, 2014, pp. 1-6.

[63] L. Kaiyuan and E. Ritchie, "Preliminary comparison study of drive motor for electric vehicle application," in *Electrical Machines and Systems, 2001. ICEMS 2001. Proceedings of the Fifth International Conference on*, 2001, pp. 995-998 vol.2.

[64] M. Gartner, P. Seibold, and N. Parspour, "Laminated circumferential transverse flux machines - lamination concept and applicability to electrical vehicles," in *Electric Machines & Drives Conference (IEMDC), 2011 IEEE International*, 2011, pp. 831-837.

[65] E. Padurariu, L. E. Somesan, I. Viorel, and L. Szabo, "Large power permanent magnet transverse flux motor, steady-state and dynamic behavior," in *ELEKTRO, 2012*, 2012, pp. 221-224.

[66] T. Raminosoa, C. Gerada, and M. Galea, "Design Considerations for a Fault-Tolerant Flux-Switching Permanent-Magnet Machine," *Industrial Electronics, IEEE Transactions on*, vol. 58, pp. 2818-2825, 2011.

[67] M. Galea, C. Gerada, and T. Hamiti, "Design considerations for an outer rotor, field wound, flux switching machine," in *Electrical Machines (ICEM), 2012 XXth International Conference on*, 2012, pp. 171-176.

[68] H. Wei, C. Ming, and Z. Gan, "A Novel Hybrid Excitation Flux-Switching Motor for Hybrid Vehicles," *Magnetics, IEEE Transactions on,* vol. 45, pp. 4728-4731, 2009.

[69] T. Raminosoa, A. El-Refaie, P. Di, H. Kum-Kang, J. Alexander, K. Grace, *et al.*, "Reduced rare-earth flux switching machines for traction applications," in *Energy Conversion Congress and Exposition (ECCE), 2014 IEEE*, 2014, pp. 318-327.

[70] J. Malan, M. J. Kamper, and P. N. T. Williams, "Reluctance synchronous machine drive for hybrid electric vehicle," in *Industrial Electronics, 1998. Proceedings. ISIE '98. IEEE International Symposium on*, 1998, pp. 367-372 vol.2.

[71] M. M. A. Ansari, W. A. Cronje, and A. Meyer, "Evaluation of a Reluctance Synchronous Motor: For use in an Electric Mine Shuttle Vehicle (EMSV)," in *Electric Vehicle Conference (IEVC), 2012 IEEE International*, 2012, pp. 1-6.

[72] F. Cupertino, G. M. Pellegrino, E. Armando, and C. Gerada, "A SyR and IPM machine design methodology assisted by optimization algorithms," in *Energy Conversion Congress and Exposition (ECCE), 2012 IEEE*, 2012, pp. 3686-3691.

[73] G. Pellegrino, F. Cupertino, and C. Gerada, "Automatic Design of Synchronous Reluctance Motors focusing on Barrier Shape Optimization," *Industry Applications, IEEE Transactions on,* vol. PP, pp. 1-1, 2014.

[74] M. Obata, S. Morimoto, M. Sanada, and Y. Inoue, "Characteristic of PMASynRM with ferrite magnets for EV/HEV applications," in *Electrical Machines and Systems (ICEMS), 2012 15th International Conference on*, 2012, pp. 1-6.

[75] N. Sakamaki and I. Morita, "Study on synchronous induction hybrid motors," in *Electrical Machines and Systems, 2009. ICEMS 2009. International Conference on*, 2009, pp. 1-6.

[76] Z. Bo, Z. Xiaoyong, Q. Li, C. Dajian, and L. Hu, "A integrated starter-generator based on flux memory machines for hybrid electric vehicles," in *Electrical Machines and Systems (ICEMS), 2011 International Conference on*, 2011, pp. 1-4.

[77] C. Yunyun, Q. Li, Z. Xiaoyong, W. Hua, and Z. Wang, "Electromagnetic Performance Analysis of Double-Rotor Stator Permanent Magnet Motor for Hybrid Electric Vehicle," *Magnetics, IEEE Transactions on,* vol. 48, pp. 4204-4207, 2012.

[78] P. Pisek, B. Stumberger, T. Marcic, and P. Virtic, "Design Analysis and Experimental Validation of a Double Rotor Synchronous PM Machine Used for HEV," *Magnetics, IEEE Transactions on,* vol. 49, pp. 152-155, 2013.

[79] Y. Pei, F. Chai, J. Shi, and S. Cheng, "Design of the double-stator permanent magnet synchronous starter and generator used in electric vehicles," in *Electrical Machines and Systems (ICEMS), 2011 International Conference on*, 2011, pp. 1-4.

[80] T. Raminosoa, T. Hamiti, M. Galea, and C. Gerada, "Feasibility and electromagnetic design of direct drive wheel actuator for green taxiing," in *Energy Conversion Congress and Exposition (ECCE), 2011 IEEE*, 2011, pp. 2798-2804.

[81] W. Wei, L. Chenjie, and B. Fahimi, "Comparative analysis of Double Stator Switched Reluctance Machine and Permanent Magnet Synchronous machine," in *Industrial Electronics (ISIE), 2012 IEEE International Symposium on*, 2012, pp. 617-622.

[82] M. Abbasian, M. Moallem, and B. Fahimi, "Double-Stator Switched Reluctance Machines (DSSRM): Fundamentals and Magnetic Force Analysis," *Energy Conversion, IEEE Transactions on*, vol. 25, pp. 589-597, 2010.

[83] E. Severson, R. Nilssen, T. Undeland, and N. Mohan, "Analysis of the bearingless AC homopolar motor," in *Electrical Machines (ICEM), 2012 XXth International Conference on*, 2012, pp. 570-576.

[84] M. Hippner and R. G. Harley, "High speed synchronous homopolar and permanent magnet machines comparative study," in *Industry Applications Society Annual Meeting, 1992., Conference Record of the 1992 IEEE*, 1992, pp. 74-78 vol.1.

[85] K. Sivasubramaniam, E. T. Laskaris, and J. W. Bray, "High Power Density HTS Iron Core Machines for Marine Applications," in *Power Engineering Society General Meeting, 2007. IEEE*, 2007, pp. 1-4.

[86] C. Young Han, L. Kwon Woo, K. Young Sun, and P. Il Han, "Analysis of Superconducting Homopolar Synchronous Motor using 3D inductance parameter," in *Electrical Machines and Systems, 2009. ICEMS 2009. International Conference on*, 2009, pp. 1-4.

[87] P. Tsao, M. Senesky, and S. Sanders, "A synchronous homopolar machine for high-speed applications," in *Industry Applications Conference, 2002. 37th IAS Annual Meeting. Conference Record of the*, 2002, pp. 406-416 vol.1.

[88] A. Walker, M. Galea, C. Gerada, A. Mebarki, and D. Gerada, "A Topology Selection Consideration of Electrical Machines for Traction Applications: Towards the FreedomCar 2020 Targets," in *Ecological Vehicles Renewable Energies (EVER), in press*, Monaco 2015.

[89] A. Walker, M. Galea, C. Gerada, A. Mebarki, and D. Gerada, "Design considerations for high performance traction machines:

Aiming for the FreedomCar 2020 targets," in *Electrical Systems for Aircraft, Railway, Ship Propulsion and Road Vehicles (ESARS), 2015 International Conference on*, 2015, pp. 1-6.

[90] H. Dogan, F. Wurtz, A. Foggia, and L. Garbuio, "Analysis of slot-pole combination of fractional-slots PMSM for embedded applications," in *Electrical Machines and Power Electronics and 2011 Electromotion Joint Conference (ACEMP), 2011 International Aegean Conference on*, 2011, pp. 611-615.

[91] J. Wang, Z. P. Xia, D. Howe, and S. A. Long, "Comparative Study of 3-Phase Permanent Magnet Brushless Machines with Concentrated, Distributed and Modular Windings," in *Power Electronics, Machines and Drives, 2006. The 3rd IET International Conference on*, 2006, pp. 489-493.

[92] O. K. Soon, K. Sung-Il, Z. Peng, and H. Jung-Pyo, "Performance comparison of IPMSM with distributed and concentrated windings," in *Industry Applications Conference, 2006. 41st IAS Annual Meeting. Conference Record of the 2006 IEEE*, 2006, pp. 1984-1988.

[93] T. M. J.R. Hendershot, *Design of brushless permanent-magnet motors*. Oxford: Clarendon Press, 1994.

[94] J. Goss, D. Staton, R. Wrobel, and P. Mellor, "Brushless AC interior-permanent magnet motor design: Comparison of slot/pole combinations and distributed vs. concentrated windings," in *Energy Conversion Congress and Exposition (ECCE), 2013 IEEE*, 2013, pp. 1213-1219.

[95] T. Miller. (2002-2009). *SPEED's Electric Machines*.

[96] L. Chong, R. Dutta, and M. F. Rahman, "Performance comparison between concentrated and distributed wound IPM machines used for field weakening applications," in *Electrical Machines and Power Electronics and 2011 Electromotion Joint Conference (ACEMP), 2011 International Aegean Conference on*, 2011, pp. 616-619.

[97] M. Galea, C. Gerada, T. Raminosoa, and P. Wheeler, "A Thermal Improvement Technique for the Phase Windings of Electrical Machines," *Industry Applications, IEEE Transactions on,* vol. 48, pp. 79-87, 2012.

[98] CD-adapco, "SPEED," vol. 9.02, ed, 2016.

[99] "MotorCAD," v9 ed: Motor Design LTD.

[100] Infolytica, "MagNet," 7.7 ed, 2016.

[101] J. Gieras and M. Wing, "Permanent magnet motor technology: design and applications," ed: Marcel Dekker, 2002.

[102] P. A. Hargreaves, B. C. Mecrow, and R. Hall, "Calculation of Iron Loss in Electrical Generators Using Finite-Element Analysis,"

IEEE Transactions on Industry Applications, vol. 48, pp. 1460-1466, 2012.

[103] A. Boglietti, "A first approach for the iron losses building factor determination," in *Conference Record of the 1999 IEEE Industry Applications Conference. Thirty-Forth IAS Annual Meeting (Cat. No.99CH36370)*, 1999, pp. 489-493 vol.1.

[104] N. Denis, S. Odawara, and K. Fujisaki, "Attempt to Evaluate the Building Factor of a Stator Core in Inverter-Fed Permanent Magnet Synchronous Motor," *IEEE Transactions on Industrial Electronics,* vol. PP, pp. 1-1, 2016.

[105] C. R. Sullivan, "High frequency core and winding loss modeling," in *Electric Machines & Drives Conference (IEMDC), 2013 IEEE International*, 2013, pp. 1482-1499.

[106] L. Chen, J. Wang, P. Lombard, P. Lazari, and V. Leconte, "Design optimisation of permanent magnet assisted synchronous reluctance machines for electric vehicle applications," in *Electrical Machines (ICEM), 2012 XXth International Conference on*, 2012, pp. 2647-2653.

[107] S. Ooi, S. Morimoto, M. Sanada, and Y. Inoue, "Performance Evaluation of a High Power Density PMASynRM with Ferrite Magnets," *Industry Applications, IEEE Transactions on,* vol. PP, pp. 1-1, 2013.

[108] R. J. Wang and G. C. Heyns, "Thermal analysis of a water-cooled interior permanent magnet traction machine," in *Industrial Technology (ICIT), 2013 IEEE International Conference on*, 2013, pp. 416-421.

[109] B. Zhang, R. Qu, J. Wang, W. Xu, X. Fan, and Y. Chen, "Thermal Model of Totally Enclosed Water-Cooled Permanent-Magnet Synchronous Machines for Electric Vehicle Application," *IEEE Transactions on Industry Applications,* vol. 51, pp. 3020-3029, 2015.

[110] C. Kral, A. Haumer, and T. Bauml, "Thermal Model and Behavior of a Totally-Enclosed-Water-Cooled Squirrel-Cage Induction Machine for Traction Applications," *IEEE Transactions on Industrial Electronics,* vol. 55, pp. 3555-3565, 2008.

[111] M. R. Guechi, P. Desevaux, P. Baucour, C. Espanet, R. Brunel, and M. Poirot, "On the improvement of the thermal behavior of electric motors," in *Energy Conversion Congress and Exposition (ECCE), 2013 IEEE*, 2013, pp. 1512-1517.

[112] Z. Li, J. Guo, D. Fu, G. Gu, and B. Xiong, "Research on heat transfer of spraying evaporative cooling technique for large electrical machine," in *Electrical Machines and Systems, 2009. ICEMS 2009. International Conference on*, 2009, pp. 1-4.

[113] M. Degano, P. Arumugam, W. Fernando, Y. Tao, Z. He, J. B. Bartolo, *et al.*, "An optimized bi-directional, wide speed range electric starter-generator for aerospace application," in *Power Electronics, Machines and Drives (PEMD 2014), 7th IET International Conference on*, 2014, pp. 1-6.

[114] R. Camilleri, D. A. Howey, and M. D. McCulloch, "Predicting the Temperature and Flow Distribution in a Direct Oil-Cooled Electrical Machine With Segmented Stator," *IEEE Transactions on Industrial Electronics,* vol. 63, pp. 82-91, 2016.

[115] M. Visaria and I. Mudawar, "Application of Two-Phase Spray Cooling for Thermal Management of Electronic Devices," *IEEE Transactions on Components and Packaging Technologies,* vol. 32, pp. 784-793, 2009.

[116] S. A. Semidey and J. R. Mayor, "Experimentation of an Electric Machine Technology Demonstrator Incorporating Direct Winding Heat Exchangers," *IEEE Transactions on Industrial Electronics,* vol. 61, pp. 5771-5778, 2014.

[117] S. Nategh, A. Krings, O. Wallmark, and M. Leksell, "Evaluation of Impregnation Materials for Thermal Management of Liquid-Cooled Electric Machines," *IEEE Transactions on Industrial Electronics,* vol. 61, pp. 5956-5965, 2014.

[118] Mathworks, "MATLAB," 2012a to 2016b ed, 2012- 2016.

[119] A. Boglietti, A. Cavagnino, D. Staton, M. Shanel, M. Mueller, and C. Mejuto, "Evolution and Modern Approaches for Thermal Analysis of Electrical Machines," *IEEE Transactions on Industrial Electronics,* vol. 56, pp. 871-882, 2009.

[120] D. G. Dorrell, "Combined Thermal and Electromagnetic Analysis of Permanent-Magnet and Induction Machines to Aid Calculation," *IEEE Transactions on Industrial Electronics,* vol. 55, pp. 3566-3574, 2008.

[121] T. A. Jankowski, F. C. Prenger, D. D. Hill, S. R. O. Bryan, K. K. Sheth, E. B. Brookbank, *et al.*, "Development and Validation of a Thermal Model for Electric Induction Motors," *IEEE Transactions on Industrial Electronics,* vol. 57, pp. 4043-4054, 2010.

[122] F. P. Incropera, *Introduction to heat transfer*, 4th ed. New York: Wiley, 2002.

[123] W. Tong, *Mechanical design of electric motors*, 1st ed. London: CRC Press, 2014.

[124] J. Pyrhonen, *Design of rotating electrical machines*, 2nd ed. Chichester, West Sussex, United Kingdom: Wiley, 2014.

[125] W. Li, X. Zhang, S. Cheng, and J. Cao, "Thermal Optimization for a HSPMG Used for Distributed Generation Systems," *IEEE Transactions on Industrial Electronics,* vol. 60, pp. 474-482, 2013.

[126] A. J. Grobler, S. R. Holm, and G. v. Schoor, "A Two-Dimensional Analytic Thermal Model for a High-Speed PMSM Magnet," *IEEE Transactions on Industrial Electronics*, vol. 62, pp. 6756-6764, 2015.

[127] (2016). *Thermal Conductivity of some common Materials and Gases*. Available: http://www.engineeringtoolbox.com/thermal-conductivity-d_429.html

[128] A. M. E.-. Refaie, J. P. Alexander, S. Galioto, P. B. Reddy, K. K. Huh, P. d. Bock, *et al.*, "Advanced High-Power-Density Interior Permanent Magnet Motor for Traction Applications," *IEEE Transactions on Industry Applications*, vol. 50, pp. 3235-3248, 2014.